Experimental Investigations on Cold-Sprayed Ti-Based Coatings for Bio-Implant Applications

Doctoral Thesis

by

"Avneesh Kumar"

(2017MEZ0034)

DEPARTMENT OF MECHANICAL ENGINEERING

INDIAN INSTITUTE OF TECHNOLOGY ROPAR

April, 2023

Experimental Investigations on Cold-Sprayed Ti-Based Coatings for Bio-Implant Applications

A Thesis Submitted
In Partial Fulfilment of the Requirements
for the Degree of

DOCTOR OF PHILOSOPHY
by

"Avneesh Kumar"

(2017MEZ0034)

DEPARTMENT OF MECHANICAL ENGINEERING

INDIAN INSTITUTE OF TECHNOLOGY ROPAR

April, 2023

DEDICATED

TO

MY LATE GRANDMOTHER

ISHWARKALI DEVI

DECLARATION

I declare that this work entitled "**Experimental Investigations on Cold-sprayed Ti-Based Coatings for Bio-implant Applications"** has not previously been accepted in substance for any degree and is not being simultaneously submitted in candidature for any other degree. This thesis is being submitted in partial fulfilment of the requirements for the degree of PhD in Mechanical Engineering. This thesis is the result of my own independent investigation, except where otherwise stated. I have acknowledged all the other sources by stating the references explicitly. I declare that any idea/data/fact/source stated in my thesis has not been fabricated/falsified/misrepresented. All the principles of academic honesty and integrity have been followed. I understand that any violation of the above will be cause for disciplinary action by the Institute and can also evoke penal action from the sources which have thus not been properly cited or from whom proper permission has not been taken when needed. I hereby give consent for my thesis, if accepted, to be available online in the Institute's Open Access repository and for inter-library loan, and for the title and abstract to be made available to outside organizations.
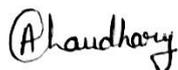
Signature

Name: Avneesh Kumar

Entry Number: 2017mez0034

Program: PhD

Department: Department of Mechanical Engineering

Date: 05-04-2023

CERTIFICATE

It is certified that the work contained in the thesis titled **"Experimental Investigations on Cold-sprayed Ti-Based Coatings for Bio-implant Applications"** by **"Avneesh Kumar"** has been carried out under my/our supervision and that this work has not been submitted elsewhere for the award of any degree.

Signature of the Supervisor
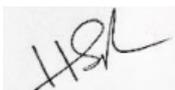
Signature of the Supervisor

Prof. Harpreet Singh

Dr. Ravi Kant

Department of Mechanical Engineering

Department of Mechanical Engineering

Indian Institute of Technology Ropar

Indian Institute of Technology Ropar

Rupnagar, Punjab 140001

Rupnagar, Punjab 140001

Date: 05-04-2023

Date: 05-04-2023

ACKNOWLEDGMENTS

LAY SUMMARY

The human body is made up of 206 bones and more than 300 joints. Synovial joints like hip, shoulder, and knee are extraordinary bio-tribological systems in humans. These joints face significant challenges during their usage as they transmit high loads and provide a wide range of movements to the body. Arthritis is a disease led to the failure of these joints, which can affect anyone irrespective of age, gender, and race. Many solutions are available to overcome the problem, including steroid injections and implants. However, steroid injections have several drawbacks, such as short life expectancy, painful while injecting, and work only for a few patients. Bio-implant devices replace joints with metallic, ceramic, or polymeric materials. The average life expectancy of a bio-implant is 10-15 years, making it a better choice than steroid injections. However, it also has some drawbacks like the material used for the implant may corrode, wear, or toxicant the human body environment. These problems can further lead to several diseases like Alzheimer, Neuropathy. Therefore, bio-implant manufacturing is very crucial.

Manufacturing of bio-implants is a two-step process: initially, the base of the bio-implant needs to be manufactured by using an economical biomaterial with desirable properties (corrosion-resistant, wear-resistant, and biocompatibility.). The second step involves the surface modification of the developed implant employing the best suitable biomaterial and surface modification techniques.

Surface coating is one of the well accepted surface modification techniques of bio-implants to achieve the desired properties. Thermal spray technology (plasma spray) is approved by the food and drug administration (FDA) USA to deposit biomaterials on bio-implant surfaces. However, high processing temperature in thermal spray changes biomaterial's characteristics such as phase change and oxidation. Cold spray, a relatively new technology, can overcome the above problems because of its low processing temperature. The most widely accepted commercially used biomaterials are hydroxyapatite and titanium alloys for the surface modification of bio-implants. Literature reports that plasma-sprayed baghdadite can replace hydroxyapatite due to its better mechanical properties.

Therefore, a new material combination, titanium/baghdadite composite, was deposited on biomedical steel using the cold spray in this work. Moreover, the coatings' mechanical, chemical and biological performance were investigated. It was observed that during the deposition biomaterials remained same. The deposited coatings were successful in reducing the corrosion and wear of bio-implant SS316L steel surface. Moreover, the surface remained biocompatible and were successful to mitigate the titanium/hydroxyapatite composite coatings. Thus, the investigated coatings can be used to enhance the service life of bio-implant surface. Though, some in-vivo testings of these coatings needs to be done in order to recommend them for actual bio-implants.

ABSTRACT

As per the published data, the orthopedic implant market is growing exponentially. The life of implants is expected to be up to 15-20 years, depending upon various factors such as gender, age, and patient's body mass index. Hence, it is crucial to enhance the service life of orthopedic implants, which may further enhance the comfort of the implant users by delaying the implant replacement surgeries.

Corrosion and wear contribute significantly to the degradation of bio-implants. Released ions and worn-out material (wear debris) leave toxic effects on the human body and promote several diseases such as Alzheimer's and Neuropathy. Therefore, the manufacturing of bio-implants is crucial. SS316L is a biomedical steel having excellent mechanical, good corrosion, and wear properties and is widely used for bio-implants manufacturing. The manufacturing of implants is a two-step process that includes manufacturing base parts and surface modification of these parts to improve their surface characteristics. Corrosion and wear largely depend on the surface properties of the bio-implants. The Food and Drug Administration U.S. has approved thermal spray coatings for implant surface modifications. However, the high temperature involved in thermal spraying causes changes in the material's original characteristics. In this regard, the cold spray process has been considered very promising for depositing temperature-sensitive materials on SS316L. Cold spraying has many advantages over thermal spraying, such as no change in phase, no oxidation, and better mechanical properties due to low processing temperature. A plenty of research work has been published on surface preparation in cold spraying. There are studies regarding substrate roughness effect on bonding in cold spray, however most of these are for the cold spraying of softer materials on soft/hard substrates. Therefore, a need was realized to understand the effect of surface preparation for cold spraying hard particles on hard substrate. Cold spraying of titanium-based powders on the SS316L substrate with different level of surface roughness is unavailable.

In the current work, single-pass Ti/20TiO$_2$ composite powder was cold-sprayed on SS316L steel substrates having three different roughness levels to understand the effect of substrate roughness on the coating adhesion. Ti/20TiO$_2$ coated substrates were analyzed using scanning electron microscopy (SEM), energy dispersive spectroscopy

(EDS), and scratch tester. The mirror-polished (MP) was found to be the most suitable surface condition to deposit the chosen Ti-based powders on SS316L steels with a good adhesion. This may be attributed to adequate Ti-particle deformation, which led to proper jetting formation and afterward good adhesion. Therefore, titanium-based powders in distinct compositions have been deposited on MP SS316L using high-pressure cold spray. Two types of reinforcement's viz. TiO_2 and baghdadite (BAG) were used. BAG is used to explore it as a replacement for mechanically weaker hydroxyapatite (HA). The deposited coatings were analyzed using SEM, EDS, and X-ray diffractometer (XRD). Furthermore, the coated and uncoated SS316L steel were characterized for porosity analysis, density calculation, surface roughness measurement, microhardness measurement, wettability, and biocompatibility. Corrosion and sliding wear behavior of the cold spray coated and uncoated SS316L steels were studied under a dry and simulated body fluid environment.

Among the cold-sprayed Ti/TiO_2 coatings, $Ti/20TiO_2$ coating exhibited a relatively rough, hard, and dense surface in comparison with the uncoated SS316L surface, the average surface roughness, microhardness, and density were found to decline with the increase in TiO_2 content. Electrochemical corrosion studies of the Ti/TiO_2 composite coatings revealed that all the coatings reduced the corrosion of the substrate. However, corrosion performance dropped with the increase in TiO_2 content. Dry sliding wear results indicated that only $Ti/20TiO_2$ composite coating was successful in reducing the wear losses of SS316L steel. Superior microhardness and better retention of TiO_2 in Ti/TiO_2 coating have been ascribed as the reasons for its superior performance. All the other Ti/TiO_2 coatings failed to protect the substrate against sliding wear. In general, abrasion wear was recognized as the dominant mechanism of wear for these coatings. Signatures of adhesive wear mechanisms were also observed over the worn-out coating surfaces. From the combined results of corrosion and sliding wear, $Ti/20TiO_2$ coating can be recommended as a potential candidate to reduce the corrosion and wear of SS316L steel.

For the cold-sprayed titanium/baghdadite (Ti/BAG) coatings, the average density and surface roughness of the coatings were observed to reduce with the increase in BAG content. The average microhardness and scratch resistance of Ti/BAG coatings increased up to 15% of BAG content, and beyond that the both start declining. Cold-sprayed Ti/BAG coatings were found hydrophilic in nature, and the hydrophilicity was

seen improving with the increase in BAG content. The coatings showed good cell viability, which was found to enhance with BAG content.

The electrochemical corrosion tests were performed for 2 hours (hr), 16 hr, and 40 hr of immersion times in simulated body fluid environment. All the Ti/BAG coatings successfully reduced the corrosion rates for all the cases of immersion times. Moreover, the corrosion resistance was found to increase with the increase in BAG content as well as immersion time. Formation of passive oxide (TiO_2) and dissolution of BAG into CaO, SiO_2, and ZrO_2 have been ascribed as the reasons for their excellent corrosion performance in simulated body fluid environments. The corrosion rates of the Ti/BAG composite coatings were compared with Ti/HA coatings, which established the Ti/BAG as a better option for the given environment. Sliding wear tests were performed following ASTM G99 standards. It was observed that Ti/15BAG composite coating performed best among all the investigated coatings against sliding wear under the dry as well as the simulated body fluid environment. The superior performance of Ti/15BAG coating could be attributed to a better combination of its microhardness and scratch resistance. Signatures of micro-cutting, micro-cracks, delamination, and material transfer were observed on the worn-out Ti/BAG coatings, indicating abrasive and adhesive wear as the sliding wear mechanism. Once again, Ti/BAG coatings were found to be superior to the reported Ti/HA coatings in terms of wear rate. Based upon the overall results, Ti/15BAG composite coating can be recommended as the best choice to reduce the corrosion and wear of SS316L steel in dry as well as simulated body fluid environments. Moreover, Ti/15BAG composite coating was found to perform better than Ti/20TiO$_2$ coating against corrosion and wear.

Laser surface melting was performed to eliminate the pores and improve the mechanical properties of as-sprayed coatings. Laser treatment of the coatings led to the recrystallization of Ti in deposited coatings without any adverse effect on the substrate. Equiaxed grains formed in the top layers of laser-treated Ti/BAG coatings, improved the density and microhardness of the as-sprayed coatings. All the laser-treated coatings were subjected to electrochemical corrosion tests in the simulated body fluid environment for 2 hr of immersion time. It was observed that the laser treatment improved the corrosion resistance of Ti/BAG coatings as compared to the respective as-sprayed coatings. Reduction in porosity and improvement in density are believed to be the reason for their better corrosion behavior in simulated body fluid. The sliding wear

performance of the laser-treated coatings was also better than these as-sprayed coated counterparts under the simulated body fluid environment. The enhanced microhardness of laser-treated Ti/BAG coatings has been ascribed as the reason for their better sliding wear resistance. The signatures of micro-cutting, delamination, and material transfer were seen on the surfaces of the worn-out laser-treated coatings, however, these were relatively less severe than that of the respective as-sprayed coatings. Abrasion and adhesion wear were recognized as the main mechanism of wear. Among the laser-treated coatings, the Ti/15BAG coating was found to be the best to control corrosion and wear. Moreover, for the tribological joints of the bio-implant, laser-treated cold-sprayed Ti/15BAG coating can be recommended as a better choice since porosity is not a major concern at these joints.

LIST OF PUBLICATIONS

Publications from Thesis

1. **A. Kumar**, H. Singh, R. Kant, N. Rasool, Development of Cold Sprayed Titanium/Baghdadite Composite Coating for Bio-implant Applications, **Journal of Thermal Spray Technology**. (2021); 30, 2099–2116.

2. **A. Kumar**, R. Kant, H. Singh, Tribological Behavior of Cold-Sprayed Titanium/Baghdadite Composite Coatings in Dry and Simulated Body Fluid Environments, **Surface and Coatings Technology**. (2021); 425, 127727.

3. **A. Kumar**, H. Singh, R. Kant, Effect of Substrate Roughness and Ceramic Content on Deposition Characteristics of Cold-Sprayed Ti/TiO$_2$ Composite Coatings, **Met. Mater. Int.** (2022). https://doi.org/10.1007/s12540-022-01323-4

4. **A. Kumar**, D. K. Goyal, R. Kant, H. Singh, Enhancing Corrosion Performance of Cold-Sprayed Titanium/Baghdadite (Ti/BAG) Bio-Composite Coatings via Laser Treatment, **Coatings**. (2022); 12(7):1010.

5. **A. Kumar**, R. Kant, H. Singh, Microstructural and tribological properties of laser - treated cold - sprayed titanium / baghdadite deposits**, Journal of Materials Research.** (2022); 37, 2698–2709.

Other Publications during PhD Program

1. N.K. Singh, **A. Kumar**, A.S.M. Ang, D.K. Mahajan, H. Singh, Characterization and Slurry Erosion Mechanisms of Nickel-Based Cermet Coatings on Monel K-500, **Journal of Thermal Spray Technology**. (2021); 30, 2138–2154.

2. G. Vinay, **A. Kumar**, P. Singh, H. Singh, Perspectives on Cold Spray: Introduction, Evolution and Future, **Under Review**

3. **A. Kumar**, G.D. Thakre, M.F. Wani, Influence of Load and Speed on Tribological Performance of Cu Nanofluids in EHL line Contacts, Materials Today Proceedings (2019) 1–9.

CONTENTS

LIST OF FIGURES

xviii

xix

LIST OF TABLES

LIST OF ABBREVIATIONS

Abbreviations	Description
AR	As-Received
ASI	Adiabatic Shear Instability
BAG	Baghdadite
BCC	Body-Centered Cubic
CoC	Ceramic-on-Ceramic
CoF	Coefficient of Friction
CoP	Ceramic-on-Polymer
CVD	Chemical Vapor Deposition
D	Depth of The Indentor
D-GUN	Detonation Gun Spray
DLC	Diamond-like Carbon
EBSD	Electron Backscatter Diffractometer
ECM	Extra-Cellular Matrix
EDS	Energy Dispersive Spectroscopy
FDA	Food and Drug Administration
F_f	Frictional Force F_f
GP	Ground-Polished
HA	Hydroxyapatite
HCP	Hexagonal Closed Packed
HPCS	High-Pressure Cold Spray
HVOF	High Velocity-Oxy Fuel Spray
HXPE	Highly Cross-Linked Polyethylene
IASI	Intra-Articular Steroids Injections
LPCS	Low-Pressure Cold Spray
MB	Metallurgical Bonding
MI	Mechanical Interlocking
MoC	Metal-on-Ceramic
MoM	Metal-on-Metal
MoP	Metal-on-Polymer

MP	Mirror-Polished
OA	Osteoarthritis
OCP	Open Circuit Potential
OM	Optical Microscopy
PEEK	Polyethylene Ether Ketone
PLS	Phospholipids
PMMA	Polymethyl Methacrylate
PoD	Pin-on-Disc
PVD	Physical Vapor Deposition
R_a	Arithmetic Mean Roughness
R_z	Ten-Point Height of Irregularities
SEM	Scanning Electron Microscopy
SOD	Stand-off Distance
Ti	Titanium
TS	Thermal Spray
UHMWPE	Ultra-High Molecular Weight Polyethylene
XRD	X-Ray Diffractometer

CHAPTER 1

INTRODUCTION

The human body is made up of 206 bones and more than 300 joints. Synovial joints like hip, shoulder, and knee are extraordinary bio-tribological systems in humans. These joints face significant challenges during their usage as they transmit high loads and provide a wide range of movements to the body. Among them, the hip is one of the busiest joints in performing its function. A typical schematic of a hip joint is shown in Fig. 1.1. At the hip, the upper part of the femur, the femoral head, separates the lower part of the pelvic, the acetabulum, by a synovial fluid cavity. Synovial fluid helps in lubrication between the contacting surfaces and also helps in supporting the load carried by the bones. The ends of these long bones are supported by a tissue called cartilage, as shown in Fig. 1.1. Cartilage helps to support the load carried by the bones at the joint and helps in lubrication between the contacting surfaces (Singleton and LeVeau, 1975).
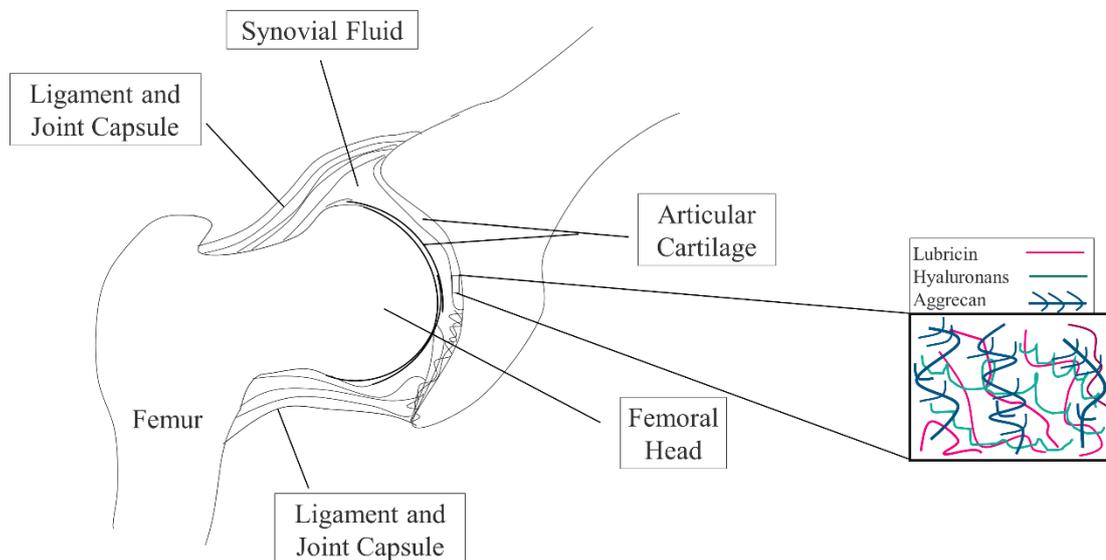
Figure 1.1: Schematic of a typical bio-tribological system (hip joint) (Singleton and LeVeau, 1975)

Cartilage is a deformable and porous tissue. It has a biphasic structure, contains 75 percent of water, and the rest is the extra-cellular matrix (ECM). The matrix consists of

collagen, proteoglycans, non-collagenous proteins, and chondrocytes. Collagen is the main fiber present in ECM and is responsible for cartilage shape. Proteoglycans are responsible for the cartilage's hydration and enduring the compressional load. Chondrocytes are specialized cells that help synthesize and maintain the cartilage matrix. The outer surface of the cartilage contains hyaluronans. Macconaill (Macconaill, 1961) reported that the load-bearing capacity of the joint majorly depends on the interstitial fluid present in the cartilage. From the tribological point of view, pressure and film thickness of interstitial fluid are the two most crucial factors for natural joints. It is reported that synovial joints like the hip show coefficient of friction (CoF) around 0.001 (Sophia Fox et al., 2009). High CoF during sliding may lead to cartilage damage and Osteoarthritis (OA). In vivo, CoF for the whole joint varies from 0.001 to 0.03. Friction between the articulating surfaces causes energy dissipation at the joint (Sophia Fox et al., 2009). High friction leads to high shear strain which further leads to the wear of cartilage. Cartilage damage leads to disruption of lubricant and further deterioration of subchondral bones.

Cartilage provides lubrication through synovial fluid. The word synovia, described as a fluid oily in nature between the natural joints, was given in the sixteenth century by Paracelsus. Synovial fluid contains hyaluronate, lubricin, and glycosaminoglycans as major components (Sophia Fox et al., 2009). Research shows two types of lubrication regimes, that is, fluid film lubrication and boundary lubrication for articular cartilage of the hip joint. Further, research revealed that the typical hip joint works as a journal bearing of a machine, and a thin film type of lubrication is present (Ure, 1955).

On the other hand, experimental data showed boundary lubrication at the hip joint (Ogston and Stanier, 1953), (Crockett, 2009). Further investigations have been conducted to understand the reason for it. The results revealed that cartilage loses its interstitial fluid and forms a boundary type of lubrication under loading conditions. However, cartilage gains its lubricity back (this phenomenon of losing and regaining lubricity is called rehydration) and works as a lubricant for the development of fluid film lubrication during rest (Burris and Moore, 2017). During boundary lubrication, molecules like hyaluronate, lubricin, and phospholipids (PLs) work as boundary lubricants and play a significant role in maintaining low friction and wear at the joint (Daniel, 2012; Ogston and Stanier, 1953).

1.1 Arthritis

Arthritis is a group of diseases representing more than 100 diseases affecting the joints and/or surrounding tissues such as bones, muscles, and tendons. These diseases affected more than 323 million people in 2017 all across the world ("Erratum: Global, regional, and national incidence, prevalence, and years lived with disability for 354 diseases and injuries for 195 countries and territories, 1990–2017: a systematic analysis for the Global Burden of Disease Study 2017 (The Lancet (2018)," 2019). There is no permanent solution available to prevent or cure Arthritis, using behavioural or medical help except few cases. Arthritis is categorized into two main groups; inflammatory arthritis and degenerative arthritis (Lorig et al., 1987).

Inflammation is a healing process of any tissue or organ that protects the viral, bacterial, or burn condition. However, inflammation occurs without reason in conditions like inflammatory arthritis, indicating that one's immune system is striking its joint. It is more predominant in females than males. In these situations, joints become stiff, inflammatory, and painful. Bone erosion is the most common effect of these symptoms. The most popular type of inflammatory arthritis is rheumatoid arthritis (Østergaard et al., 2008). The immune system's attack on joints also promotes degenerative arthritis; however, the main cause of failure is the breakdown of the extra-cellular matrix, intracellular alarming, and plasma protein damage of cartilage tissue. Sometimes this condition may occur because of some major abnormalities in the joint. This cartilage thinning and joint space narrowing phenomenon is called osteoarthritis (OA). However, OA also reportedly follows the inflammation of the synovial membrane (Abramoff and Caldera, 2020). OA is prominently affecting the younger generation. Kurtz et al. (Kurtz et al., 2009) reported in their study that OA caused 41% of younger patients (less than 65 years) to have a hip implant in 2006, which will increase to 52% in 2030.

1.2 Solutions to Arthritis

Among the synovial joints, the hip is one of the essential joints when it comes to load-carrying capacity. Arthritis is one of the most common reasons for hip joint failure, as discussed above. Other than that, it can also fail in some adverse conditions like joint abnormalities, excessive load transmission, and some accidental injuries. Once the hip joint fails, there is no promising recovery solution. However, some temporary solutions such as non-steroid anti-inflammatory

drugs or Intra-articular Steroids Injections (IASI) are available in the market. They may help to save the joint for a few months. Another possible solution is hip implantation.

1.2.1 Steroid Injections Therapy

IASI therapy procedure includes injecting steroids into the hip capsule to overcome the inflammatory, stiffness, and painful condition. The most popular steroids used in this therapy are corticosteroid and hyaluronic acid (Altman, 2003), (Bowman et al., 2018). Delgado-Noguera et al. (Delgado-Noguera et al., 2016) reviewed the advantages and disadvantages of corticosteroid injection therapy on children with inflammatory arthritis and concluded that corticosteroid injection could be effective for rheumatoid arthritis patients. Qvistgaard et al. (Qvistgaard et al., 2006) studied the effect of corticosteroid and hyaluronic acid in the intra-articular treatment of degenerative arthritis. They concluded corticosteroids could be more beneficial in combating osteoarthritis than hyaluronic acid. Hyaluronate is a high molecular weight molecule that naturally occurs within the cartilage and synovial fluid, and its primary function is to help synovial fluid serve as a lubricant (Sophia Fox et al., 2009). Hyaluronic acid is generally used to improve the synovial fluid's viscosity and the joint's gliding motion. However, these steroids have some disadvantages, such as bone loss and erythema (Sedrak et al., 2021). IASI therapy is quite painful and costly; infection while injecting is high, and short life expectancy is an issue. There are always compatibility issues, and these injections do not work for all patients (Oren-Ziv et al., 2015), (Smolen and Aletaha, 2015).

1.2.2 Bio-implantation

Bio-implant is the equipment used to substitute and entertain a missing natural body part. A hip implant is a device used to replace an arthritic hip for the proper functioning of the hip joint. The schematic of hip implant is shown in Fig. 1.2.
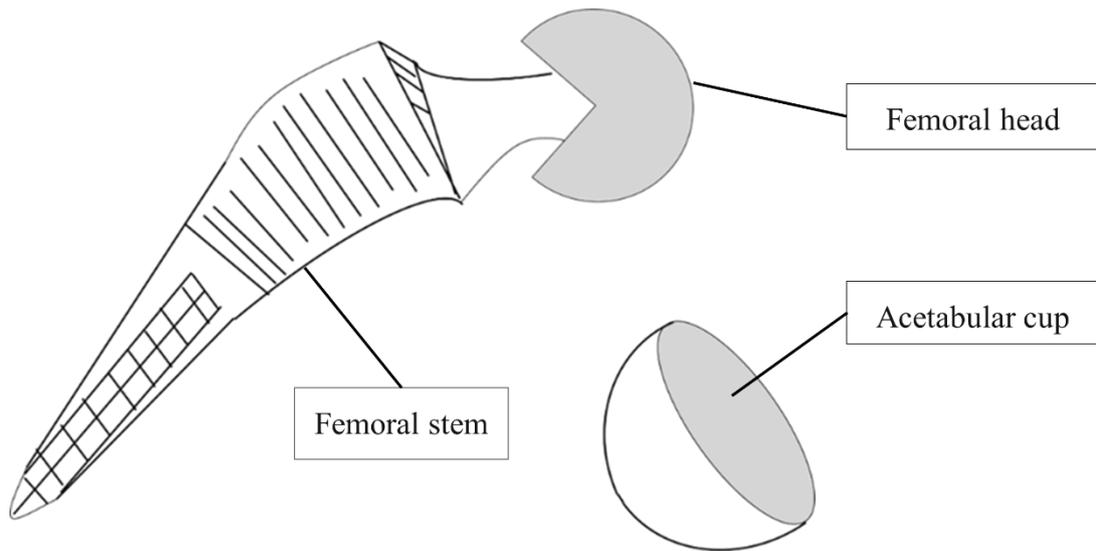
Figure 1.2: Schematic representation of hip implant components

In the 1890s, the concept of hip implants came into existence when German scientist Professor T. Gluck presented his work to replace the femoral head of a tuberculosis patient's hip joint with ivory (Gluck, 1890). However, this solution did not last long due to the development of infections using these materials. Later in 1923, Smith-Peterson proposed to use glass to replace the femoral head. However, it had some issues due to which, in 1938, they used cobalt-chromium (Hernigou, 2014). These implants also failed to achieve desired objectives due to wear problems. John Charnley developed a cemented low friction hip implant (in 1961) which proved to be a benchmark in the history of the hip implant. He achieved low friction and minimal wear using stainless steel as femoral head material and polyethylene as acetabular material (Bezwada et al., 2012).

Over the years, with the advancement in technology, hip implant life has reached up to 10-15 years. Nowadays, patients, irrespective of their age, are having these treatments, so it is necessary to enhance the service life of these implants. To achieve better performance, the fixation of the implant is crucial. There are two types of fixations which have been tried by clinical surgeons, are, cemented fixation and uncemented fixation. In cemented fixation, the femoral stem is covered by bone cement, and the acetabular cup is made up of cemented material and directly fixed into the pelvic bone; cemented material is generally polymethyl methacrylate (PMMA). PMMA is a polymer that does not make any chemical bond with the bone. For uncemented fixation, the

surface of the implants is usually made rough and porous using a coating of material like hydroxyapatite (Morshed et al., 2007), (D'Antonio et al., 2001). The latter helps in bone growth onto the surface of the implant. The major components of a typical hip implant are the femoral stem, femoral head, and acetabular cup. A couple of hip implants are available in the market - modular and monoblock designs are the most common among them. In modular design, the femoral head and stem are made as different parts and connected through a taper locking mechanism. The acetabular cup consists of a shell fixed to the pelvic bone and a liner attached inside the shell. In monoblock design, the femoral head and stem come in one piece. The acetabular cup also comes in one piece (Gao et al., 2017). Several factors influence the life of a hip implant, such as gender, age, and body mass index of the patient (X. Zhang et al., 2019). Diseases like hypertension and diabetes in patients also adversely affect the life of hip implants (Memtsoudis et al., 2010). Moreover, implanted material is the most influential parameter affecting a hip implant's life.

1.3 Biomaterials

Biomaterials are the materials used to replace human bones or tissues without leaving any harmful effects on the human body. The life of implants largely depends on the properties, functions, biocompatibility, and structure of biomaterials. Thus, the selection of biomaterials is critically important for bio-implantations. Several materials have been tried over the years, from ivory to titanium (Ti) alloys (Gluck, 1890), (Ghosh et al., 2018). The following combinations have been tried for hip implantation based on the materials used; metal-on-polyethylene (MoP), metal-on-metal (MoM), ceramic-on-metal (CoM), ceramic-on-ceramic (CoC), ceramic-on-polymer (CoP).

1.3.1 Ceramics

Since the first use of hip arthroplasty, ceramics have been popular for hip implants because of their high wear resistance. Ivory was one of the first ceramic materials that have been used for hip implantation [1]. Following that, many other materials were explored, including alumina, zirconia, titania, and hydroxyapatite (Khanna et al., 2014), (Luo et al., 2018), (Herrera et al., 2015). Ceramic materials are usually hard and brittle, which causes the generation of an irritating noise (squeaking) during rubbing in CoC (Askari et al., 2015). The fracture of ceramic hip implants is also a very common cause of implant failure because of their poor fracture toughness (Yoo et al., 2005).

1.3.2 Metals and Their Alloys

Metals are the most widely accepted biomaterials for hip implants because of their good mechanical, chemical, and biological properties. Popular metallic materials used by surgeons for hip implantation have the common problem of higher elastic modulus, resistance to bone growth, and poor wear resistance. Smith and Peterson (Hernigou, 2014) used cobalt-chromium as an implanted material; the low chemical inertness of cobalt-chromium is a concern for implants. After a few years, John Charnley used stainless steel as a hip implant biomaterial; stainless steel has low strength, good corrosion resistance, and ductility. Later, it is followed by the use of Ti and its alloys, which is now the most popular choice for hip implantation among other metal counterparts because of their excellent corrosion resistance and biocompatibility.

1.3.3 Polymers

The use of polymers as implanted liner material for hips has grown over the years because of their good biocompatibility and high load-carrying capacity. The three important categories of polymers for hip liners are; polyethylene ether ketone (PEEK), highly cross-linked polyethylene (HXPE), and now ultra-high molecular weight polyethylene (UHMWPE). Charnley introduced UHMWPE in 1962 to overcome the bioavailability issue of stainless steel for hip implant application. The most important characteristic of these polymers is that they do not chemically react with the human body environment and hence gained much popularity for hip implant bearings. However, lack of wear resistance and degradation in the human body are the major problems with these materials.

1.4 Problems Associated with Bio-implants

Bio-implants face several issues when implanted into the human environment, including biocompatibility, corrosion, and wear. Therefore, it is important to consider these issues before implanting the biomaterial in the human body. These issues are discussed below in detail;

1.4.1 Biocompatibility

The ability of a material to sustain itself in a biological environment without leaving any harmful effect on surroundings can be defined as biocompatibility (Asri et al., 2017), (Jacobs et al., 1998). The biocompatibility of bio-implants depend on numerous factors, including biomaterial composition, surface roughness, surface wettability, and size of the implants (Singh and Dahotre, 2007). The biological reaction between

7

implants and its surrounding sometime leads to the degradation of biomaterials and toxic effect on the body's environment. Corrosion of biomaterials under the human body leads to the release of ions, which can be toxic to the human body and can also reduce the life of implants. For example, Co-Cr alloy-based implants release cobalt and chromium ions, forming cancerous tumours. Similarly, corrosion of stainless steel leads to the release of chromium and nickel, which caused to affects the skin and central nervous system. Ti-based alloys such as Ti6Al4V lead to the release of vanadium and aluminum, and these cause diseases such as Alzheimer's and Neuropathy (Jacobs et al., 1998). Wear of biomaterials generates debris, damaging the nerves of the human body when flowing inside the human body. Also, this wear debris reacts with the biological system and causes osteolysis and allergy (Tritschler et al., 1999; Wang et al., 2017). The design of implants also influences the biocompatibility of bio-implants; it makes the surgery painful and also affects the life of implants. Biofilm formation is one of the major factors that influence the biocompatibility of implants. It forms when pathogens attach to the implant surface and produce an extra-cellular polymeric substance. Biofilm on implant surfaces can severely affect implants' life and lead to health issues (Arciola et al., 2012; Barros et al., 2015)

1.4.2 Corrosion

Corrosion is defined as the deterioration of material while exposed to the surrounding environment. It is one of the major reasons behind the failure of metals and their alloys when implanted in the human body (Eliaz, 2019). The human body environment is highly corrosive; implants release ions in the human body through chemical or electrochemical reactions. These chemical reactions proceed towards a thermodynamic equilibrium, which can be evaluated through electrochemical behavior testing in electrochemical cells. In electrochemical cells, oxidation and reduction are the two important processes taking place at the anodic and cathodic sites, respectively. At an anode, metal or its alloys are forced to release electrons by supplying electric energy from the external source, which leads to oxidation at the anode. At equilibrium, electrons flowing on both surfaces become equal; hence, the net current flow into the cell becomes zero. In other words, the rate of oxidation and reduction become equal. At equilibrium, the current flowing through the electrodes is called corrosion current (i_{corr}) and the corresponding potential is called open circuit potential or corrosion potential

(E_{ocp} or E_{corr}) (Popov, 2015). The human body is corrosive as it has a pH value of 7-7.35 (Kokubo and Takadama, 2006).

Most biomaterials release ions when exposed to the human body environment. However, on exposure, they form protective oxide layers between the metal and electrolyte (biological fluid) and provide resistance against corrosion. The corrosion response of biomaterials depends on various factors such as composition, surface properties, and microstructure (Jacobs et al., 1998). For instance, stainless steel has chromium and, when exposed to bio-fluid, forms chromium oxide and protects the steel substrate against corrosion (Chen and Thouas, 2015). Similarly, Co-Cr-based alloys also form a protective chromium oxide layer (Eliaz, 2019). In the case of Ti and its alloys, they form TiO, TiO_2, and Ti_2O_3 when exposed to body fluid. These oxides are very thin, mostly in nanometres, and protect Ti sublayers against corrosion (Pouilleau et al., 1997).

Pitting, galvanic, fretting, crevice, stress corrosion cracking, and fatigue corrosion are some popular types of corrosion occurring in implant biomaterials (Chen and Thouas, 2015). Pitting is characterized as a localized form of corrosion. It normally occurs due to the collapse of passive layers over the metallic subsurface (Olmedo et al., 2008). Galvanic corrosion is more common when two or more metals with different nobility are placed in a corrosive environment and connected electrically. The metal with lesser nobility works as the anode (experiences high corrosion) and will lead to galvanic corrosion (Soares et al., 2021). Fretting corrosion occurs due to the small amplitude vibrations induced by rubbing action under a corrosive environment. Orthopedic implants undergo fretting corrosion at the interface of the joints, such as the femur stem and bone in the hip, at the time of implantation or after some years of service (Tritschler et al., 1999). Crevice corrosion occurs in the space between two surfaces, usually because of the stagnant electrolyte. In orthopedic implants, it is a very common phenomenon (for example, at the interface of the femoral head and femoral stem) (Levine and Staehle, 1977). Degradation of materials under cyclic loading in a corrosive medium leads to fatigue corrosion. This leads to the formation of cracks into the implanted surfaces. Corrosion-induced pitting accompanied by cyclic loading is normally the cause of crack initiation in implants (Fleck, 2008). Besides this, stress corrosion cracking is a very common type of degradation of implanted biomaterials. It occurs due to the tensile stress-induced crack under corrosive media. The tensile stress

may develop because of heat treatments, cold working, machining, and/or welding (Jafari et al., 2015).

1.4.3 Wear

Wear is defined as a progressive loss of material under the action of rubbing between two contacting surfaces. It is one of the primary reasons for the failure of bio-implants. Wear of implant surfaces causes the loosening of implants and leads to osteolysis (Harris, 2001). Therefore, improving the wear resistance of implants is one of the key areas in orthopedic implants. CoC bearing surfaces show the minimum volumetric wear among MoP, CoP, MoM, and CoM bearings (Ciulli et al., 2014). However, the fracture of ceramic surfaces and squeaking limit its application for implantations.

On the other hand, MoM shows good mechanical, chemical, and biological properties but lacks wear resistance. Cobalt-chromium alloys on cobalt-chromium alloys are some of the most widely used MoM bearing implants system because of their better wear resistance than the other MOM systems (Chan et al., 2018). Poor wear resistance causes the generation of wear debris, which further leads to damage to nerves (Harris, 2001).

Based on the interaction between the bearing surfaces, abrasion, adhesion, fretting, and tribo-corrosion wear are recognized as some of the popular wear mechanisms in bio-implants. Abrasion is defined as the removal of material because of the rubbing of two solid surfaces. The sliding of one surface over the other is the main cause of abrasion. After implantation, total joint replacements such as knee or hip face abrasive wear under the human body (Hembus et al., 2018). Adhesive wear is defined as the transfer of one material over the other contacting surface. It occurs mainly due to the formation of weld junctions between the contacting surfaces. The reason for the formation of these weld junctions is the rise in temperature at the contact due to the shearing action. Adhesive wear of metallic biomaterials is a common mode of implant wear (Toh et al., 2017). Fretting wear is a low amplitude, high-frequency mode of wear under the action of rubbing. It is inevitable in the implants at the time of implantation as well as after a few years of service. Bio-implants face fretting wear at the interface of the joints, such as the femur stem and bone in the hip (Tritschler et al., 1999). Tribo-corrosion is another type of implant wear in the human body environment. It is a combined effect of corrosion and wear type of failures. Total joint replacements (hip, knee, shoulder) are some of the highlighted areas for tribo-corrosion (Mathew et al., 2009).

1.5 Surface Modification of Bio-implants

Surface modification of bio-implant surfaces is a widespread area of research. The surface modification of implants aims to achieve a combination of good biological, chemical, and mechanical responses from the surface under the human body environment. A range of surface modification techniques have been explored to improve the quality of implant surfaces. Based on the mechanisms, three routes (chemical, mechanical, and physical) are identified as surface modification routes for implant manufacturing. Food and Drug Administration (FDA) US has approved plasma spraying (one of the physical routes for surface modifications) for coating bio-implant surfaces (Sun, 2018).

In the present research work, Ti, titanium oxide (TiO_2), and baghdadite (BAG) have been selected as the coating materials on stainless steel 316L (SS 316L). Different compositions of Ti/TiO_2 and Ti/BAG composite powders have been prepared by mechanical mixing of Ti, TiO_2, and BAG powders. Cold spray, a relatively new thermal spray technology, is used to obtain composite coatings of Ti/TiO_2 and Ti/BAG composite coatings on SS316L substrate. The as-sprayed coatings are characterized using scanning electron microscopy/ energy dispersive spectroscopy (SEM/EDS) and X-ray diffraction (XRD). Subsequently, the electrochemical corrosion response of the coated and uncoated samples has been evaluated under simulated body fluid enviornment. The sliding wear behavior of as-sprayed coatings has also been investigated under dry and simulated body fluid environments. Furthermore, post-laser processing of as-sprayed Ti/BAG composite coatings is explored to investigate its effect on microstructure, corrosion, and sliding wear.

This chapter presents a comprehensive literature survey related to the present research work. It contains the work done on corrosion of bio-implants, wear of bio-implants, and several surface modification techniques used for bio-implant applications. After a comprehensive review of cold-sprayed coatings for biomedical applications, research problem has been formulated at the end of the chapter.

2.1 Corrosion of Bio-implants

Corrosion of bio-implants (metallic) is inevitable because of the corrosive human body environment. The body fluid consists of many anions such as phosphate, bicarbonate, and chloride, cations like K^+, Mg^+, Ca^+, and Na^+ high molecular weight species and low molecular weight polymeric components with dissolved oxygen (Manivasagam et al., 2010). These molecules can disturb the equilibrium of corrosion reactions over the implanted biomaterials in terms of misbalancing the pH value and transporting protein with metal ions. As per the ISO guidelines (ISO, n.d.), the tolerable limit of implant biomaterials for corrosion rate is 1 micron/year. The most common types of failure for implants are fretting, pitting, uniform, fatigue, stress corrosion cracking, and galvanic corrosion (Sciences, 1999).

Corrosion usually leads to erosion of biomaterials and further causes the implant's fracture. Liu et al. (Liu et al., 2019) studied the fretting-induced crevice corrosion for SS316L under a simulated body fluid environment. Results of their study indicated that fretting plays a substantial role in the initiation of crevice corrosion, which contributes to the bio-implants failure. It is because fretting disrupts the protective passive oxide layer from the implant steel surface. Amel-Farzad et al. (Amel-Farzad et al., 2007) examined a femoral SS316L implant fractured inside the human body (Fig. 2.1). They observed the signatures of crevice corrosion pitting, crevice-induced cracking, and fatigue. A drop in pH and the sulfide inclusion were believed to be the reason for its failure. In another study, Aksakal et al. (Aksakal et al., 2004) examined failed SS316L and Ti6Al4V bio-implants from 1993 to 2002. Metallurgical analysis of their work

revealed that corrosion was the major cause of these implant failures. Kheder et al. (Kheder et al., 2021) examined the oral tissues after a few months of dental implantation and found worn-out titanium particles in the system. Tribo-corrosion is believed to be one of the reasons for the degradation of this implant. However, no adverse biological effects were observed because of corrosion-induced ions release. Wang et al. (Wang et al., 2022) studied the CoCrMo failed hip implants regarding the chemical nature and formation mechanism of fretting corrosion particles. Gilbert et al. (Jeremy Gilbert et al., 1994) examined the fractured hip implant made up of cobalt alloy. They observed that the fracture initiated from the grain boundaries, which occurred due to the intergranular corrosive attack at the grain boundaries of the microstructure.

Merritt and Brown (Merritt and Brown, 1995) examined the chromium ions released from stainless steel and cobalt-chromium alloys. They observed that the red blood cells interact with Cr^{6+} ions and rapidly convert them into Cr^{3+} ions. Cr^{3+} ions are proven to leave carcinogenic and mutagenic effects on DNA (Schaffer et al., 1999). Ti-based alloys are also known to leave toxic effects on the human body. TiAl4V releases Al and V ions when exposed to the human body environment. Walker et al. (Walker et al., 1989) studied the effect of aluminum ions on the structure of the liver and brain. They observed that aluminum altered the structure-property of the brain and liver, which could be much more severe for the brain than the liver, leading to Alzheimer's disease. Costa et al. (Costa et al., 2019) studied the effect of vanadium ions released by the corrosion of Ti6Al4V implants. They suggested that the vanadium ions may leak to blood vessels from the implants and may bound to hyaluronic acid and human serum albumin in synovial fluid. Their cell viability analysis concluded that the amount of vanadium observed at the joints might lead to a potentially dangerous condition. Venkatraman et al. (Venkatraman et al., 2020) reviewed the toxicity due to cobalt after hip arthroplasty. Their review suggested that cobalt can disrupt neuronal metabolism and cause spasticity (muscle stiffness).
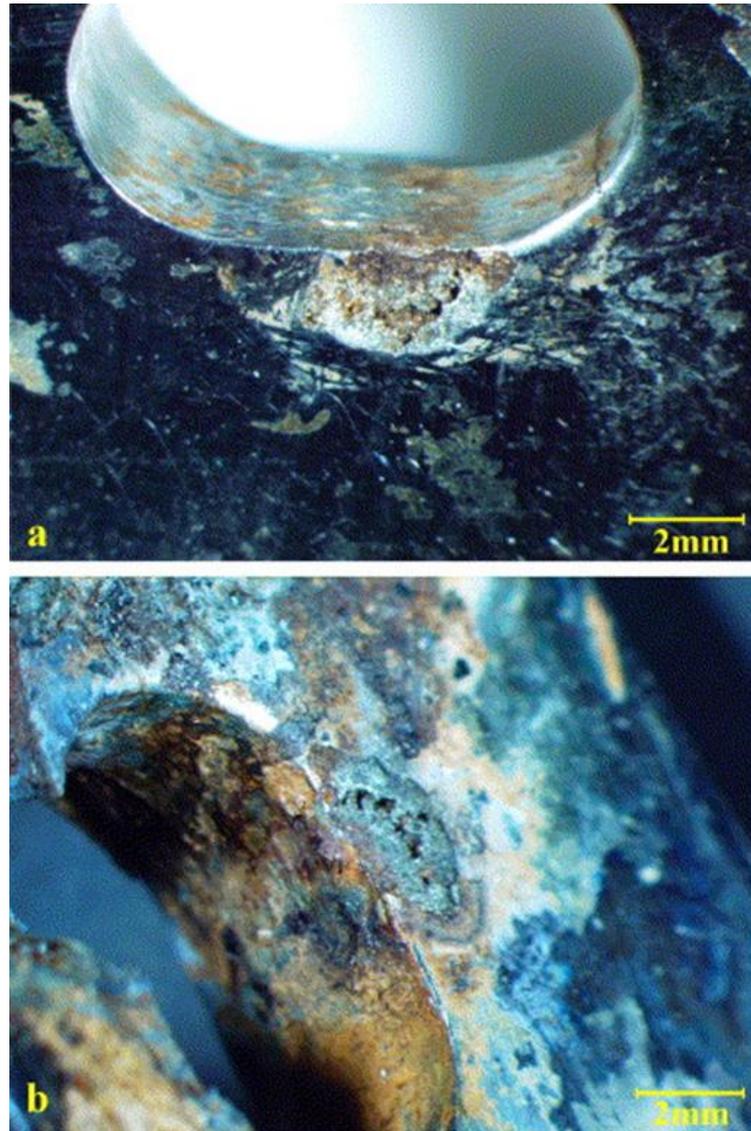
Figure 2.1: Stainless steel corrosion-induced failed implant (femoral head) (a) after cleaning (b) before cleaning (Amel-Farzad et al., 2007)

2.2 Wear of Bio-implants

The human body is made up of many tribological joints, in which rubbing action of one surface over the other leads to the degradation or wear of bio-implants. The major mode of implant failure during wear is abrasion. Besides this, bio-implants also fail due to erosion, fretting, tribo-corrosion, material transfer (adhesion), and fatigue wear. Abrasion involves the cutting or ploughing action of a hard surface on a softer surface because of rubbing action. There are two modes of abrasion: two body abrasion and three body abrasion. Rubbing of two surfaces in direct contact is known as two-body abrasion. Three-body abrasion occurs when the worn-out material is also involved in

the rubbing action (Affatato and Brando, 2013). Adhesion occurs when the material gets transferred from one surface to the other due to generation of high temperature at the contact under the action of sliding load. This high temperature leads to the formation of weld junctions at the contact (asperities in contact), which get ruptured under the application of shear force, leading to loss of materials. Tribo-corrosion involves the corrosion-induced wear of implants, during which the surface of the implant gets deteriorated due to corrosion leading to the formation of wear debris. Erosion wear in bio-implants is caused due to the interaction of implant surfaces with the surrounding body fluid environment. Fatigue wear is also one of the prominent causes of joint failure. It occurs when local stresses generated in the bio-implants exceed the fatigue strength of the material. Fretting wear is another mode of wear where the material gets worn out due to small amplitude high-frequency vibrations. Bio-implants may face one or more mechanisms of wear depending upon the location, movements, and patient conditions (Skjöldebrand et al., 2022).

The wear of bio-implants leads to the generation of wear debris, which can damage the nerves of the patient. Cooper et al. (Cooper et al., 1992) discussed the effect of uncemented fixation in total hip arthroplasty in terms of wear at the interface of bone and implant. They observed that uncemented fixation leads to the generation of wear debris which can cause osteolysis. Schematic representation of the implant loosening and osteolysis due to wear of implants is shown in Fig. 2.2 (Syggelos et al., 2013). The release of wear debris provokes a cellular host response. Macrophages (the most important cells of the tissue) interact with the wear debris and release some soluble chemicals, which flow between the implant surface and bone through the joint fluid. It further interacts with the bony tissue, leading to osteolysis and implant failure. Sochart (Sochart, 1999) investigated the relationship between wear and aseptic loosening of hip implants (235 hips). He reported that 14% of the hip implants faced osteolysis, and the revision of these implants is associated mainly with osteolysis. Wang et al. (Wang et al., 2017) investigated wear debris generated from the CoCrMo MoM hip implant after wear testing inside the hip simulator. They observed that formed wear debris release ions, which can cause numerous biological issues to the patient.
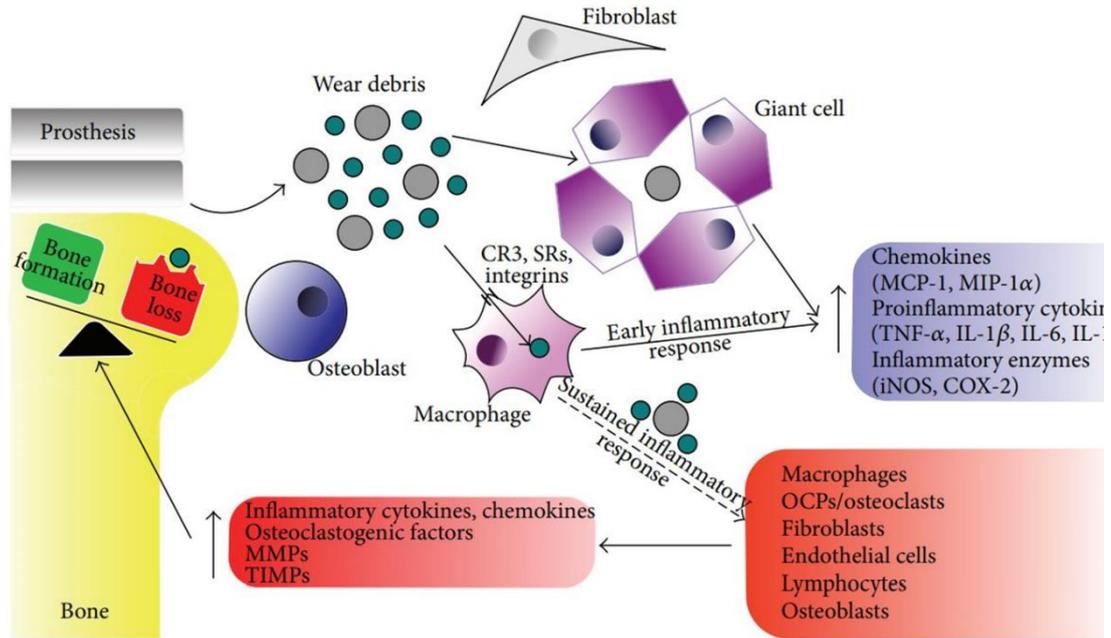
Figure 2.2: Schematic representation of the implant loosening and osteolysis due to wear of implants (Syggelos et al., 2013)

2.3 Manufacturing of Bio-implants

Bio-implants manufacturing is a two-step process: base parts manufacturing and surface modification of base parts. Additive manufacturing is one of the most promising routes for manufacturing of base parts nowadays. For instance, Singh et al. (Singh et al., 2018) prepared a hip implant using fused deposition modelling (FDM) and investigated its corrosion performance and in vitro biocompatibility in the human body environment. Based on the analysis, they concluded that they had achieved appreciable corrosion response and biocompatibility. Further, they suggested depositing bio-compatible coatings for better results. Casting is another popular method to prepare the base part of the bio-implants. Mohammadi et al. (Mohammadi et al., 1995) processed Ti rod and cast bio-implant out of it. In another work, Dargusch et al. (Dargusch et al., 2022) fabricated biodegradable magnesium-based bioimplants using a roll casting process. The results of their study revealed that they could achieve appreciable mechanical and biological properties. However, further improvements were suggested to be done in order to achieve better mechanical, chemical, and biological responses. In this context, surface modification of these bio-implants is needed and which is discussed in the next section in a greater detail.

2.4 Surface Modification of Bio-implants

Surface modification of bio-implant surfaces is a widespread area of research. Surface modification of implants aims to achieve an improved biological, chemical, and mechanical response under the human body environment. A report published in 2016 by Sathguru Management Consultants Private Limited estimated that the Indian orthopedic implant business would reach 2500 million USD by 2030 (Paper, 2016). Hence, it is crucial to enhance the service life of orthopedic implants, which may further improve the business.

A range of surface modification techniques has been explored to improve the quality of implant surfaces (Catauro et al., 2019; Choy, 2003; Mohan et al., 2012; Su et al., 1997; Uwais et al., 2017). Based on the mechanisms, three routes (chemical, mechanical, and physical) are identified as surface modification routes for bio-implant manufacturing (Fig. 2.3). A schematic representing the various requirements expected from a typical coating for the protection of bio-implant is shown in Fig. 2.4.
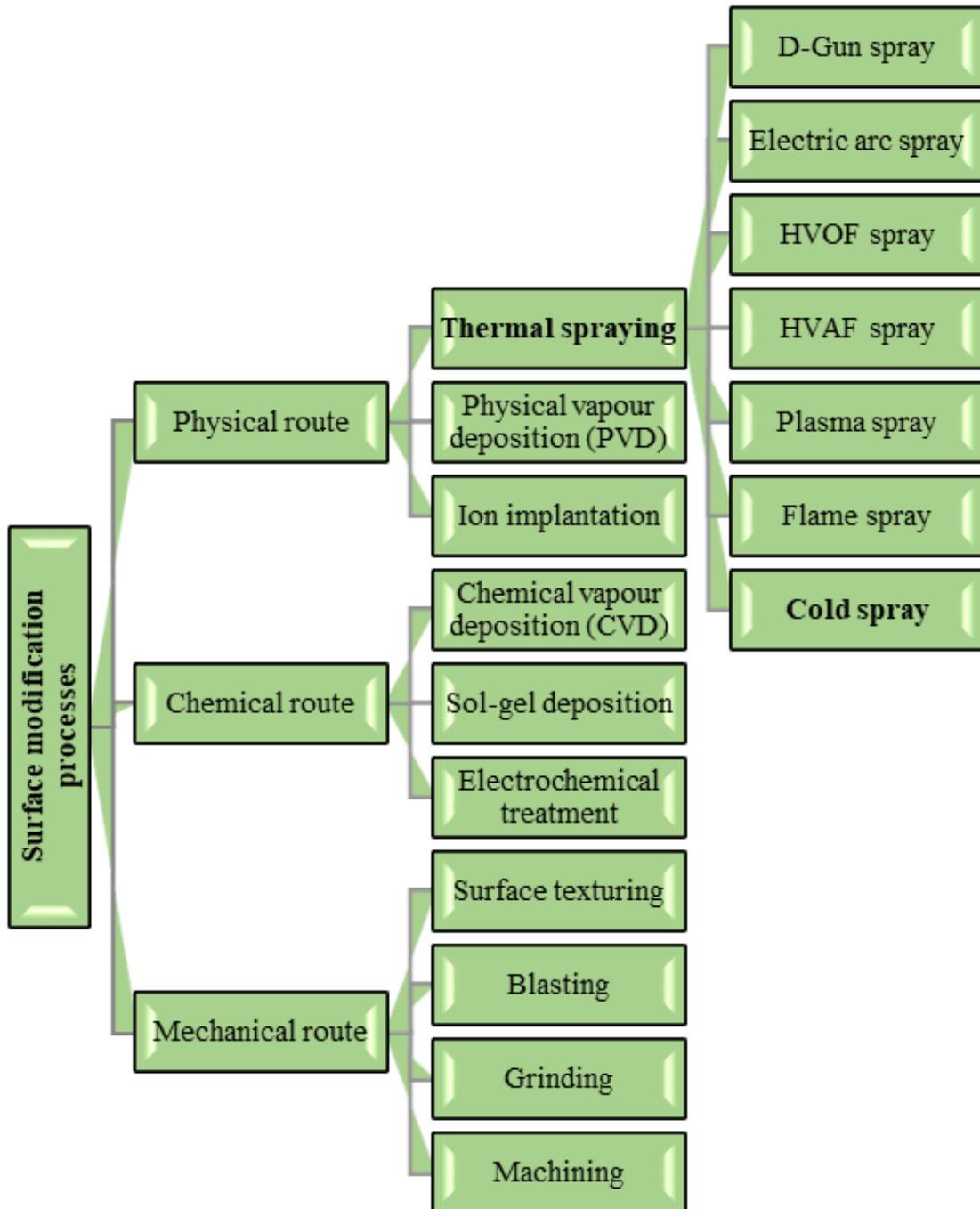
Figure 2.3: Classification of various surface modification routes for bio-implant
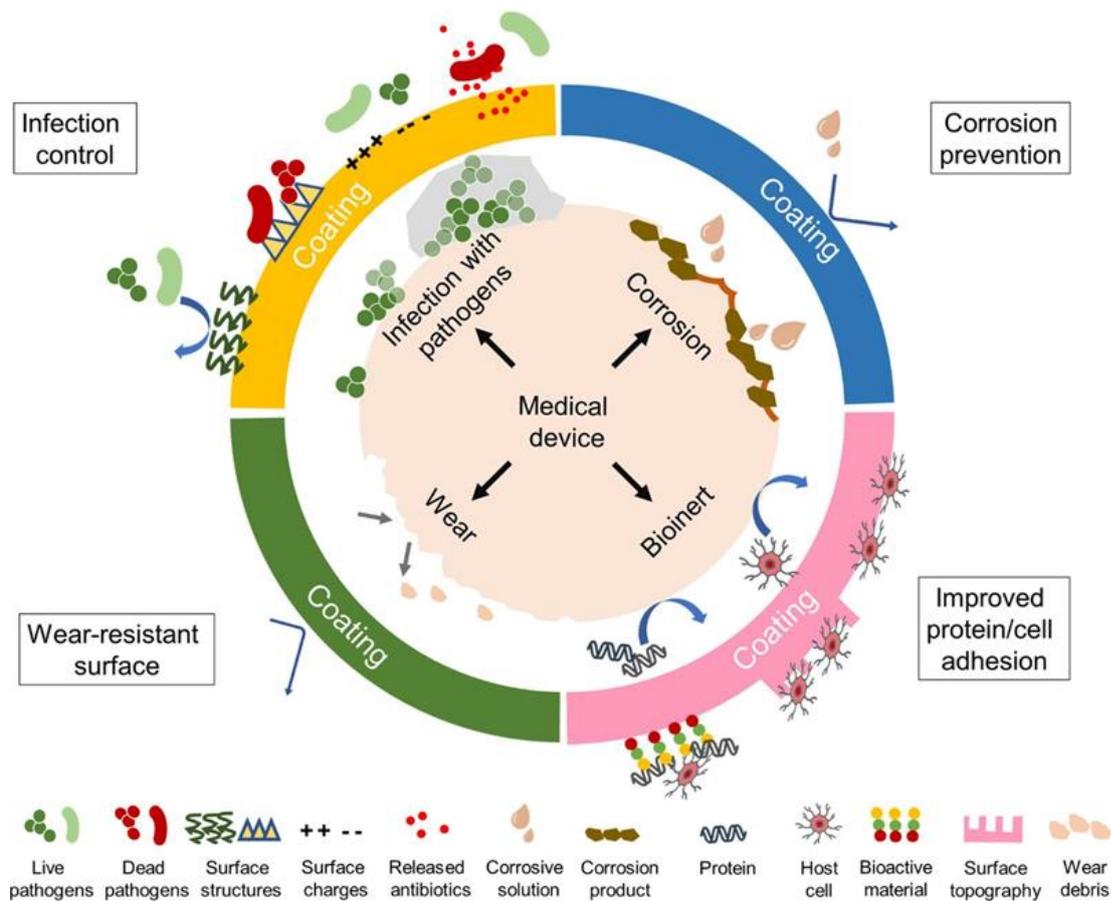
Figure 2.4: A schematic representation of the required characteristics of the coating for the bio-implant protection, Adapted with permission from Ref. (Liao et al., 2022), copyright 2022 Elsevier (Appendix)

Surface modification using the chemical method is one of the popular routes to enhance corrosion, wear, and biological performance. Some of the most widely used chemical methods are sol-gel, chemical vapor deposition (CVD), and electrochemical treatment. Sol-gel is a chemical process of converting small molecules into solid materials. This method is popular for forming ceramic coatings such as hydroxyapatite (HA), TiO_2, and SiO_2 (Kim et al., 2004; Qin et al., 2020). CVD involves deposition of a coating by chemical reaction on the implant surface by the surrounding gas under vacuum. Darr et al. (Darr et al., 2004) deposited hydroxyapatite (HA) on the Ti substrate using CVD. Corona-Gomez et al. (Corona-Gomez et al., 2017) deposited diamond-like carbon (DLC) coating on CoCrMo alloy using CVD and tested its response for wear in the human body environment. The electrochemical method includes anodic oxidation,

cathodic treatment, and electrophoretic deposition. As the name suggests, these process involve the combination of electrical energy and chemical reaction. The coatings can be deposited by supplying energy to the electrochemical cell, which triggers chemical reaction between the electrodes and electrolyte. These are effective, economical, and low-temperature processes to obtain high-quality coatings on a metallic substrate. However, these process pose significant environmental hazards.

The mechanical routes of surface modification include surface texturing, blasting, grinding, and machining. These surface treatments help in achieving the required surface response (adhesion, differentiation, and proliferation of cells) and good implant fixation with the host tissue (Le Guehennec et al., 2008). Additionally, these methods also help to clean the implant surface from impurities.

The physical routes of surface modification utilize electric, thermal, or kinetic energy. Physical vapor deposition (PVD), ion implantation, laser deposition, and thermal spraying are some of the most widely used physical methods to improve the surface characteristics of implants (Bakhsheshi-Rad et al., 2017b). Among these, thermal spray (TS) deposition is one of the most widely accepted surface modification techniques for bio-implant manufacturing. The Food and Drug Administration (FDA) USA has approved thermal spraying (plasma spraying) as a surface modification technique for implant manufacturing (Sun, 2018).

2.5 Thermal Spraying

Thermal spray utilizes thermal and kinetic energy to deposit materials over a biomedical surface. A schematic representation of thermal spraying process is shown in Fig. 2.5. Any material (metal or non-metal) that melts without decomposing can be sprayed to build up coatings using thermal spray technologies. On impact, because of the elastic and plastic deformation of molten or semi-molten particles, splats form, and bonding occurs. Therefore, the processing medium and heating source are required to deposit coating material onto the substrate. Thermal spraying processes have a wide range of applications, including developing coatings and repairing implant surfaces. Schematic representation of feedstock particle temperature and particle velocity for different thermal spraying processes is shown in Fig. 2.6.
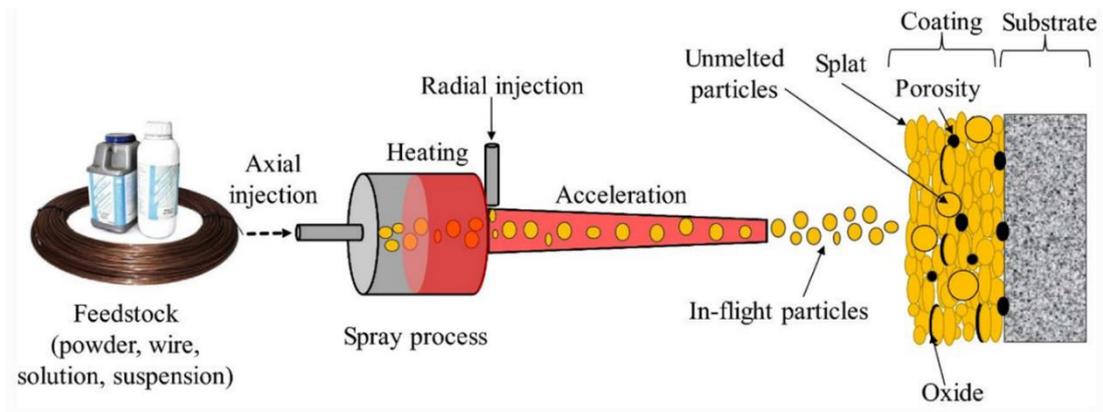
Figure 2.5: Schematic diagram of thermal spray process showing its working principle (Sadeghi et al., 2019)
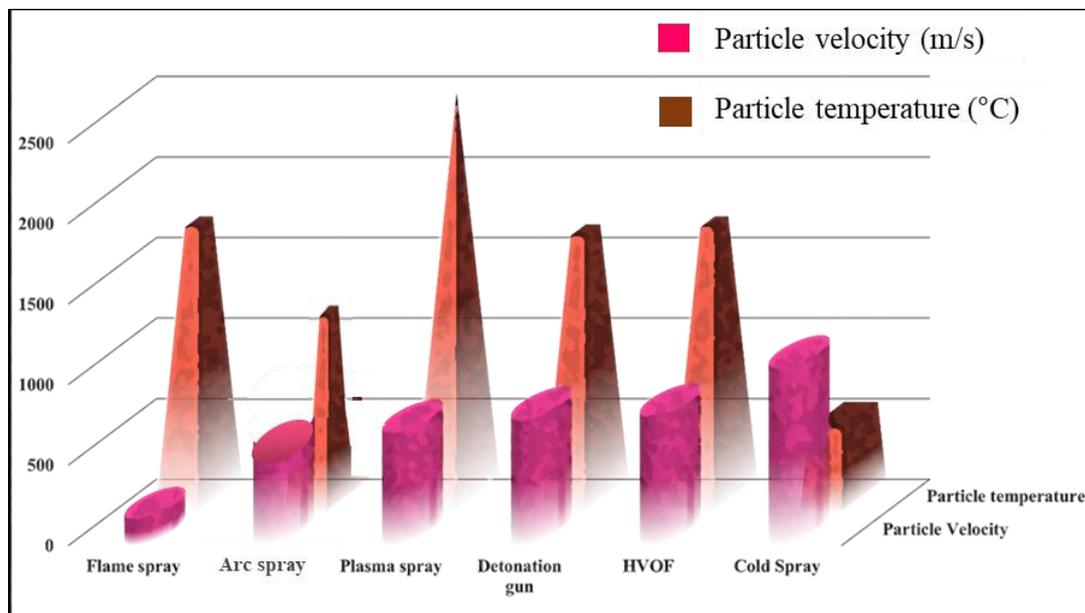
Figure 2.6: Schematic representing the velocity-temperature range of particles in various thermal spray processes (Amin et al., 2016)

2.5.1 Flame Spray

The flame spray is the first coating technique developed in the thermal spray chronology. The flame spray equipment and processing costs are low compared to the other thermal spray processes. Here chemical energy of the fuel (acetylene, propane, propylene, and hydrogen) is utilized to generate flame in the presence of oxygen. The temperature of the generated flame varies from 3000 °C to 3500 °C. This high temperature helps to melt feedstock material (powder or wire). With the help of carrier

gas, the molten material is propelled towards the substrate surface. The speed molten material is generally low (100 m/s). The key processing parameters to achieve the desired coating in this process are fuel-to-oxygen ratio and flow rate. The coatings deposited using flame spray are relatively porous and have a coarser microstructure (Amin et al., 2016; Ndumia et al., 2021). Sarao et al. (Sarao et al., 2012) fabricated titania/hydroxyapatite coatings on titanium substrate using flame spray and reported that the deposited coatings successfully protected the substrate against corrosion in Ringer's solution.

2.5.2 Electric Arc Spray

M.U Scoop developed this process in 1910. Economically, it is the most efficient process to produce coatings in the thermal spray category. It utilizes an electric arc to heat the feedstock wire materials. Compressed air or nitrogen can be used to propel the feedstock materials towards the substrate. This process is only applicable to electrically conductive materials (Ndumia et al., 2021). The transfer of heat energy from coating to the substrate is relatively lesser than the other thermal spray processes because of the non-existence of flame/plasma. Splats formed in this process are usually of the same size but coarser than the other processes. However, the size distribution depends upon the process parameters (Amin et al., 2016).

2.5.3 Detonation Gun (D-Gun) Spray

This process is based on the explosion of the gas mixture. A mixture of fuel, oxygen, and feedstock material is detonated inside a long barrel by electric spark. On explosion, it generates shock waves that help to heat and accelerate the mixture towards the free end. This process can be detonated 1-15 times in a second. After each cycle, the barrel is purged with inert gas before loading the mixture. This process produces high temperature and high velocity such that the powder particles melt completely and strike onto the substrate with supersonic velocity. This produces dense and highly adhered coatings (Davis, 2004). The size of the splats formed during the deposition is usually finer than the other thermal spraying processes. The coatings prepared using D-Gun generally show lesser oxide content due to the smaller splat size and lesser dwell time (Amin et al., 2016). Amin et al.(Bulina et al., 2021) prepared HA coating on Ti substrate using D-Gun spray and reported that the HA has not experienced decomposition due to vary small exposure time.

2.5.4 High Velocity-Oxy Fuel (HVOF) Spray

As the name suggests, HVOF spray is a high-velocity process, in which the molten material with supersonic velocity strikes the substrate surface. A mixture of fuel (hydrogen, propylene, or kerosene) and oxygen is ignited inside the combustion chamber. The generated stream of combusted gas passes through a Laval nozzle to achieve supersonic velocity. The feedstock materials are fed into the combustion chamber either axially or radially at the exit of the nozzle to strike on the substrate surface. The process produces a dense coating with good adhesion onto the substrate surface (Amin et al., 2016; Davis, 2004). HVOF sprayed coatings are usually known for their good wear and corrosion resistance behavior due to their good bond strength and hardness. Henao et al. (Henao et al., 2018) explored the microstructural, mechanical, and biological behavior of HVOF-sprayed hydroxyapatite/titania composite coating on titanium alloy in Hank's solution. Results of their study indicate that the HVOF sprayed coatings can provide a promising solution for implant surface modification.

2.5.5 Plasma Spray

Plasma is a state of matter that can be achieved by supplying sufficient energy to gas for ionizing and producing heat. The plasma spray process utilizes DC electric heat source to generate plasma. Gases like helium, argon, and/or hydrogen are used in plasma spraying. The temperature of generated plasma may vary from 8000K to 20000K, making it possible to melt almost any material. The feedstock powder is introduced in the pressure stream and is propelled towards the substrate surface with a high velocity (100-300 m/s) (Amin et al., 2016; Davis, 2004), leading to the formation of splat-micro structured coating. Plasma spraying is one of the most accepted surface modification techniques for biomedical applications. However, the selection of process parameters is crucial in plasma spraying as they influence the phase structure of the deposits. Atmospheric plasma spray produces porous coatings, which are good for bone-tissue engineering. Plasma spraying in vacuum enviornment is usually done for achieving dense and high strength bio-coatings on implant surfaces (Tejero-Martin et al., 2019). Berndt et al. (Berndt et al., 2014) discussed the dissolution behavior of hydroxyapatite while spraying using various thermal spraying processes. Plasma spray restricts the crystallinity of hydroxyapatite in deposited coating due to which FDA has approved

plasma spray for the deposition of hydroxyapatite coatings for biomedical applications (Sun, 2018).
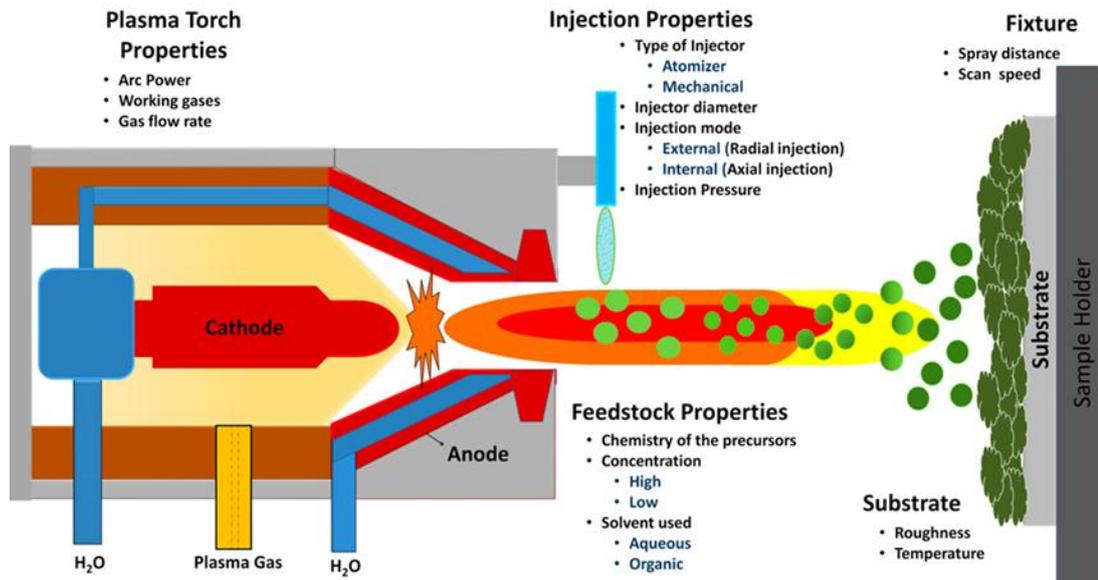
Figure 2.7: Schematic diagram of plasma spray process showing its working principle (Unabia et al., 2018)

2.5.6 Cold Spray

(A) History

S. H. Thurston, in 1900 (Thurston, 1900), filed a patent for depositing a metal over another with the ballistic impingement of powder particles by high-pressure gas, and claimed that this technology works on a maximum velocity of 350 m/s at room temperature. However, this technology was limited because of its low velocity. Later in 1958, Rocheville (Rocheville, 1963) filed another patent based on the same method but using a De Laval nozzle to enhance the velocity of the sprayed particles. This technology also failed to achieve higher powder particle velocity because of the powder feeder and nozzle design. Later on, Professor Anatoli Papyrin and his colleagues (Alkhimov et al., 1990) accidently invented cold spray technology in 1980s at the Institute of Theoretical and Applied Mechanics Russia while studying the supersonic flow of particles in a wind tunnel.

A series of works has been published by the A.N. Papyrin and A.P Alkimov from 1986 to 1989, claiming a device and a method to deposit powder particles (1-200 micron)

with highly pressurized unheated gas with gas stream velocity of 650-1200 m/s (Anatoly, 1994; Papyrin et al., 2006). Subsequently, plenty of work has been published to enhance overall performance of cold spray process, including nozzle design optimization. The nozzle design is one of the key factors to enhance the system's overall performance. Numerous patents have been filed to optimize design of the nozzle, including that by Alkimov et al. (Alkhimov et al., 2000), claiming that more spray area with a limited angle of divergence at the constant gas flow could enhance the performance of the process. Similarly, many inventions have been reported by the researchers with regard to the design of the nozzle to achieve better performance (Schmidt and De, 2006; Sekhar, 2007; Steenkiste, 2007). Henrich et al. (Marcucci Ribeiro, 2004) made the a very promising design by introducing a De Laval nozzle with a powder tube and axial injection of the particles into the nozzle. There exist several other patents claiming the development of portable cold spray systems with better performance (Kashirin et al., 2003; Nikitin et al., 1999). In terms of feedstock, several works have been patented/reported to deposit composite powders of ductile and brittle materials (Application, 2008; Tepzz et al., 2016). Buzdygar et al. (Buzdygar et al., 1993) published a patent on the deposition of ductile metals and their alloy mixed with ceramic.

(B) Principle of Cold Spraying

Cold spraying is a solid-state deposition process where phase change and oxidation-like problems can be avoided, making it advantageous over other thermal spray processes. An optimum combination of temperature and velocity is utilized in cold spray to deposit metallic or composite powders. The temperature of the feedstock powder is maintained below its melting point. A specially designed De-Laval nozzle is utilized to convert the high-pressure gas and powder mixture into a supersonic jet. Upon exiting the nozzle, the powder particles undergo sufficient plastic deformation and bond with the substrate upon impact (Assadi et al., 2003; Moridi et al., 2014)." The cold spray system consists of several key components, including carrier gas cylinders, a powder feeder, gas heater, convergent-divergent nozzle, and spraying arm. The overall cost of the system is determined by a number of factors, such as the gas type, gas pressure, gas temperature, nozzle type, and infrastructure requirements. In addition to the system itself, the consumables needed for the process include carrier gas, coating powders, nozzles, and electricity. A schematic representing the cold spray process is shown in Fig. 2.8. Based

on the processing gas pressure, two systems are available commercially: low-pressure cold spray (LPCS) and high-pressure cold spray (HPCS). The operating pressure range in LPCS is 5-15 bar, whereas for HPCGS, it varies from 10 to 70 bar. HPCS has many advantages over LPCS, including higher deposition efficiency, better adhesion strength, better cohesive bond strength, wider range of feedstock powders and relatively denser coatings (Champagne, 2007; Karthikeyan, 2004). Helium or nitrogen gas can be used to achieve high particle impact velocity in HPCS. However, with LPCS, compressed air can be used as a processing gas, which makes it a relatively economical process. The HPCS system involves the division of compressed gas into two separate streams. The first stream, referred to as the propulsive gas, is heated to a high temperature using a gas heater. The second stream, known as the powder carrier gas, carries the powder feedstock via a powder feeder into a nozzle. These two gas streams are mixed together in the upstream section of the nozzle and expand downstream, generating a supersonic flow. On the other hand, LPCS utilizes a single stream of preheated gas, where the powder material under atmospheric pressure sucked radially in the diverging section of the nozzle. The cold spray system has several advantages such as high deposition efficiency, high deposition rate, compressive residual stresses in coatings, ultra-thick coatings, and low processing temperatures (Champagne, 2007). The application of cold spray is wide, with possible uses in aerospace, shipbuilding, and healthcare. Cold sprayed coatings can be used to enhance the components' mechanical, thermal, and electrical properties including high corrosion and wear resistance (Kumar et al., 2015; Moridi et al., 2014; Singh et al., 2015, 2019).
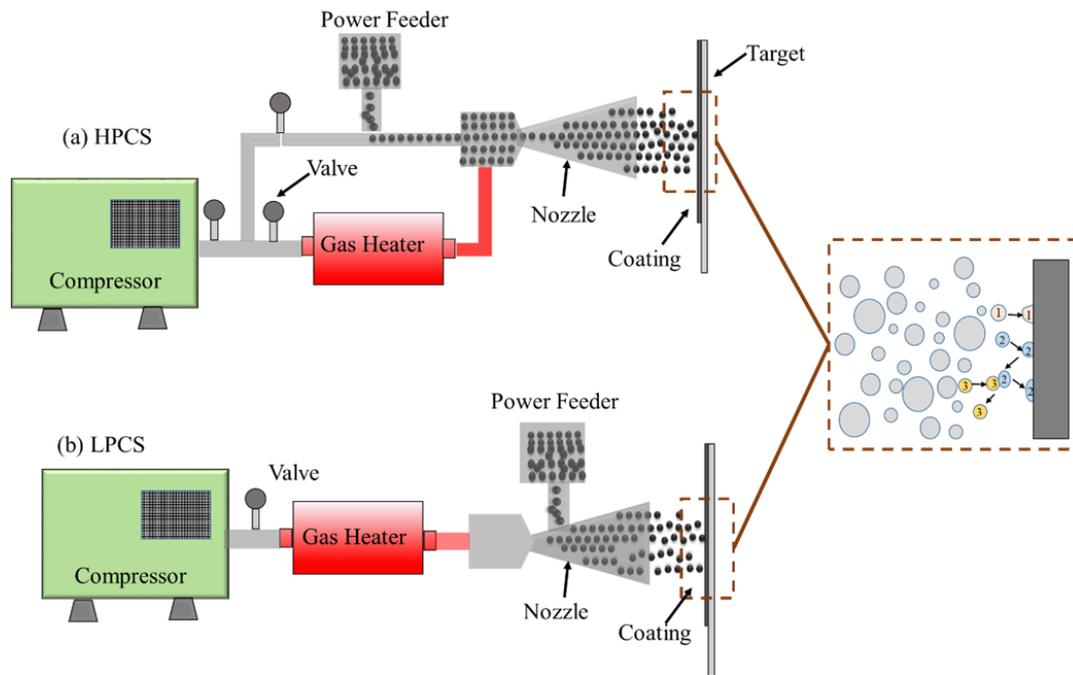
Figure 2.8: Schematic of the cold spray system representing its working principle(a) high pressure cold spray (b) low pressure cold spray (Adaan-Nyiak and Tiamiyu, 2022)

(C) Bonding Mechanism

The bonding mechanism in the cold spray is not fully understood yet. The most popular theories on the bonding of feedstock in cold spray describe that the kinetic energy of powder particles gets converted into heat energy due to high energy impact (Assadi et al., 2003; Guetta et al., 2009), which further helps in mechanical interlocking (MI) and metallurgical bonding (MB) with the subsurface. Mechanical interlocking occurs when the feedstock is harder, the substrate is softer, or both are softer. On impact, feedstock particles penetrate into the substrate and get interlocked. However, in case of the harder substrate, bonding between the substrate and particle occurs primarily due to metallurgical interactions. Both phenomena (MI and MB) play their part in building up the coating in the cold spray process. One school of thought suggests that clean metal surfaces require substantial deformation and pressure to achieve intimate contact. The bonding process in this method is similar to the explosive welding process. It is generally acknowledged that the creation of a solid-state metal jet at the point of impact of particle and substrate is the reason for bonding in cold spray. This jet is believed to break up surface layers and promote better contact between the two metal plates (Dykhuizen et al., 1999). In the literature, many theories are given to explain the

metallurgical bonding or the formation of jetting in cold spray. Adiabatic shear instability (ASI) is one of the most appreciated theories among all to explain the metallurgical bonding in cold spray. Assadi et al. (Assadi et al., 2003) introduced ASI for bonding particles in cold spray. ASI is defined as the combined effect of a sudden rise in temperature, severe plastic deformation, and loss in flow strength of the particle at the interface, which occurs within a few nanoseconds of impact (Fig. 2.9). A change in flow stress, plastic strain, and interface temperature for copper particle impact on copper substrate is shown in Fig. 2.9. Beyond a certain velocity (critical velocity), sudden rise in flow stress, plastic strain, and interface temperature are believed the indication of bonding (ASI) in cold spray. ASI is recognized as a tool for predicting critical velocities for different material combinations. Critical velocity is defined as the minimum velocity beyond which material gets deposited on a subsurface. If the impact velocity is much higher than the critical velocity, then erosion of the substrate surface may occur. On the other hand, if the impact velocity is lower than the critical velocity, particles bounce back without depositing.

The critical velocity depends on many factors, such as material properties, gas temperature, and pressure (Assadi et al., 2016, 2011, 2003; Schmidt et al., 2006; Wang et al., 2014). It is believed that ASI causes the formation of jet-like features at the outer periphery of the particle (Assadi et al., 2003; Grujicic et al., 2003). Moreover, it is observed that the formed jet cleans the substrate surface by removing the oxide layer, if present at the outer periphery of the particle or on the substrate, hence providing a coherent surface for the bonding in cold spray (Assadi et al., 2003; Dykhuizen et al., 1999; Schmidt et al., 2006; Steenkiste et al., 2002). This interfacial jetting mainly depends upon the particle-substrate characteristics and their interactions (Assadi et al., 2016, 2003; Guetta et al., 2009; Hassani-Gangaraj et al., 2018; Hussain et al., 2009; Kumar et al., 2016).
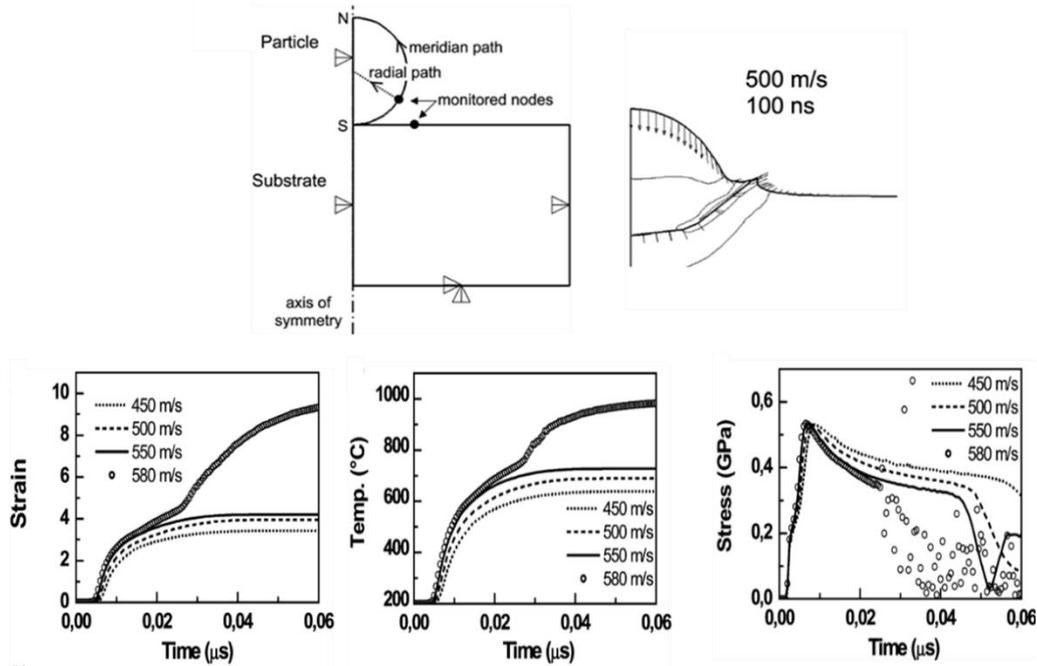
Figure 2.9: Representation of adiabatic shear instability (ASI) induced jetting or bonding in cold spraying of the single particle (Assadi et al., 2003), copyright 2023 Elsevier (Appendix).

On the other hand, Hassani-Gangaraj et al. (Hassani-Gangaraj et al., 2019) did not seem to accept that ASI is responsible for bonding in cold spray. They contradicted Assadi et al. (Assadi et al., 2003) and postulated a new hypothesis for bonding in cold spray. They suggested that the high-velocity impact of the particle leads to the generation of shock pressure waves, which try to release from the edges of the particles. They also suggested that the particle tries to flatten on high energy impact. If the pressure shock velocity exceeds the flattening velocity of the particle, pressure waves released from the edges lead to jetting formation, leading to bonding. This mechanism is named as hydrodynamic instability. Single particle impact behavior with and without ASI is shown in Fig. 2.10, which indicates that the ASI does not lead to jetting/bonding in cold spray. Additionally, the jetting formation due to the release of shock pressure waves are shown at different time zone in Fig. 2.10. In response to this hydrodynamic plasticity, Assadi et al. (Assadi et al., 2019) replied that the critical velocity cannot be the function of the bulk speed of sound (pressure waves) as it does not take material properties and operating parameters into consideration for cold spraying. Hassani-Gangaraj et al. (Hassani-Gangaraj et al., 2019) responded to the questions of Assadi et al. [68] on their mechanistic framework in terms of temperature effects, strength effects, and particle size effects.
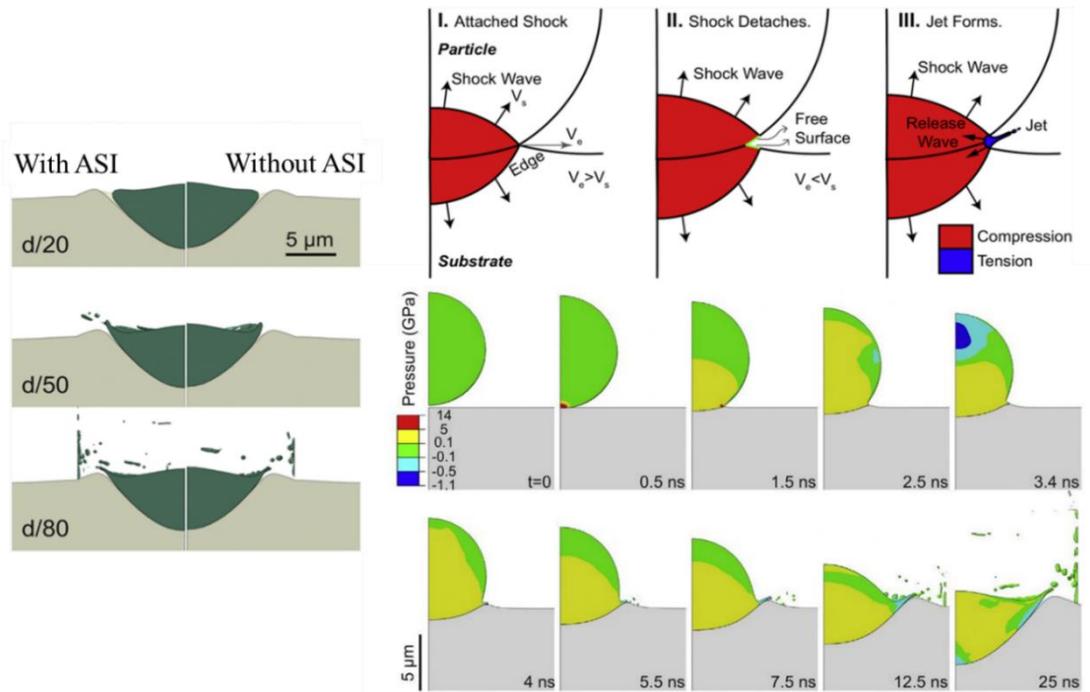
Figure 2.10: Representation of hydrodynamic plasticity induced jetting or bonding in cold spraying of a single particle (Hassani-Gangaraj et al., 2018), copyright 2023 Elsevier (Appendix).

Furthermore, several other theories have been proposed to explain the bonding in cold spraying of metals, some of which are; Ko et al. (Ko et al., 2016) discussed the bonding of soft particles (Cu and Al) on hard substrate (AlN and ZrO_2). They suggested that the high energy impact of soft particles on hard substrate leads to a restructuring of the interface and results in atomic mixing and amorphization. Yin et al. (Yin et al., 2021) discussed the condition for atomic or vortex-like mixing of interfaces in cold spraying. The suggested that interfacial mixing is only possible if the interface goes through severe plastic deformation, and it also depends on the properties of the interacting materials. In another study, Zou et al. (Zou et al., 2009) studied nickel particles at the interface using electron backscatter diffraction (EBSD) and observed a non-uniform microstructure with a very small grain size (in nanometres). Dynamic recrystallization of nickel due to high energy impact was believed to be the reason for this, as it provides additional softening at the interface. In their review of cold spray process, Schmidt et al. [72] reported that particle interface temperature could reach close to its melting point depending upon the impact energy, which promotes bonding.

(D) Substrate Preparation

Although, pre-deposition substrate surface preparation has been widely studied in cold spray, however, there are still many contradictions (Hussain et al., n.d.; Kumar et al., 2016; Sharma et al., 2015; Singh et al., 2020b). Bonding in cold spray occurs due to either mechanical anchoring of particles to the substrate, metallurgical bonding with the substrate, or both. Grit blasting is one of the most widely used methods for preparing substrate surfaces in cold spraying to achieve good bonding strength. It leads to the activation of the substrate surface by generating rougher peaks and deeper valleys, which further helps in particle interlocking with the substrate. Kumar et al. (Kumar et al., 2009) reported that grit-blasted substrate surfaces are better for good bonding in cold spray. Also, they tried to optimize the roughness value for cold spraying by focusing on the grit size and mechanical properties of the powder particles and substrate. Richer et al. (Richer et al., 2006) also reported that rougher surfaces are good for adhesion, and the surface preparation does not significantly affect the coatings' microstructure, macrostructure, and deposition efficiency.

On the contrary, Hussain et al. (Hussain et al., n.d.) showed that the copper particles make better bonds with the mirror-polished surface of aluminum alloy substrate. Singh et al. (Singh et al., 2020a) have supported the above statement by experimentally proving that the adhesion between the copper coating and steel substrate of mirror-polished surfaces is better. Sufficient penetration and plastic deformation of cold sprayed copper particles on mirror-polished steel substrate surface leading to good jetting formation during the deposition has been ascribed as the main reason for the better bonding. Hard particles striking the softer substrate surface lead to the substrate's deformation, and hence substrate surface roughness does not leave any significant effect on bonding and deposition. However, in the case of soft particle striking on hard rough substrate surface texture significantly affects deposition and bonding behaviour.

(E) Effect of Nozzle Design

In cold spraying, bonding depends on the impact energy of the powder particles. The nozzle design is one of the key factors in achieving desired impact energy. Sakakai et al. (Sakaki and Shimizu, 2001) reported the effect of nozzle geometry on coating build-up by numerical simulation using the computational fluid dynamics approach. They studied three different nozzle geometries, viz. convergent-divergent nozzle, convergent

barrel, and convergent-divergent barrel, for the impact velocity of particles and gas. The study revealed that the convergent-divergent nozzle provides the best particle velocity and temperature. Li et al. (Li et al., 2006) proposed a convergent barrel using numerical simulations for cold spraying. They suggested that particles can achieve high temperature but with low velocity using a convergent barrel under the same processing conditions compared to a convergent-divergent nozzle, which can facilitate thermal softening of the particle. Chavan et al. (Chavan et al., 2019) studied the effect of nozzle throat cross-sectional area on the properties and microstructure of cold-sprayed deposits. They observed that the nozzle with a throat height to length ratio greater than 0.02 provides the best microstructure and mechanical properties among the others. It is related to the boundary layer effect on particle velocity distribution. Klinkov et al. (Klinkov et al., 2011) introduced a new design of cold spray nozzle, which provides a high-velocity two-phase flow with an intense flow swirling using a double-edged bevel axis. The design was expected to offer more deposition area with a higher angle of particle deposition. Particle velocity at the exit of the nozzle also depends on the cross-sectional shape of the nozzle, as it may lead to a bow-shock effect (Jodoin, 2002). Tabbara et al. (Tabbara et al., 2011) studied the effect of cross-sectional shape (circular, elliptical, and rectangular) on particle velocity at the exit of the nozzle. They revealed that a circular cross-section provides relatively higher particle velocity at the exit of the nozzle among the studied design.

(F) Process Parameters for Cold Spraying

Powder Shape and Size

The coating properties and deposition efficiency largely depend on the shape and size of the feedstock powdered material in cold spraying. As per the energy-momentum theory, large particle size reduces the impact velocity of the particles and hinders the deposition. However, it is also believed that larger particles carry more heat with them because of their large surface-to-volume ratio, which helps achieve ASI (Bhattiprolu et al., 2018; Goldbaum et al., 2012; Grujicic et al., 2004; Ning et al., 2007). ASI is used to determine the critical velocity of the particles in literature. Assadi et al. (Assadi et al., 2003) calculated the critical velocity of a copper particle on a copper substrate by considering a particle size of 25 microns. They also measured the critical velocity experimentally and found that it decreases with an increase in particle size. However,

beyond 50 microns, a minimal effect on critical velocity was observed (Schmidt et al., 2006). The smaller particle size faces a reduced flattening ratio, leading to poor bonding. Other than this, smaller particles may also lead to bow-shock. Previous studies revealed that powder sizes ranging from nanowires to 400 microns could be sprayed in cold spraying. However, to achieve the optimum results regarding deposition efficiency and coating properties, 1-50 micron particle size is preferable (Gao et al., 2008). Particle morphology influences the bonding and deposition characteristics of deposits in cold spraying. Particles with spherical shapes are assumed to give better adhesion and overall performance. Spherical particles lead to proper splat formation and produce denser coatings (W. Y. Li et al., 2007).

On the other hand, irregular shape particles are believed to attain more velocity under the same processing conditions and cause the development of porous coatings. Palodhi et al. (Palodhi et al., 2021) studied the effect of particle size and morphology on the critical velocity and deformation behavior. They reported that irregular particles tend to produce more stress concentration at the sharp edges, which led to the deformation of particles but not the substrate. This also affects the flattening of particles; the more curvature, the better the flattening and bonding. Many other studies reported that spherical particle bonds well, but irregular particle provides higher deposition efficiency than spherical particles (Huang et al., 2019; Jodoin et al., 2006; Wong et al., 2013).

Processing Gas

The type of processing gas used highly influences the performance of developed coatings in cold gas spraying. Only inert gas is used in cold spray systems to protect the coating from oxidation-like problems. Compressed air, nitrogen, and helium have been widely explored as processing gases. Compressed air and nitrogen are used in the LPCS system, where the powdered materials' critical velocities are comparatively low. In HPCS systems, nitrogen and helium are used as a processing gas. Nitrogen is economically cheap and easily available and hence is widely used. However, helium coating is better than nitrogen in achieving higher particle velocity at lower stagnation pressure and temperature. This is because the specific heat of helium is higher than nitrogen, which leads to better heat transfer between gas and particle. The heated particles carry more heat, leading to more softening, better deformation, and good adhesion (Balani et al., 2005). Kuhn et al. (Khun et al., 2016) deposited Ti6Al4V on Ti6Al4V by cold spray in a nitrogen as well as helium environments. They revealed that

coating with helium produced a denser coating showing better adhesion, hardness, wear resistance, and corrosion resistance. Wong et al. (Wong et al., 2011) discussed the influence of helium and nitrogen gases on the deposition characteristics of pure cold-sprayed titanium coatings. They concluded that deposition efficiency and density of the coatings are the functions of impact particle temperature. They obtained high deposition efficiency and denser coatings with nitrogen as processing gas than helium while keeping the same particle impact velocity. It was because of a greater amount of consolidated region between the particles and the material jetting.

Stand-off-Distance

The stand-off distance (SoD) is one of the major parameters that severely affects the adhesion, deposition efficiency, and microstructure of the coatings in cold spraying (Chun et al., 2012; Li et al., 2008). Pattison et al. (Pattison et al., 2008) reported that small SoD leads to the formation of the bow-shock effect between high-velocity jet and substrate. Bow-shock is believed to significantly influence the impact velocity of the feedstock particle and bonding. Bow-shock is defined as the generation of shockwaves due to gas and particle stream's high-velocity impact on the substrate. Since generated shockwaves cannot travel further due to the substrate, they tend to remove the particles from the substrate. Therefore, it is essential to select the SoD in such a way so that the particle velocity exceeds the gas velocity on impact, which further will help in minimizing the bow-shock effect (Pattison et al., 2008). Li et al. (Li et al., 2008) reported in their work that SoD directly influences the deposition efficiency of the process and affects the microstructure and mechanical properties of the coatings. In another work, Feng et al. (Feng et al., 2014) studied the effect of SoD on the deposition efficiency and thickness of NiCoCrAlY cold-sprayed coating. They observed that they were not able to deposit complete coatings above 50 mm of SoD, and the coating thickness was also asymmetrical. However, for 25 mm of SoD good homogeneous coatings were achieved.

Traverse Speed

The quality of the coating in cold spraying also depends upon the traverse speed of the nozzle. It influences cold-sprayed coatings' deposition efficiency and mechanical properties (Tan et al., 2017). Seraj et al. [137] reported in their work that the deposition efficiency of cold sprayed stellite 21 powder on carbon steel increased from 23% at 20 mm/s to 48% at 300 mm/s and then dropped down to 30% at 400mm/s. Furthermore, it is observed that an increase in traverse speed led to a decrease in the microhardness of

the coatings. They concluded that after 100 mm/s, the coating quality reduced in terms of mechanical properties such as porosity, microhardness, and coating thickness. In another study, Tan et al. (Tan et al., 2017) investigated the effect of traverse speed on coating porosity, microhardness, and adhesion strength in cold spray. They reported that the high traverse speed led to an increase in porosity, decrease in microhardness, and increase in adhesion strength. It is because high traverse speed leaves minimal heating effect and restricts the deformation of particles, which means more inter-splat gaps, lesser strain hardening, and poor deposition.

Gas Temperature and Pressure

The cold spray process is known for its low-temperature features; it has been noticed that gas temperature influences the deposition efficiency, critical velocity, and coating build-up. The gas velocity inside the nozzle depends upon the temperature of the gas and further influences the particle velocity. The gas temperature also influences the particle impact temperature. Therefore, high gas temperature contributes significantly to the bonding in cold spraying (Papyrin et al., 2006). Yin et al. (Yin et al., 2014) examined the effect of gas temperature on deposition and particle acceleration. They reported that higher gas temperature resulted in more particle impact velocity. The additional heating of the particle due to high gas temperature led to thermal softening of the particle, which also reduced the critical velocity. Hence, improved deposition efficiency and bonding were achieved. Assadi et al. (Assadi et al., 2016) discussed the effect of particle impact temperature on critical velocity in their work by considering the particle's mechanical and thermal properties. Their study revealed that high particle temperature promotes ASI and reduces the critical velocity. In another study, Lee et al. (Lee et al., 2007) reported that deposition efficiency improves with higher gas temperature and the same particle velocity. They observed that critical velocity got decreased by 50 m/s when the processing gas temperature was increased by 100 °C for the given particle-substrate system (Cu-Sn alloy on aluminum).

The influence of pressure can be realized by comparing the LPCS system to HPCS system. LPCS and HPCS system work in the range of 5-15 bar and 10-70 bar, respectively. Depending upon the feedstock materials and the required properties of the coatings, both systems can be used efficiently. Low pressure enables the production of porous and denser coatings of softer materials. However, the feedstock materials with high critical velocity (Ti, W, Ta, and SS316L) are difficult to deposit using LPCS

systems as these systems are inadequate to attain high particle impact velocity (Huang et al., 2019; Ning et al., 2007). Increased gas pressure helps achieve higher impact velocity, which further promotes bonding in cold spray. High gas pressure leads to high cohesion strength, adhesion strength, mechanical properties, and density of the coatings (Zahiri et al., 2006). Lee et al. (Lee et al., 2008) produced aluminum coating on nickel substrate at low and high-pressure conditions. They observed that at low pressure, the deposition efficiency was lower, but the hardness of the coating was higher because of the peening effect. Schmidt et al. (Schmidt et al., 2009) studied the effect of gas pressure on particle impact temperature and particle impact velocity in cold spray. They reported that high pressure leads to high particle impact velocity and temperature, which promotes the ASI. Hence, better deposition efficiency and bonding were achieved.

2.6 Cold Sprayed Coatings for Biomedical Applications

Various biomaterials viz metals, ceramics, and composites have been deposited using the cold spray. Many studies indicate that cold-sprayed coatings successfully protect the substrate from corrosion and wear while retaining their biological characteristics. The optimization of process parameters and selection of biomaterials are crucial to deposit a good quality of the coating. The deposited biomaterials using cold spray are as follows;

2.6.1 Metallic Biomaterials

Metals are well known for their good chemical, mechanical, and biological properties for biomedical applications. Therefore, the temperature-sensitive metals have been cold sprayed to avoid phase change and oxidation. Ti is one of the most used biomaterials for bio-implants because of its high strength-to-weight ratio, excellent corrosion resistance, and biocompatibility. Wong et al. (Wong et al., 2013) deposited Ti on mild carbon steel with different powder morphology, spherical, irregular, and sponge. They reported that the deposited coatings using spherical powders showed dense structure and superior deposition efficiency. Li et al. (Wen Ya Li et al., 2007) investigated Ti cold sprayed coatings microstructure and reported that angular Ti powder could be used to obtain porous coatings, which is a favourable condition for biomedical applications. Palodhi et al. (Palodhi et al., 2021) investigated the feedstock titanium and copper particles' deformation behavior and critical velocity with different sizes and morphologies. They demonstrated that the irregular particles show higher deposition efficiency with poor adhesion because of lesser deformation. Copper has also been cold

sprayed on biomedical surfaces due to its antibacterial properties (Durdu, 2019). Cold spraying of copper can be considered for developing antimicrobial, corrosion-resistant, and conductive coatings because cold spraying leads to the development of dense and oxide-free coatings. Tantalum is also a well-known biomaterial that is cold sprayed to produce coatings for biomedical applications. Tantalum has excellent biocompatibility, good mechanical properties, and corrosion resistance, making it a suitable candidate for biomedical applications. Therefore, tantalum coatings are preferable and cold spraying of tantalum has been explored and reported in the literature (Koivuluoto et al., 2009; Soro et al., 2019). Tang et al. (Tang et al., 2020) deposited tantalum on titanium substrate to enhance the bioactivity and biocompatibility of the titanium implants. They observed that tantalum produced a rough and porous coating which further improved the bioactivity of the implant surface. However, the high cost of tantalum limits its application.

Cold spraying of metallic alloys has also been considered for biomedical applications. For instance, Ti-alloys have been deposited using cold spray and tested for biomedical application (Goldbaum et al., 2012; Li et al., 2020). Bhattiprolu et al. (Bhattiprolu et al., 2018) deposited three distinct Ti6Al4V powders (hydride de hydride, gas atomized, and plasma atomized) using cold spray for biomedical applications to explore the microstructural features of the deposit. They reported that hydride de hydride powder resulted in high-quality coating with good adhesion strength and density.

Similarly, stainless steel has also been cold sprayed and investigated for biomedical applications (Huang et al., 2019), (Sova et al., 2013). Dikici and Topuz (Dikici and Topuz, 2018) deposited SS 316L austenitic steel on aluminum alloy using cold spray and explored its chemical and biological response in a simulated body fluid environment. Their study revealed that the coating successfully reduced the corrosion current density and shifted the corrosion potential in the noble direction. Cold spraying of Co-Cr alloys has also been done to investigate their feasibility as a biomedical coating (Al-Mangour et al., 2013). Co-Cr alloys are well-accepted biomaterials because of their superior mechanical, good chemical, and acceptable biological properties. Co-Cr alloys are relatively difficult to deposit among the above-discussed materials. It is because they possess uniquely different thermal and mechanical characteristics. Al-Mangour et al. (Al-Mangour et al., 2013) mixed powders of SS316L with Co-Cr alloys and prepared metal matrix cold sprayed coatings in different compositions. They investigated the

deposits against corrosion for biomedical applications, and the results of their study revealed that the deposits successfully outperformed pure SS316L cold sprayed coatings in terms of corrosion under Hank's solution.

2.6.2 Ceramic and Composite Biomaterials

Depositing bio-ceramics using cold spray has been considered challenging because of their poor plastic deformation. However, many efforts have been made to deposit ceramics using cold spray due to their high corrosion resistance and bioactivity. Toibah et al. (Toibah et al., 2016) studied the feasibility of depositing TiO_2 using cold spray. They prepared TiO_2 nanostructured powder with the addition of $(NH_4)_2SO_4$ and cold sprayed. The results of their study indicated that the deposition of TiO_2 is feasible with a coating thickness of approximately 140 microns but with poor mechanical properties. Hajipour et al. (Hajipour et al., 2018) studied the effect of powder; (a) TiO_2 nanopowders and (b) agglomerated TiO_2 powder, prepared using polyvinyl alcohol and nanoparticles. The results of their study showed that the agglomerated powder provided better bonding as they overcame the bow-shock successfully. Vilardell et al. (Vilardell et al., 2020) cold sprayed hydroxyapatite and compared its in-vitro results with plasma sprayed and HVOF sprayed hydroxyapatite coatings. The results of their study revealed that CS coating showed better proliferation after 14 days of incubation, due to a higher amount of retained crystallinity during cold spray. Much work has been done on bio-metal/bio-ceramic composite feedstock due to the difficulty in depositing bioceramics. Bio-metals work as a matrix in composite and bio-ceramic as reinforcement. Therefore, the bio-metal interlocks the bio-ceramic in between. Gardon et al. (Gardon et al., 2014) prepared a cermet coating of hydroxyapatite and titanium using cold spray. They revealed that a high amount of hydroxyapatite reduces the quality of the coatings in terms of mechanical properties. In another work, Zhou and Mohanty (Zhou and Mohanty, 2012) deposited titanium/hydroxyapatite cold sprayed coatings with good mechanical properties and studied their efficacy against corrosion under simulated body fluid. The results of their study revealed that the deposited coatings were successful in serving as a barrier to corrosion between the electrolytes and subsurface. Li et al. (Li et al., 2017b) deposited hydroxyapatite/gentamicin sulfate composite coating using cold spray and tested it for antimicrobial properties. The results of their study indicated that the deposits successfully resisted bacterial activity with excellent biocompatibility. Tang et al. (Tang et al., 2019) studied the bioactivity of cold-sprayed

tantalum/hydroxyapatite mechanically milled cold spray composite coating under simulated body fluid. The results revealed that the prepared cold sprayed coating offered high bioactivity because uniformly distributed hydroxyapatite increased the degree of supersaturation of simulated fluid in terms of apatite. Nanocomposite of nanodiamond/hydroxyapatite have been synthesised and vacuum cold sprayed to obtain biofunctionalized surface for biomedical applications (Li et al., 2017a). Graphene is believed to possess antibacterial characteristics along with its good mechanical properties. Therefore, hydroxyapatite/graphene composites have also been explored using cold vacuum spray for their chemical and biological properties (Liu et al., 2014).

Besides these, some metal matrix metal reinforcement composite coatings have also been produced using cold spray. For instance, Zeng et al. (Zeng et al., 2020) investigated biocompatibility and bioactivity of titanium/tantalum cold sprayed composite coating. The study reports that the deposited coating offered strong bonding to the substrate without any phase change. Also, the improvement in cell propagation on the composite surface was observed.

2.7 Laser Surface Melting

Laser surface remelting is well known for the surface modifications of coatings to improve microstructure, microhardness, and wear resistance. A high-power laser source generates a laser beam to irradiate the coated surface in the laser-treatment process. The irradiated surface forms a melt pool allowing the materials to form better metallurgical bonds (Olakanmi, 2016; Singh et al., 2005). As the laser source move past the melt pool, the material starts solidifying from the solid surface to the melted surface and leads to the development of residual stresses. Zhang and Kong (Zhang and Kong, 2018) reported that the developed residual stresses caused by the laser surface melting of cold spray aluminum coatings on S355 improved the bonding strength. Sova et al., 2013 (Sova et al., 2013) deposited SS316L on the aluminum substrate using cold spray and discussed the microstructure and mechanical properties before and after surface melting of the deposits. They reported that the deposited coatings became denser and harder after laser remelting. Poza et al., 2014 (Poza et al., 2014) discussed the laser remelting effect on mechanical characteristics of Inconel 625 cold-sprayed deposits. They investigated that laser treatment helps in increasing the elastic modulus of the cold-sprayed coatings due to the increase in density. Rubino et al. (Rubino et al., 2016) deposited Ti coating on

aluminum alloy using cold spraying; after laser treatment, the density and microhardness of the coatings have been reported to be increased. Jing and Dejun (Jing and Dejun, 2018) discussed the laser treatment effect on cold sprayed aluminum coating for wear. They reported that laser treatment significantly reduced the friction and wear of the coatings against Si_3N_4 in a 3.5% NaCl solution

2.8 Biomaterials for Present Work

Titanium is a lightweight biomaterial with good mechanical, chemical, and biological properties. It exists in two forms; below 880 °C hexagonal closed packed (HCP) structure and above 880 °C body-centered cubic (BCC). HCP-Ti and BCC-Ti are also known as α-Ti and β-Ti, respectively. The temperature for the transformation of α-Ti into β-Ti largely depends on the alloying elements such as aluminum, oxygen, nitrogen or iron, chromium, and niobium (Sasikumar et al., 2019). The elastic modulus of α-Ti is close to the bone's elastic modulus, which is a good characteristic for avoiding stress shielding of the implants. Besides this, α-Ti is well-known for excellent corrosion resistance in the human body environment (Geetha et al., 2009).

Titanium dioxide (TiO_2) is a well-known biocompatible, non-toxic biomaterial. It is usually found in one of these three forms: rutile, anatase, and brookite (Pouilleau et al., 1997). Rutile is a tetragonal crystal structured thermally stable phase of TiO_2. Anatase is also tetragonal but metastable in nature. It changes to rutile when annealed or calcinated at high temperatures. Anatase TiO_2 is believed to improve protein adsorption, osteoblastic adhesion, and bioactivity (Webster et al., 1999). Brookite is another phase of TiO_2 biomaterial; it is rare compared to rutile and anatase. Studies have shown that TiO_2 can generate hydroxyl groups ($-OH^-$) on its surface under humid conditions, which can then combine with calcium ions (Ca^{2+}) and phosphate groups (PO_4^{3-}) from physiological fluid to form bone-like apatite compounds. This process facilitates osteoblast cell adhesion and proliferation, indicating that TiO_2 exhibits excellent biocompatibility and can be classified as a bioactive material (Lindberg et al., 2008, Wu et al., 2003). Animal experiment studies have also demonstrated excellent osseointegration ability of TiO_2 (Erli et al., 2006). Compared to regular titanium film, TiO_2 film has even more promising potential for successfully modifying implant surfaces due to its remarkable biological characteristics. Therefore, TiO_2 is selected as one of the biomaterials as reinforcement for this study.

Baghdadite (BAG), a calcium zirconium silicate, is a relatively new material having good chemical and biological properties (Bakhsheshi-Rad et al., 2017a). Zirconium present in calcium silicate enhances its mechanical and chemical properties compared to other calcium silicates (Schumacher et al., 2014). As per the open literature, BAG promotes cell adhesion, cell growth, and osteogenic differentiation of stem cells. It also encourages the activity of osteoclast cells and the proliferation of osteoblastic cells and shows no toxicity (Ramaswamy et al., 2008). Pham et al. (Pham et al., 2019) reported in their work that BAG can be a replacement for hydroxyapatite, which is a very well-known and commercially used biomaterial for bio-implant applications. However, they noted that during plasma spraying, BAG underwent a phase change that caused a significant drop in its crystallinity from 55% to 21%. Therefore, BAG is chosen as one of the biomaterials in this study for cold spraying MMC, to fully leverage its benefits as a reinforcement.

2.9 Problem Formulation

In the last few years, the demand for orthopedic implants has increased to meet the needs of people requiring implants. Historically, implants have been extensively used for supporting a person with a bone injury or diseases that degrade bones. It is expected that the business of bio-implants will reach 2.5 billion USD by 2030 (Paper, 2016). Corrosion and wear of these implants are serious problems because they can affect the mechanical, chemical, and biological properties of these bio-implants. The release of ions due to corrosion may affect the interaction between bones and implant surface and may leave some adverse biological effects. Literature on bio-implant failure suggests that corrosion is one of the major reasons for implant failures, as discussed above (Godwin et al., 2021). Wear of implant surfaces leads to the generation of wear debris, which can be caused damage to the nerves of the patient. Hence, selecting an appropriate material processing technology is required to prepare corrosion and wear-resistant surface.

Thermal spray coating techniques are widely used for developing high corrosion and wear-resistant coatings for biomedical applications. However, phase change and oxidation during thermal spraying are some of the major issues biomaterial faces (Champagne, 2007). Therefore, it is a challenge to develop an effective coating on the biomedical surface (biomedical steel, SS316L) to enhance the corrosion and wear

resistance of the sub-surface (biomedical steel) without phase change and oxidation. Cold spraying has been identified to overcome the drawbacks of already existing thermal spray coatings. Ti, TiO_2, and BAG have been selected as the biomaterials for cold spraying on SS316L substrate. Ti has been chosen because of its good mechanical, chemical, and biological properties in the human body environment. Osteoblastic adhesion and good corrosion resistance of TiO_2 are the reasons for its selection in this work. BAG, a relatively new material known for its good bioactivity and mechanical properties, has been considered for this study to explore possibility of replacing mechanically-weaker HA.

The aim of the present research is to develop Ti-based composite coating using cold spray technology and examine for corrosion and wear response under a simulated body fluid environment. The above-discussed biomaterials have been chosen after an extensive study of various biomaterials. After an exhaustive literature review, cold spraying has been selected as a modification process. Cold spraying is well known for depositing temperature-sensitive biomaterials without changing their original phase and characteristics, as discussed above. It is believed that the results of this research work would be a novel contribution to the healthcare sector.

2.10 Objectives of Present Research Work

- To study the effect of substrate surface roughness on deposition characteristics of cold-sprayed Ti-based composite powder on the SS316L substrate

- To develop Ti/TiO_2 and Ti/BAG composite coatings using cold spray on SS316L steel

- To explore the effect of TiO_2 in Ti/TiO_2 cold-sprayed composite coatings on electrochemical and tribological performance under a simulated body fluid environment

- To study the effect of BAG content in cold-sprayed Ti/BAG composite coatings on electrochemical and tribological performance under a simulated body fluid environment

- To investigate the effect of laser post-treatment on corrosion and tribological properties of cold-sprayed composite coatings.

This chapter contains an inclusive explanation of the materials selection, coatings deposition, coatings characterization, and performance testing. Beside these, details and specifications of the various equipments used in the present research work have been described.

3.1 Raw Materials

3.1.1 Austenitic Stainless Steel (SS316L) Substrate

The current study utilized Austenitic Stainless Steel (SS316L) as the substrate material, which is a commonly used material for manufacturing bio-implants. The low carbon percentage in SS316L inhibits the formation of carbides at the grain boundaries when exposed to a simulated body fluid environment, thereby preventing intergranular crack formation or fracture of the steel. Furthermore, SS316L exhibits better tensile strength, yield strength, and ductility than other bio-metals, making it an excellent choice for orthopaedic implant applications. The substrate material was purchased in the form of 5 mm thick plates, and its chemical composition is detailed in Table 3.1.

Table 3.1: Chemical composition of SS316L steel substrate used for cold spray Ti/BAG coatings

Elements	Fe	Cr	Ni	Mo	Mn	C	P	Si
Composition (%)	Balance	16.17 %	10.02 %	2.06 %	0.87 %	0.01 %	0.03 %	0.23 %

3.1.2 Commercial Pure Titanium Powder

The current research work has chosen commercially pure titanium (Cp-Ti) as one of the coating powders due to its known high ductility, good strength, and excellent corrosion resistance. The Cp-Ti powder, which was procured from Nanoresearch Elements USA, has an average particle size of approximately 40 µm and is manufactured using the

pyrometallurgical process. For this study, two types of Cp-Ti powders were selected, one with a spherical shape and the other irregular in shape. The morphology, composition, and phase of the procured powder were confirmed using scanning electron microscopy (SEM, JEOL, JSM-6610LV, Japan), energy dispersive spectroscopy (EDS, JEOL, JSM-6610LV, Japan), and X-ray diffractometer (XRD, X-Pert Pro, Panalytical, Netherlands) analysis, which can be seen in Fig 3.1 and Fig. 3.2.

3.1.3 Baghdadite (Calcium Zirconium Silicate)

For cold spraying, another feedstock powder selected was Baghdadite (BAG), which is a calcium zirconium silicate. BAG is well-known for its high chemical stability and biological activity as a biomaterial, and there are reports indicating that it could replace hydroxyapatite for future biomedical applications. The BAG powder used in this research work was produced by mixing zirconium oxide (ZrO_2), silica (SiO_2), and calcium carbonate ($CaCO_3$) powders in a 1:2:3 molar ratio, followed by sintering. The resulting powder mixture was crushed using a ball mill to obtain the BAG powder (Pham et al., 2019). Initial trials for coating development were conducted using this powder, and the final coatings were deposited using BAG powder procured from Nanoresearch Elements USA. SEM and XRD analyses of the powder used are presented in Fig. 3.1 and Fig. 3.2, respectively.

3.1.4 Titanium Dioxide

Another feedstock powder material used in this study is titanium dioxide (TiO_2), which is widely recognized as a biocompatible and non-toxic biomaterial. TiO_2 commonly exists in three forms, namely rutile, anatase, and brookite (Pouilleau et al., 1997). Anatase TiO_2 powder with a particle size range of 10-40 microns was obtained from Nanoresearch Elements USA. The powder's morphology and phases were confirmed through SEM and XRD analyses, as illustrated in Fig. 3.3.

3.2 Development of Coatings

3.2.1 Substrate Preparation

Prior to developing the coatings, three substrate surfaces with different roughness values were prepared by polishing with emery papers of varying grit sizes, as presented in Table 3.2. The as-received (AR) substrate had an average arithmetic mean surface roughness value of 5 microns. The ground-polished (GP) substrate was polished down

to 800-grit emery paper to achieve a roughness value of 0.3 microns. The mirror-polished (MP) surface was obtained by polishing down to 2000-grit emery paper followed by velvet polishing, which involves polishing the samples on velvet cloths in the presence of diamond paste. The surface roughness of the prepared substrate samples was determined using a surface profilometer (HandySurf E-35-A/B, Accretech, Japan), and an average of ten readings of Arithmetic mean roughness (R_a) and ten-point height of irregularities (R_z) values were reported. Additionally, the substrate samples were cleaned ultrasonically before the deposition of coatings.

Table 3.2: Details of the substrate (SS316L) surface preparation for cold spray deposition of Ti/TiO$_2$ composite powders

S.No	Substrate designation	Arithmetic mean roughness (R_a) µm	Ten-point height of irregularities (R_z)	Up to emery papers' grade (grit size)
1	As-received (AR)	5.00 ± 0.85	22.31 ± 3.14	No
2	Ground-polished (GP)	0.30 ± 0.02	2.33 ± 0.38	800
3	Mirror polished (MP)	0.04 ± 0.01	0.86 ± 0.23	2000 grit followed by diamond paste polishing on velvet cloth

3.2.2 Preparation of Composite Powders

Ti and TiO$_2$ powders were mixed in various (wt. %) ratios to understand the effect of TiO$_2$ in feedstock material on the deposition of Ti/TiO$_2$ composite coatings and their characteristics, as shown in Table 3.3. The mixing was done using a magnetic stirrer (Optima, MS 300, India) operating at 1000 rpm for 30 min at room temperature. Following the same procedure, Ti and BAG powders were also mixed in various (wt. %) ratios to develop four composite compositions for the deposition of Ti/BAG composite coatings, as shown in Table 3.4.

Table 3.3: Details of the feedstock powder material used for the deposition of Ti/TiO$_2$ composite coatings on different SS316L substrate in cold spraying

S. No	Feedstock designation	Composition (wt %)		Morphology
		Ti	TiO$_2$	
1	P1 (Ti/20TiO$_2$)	80	20	Ti-Spherical shaped, TiO$_2$- Spherical shaped
2	P2 (Ti/20TiO$_2$)	80	20	Ti-Irregular shaped, TiO$_2$- Spherical shaped
3	P3 (Ti/40TiO$_2$)	60	40	Ti-Irregular shaped, TiO$_2$- Spherical shaped
4	P4 (Ti/60TiO$_2$)	40	60	Ti-Irregular shaped, TiO$_2$- Spherical shaped

Table 3.4: Details of the cold sprayed Ti/BAG-based composite coatings investigated in the present study

S. No.	Coating designation	Composition (wt %)	
		Ti	BAG
1	Ti/10BAG	90	10
2	Ti/15BAG	85	15
3	Ti/20BAG	80	20
4	Ti/25BAG	75	25
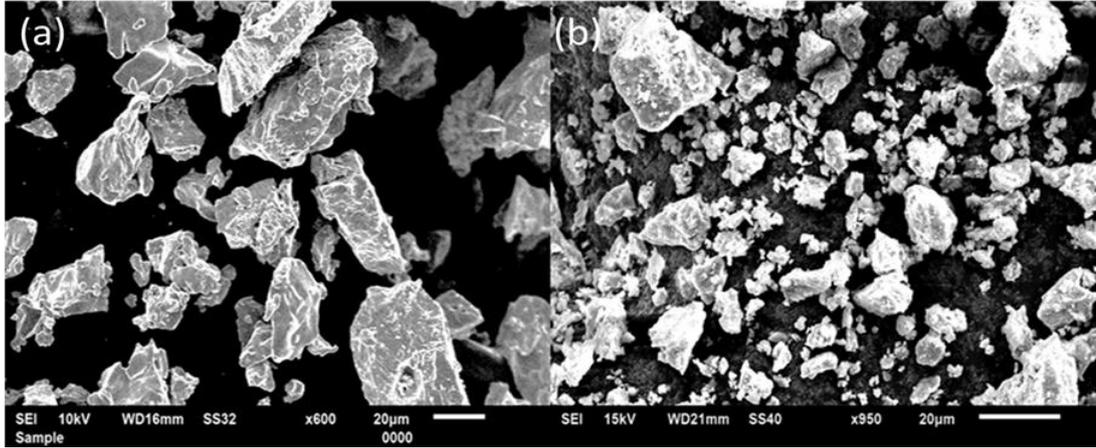
Figure 3.1: SEM micrographs of feedstock powders (a) Titanium (b) BAG used for the development of cold sprayed Ti/BAG composite coating on SS316L
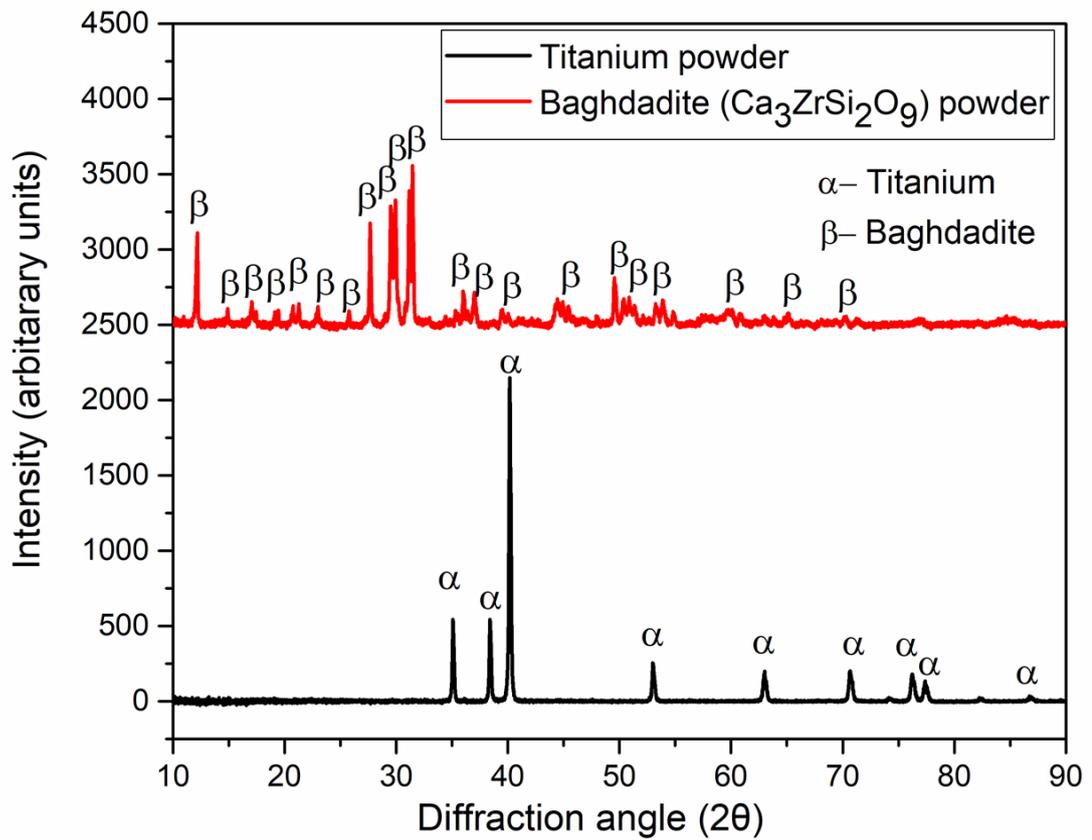
Figure 3.2 XRD analysis of the feedstock powders used for the development of cold spray Ti/BAG composite coatings on SS316L
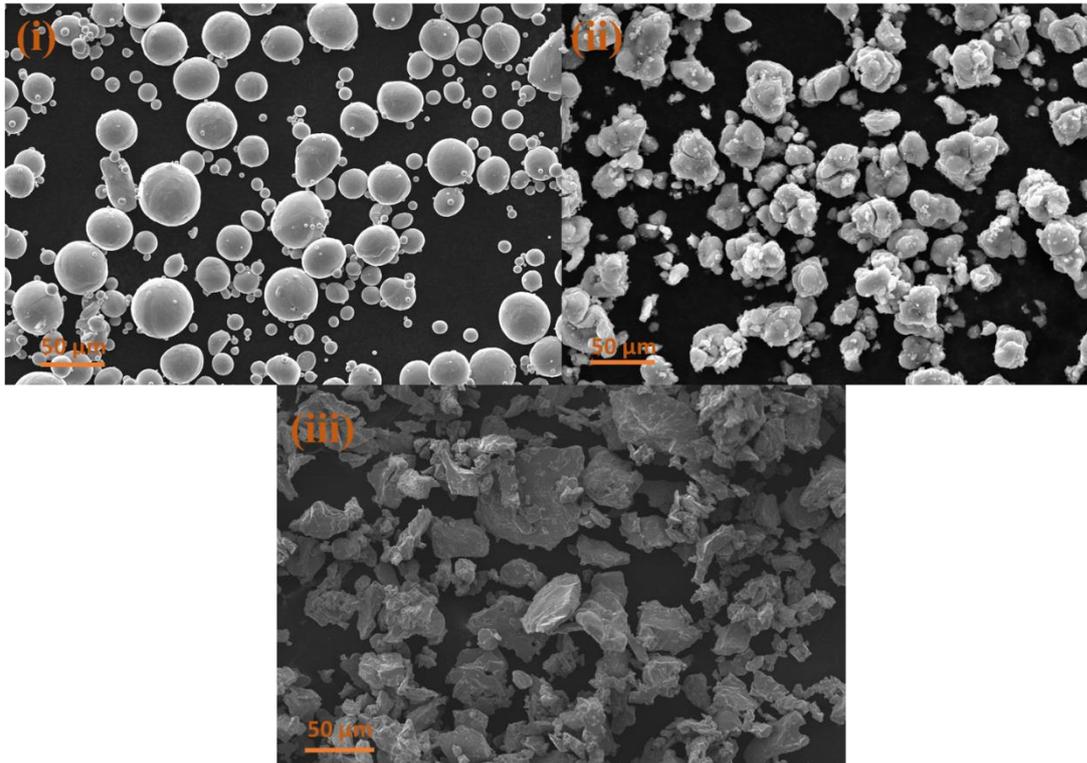
Figure 3.3: SEM micrographs of the powders used for the cold spraying of Ti/TiO$_2$ composite on SS316L substrate (i) Spherical titanium powder (ii) Spherical titanium oxide powder (iii) Irregular titanium powder

3.2.3 Deposition of Coatings

The deposition of composite coatings on SS316L was carried out in this study using a high pressure cold spraying equipment (Plasma Giken, PCS-100, Japan) as shown in Fig. 3.4. This system has the ability to spray up to 50 bar of gas pressure and 1000 °C of gas temperature and is equipped with a robot (KRC4 60-3, KUKA, Germany) with six degrees of freedom. Several trials were conducted to achieve good adhesion of the prepared composite powders on the SS316L substrate. Nitrogen and helium can be used as the processing gas in this system, but nitrogen was selected in this research work due to its low cost and easy availability. The deposition characteristics were studied by keeping the number of passes constant for all the composite coatings. Specifically, eight passes were made for Ti/TiO$_2$ composite coatings, and nine passes were executed for Ti/BAG composite coatings.

To deposit Ti/20TiO$_2$ on SS316L substrate, several experiments were conducted varying gas pressure (25-50 bar) and gas temperature (500-900 °C). The best coating thickness was achieved with a gas pressure of 40 bar, a gas temperature of 700 °C, a stand-off

distance of 2.5 cm, and a traverse speed of 20 cm/s. For uniformity, eight passes were made in all the cases to achieve the best possible thickness of the coatings. These parameters were used to deposit Ti/20TiO$_2$ on SS316L substrates, having three levels of surface roughness. After establishing the best surface condition (mirror-polished, MP) for the cold spray deposition, different powder compositions (as shown in Table 1) were deposited on MP SS316L substrate using the same aforementioned process parameters. Whereas, to deposit the Ti/BAG composite coatings, a constant pressure of 30 bar and a temperature of 900°C were maintained. Being a new material and substrate combination, a series of trial experiments were performed to identify these parameters, with a gas pressure in the range of 15-30 bar and a gas temperature range of 600-900°C.
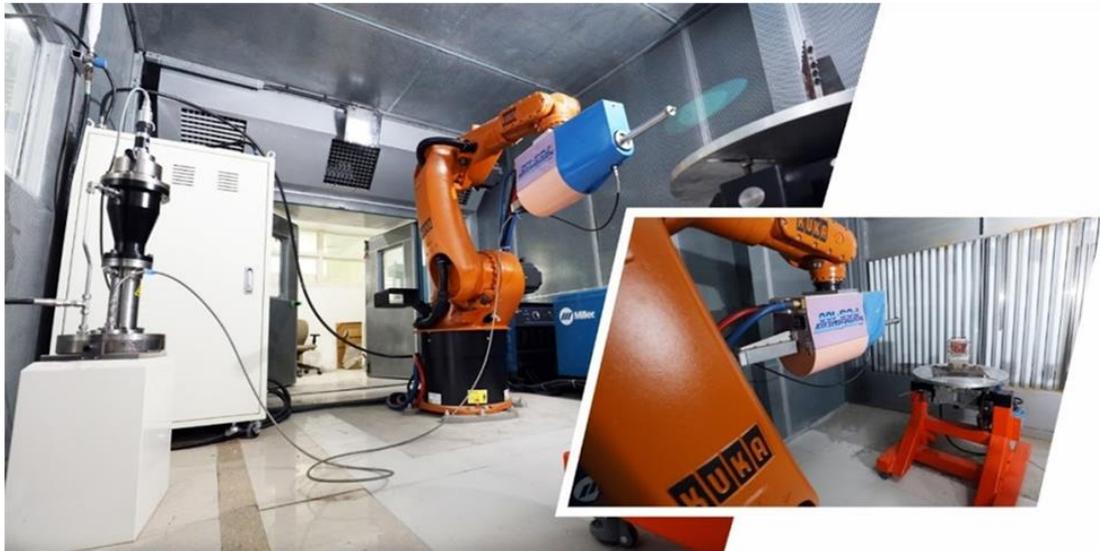
Figure 3.4: High pressure cold spray system at Indian Institute of Technology Ropar, Punjab, India

3.3 Laser Post-processing

Laser post-processing was done using a continuous beam fiber laser source (MFSC-1000, Abro, India) in an argon atmosphere to limit the oxidation of cold-sprayed deposits. The emissivity of the coatings was measured and verified by temperature mapping using a thermal imaging camera (A315, Flir, Sweden) and thermocouple at different temperatures. Marrocco et al. (2011) previously optimized the laser process parameters for cold-sprayed Ti free-standing deposits, which were used as starting process parameters in the current work. The laser treatment trials were conducted using a range of laser power from 400 W to 500 W, spot diameter of 3 to 5 mm, and traverse speed of 2000 to 3000 mm/min. The objective was to identify the process parameters

that would elevate the surface temperature of the coating above the recrystallization temperature of titanium while minimizing heat dissipation to the substrate. The Ti/15BAG coating was chosen for laser remelting trials because of its superior mechanical and tribological properties compared to the other investigated coatings. Once the desired results were achieved, the identified process parameters were used for laser-remelting of all the cold-sprayed Ti/BAG composite coatings.
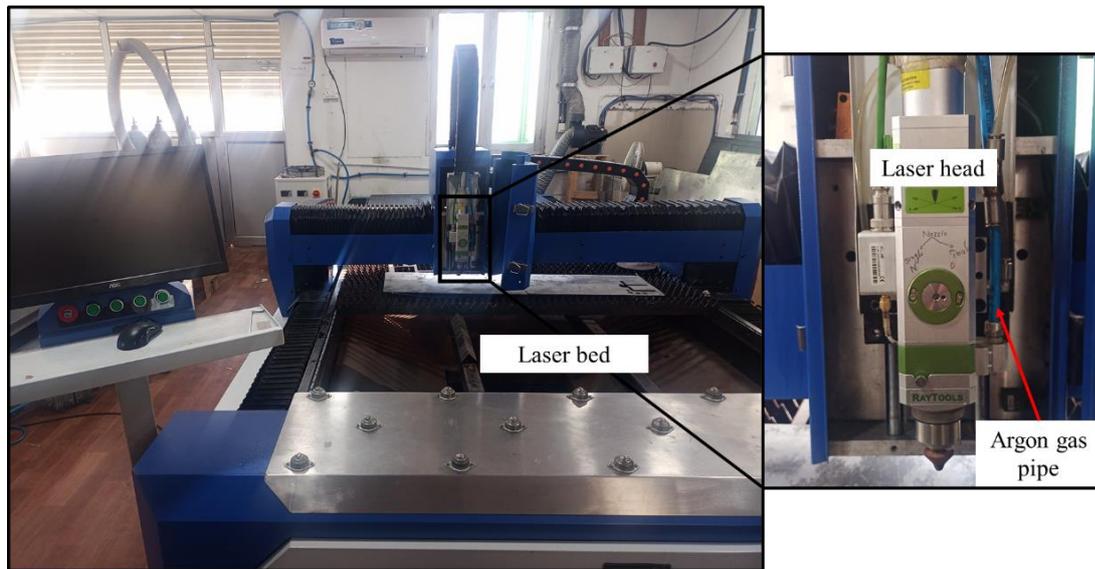
Figure 3.5: Laser setup used for the post-processing of cold-sprayed Ti/BAG coatings on SS316L steel substrate

3.4 Characterization of Coatings

3.4.1 Metallographic Sample Preparation

The as-sprayed coated samples were sectioned using a wire-cut electric discharge machine (WEDM, Electronica-Sprintcut, India) for cross-sectional analysis. The sectioned samples were mounted in Bakelite using hot mounting machine (Automount, Metatech Industries, India). The mounted samples were polished using emery papers from 220 to 2000-grits followed by velvet polishing to obtain mirror finish surface and to eliminate the effect of temperature due to WEDM cutting. Finally, Kroll's etchant (95% H_2O, 2% HF, and 5% HNO_3) was used for etching the samples to reveal the microstructural details in some cases.

3.4.2 Microstructural Characterization

Optical microscopy (OM, Leica, Germany) was used to study the surface morphology as well as microstructure of as-sprayed coatings. OM was also done on the coated samples subjected to scratch testing. SEM/EDS was used to reveal the surface and cross-sectional microstructure, morphology along with the composition of the as-sprayed as well as laser-treated coatings. Post-corrosion and post-wear analysis were also performed using SEM/EDS to reveal the failure mechanism of the coatings. XRD analysis of the raw material and as-sprayed coatings was done to investigate the phase change during cold spraying. XRD analysis was also done to elucidate the phase change due to laser surface treatment. The diffraction data was collected using Cu-Kα radiation with a voltage of 40 KV and a current of 30 mA. The scan covered the 2θ range of 10-80° at a speed of 1 kcps. The dwell time was set at 2 s, and the step size was 0.5°. The present phases were then identified by matching the obtained diffraction pattern with JCPDS data cards.

3.4.3 Mechanical Characterization

Average surface roughness (R_a) and ten point height irregularities (R_z) of coated and uncoated steels were measured using a roughness tester (HandySurf E-35-A/B, Accretech, Japan). The equipment was calibrated before the measurement using a calibration block. The stylus of the equipment was made to run over the coated and uncoated steels. Roughness measurements were performed with the cut-off length of 2 mm and a measuring speed of 0.5 mm/second. Ten values of the roughness parameters were taken for each sample, and subsequently, the average of these values was reported for each case. The thickness of the coatings was measured using OM and SEM.

The apparent porosity of the as-sprayed coatings was determined by analyzing the SEM micrographs from several sites using ImageJ software following ASTM E2109-01. The microhardness was measured from cross-section of the coatings and the substrate using micro-hardness tester (Wilson, 402MVD, Illinois) equipped with a Vickers indenter following ASTM C1327. The indenter was made of diamond having a square based pyramid shape with an apex angle of 136° 5'. For the measurement, the load applied was 500 g for 10 s dwell time. A minimum of 10 indents were taken for each coating and the substrate across the transverse section, and subsequently the average of these value is reported.

Scratch test was performed to investigate the relative bond strength of the as-sprayed coatings using micro-scratch tester (DUCOM, TR-101, India). The stylus Rockwell C diamond indentor with a diameter of 40 µm made up of diamond was used to scratch the coated steels surface. The testing was done under constant loading and ramp loading conditions with 20 N/mm of sliding speed.

The sessile drop method was used to measure the contact angle of cold sprayed Ti-based composite coatings and substrate with a Goniometer (HO-ED-S-01, Holmarc Pvt. Ltd., India). The images of the distilled water drops were stored by a video camera. Image J software (5 readings per sample) was used to measure the contact angle from the shape of the drop. Readings were taken from each drop's average of left and right contact angle for each sample, and for one sample, three drops were analyzed.

3.4.4 Biocompatibility Analysis

The cell viability of the developed coatings was performed on mouse preosteoblast cells (MC3T3-E1, passage 11-12) using reported protocol with slight modification (Ref 29). The cells were cultured in tissue culture treated 25 flask with media MEM-a, containing 10% fetal bovine serum (FBS, Gibco) with 1% antibiotic solution. The culture medium was replenished every 48 h, and the sub-confluent cells were harvested using the trypsin-EDTA solution. Approximately 10,000 cells/well were seeded in treated tissue culture using 48 well plates and incubated for 24 h in a humidified atmosphere having 5% CO_2 at 37 °C. The samples were suspended in ethanol, sonicated for 30 min, and air-dried. The sterilization was done using a UV light for 30 min. Each sample was incubated in a-MEM media for 24 h at 37 °C and then passed through a 0.22 µm syringe filter. The media of cells cultured in 48 well plates were replaced with filtered extracts, and cells were further incubated for 24 h. An amount of 30 µL MTT solution (5 mg/mL) was added to each well, and the plate was incubated at 37 °C for 3.5 h. The resulting formazan crystals were dissolved in DMSO (100 µL), and absorbance was recorded at 570 nm using a Tecan Infinite M Plex plate reader.

Firstly, the sample size is selected in order to minimize the variability and ensure that any significant differences between the investigated coatings can be detected. The cell viability of the different coatings was evaluated by testing three samples of each composition. The percentage of cell viability was calculated by comparing the absorbance of treated cells with the untreated cells.

Secondly, untreated cells were used as a reference point to ensure that any observed effects were not due to experimental error. This provides a baseline for comparison and helps to establish whether the treatment or condition being tested has a significant effect on cell viability. The p-value was calculated using ANOVA software, with a significance level of 0.05.

3.5 Corrosion Analysis

3.5.1 Experimental Setup

Potentiodynamic polarization and electrochemical impedance spectroscopy (EIS) tests were performed to check the efficacy of the coated and uncoated SS316L steels against corrosion. The mediums for corrosion testing were Ringer's and Hank's solution. The Ringer's solution was having a chemical composition of 9 g/L of NaCl, 0.24 g/L of $CaCl_2$, 0.43 g/L of KCl, and 0.2 g/L of $NaHCO_3$, whereas Hank's solution was having 8 g/L NaCl, 0.35 g/L $NaHCO_3$, 0.4 g/L KCl, and 0.185 g/L $CaCl_2$. The coated and uncoated SS316L steels were tested in a standard 3-electrode electrochemical cell (PTC1, Gamry Instruments, US), in which coating/substrate was used as working electrodes, Ag/AgCl as a reference electrode and graphite as the counter electrode. The coated face of the SS316L steel was exposed to corrosive medium, while the remaining area was masked using a masking tape. The samples were dipped into the solution during testing with required circuit connections. The experiments were performed by scanning the potential range from 0.5 V to -0.5 V, at a scanning rate of 0.001 V/s, with an initial delay of 3600 s. The Echem analysis software was used for the analysis of the data. Tafel extrapolation method was used to determine the corrosion potential and corrosion current density from the polarization curves of coated and uncoated steel samples.

3.5.2 Post-corrosion Analysis

Post-corrosion analysis was performed to understand the corrosion mechanism. SEM was used to reveal the microstructural changes due to corrosion. Phases were identified using XRD after corrosion testing. Additionally, elementals maps of the corroded samples were also taken using EDS.

3.6 Tribological Analysis

3.6.1 Experimental Setup

Pin-on-disc sliding wear test was conducted in a dry and simulated body fluid environment on a universal tribometer (UMT-2, Bruker, US) at room temperature following ASTM G99 [41]. Hank's solution was used as a lubricant in this study. The container of the tribometer is equipped with a rotating disk setup, into which Hank's solution is introduced. Alumina discs of diameter 6 cm were used as counterparts with a normal load of 2 N and sliding speed 0.1 cm/s for a sliding distance of 3.6 m. Cold sprayed coated pins of 6.3 mm diameter were used for the analysis. Schematic representation of pins are shown in Fig. 3.5. Weight loss and coefficient of friction (CoF) were recorded for each coating. The coatings were removed from the substrate using WEDM to measure the density of all the investigated samples. Archimedes's principle was used to determine the density of all the investigated coatings. The removed coatings were weighed in air and then weighed in distilled water using a density meter (METTLER TOLEDO, MS 105, Switzerland) with an accuracy of 0.01 mg. Five readings for each coating were taken, and an average value is reported. Equations (3.1) and (3.2) were used to calculate the volume loss and wear rates for the developed coatings.

$$\text{Wear volume} = \frac{\text{Mass before test} - \text{mass after test}}{\text{Density of the composite coating}} \qquad (3.1)$$

$$\text{Wear rate} \left(\frac{\text{mm}^3}{\text{N} - \text{m}}\right) = \frac{\text{Wear volume}}{\text{Applied load} \times \text{Sliding distance}} \qquad (3.2)$$
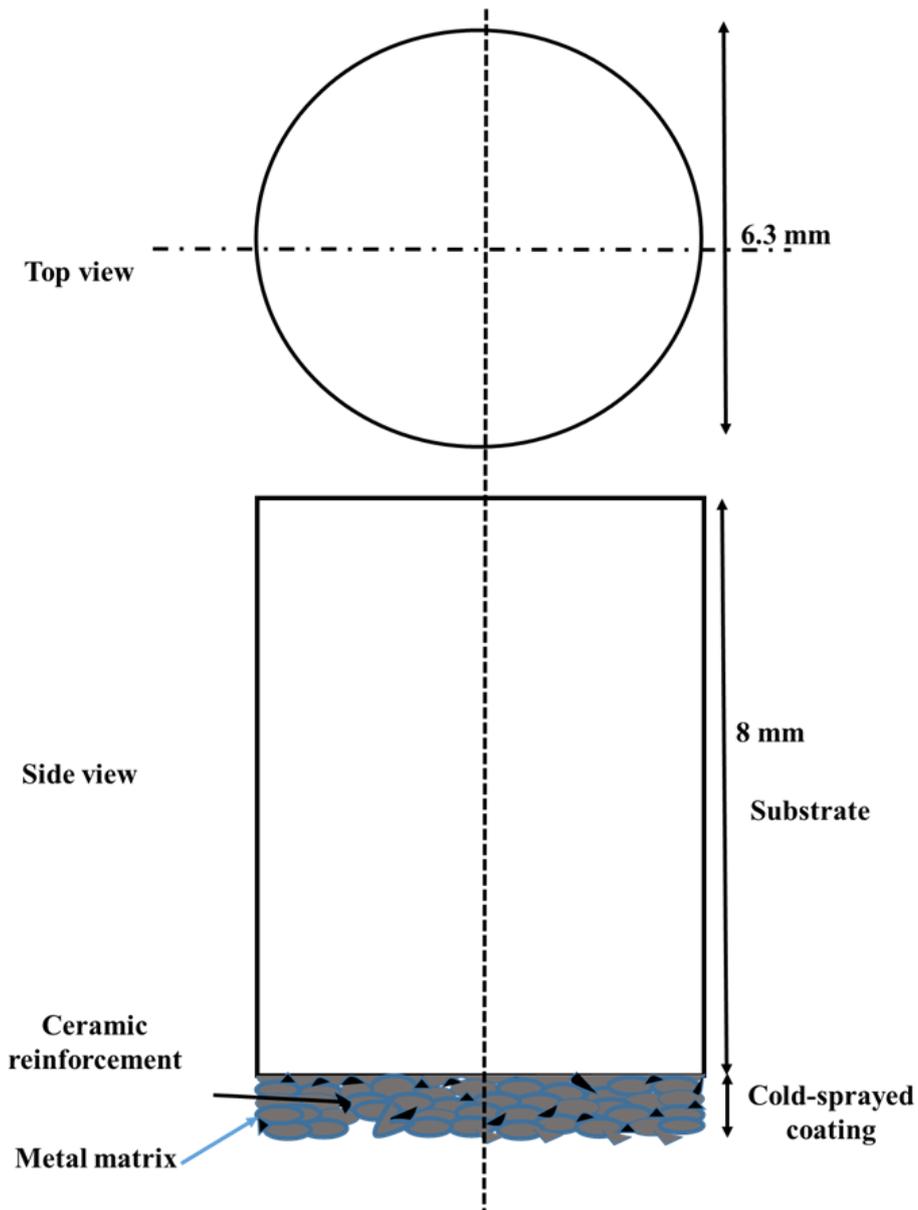
Figure 3.6: Schematic representation of pins used for sliding wear test of cold-sprayed Ti-based coatings against alumina disk.

3.6.2 Post-wear Analysis

Post-wear analysis was done to evaluate the effectiveness of the cold-sprayed coatings to minimize the wear losses of SS316L steel. The in-depth study of the worn-out coatings was done using SEM/EDS analysis to explore the wear mechanism. A detailed discussion on the obtained micrographs is reported in chapter 6.

CHARACTERIZATION OF COATINGS

This chapter describes the results related to substrate preparation for developing Ti-based coatings by cold spray. The development and characterization of Ti-based coatings on biomedical steel (SS316L) have also been discussed in detail. The substrate and coatings have been characterized using various tools such as optical microscopy (OM), scanning electron microscopy (SEM), energy dispersive spectroscopy (EDS), and X-ray diffractometer (XRD). Besides these, roughness tester, microhardness tester, scratch tester, and ImageJ software have also been used to characterize the coatings.

4.1 Substrate Preparation Analysis for Ti-based Coatings

A single pass of Ti/20TiO$_2$ composite powder (P1) was cold-sprayed on mirror-polished (MP), ground-polished (GP), and as-received (AR) SS316L steel substrates to investigate the adhesion between the particles and the substrate. Fig. 4.1 shows the roughness profiles of all the substrates along with arithmetic mean roughness (R$_a$) and ten-point height irregularities (R$_z$) values. For MP substrate, R$_a$ and R$_z$ values were in the range of 0.04 µm and 0.320 µm, respectively, which are very small (negligible) compared to the particle size range. The R$_a$ and R$_z$ values for GP surface were 0.3 µm and 2.4 µm. For the AR surface, these values were R$_a$-4.950 µm and R$_z$-22.320 µm, which has significantly higher peaks and deeper valleys.
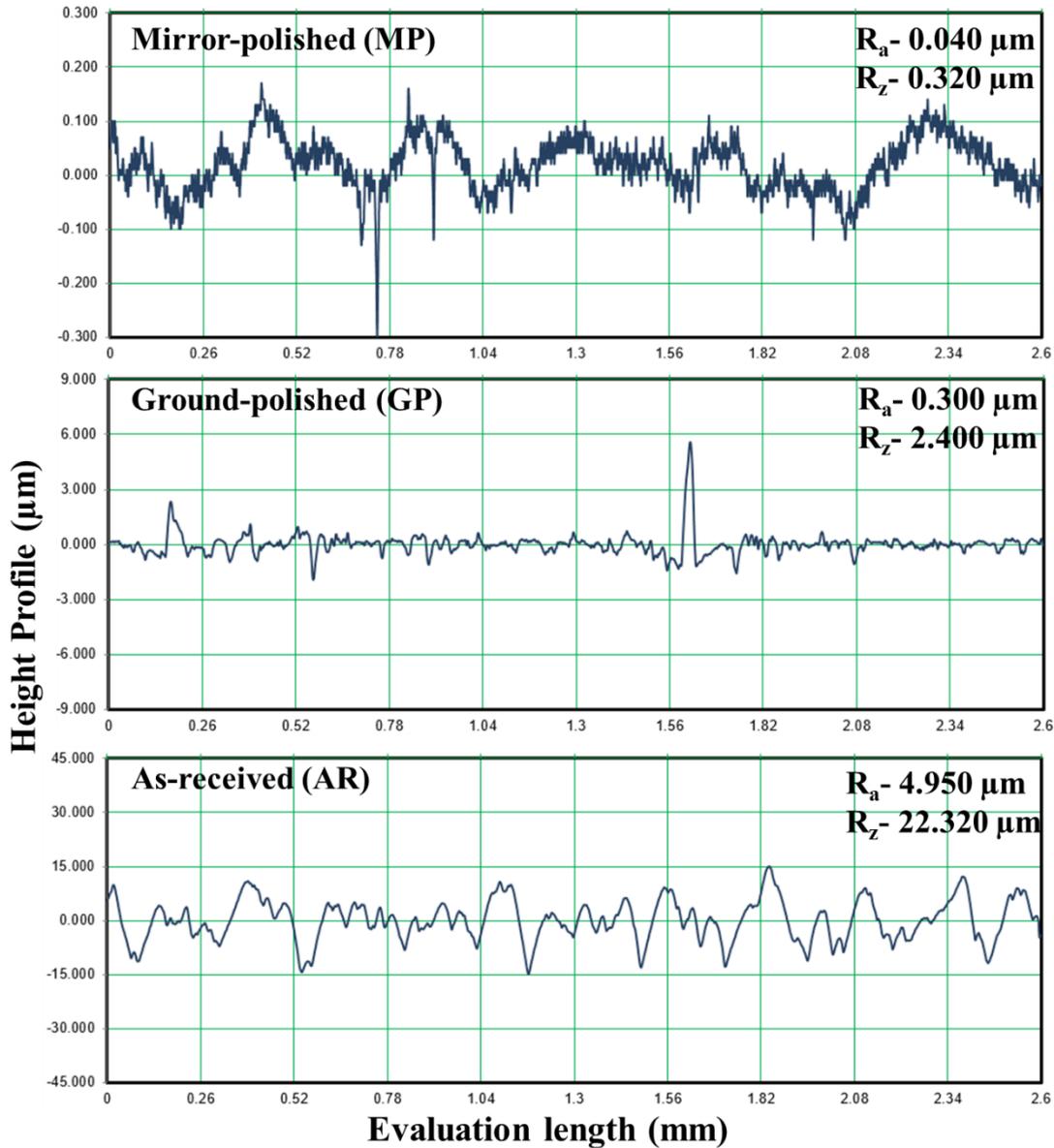
Figure 4.1: Surface roughness profiles of SS316L substrate steel subjected to various roughness levels prior to the deposition of cold spray coatings

The SEM surface micrographs of the prepared substrates are shown in Fig. 4.2. AR substrate has been characterized as a rough surface. The grinding grooves formed due to the sample cuttings are visible on the AR substrate; these grooves have deep valleys and high peaks. In the case of GP substrate, samples have been polished down to 800 grit of emery paper, led to reduction in peak height, on comparison with AR case. The shearing of the substrate surface due to polishing have led to the plastic deformation of these peaks, further filling the deeper valleys. In the case of MP substrate, specimens

have been polished down to 2000 grit emery paper followed by diamond paste polishing on a velvet cloth. Hence, a mirror-polished surface has been achieved (Fig. 4.2).
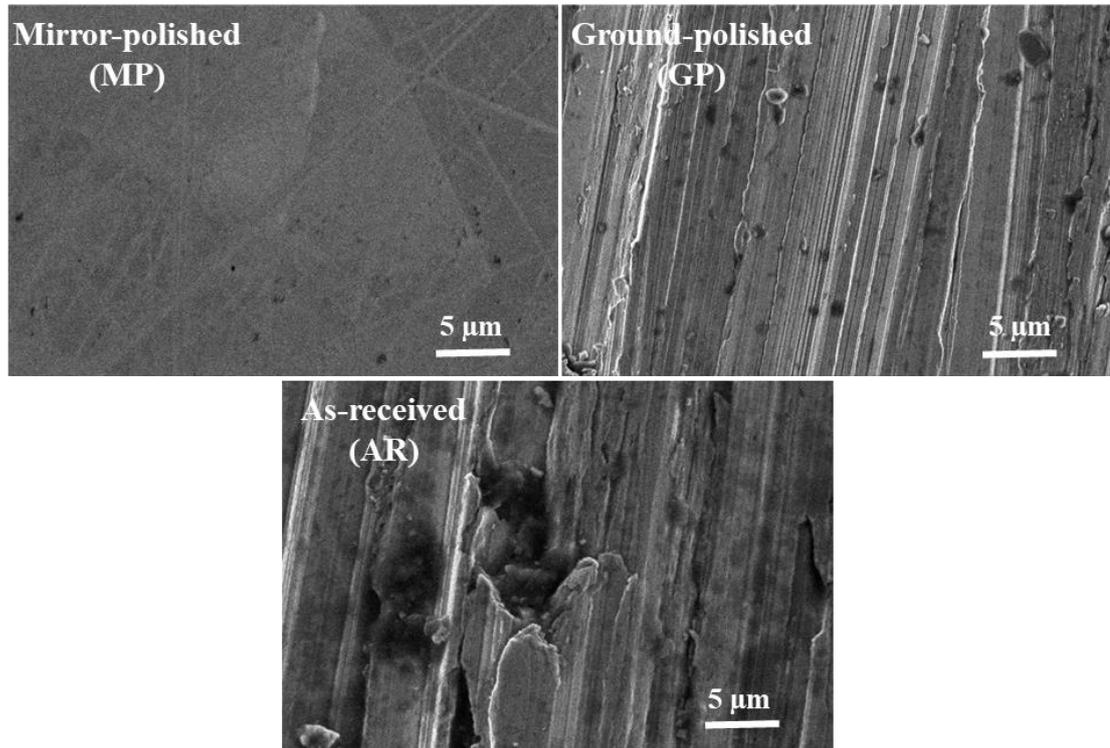
Figure 4.2: SEM micrographs of SS316L steel substrate surface used for cold spraying of Ti/TiO$_2$ powders (i) as-received (ii) ground-polished (iii) mirror-polished

SEM cross-sectional micrographs of all three single-pass cold-sprayed Ti/20TiO$_2$ coatings are shown in Fig. 4.3. The analysis shows that the interfacial bonding is best in MP case, whereas it seems to be poorest in GP case. In case of GP substrate, there is a clear indication of a continuous microgap between the coating and GP substrate. The deformation of the particle has been affected more severely in comparison with the AR substrate, which may be caused by the absorption of kinetic energy by a larger number of smaller peaks and valleys present in the substrate. In between the deformed Ti particle, TiO$_2$ traces can also be observed. Fig. 4.3 (i) shows the Ti/20TiO$_2$ composite coating over AR substrate indicating some cracks, micro-gaps and voids at the interface of the coating and substrate. These are indications of poor bonding, which could be attributed to the insufficient deformation of the Ti-particles. It is believed that the kinetic energy of the impacting particles has partially been absorbed in deformation of the relatively larger peaks on the substrate surface due to which deformation of the Ti-

particles remained insufficient. In other words, the AR substrate surface causes the non-uniform plastic deformation and temperature distribution of the impacting particle and prevents the intimate bonding at the interface (Tan et al., 2019).

In the case of MP substrate, no gap or crack was observed between the coatings and substrate. Additionally, Ti particles were found to be completely deformed and adhered over the substrate. The greater chances of conversion of a relatively large amount of kinetic energy into heat energy owing to the larger contact area can be one of the reasons for this observation. This high heat energy might have led to the localised melting at particle/substrate interface, leading to a good metallurgical bonding. TiO_2 can also be observed reinforced at several places in the coating.
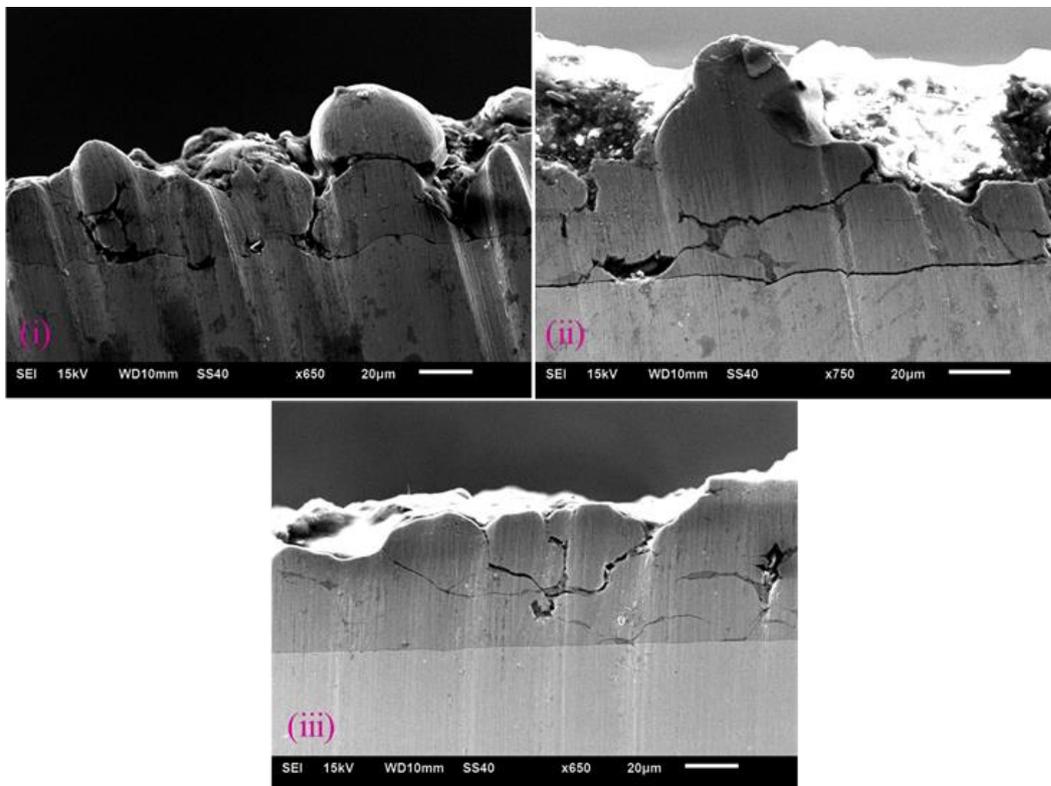
Figure 4.3: Cross-sectional SEM analysis of the single-pass cold-sprayed Ti/20TiO$_2$ composite coatings on SS316L having various surface conditions (i) as-received (AR) (ii) ground-polished (GP) (iii) mirror-polished (MP)

The scratch adhesion testing was performed to assess the adhesion of the coating over the substrate. The coefficient of friction (CoF), frictional force (F_f), and the residual depth of the indentor (D) against the normal applied load are reported in Fig. 4.4 and Fig. 4.5. The data is drawn for progressively increasing load from 0-80 N for all the

three cases: MP, SP, and AR substrates. Sudden change in CoF and F_f accompanied with D indicates the coating's failure. Two types of failures have been identified from the results: cohesive failure of the coating (start of inter-splat failure, represented by Lc_1) and adhesive failure (start of coating delamination from the substrate, represented by Lc_2). The CoF and F_f for Ti/20TiO$_2$ composite coatings on MP substrate have dropped suddenly at an applied normal load of 22 N. Sudden change in D can also be observed at the exact location, which has been identified as Lc_1 region. Furthermore, this synergic change in CoF, F_f, and D is observed at 68 N and has been identified as the Lc_2 region. Similarly, sudden change in CoF, F_f, and D has been observed at an applied normal load of 4 N for the coating deposited on GP substrate. This change is so significant that the region can be identified as Lc_1 and Lc_2. In the case of the coating deposited on AR substrate, CoF, F_f, and D have shown a sudden change at 13 N of applied normal load, which has been identified as Lc_1. Lc_2 region has been identified at a normal load of 33 N due to the change in CoF, F_f, and D. Fig. 4.5 (b) shows the critical load value of Lc_1 and Lc_2 type of failures of the coating on different substrates. The critical load is observed to be maximum in the case of MP substrate and minimum on GP substrate, indicating that the MP substrate surfaces are better for developing Ti/TiO$_2$ composite coatings. These results are in agreement with the earlier reported data for copper coating on SS316L substrate (Singh et al., 2020a). Fig. 4.6 shows the micrographs of the damaged surface (Lc_1 and Lc_2 region) after the scratch testing for all the composite coatings. The width of the scratches has been found to be minimum for MP substrate and maximum for GP substrate in both regions (Lc_1 and Lc_2). The traces of the delaminated coating from the substrate have also been observed around the scratches in the Lc_2 region for all cases. Out of all the images, only AR-Lc_2, GP-Lc_1 & Lc_2 exhibit a zig-zag scratch pattern, which may have been caused by the interaction between the substrate surface peaks and the indentor. The roughness of the substrate might have obstructed the movement of the indentor upon contact, resulting in the zig-zag scratch pattern. In contrast, straight scratches were observed in all the other cases, where the indentor was in direct contact with either the coatings or the MP substrate.
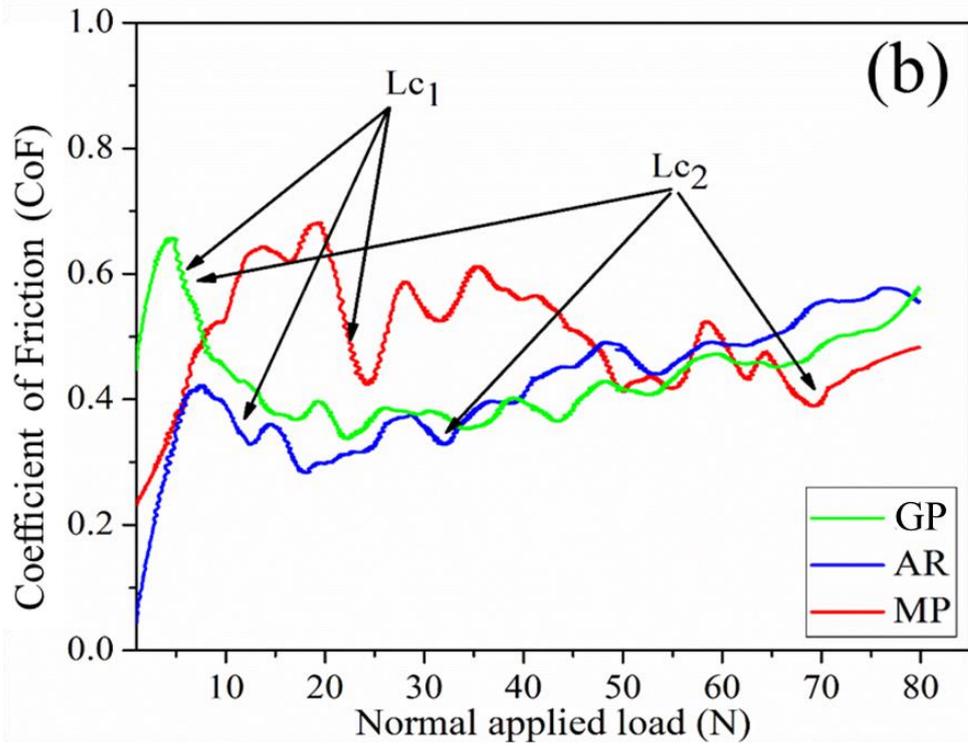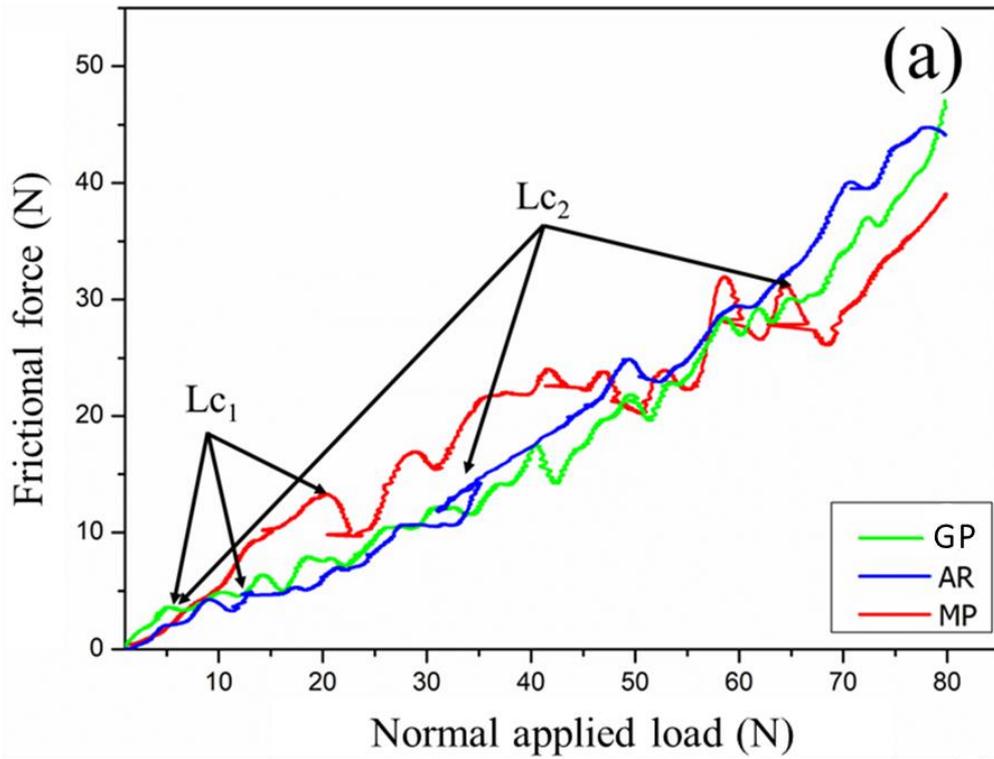
Figure 4.4: Scratch results of cold-sprayed Ti/TiO$_2$ deposits on different substrate conditions (a) frictional force *vs* normal applied load (b) CoF *vs* normal applied load
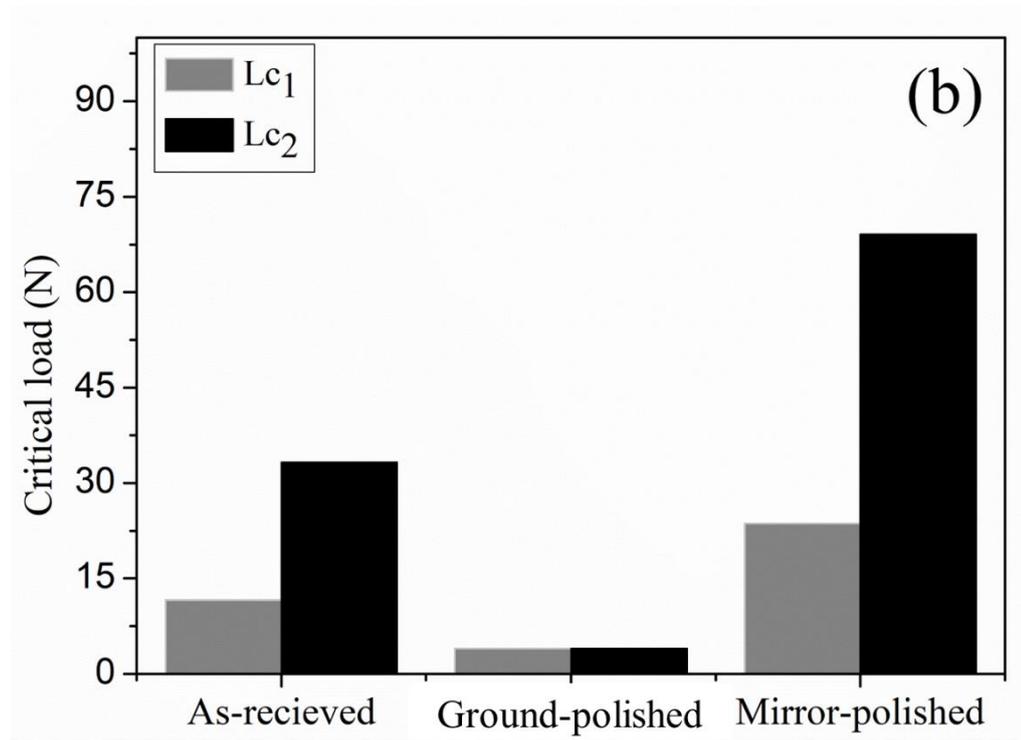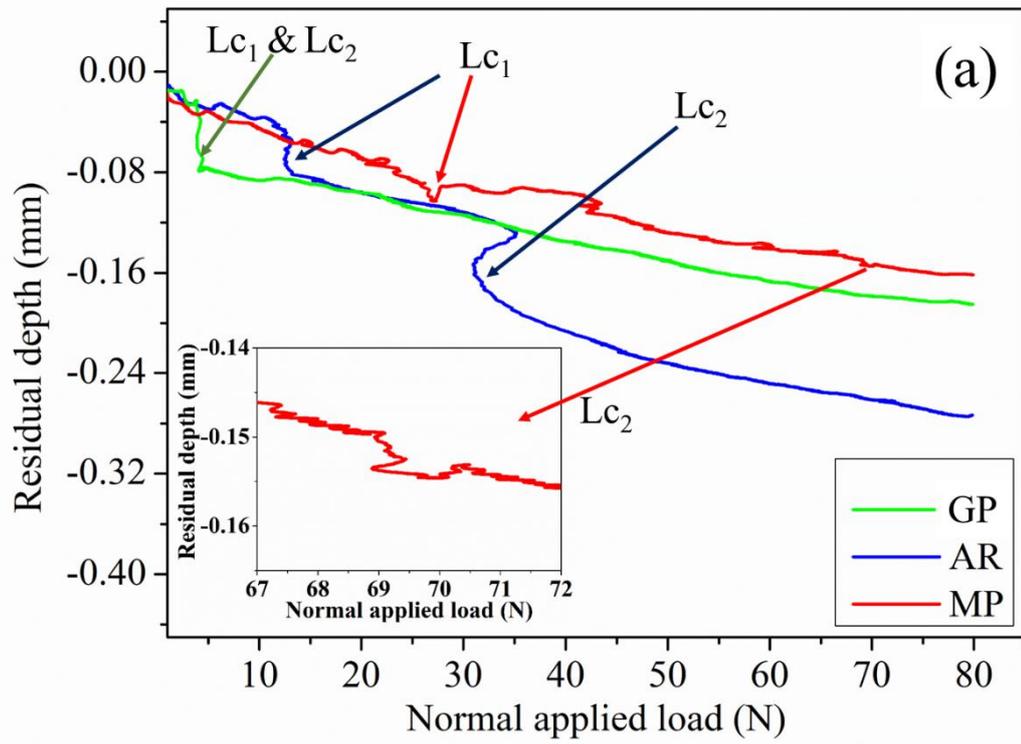
Figure 4.5: Scratch results of cold-sprayed Ti/TiO$_2$ deposits on different substrate conditions (a) residual depth *vs* normal applied load (b) critical load
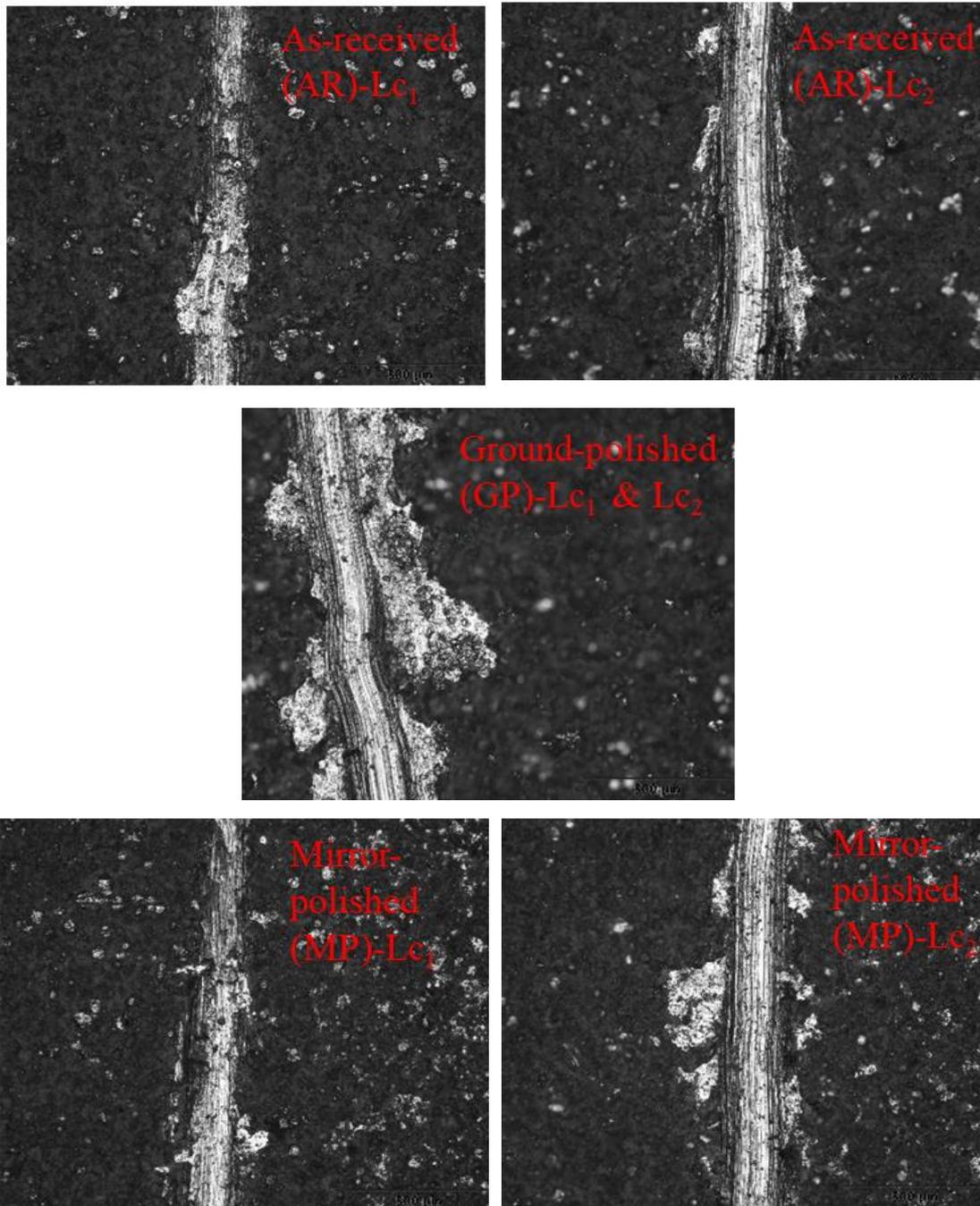
Figure 4.6: Optical micrographs of cold-sprayed Ti/20TiO$_2$ coatings on SS316L
steels subjected to scratch test

4.2 Characterization of Titanium/Titanium Oxide (Ti/TiO$_2$) Composite Coatings

4.2.1 Microstructural Characterization

The Ti/TiO$_2$ composite powders (P2, P3, and P4) were cold-sprayed over MP SS316L
substrate in different compositions (Chapter 3) to investigate the effect of ceramic

content in feedstock on bonding and performance of the coatings in terms of corrosion and wear resistance. The number of passes in all the coating compositions was kept the same as eight (8). The cross-sectional images of the deposited coatings are reported in Fig. 4.7. From Fig. 4.7, it is clearly visible that all the coatings have adhered well to the substrate. There is no gap or voids observed at the interface. The Ti particles seem to deform completely, and the fracture of TiO_2 particles can be observed in between the Ti splats. It is because the critical velocity to achieve bonding for Ti is relatively higher when compared with the TiO_2 particle or because the fracture toughness of Ti is higher than that of the titanium oxide (Nadaraia et al., 2021; Wang et al., 2021; Wong et al., 2010; YAMADA et al., 2009).

The percentage area fraction of the TiO_2 particles in each of the coatings at different locations from cross-sectional SEM micrographs has been measured from the respective cross-sectional images using ImageJ software. It is observed from the analysis that the TiO_2 particles cover 10-16% of the cross-sectional surface area at the bottom of the Ti/20TiO$_2$ coating. However, at the top, it varies from 18-30%. In the case of Ti/40TiO$_2$, it varies from 2-7% at different locations. Few traces of TiO_2 are observed at the top and at the Ti/60TiO2 coating interface. It may be because of the fracture of TiO_2 particles onto the substrate and/or Ti particles. Fig. 4.7 depicts that the coating thickness of the deposited coatings has decreased as the ceramic content is increased in the feedstock. From the SEM images and image J software analysis (average of a total of 8 readings each), the coating thickness of the cold spray deposits has been measured and reported in Table 4.1. The coating thickness has decreased with the increase in ceramic content. In Ti/60TiO$_2$ composite coating, the coating thickness is very less, around 35 microns. It may be because the high ceramic content leads to poor deposition efficiency caused by the more frequent interaction of ceramic-ceramic and ceramic-metallic particles, which may have affected the impact velocity of the metallic particles (Irissou et al., 2007; Wang et al., 2010). The density of the deposited coatings is reported in Table 4.1, and it can be observed that the density of developed composite coatings has decreased with the increase in ceramic content. Ceramic present in the feedstock is believed to leave the hammering or tamping effect, leading to a dense coating microstructure (W. Y. Li et al., 2007; Sabard et al., 2020). However, higher amounts of ceramic content hinder the deposition of metallic particles. Subsequently, cold spraying results in the

development of coatings with poor microstructural and mechanical properties (Wang et al., 2010).
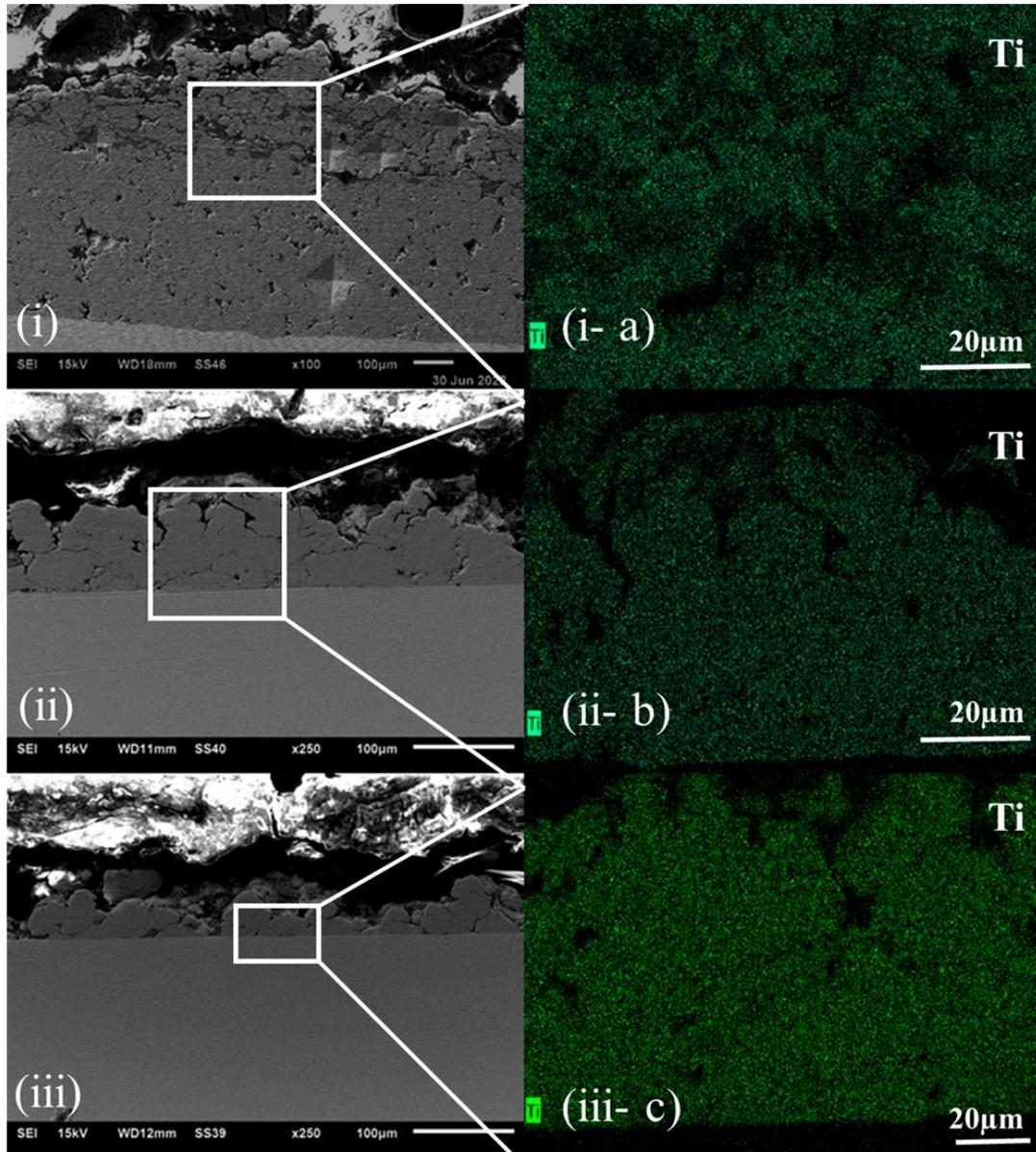
Figure 4.7: Cross-sectional SEM and EDS micrographs of the cold-sprayed coatings on mirror-polished SS16L substrate (i) Ti/20TiO$_2$ (ii) Ti/40TiO$_2$ (iii) Ti/60TiO$_2$

SEM surface micrographs and the EDS maps of the developed coatings are shown in Fig. 4.8. EDS maps depict that the retention of TiO$_2$ is maximum in Ti/20TiO$_2$ case, which is in good agreement with the above discussion. Also, it is noticeable that with the rise of TiO$_2$ content in feedstock, retention of TiO$_2$ has dropped. It may be because the probability of inter-particle interaction increases with the increase in TiO$_2$ content,

which restrict the deposition of Ti particles and consequently less interlocking of TiO_2. SEM images show the coated samples' morphology; Fig. 4.8(a, a-1) indicate that the topmost layer of the coating has undergone relatively smaller plastic deformation during cold spraying due to the hammering of TiO_2 particles on already deposited Ti particles. Fig. 4.8 (b, b-1) show that with the rise in TiO_2 content to 40%, the deformation of Ti particles became relatively severe. In the case of Ti/60TiO_2 coating, the Ti particles have deformed more severely than that in the other two cases (Fig. 4.8 (c, c-1)). It means that the Ti particles got significantly hammered by many TiO_2 particles during deposition. Similar observations are reported by Zhang et al. (Z. Zhang et al., 2019) for cold spraying of Al2024/Al_2O_3 composite powders on AA 2024-T3 substrate.
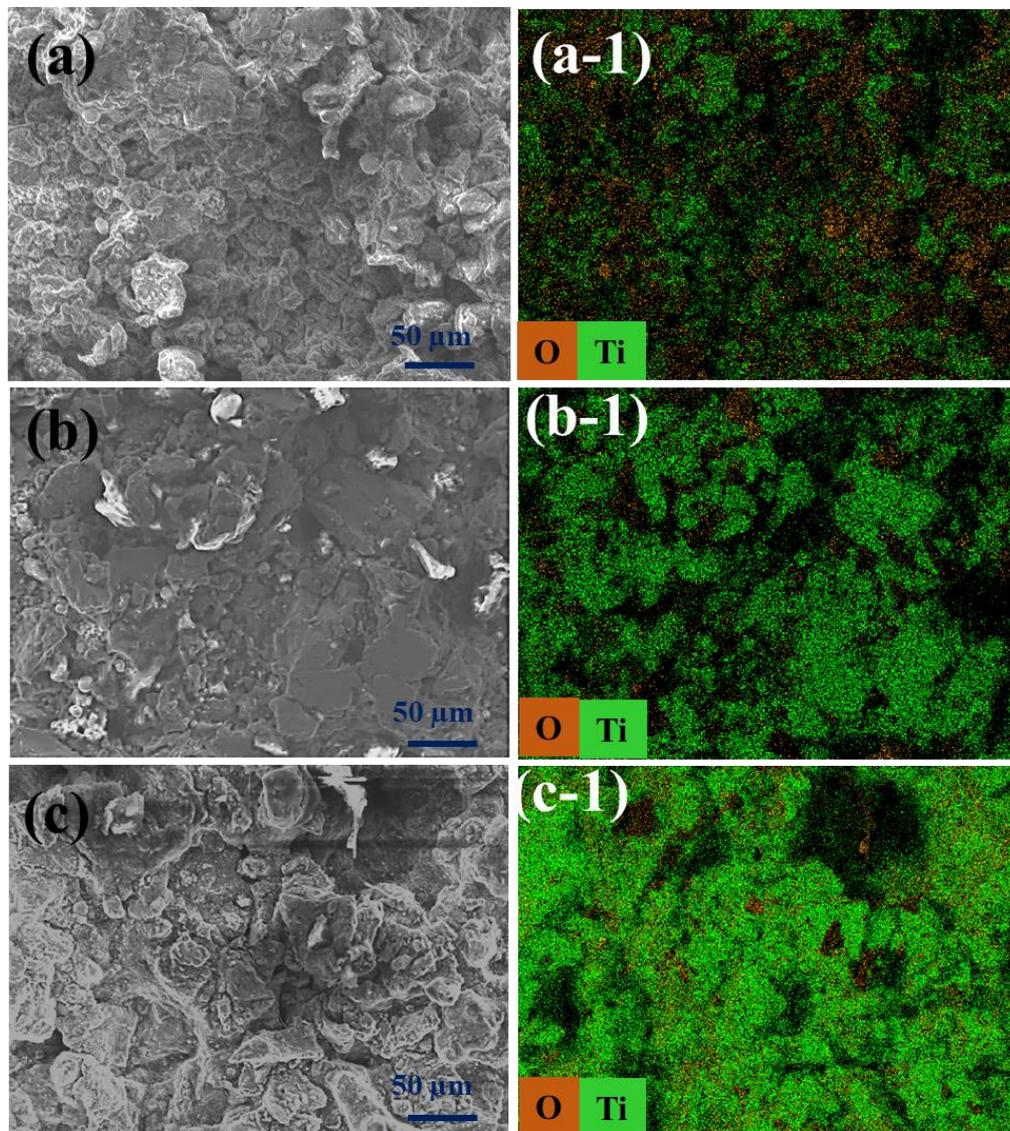
Figure 4.8: SEM/EDS micrographs of coated samples (a, a-1) Ti/20TiO_2 (b, b-1) Ti/40TiO_2 (c, c-1) Ti/60TiO_2

4.2.2 Microhardness Analysis

The microhardness data of the as-deposited Ti/TiO$_2$ composite coatings are shown in Table 4.1. The results reveal that the Ti/20TiO$_2$ composite coating has better microhardness than the substrate (183± 4 HV), that is, 245 ± 11 HV. The microhardness of other coatings is relatively lesser than the substrate. The particles rebound after a threshold value of ceramic content in the feedstock and do not leave enough tamping effect. Moreover, high ceramic content leads to poor cohesive strength in the coating (Wang et al., 2010), hence leading to lesser microhardness. The microhardness of Ti/60TiO$_2$ composite coating could not be measured due to its lesser thickness. The surface roughness values of the as-deposited cold spray coatings is reported in Fig. 4.9, which indicate that the surface roughness decreases with the increase in oxide/ceramic (TiO$_2$) content into the feedstock material. One of the reasons behind this can be the hammering effect or tamping effect. The ceramic-ceramic (TiO$_2$/TiO$_2$) and ceramic-metallic (TiO$_2$/Ti) particles' interaction increases with the increase in ceramic (TiO$_2$) content, which produces hindrance in the further deposition. However, before they can bounce back, these particles strike over the already deposited particle, helping in their further deformation (Li and Li, 2003). Fig. 4.7 shows that the deformation of sprayed powder is relatively lesser in Ti/20TiO$_2$ than in the Ti/40TiO$_2$ and Ti/60TiO$_2$ composite coatings, and it increases with the increase in TiO$_2$ content. Hence, more deformation leads to the development of coatings with lesser surface roughness. Other than this, the coated area covers a significant amount of TiO$_2$ particles in Ti/20TiO$_2$ coating, which decreases with the increase in TiO$_2$ content. However, beyond 20% of TiO$_2$ content, these are fractured particles of TiO$_2$ primarily due to the higher amount of TiO$_2$.

Table 4.1: Mechanical properties of the as-deposited Ti/TiO$_2$ composite cold spray coatings on MP SS316L substrate

S.No	Coating designation	Density (g/cm^3)	Micro-hardness (HV$_{0.5}$)	Coating thickness (μm)
1.	Ti/20TiO$_2$	3.731 ± 0.072	245 ± 11	530 ± 23
2.	Ti/40TiO$_2$	2.980 ± 0.061	158 ± 13	92 ± 14
3.	Ti/60TiO$_2$	------------	----------	35 ± 17
4.	Substrate (SS316L)	----------	183± 4	-----------
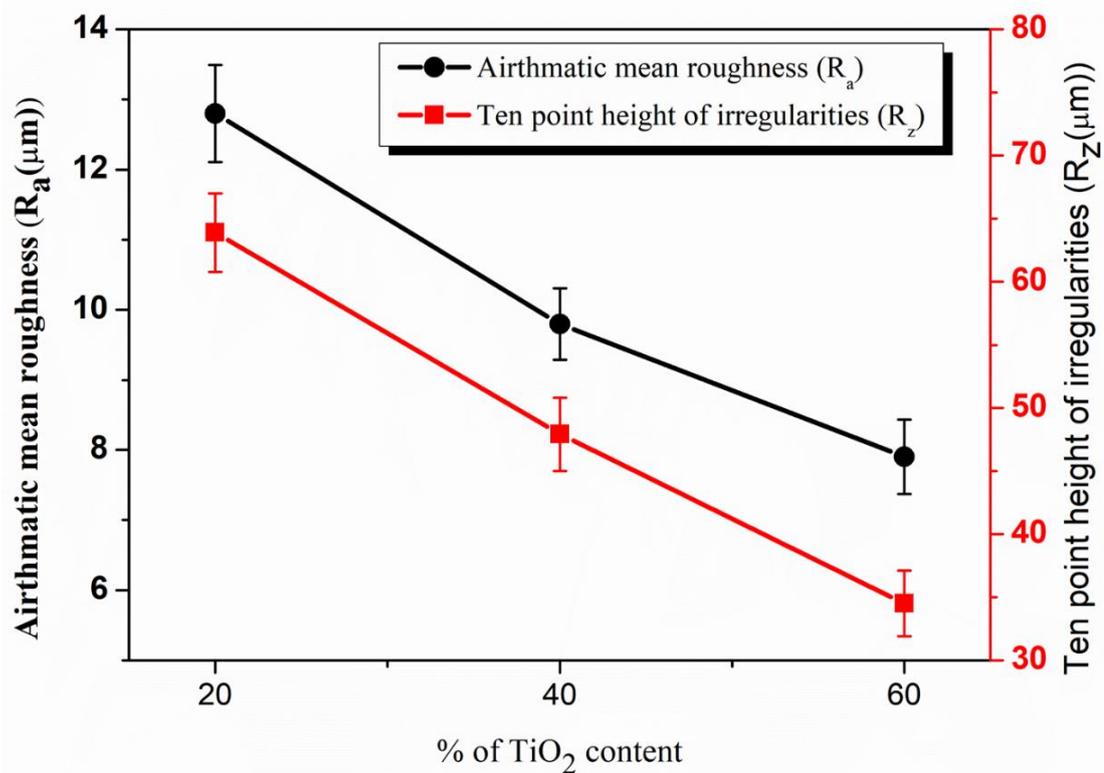
Figure 4.9: Surface roughness plots of the as-deposited Ti/TiO$_2$ composite cold spray coatings

4.3 Characterization of Titanium/Baghdadite (Ti/BAG) Composite Coatings

4.3.1 Microstructural Characterization

The powders are irregular in shape (as shown in previous chapter), which is a desirable attribute since such particles need lesser energy to attain critical velocity for the deposition in cold spray (Jodoin et al., 2006; MacDonald et al., 2017; Munagala et al., 2018). MP steel substrate (SS316L) was selected for the deposition of coatings because of their good adhesion with the Ti-based feedstock in cold spray, as discussed above. The cross-sectional micrographs of the as-sprayed Ti/BAG composite coatings are shown in Fig 4.10. From the micrographs, it is clear that the coatings are in continuous contact with the respective mirror polished steel substrate, and there are no voids or cracks at the interfaces. Ti particles are completely deformed and integrated into the layers. However, there is a presence of micro-pores along some of the particle-particle interfaces. The number of pores increases with the increase in the BAG content. The

void formation may be attributed to the ceramic nature of BAG, which on solid-state impact (cold spray) would result in fracture of the particle (Qin et al., 2021).
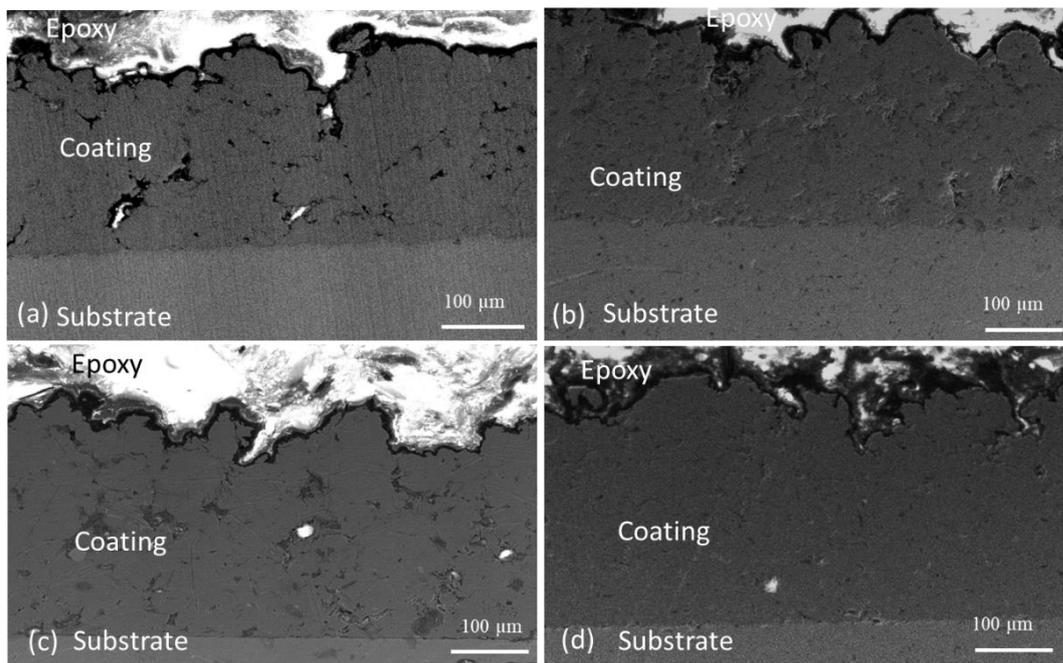
Figure 4.10: Cross-sectional SEM micrographs of cold sprayed Ti/BAG composite as-sprayed coatings on SS316L steel substrate (a) Ti/25 BAG (b) Ti/20BAG (c) Ti/15BAG (d) Ti/10BAG

Fig. 4.11 shows the XRD analysis of the cold-sprayed Ti/BAG composite coatings. The results indicate no change in phase post-cold spraying, which is a desirable feature for our application. Also, post spraying titanium peaks were observed a little wider compared to those for the feedstock powder. It is because of the plastic deformation of the powder particles during spraying.
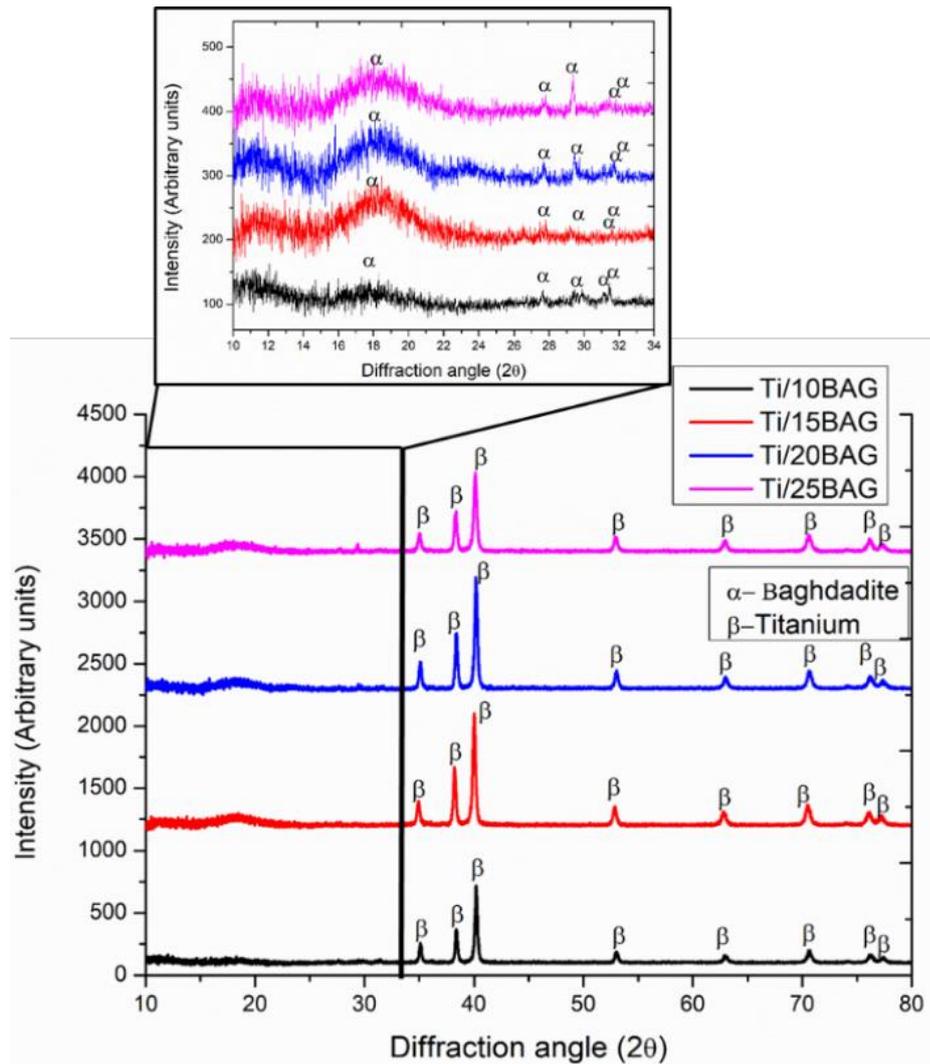
Figure 4.11: XRD analysis of cold sprayed Ti/BAG composite coatings on SS316L

Fig. 4.12 shows the elemental mappings of the cold-sprayed Ti/BAG composite coatings along their cross-sections and top surfaces, respectively. The mappings reveal that in Ti/BAG composite coatings, the major elements present are titanium (Ti), calcium (Ca), silicon (Si), oxygen (O), and zirconium (Zr). The mappings also show that Ti and BAG constituents prevail at alternate locations in the coating microstructure, indicating a typical metal matrix (Ti) composite embedded with the secondary phase (BAG). The Image J software was used to analyze and calculate volumetric retention from cross-sectional SEM/EDS images (Fig. 4.12 and Fig. 4.13). Further, volumetric retention was converted into weight retention. These analyses indicate that BAG content has reduced after the deposition in the range of 20-35% depending upon the overall coating composition. Moreover, the distribution of BAG in the coatings is found to be non-homogeneous.
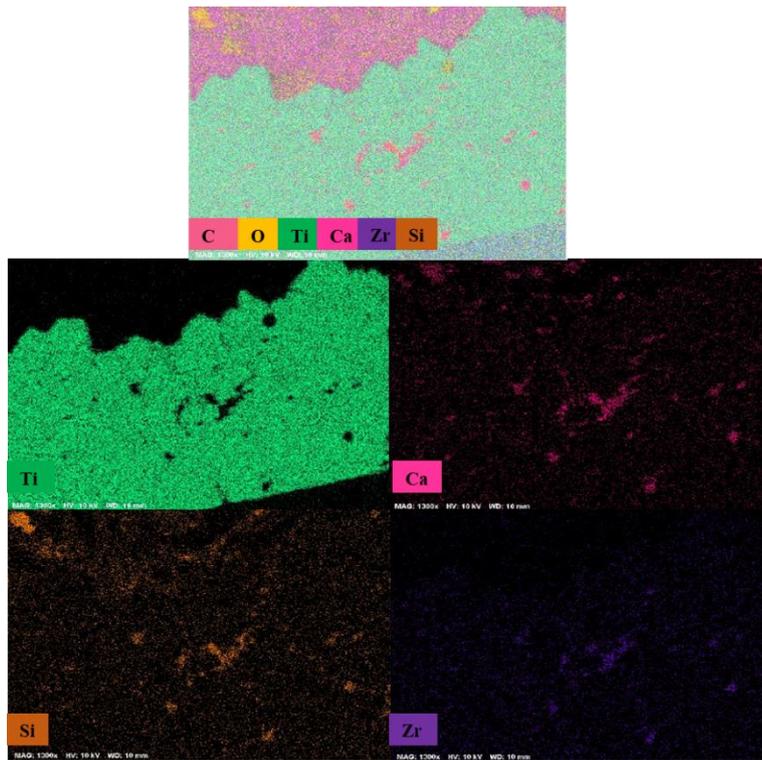
Figure 4.12(a): Cross-sectional EDS mappings of the cold-sprayed Ti/10BAG composite coatings on SS316L
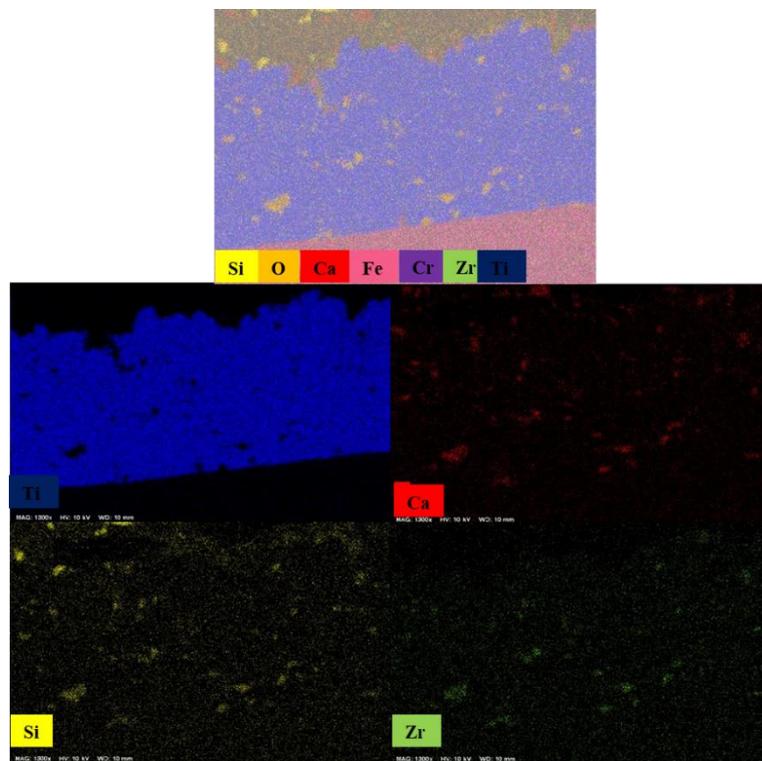
Figure 4.12(b): Cross-sectional EDS mappings of the cold-sprayed Ti/15BAG composite coatings on SS316L
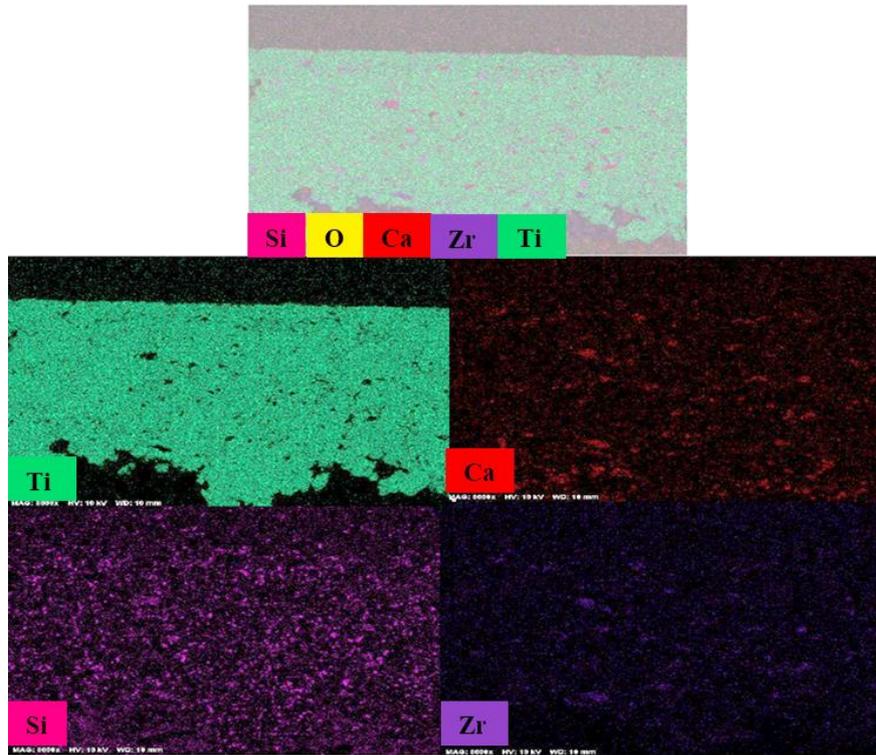
Figure 4.12(c): Cross-sectional EDS mappings of the cold-sprayed Ti/20BAG composite coatings on SS316L
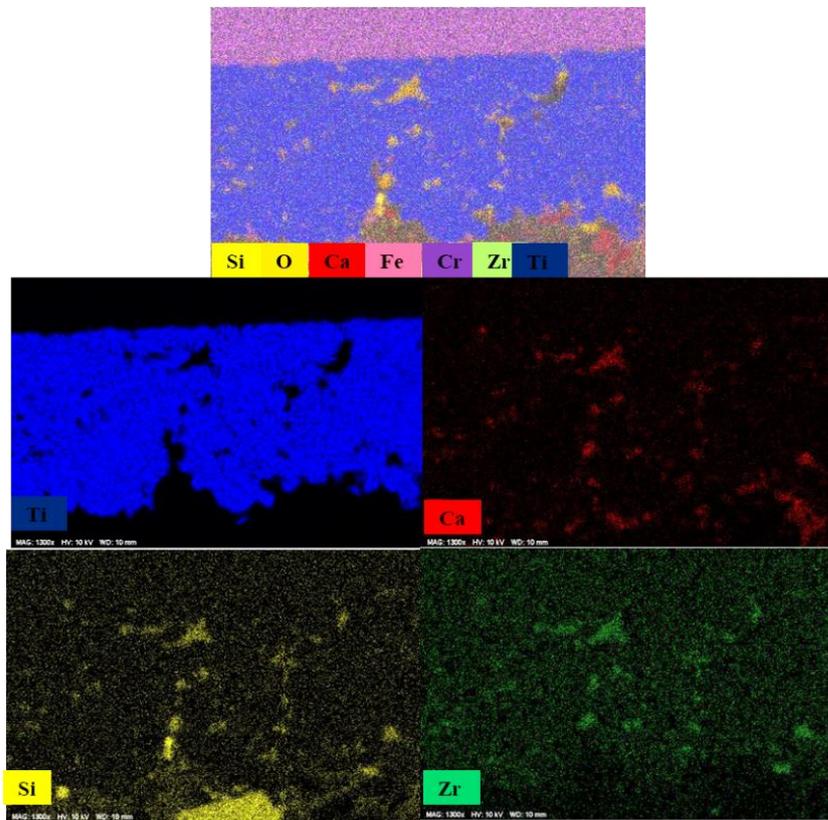
Figure 4.12(d): Cross-sectional EDS mappings of the cold-sprayed Ti/25BAG composite coatings on SS316L
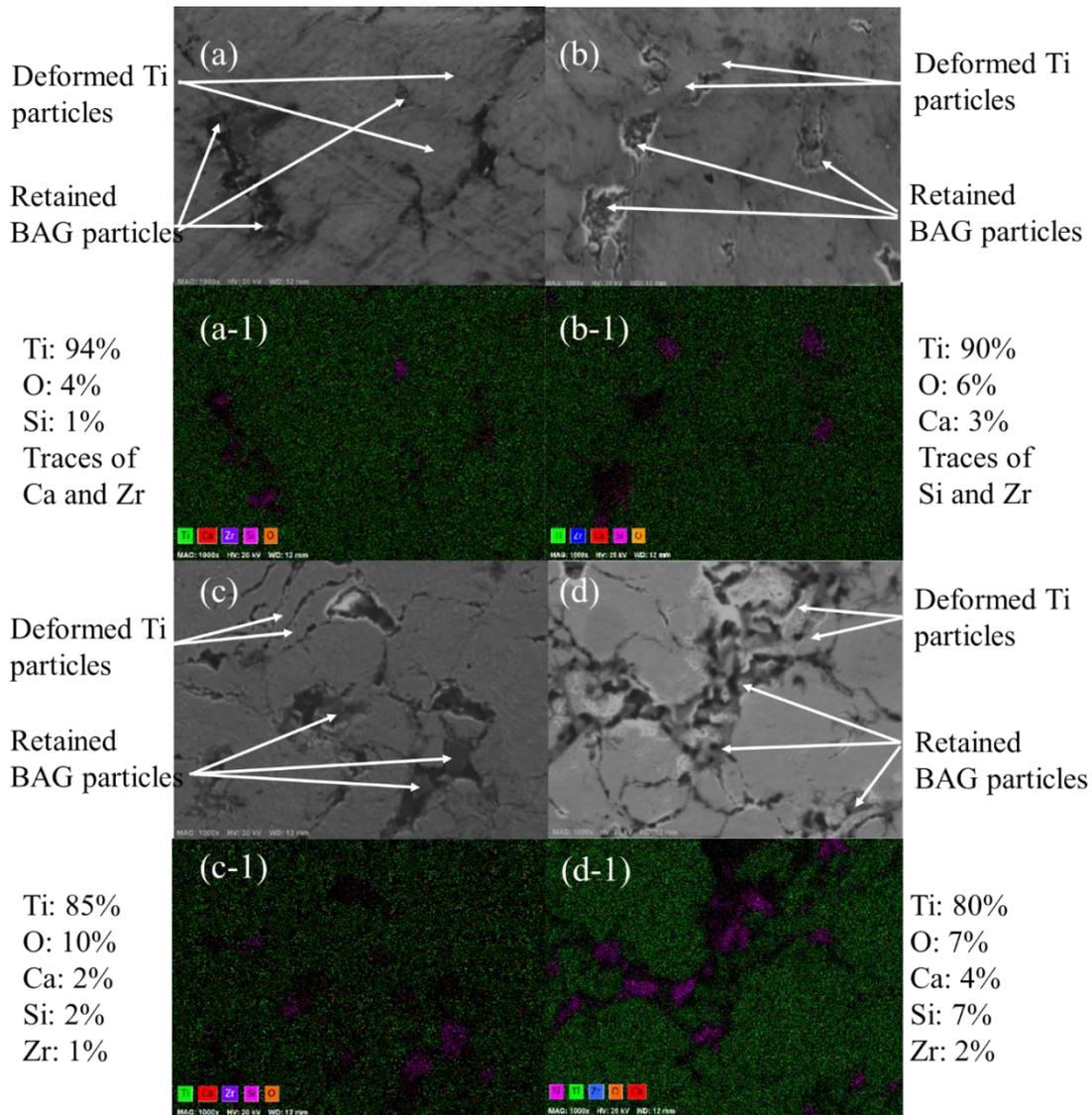
Figure 4.13: Cross-sectional SEM/EDS mapping of cold-sprayed Ti/BAG composite coatings on SS316L substrate with chemical composition (a, a-1) Ti/10BAG (b, b-1) Ti/15BAG (c, c-1) Ti/20BAG (d, d-1) Ti/25BAG

Surface SEM images along with chemical compositions are also reported, as shown in Fig. 4.14. The results revealed that the BAG was successfully deposited in the Ti matrix using the cold spray, and a reasonably good quality of the coatings is achieved. From Fig. 4.10 and ImageJ software (ten readings per each coating), it is clear that the coating thickness (Fig. 4.15 (a)) is decreased continuously from 236 ± 11 μm to 153 ± 8 μm with the increment in BAG content which may be because of the increment in ceramic content. It is reported that the increase in ceramic content reduces the bonding strength between the particles (Yandouzi et al., 2009). It is pertinent to mention that the number

of passes were kept the same in all the cases. The interaction between BAG-BAG particles dominates with the increment in BAG content. Since it is well known that the ceramic particles do not bond with each other, therefore a drop in deposition efficiency is expected, leading to lesser coating thickness with the same number of passes as the BAG content is increased. Similar results were reported by Wang et al. (Irissou et al., 2007) for Al/Al_2O_3 composite coatings on magnesium substrate. Irissou et al. (Wang et al., 2010) discussed the effect of alumina (Al_2O_3) in cold-sprayed Al/Al_2O_3 composite coatings on mild steel in their work. They reported that deposition efficiency decreased after a threshold value of alumina content in feedstock.
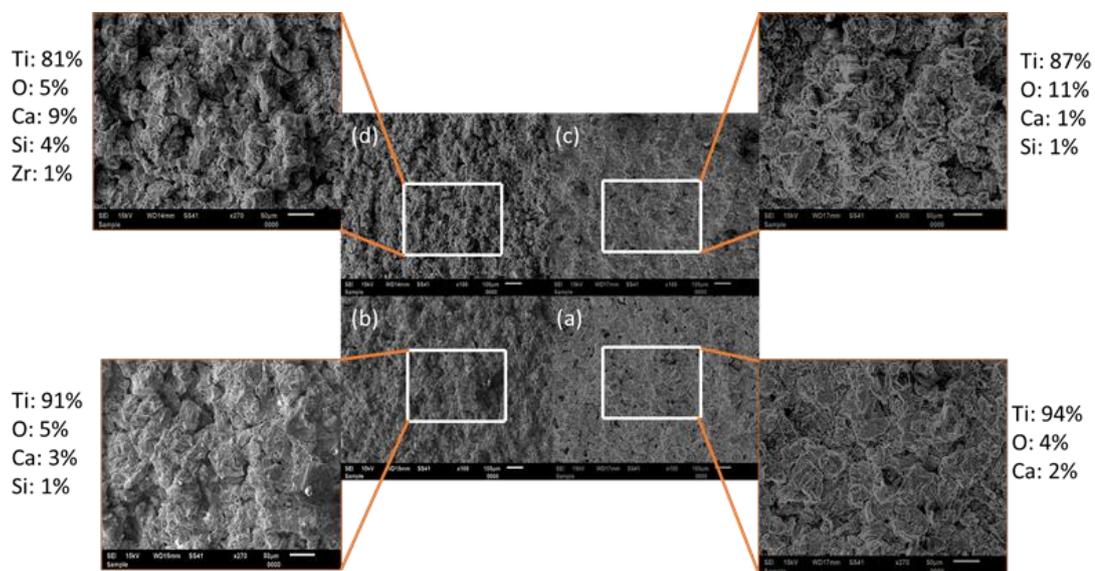
Figure 4.14: Surface SEM micrographs of the cold-sprayed Ti/BAG composite coatings on SS316L substrate with chemical compositions (a) Ti/10BAG (b) Ti/15BAG (c) Ti/20BAG (d) Ti/25BAG

4.3.2 Mechanical Characterization

Sousa et al. (Sousa et al., 2020) reported that the coatings around 200 µm thick are sufficient to develop a barrier to corrosion. Being a new material and substrate combination, several trial experiments were conducted (Gas pressure range: 15-30 bar and gas temperature range: 600-900 °C) to arrive at the reported parameters. The coating thickness was chosen as the output response with 200 µm as the threshold value. From the results shown in Fig. 4.15 (a), it is observed that the porosity of the sample increases with the increment of BAG content. It may be because when ceramic/metallic particles impact on metallic/ceramic particles, ceramic particles either fracture or show no significant plastic deformation and lead to poor bonding or voids/gaps at the splat

boundaries (Seo et al., 2012; Shockley et al., 2015). As the ceramic content increases, this interaction of ceramic-ceramic particles or ceramic-metallic particles also increases, leading to more voids/gaps at the splat boundaries. Porosity may or may not affect the coating's corrosion performance, but it affects the osseointegration ("An Open-Porous Titanium Coating for Advanced Osseointegration Poster No . 2216 • 55th Annual Meeting of the Orthopaedic Research Society," 2000).

Surface roughness plays a vital role in biomedical coatings as it provides more surface area for cell adhesion or cell growth. Simultaneously, surface roughness also affects the corrosion performance as it allows more area to corrode (Krishna et al., 2020). The results plotted in Fig. 4.15 (b) indicate the improvement in as-sprayed surface roughness with BAG content progression. From the graph, it can be observed that an increase in surface roughness from Ti/10BAG to Ti/15BAG is way less than Ti/15BAG to Ti/20BAG and Ti/20BAG to Ti/25BAG coatings. It may be due to the fact that with an increase in ceramic content, chances to get bonded with the metallic particles on the top layer will decrease due to the increase in the interaction of ceramic-ceramic particles. As ceramic content increases, deposition efficiency decreases due to the increment in ceramic-ceramic particle interaction. In other words, more particles rebound without bonding and lead to relatively higher tamping effect (Li and Li, 2003; Sabard et al., 2020). However, irregular powders morphology was observed to leave a very less tamping effect and result in higher porosity and greater roughness (Qiu et al., 2020, 2018).
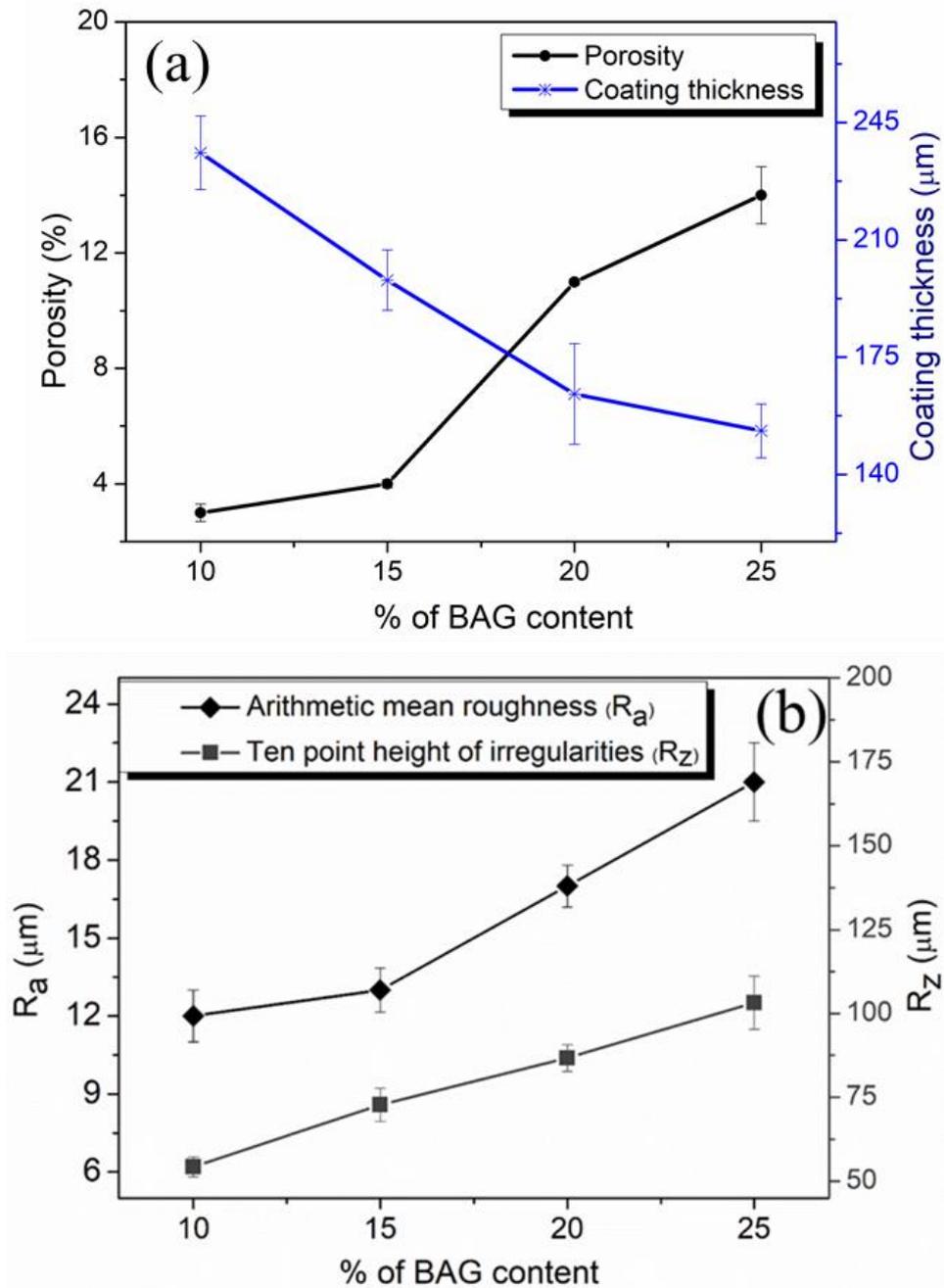
Figure 4.15: (a) Porosity and coating thickness (b) surface roughness analysis of the as-received cold spray Ti/BAG composite coatings on SS316L

The bonding strength of the coatings was measured and reported in terms of the load (critical load) required to delaminate the coating material from the coating itself (cohesive or inter-splat failure) or from the substrate surface (adhesive failure). Scratch test results of the developed cold-sprayed Ti/BAG composite coatings are reported in Fig. 4.16. The data has been plotted as coefficient of friction (CoF) vs. scratch length for a constant load of 100 N and progressively increasing load of 20-140 N. Sudden

drop in CoF represents the failure of the coatings. In both the conditions, that is, at constant load and progressive load, the graph follows the same trend. However, the applied load is not sufficient to remove the coating from the substrate (adhesive failure) for the given scratch length, but some abrupt changes in CoF indicate that the coatings have started failing (cohesive or inter-splat failure). For constant load conditions, Ti/25BAG composite coating is observed to fail at 2 mm, followed by Ti/20BAG composite coating at 2.5 mm scratch length. Further, Ti/10BAG composite coating is failed at 3.9 mm scratch length, followed by Ti/15BAG composite coating failed at 4.1 mm scratch length. The same trend is observed in progressively increasing applied load conditions. Furthermore, data has been plotted for progressively increasing load conditions in terms of CoF vs. normal load. The plotted data also followed the above-mentioned trend. Critical load reported in Fig. 4.16(d) shows that Ti/15BAG coating has performed best and Ti/25BAG composite coating performed worst among all the investigated coatings.

The influence of BAG composition on microhardness is reported in Fig. 4.16(d). It is observed that the microhardness of the cold-sprayed Ti/BAG composite coatings increases with the increment in BAG content until it reaches the maximum value and then decreases. The reason for this can be the inter-particle interaction of BAG powder particles. As BAG content increases, inter-particle interaction of the BAG powder particle increases, which may lead to a lack of bonding between the coating layers and further affects the microhardness of the cold-sprayed Ti/BAG composite coatings. In other words, deposition efficiency decreases with the increment in ceramic content due to the increment in ceramic-ceramic particle interaction. The rebound particle hammers the exposed surface and lead to increase in hardness of the coating (Qiu et al., 2018). The microhardness of the developed coatings is better than the substrate in Ti/10BAG and Ti/15BAG composite coatings. The maximum value of microhardness is 176 ± 4 HV obtained for Ti/15BAG composite coating. It is believed that whenever ceramic content in feedstock crosses the threshold value the hammering effect may not be sufficient to help the extra deformation of earlier deposited particles and further may cause in weaker bonding and porous coating (Seo et al., 2012). Also, it has been observed from Fig. 4.15(a) and Fig. 4.16(d) that the coatings having porosity greater than 5% possess lower microhardness owing to their poor inter-splat bonding. These results are also supported by the critical load required for the failure of the coating in

scratch analysis (Fig. 4.16(d)). The critical load and microhardness values have been observed to follow the similar trends.
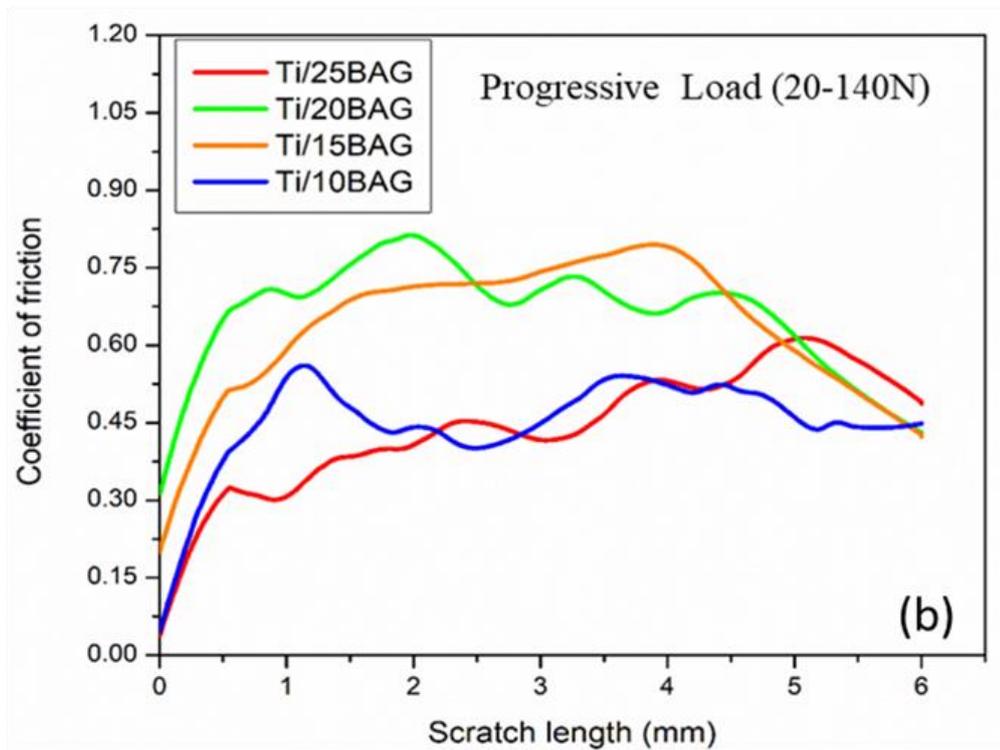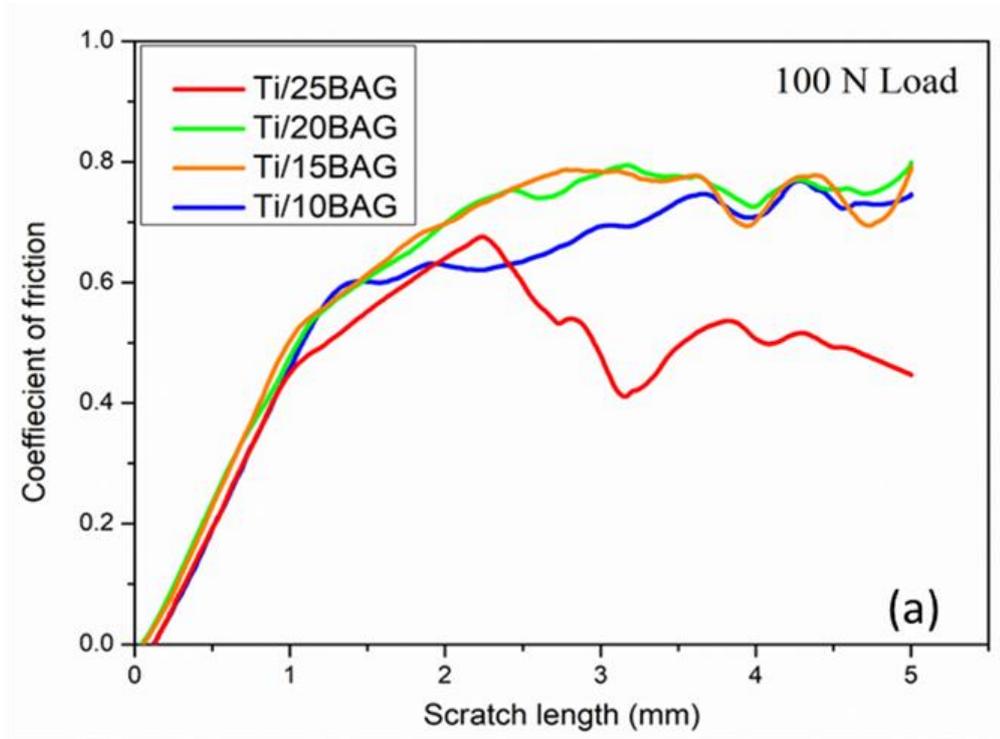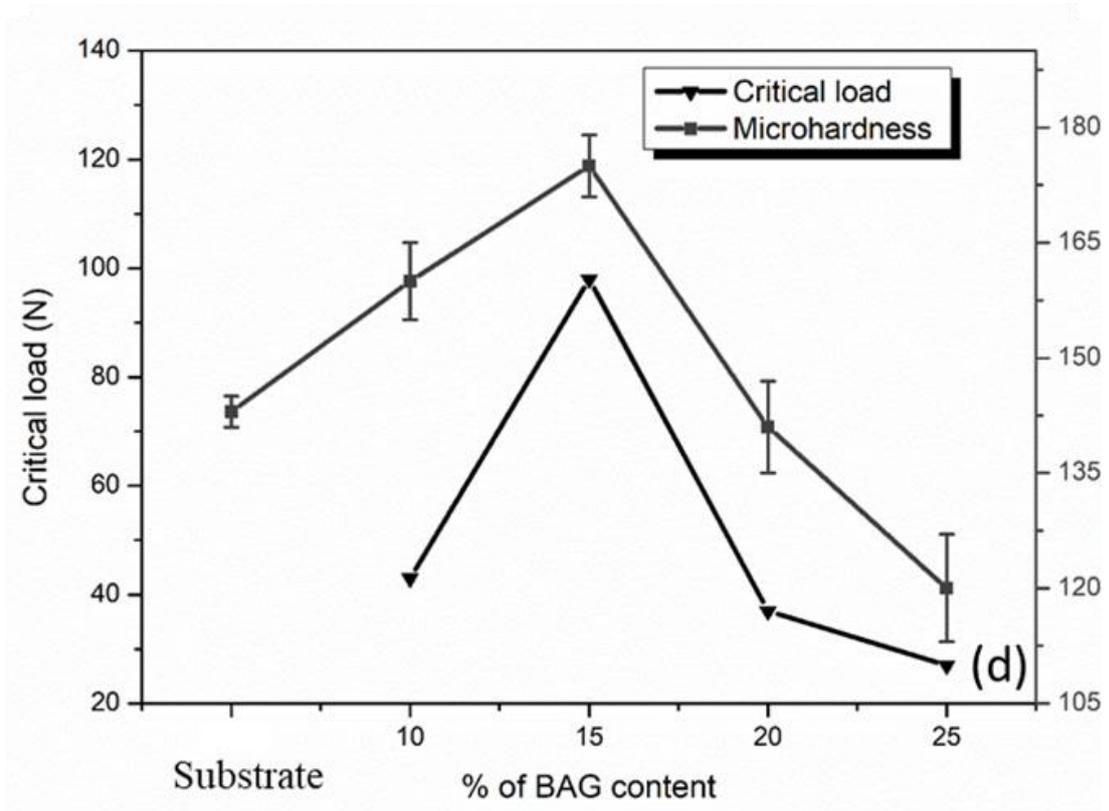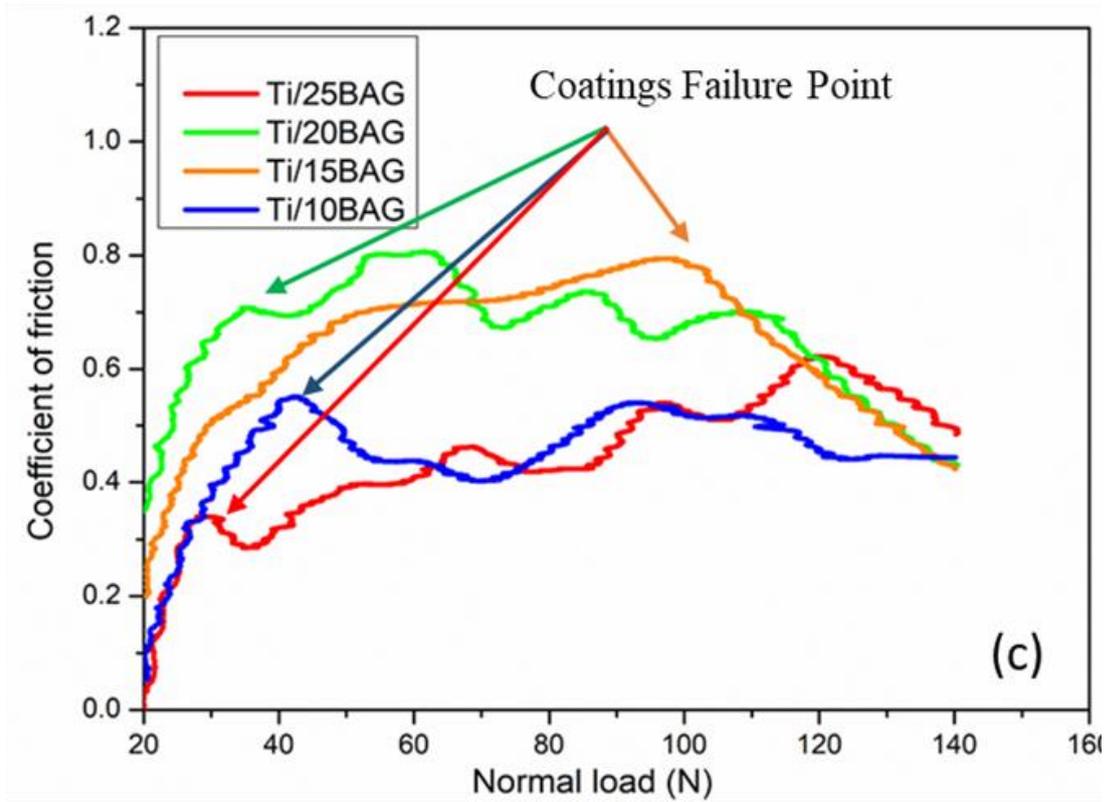
Figure 4.16: Scratch and microhardness results of the cold spray as-received
Ti/BAG composite coatings on SS316L steel

Post-scratch analysis has been performed in order to understand the scratch failure of the developed coatings. Fig. 4.17 and 4.18 display the optical micrographs of the scratch at the start point, failure point, and at the end point for constant and progressively applied normal load. From the micrographs, it is observed that Ti/15BAG composite coating scratch width is relatively smaller, which further signifies the resistance to the failure of the Ti/15BAG composite coating is superior among the analysed coatings. At the point of failure, some cracks were observed, and reported failure cracks are more severe in progressive applied normal load (Fig. 4.18). Moreover, the severity is maximum in Ti/25BAG composite coatings.
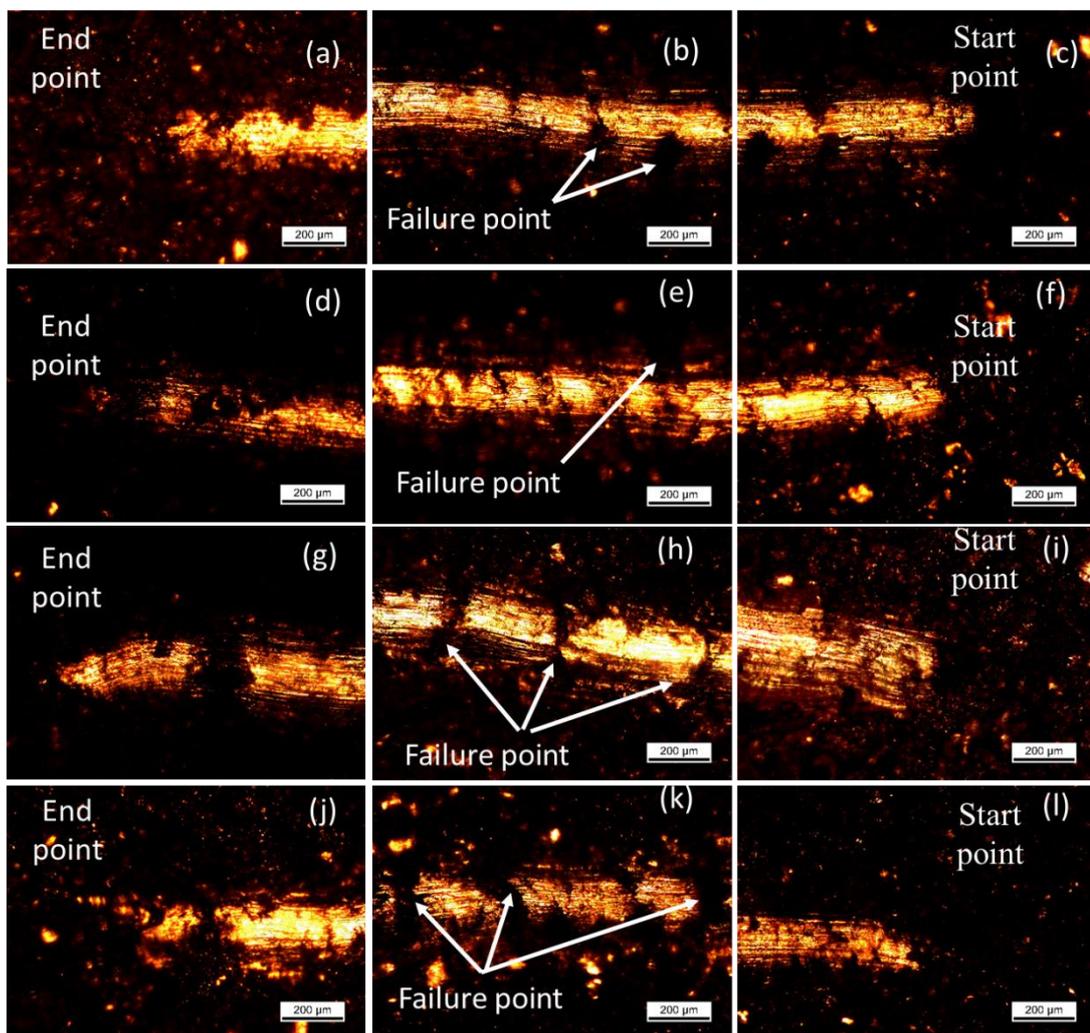
Figure 4.17: Optical micrographs of scratch at constant load (100 N) of the as-sprayed cold spray Ti/BAG composite coatings on SS316L (a, b, c) Ti/10BAG (d, e, f) Ti/15BAG (g, h, i) Ti/20BAG (j, k, l) Ti/25BAG
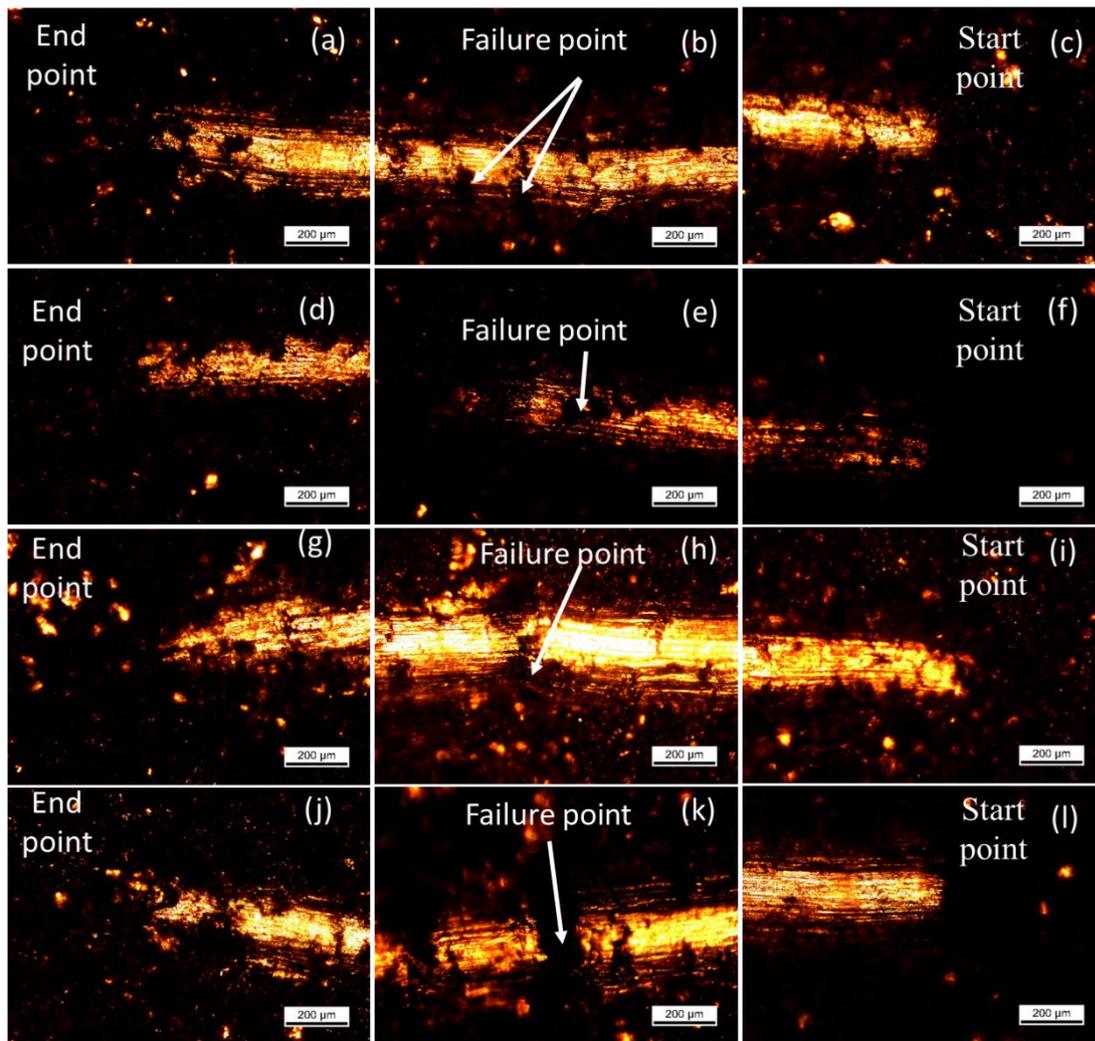
Figure 4.18: Optical micrographs of scratch at progressive load (20 N to 140 N) of the as-sprayed cold spray Ti/BAG composite coatings on SS316L (a, b, c) Ti/10BAG (d, e, f) Ti/15BAG (g, h, i) Ti/20BAG (j, k, l) Ti/25BAG

Fig. 4.19 displays the depth of the scratch for the progressive load conditions at the end of the scratch. The results indicate that the indentor reached maximum depth up to 100 microns in Ti/25BAG composite coating, which is less than the thickness of the coatings (Fig. 4.10). Similarly, indentor penetrated Ti/15BAG composite coating up to around 62 microns. These results signify that the Ti/15BAG composite coating's resistance to scratch is superior among the developed coatings. It can be because the bonding between the plastically deformed Ti/15BAG powder particles is prominent among all other investigated coatings. Also, it indicates that the coatings are well adhered to the substrate, and no adhesive failure is observed between the substrate and coatings.

However, cohesive failure between the Ti-Ti and BAG-BAG particles and adhesive failure between Ti- BAG particles could be the reason for coating failures.
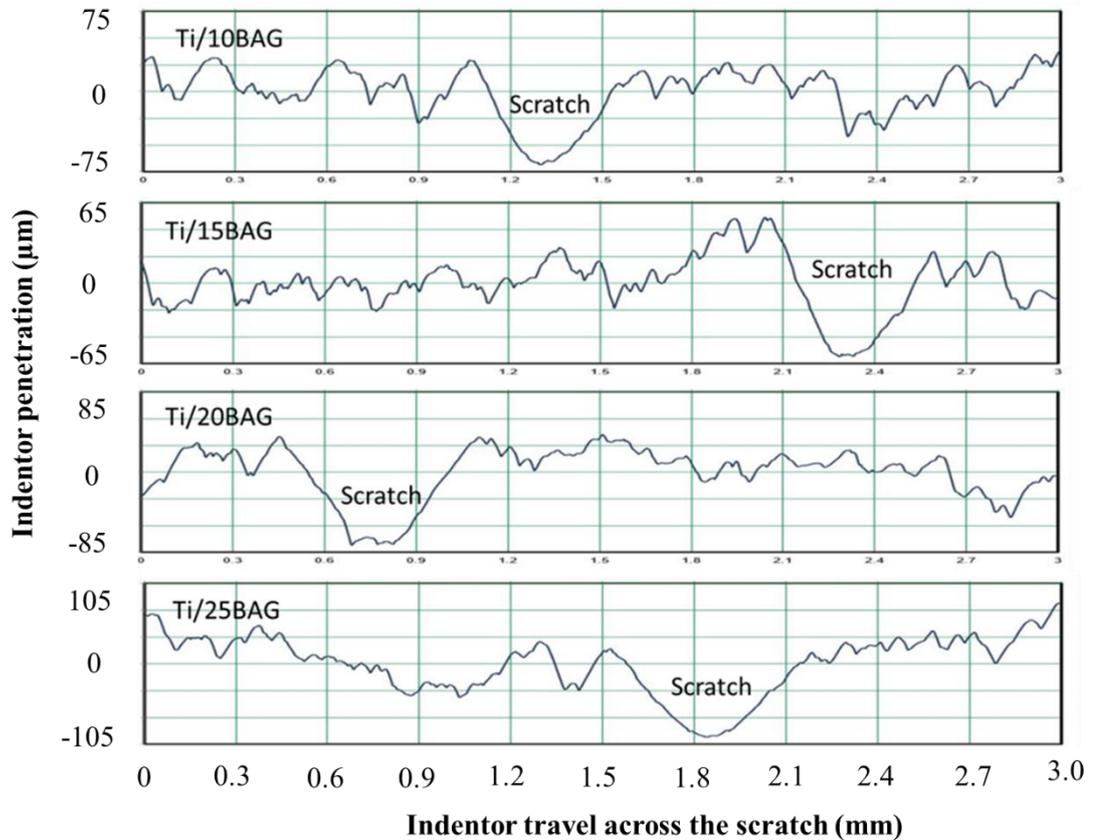
Figure 4.19: Scratch profile of the cold-sprayed Ti/BAG composite coatings after scratch test performed at progressive load (20 N to 140 N)

Contact angle measurement is one of the most commonly used techniques to study hydrophilic or hydrophobic surfaces for biomedical applications. Distilled water has been used as the liquid to measure the contact angle of the cold-sprayed Ti/BAG composite coatings. The drop of the liquid was dropped on the substrate and cold-sprayed Ti/BAG composite coatings, and the focused images were captured. Fig. 4.20 shows the static contact angles for the cold-sprayed Ti/BAG composite coatings and substrate. The decreasing trend of the contact angle with the percentage of BAG was observed. The contact angle is tuned from 87 to 31° with BAG content. The substrate contact angle is observed 41°. As evident from Fig. 4.20, all composite coatings are hydrophilic in nature which is a favourable condition for the intended application. Moreover, as the BAG content increases, the contact angle of the coatings shifts towards hydrophilicity which indicates the progression of surface energy in the cold-sprayed

85

Ti/BAG coatings. The contact angle is shifted towards the hydrophilicity with the increment in surface roughness of the coating (Fig. 4.15); a similar trend is also reported by Kubiak et al. (Kubiak et al., 2011).
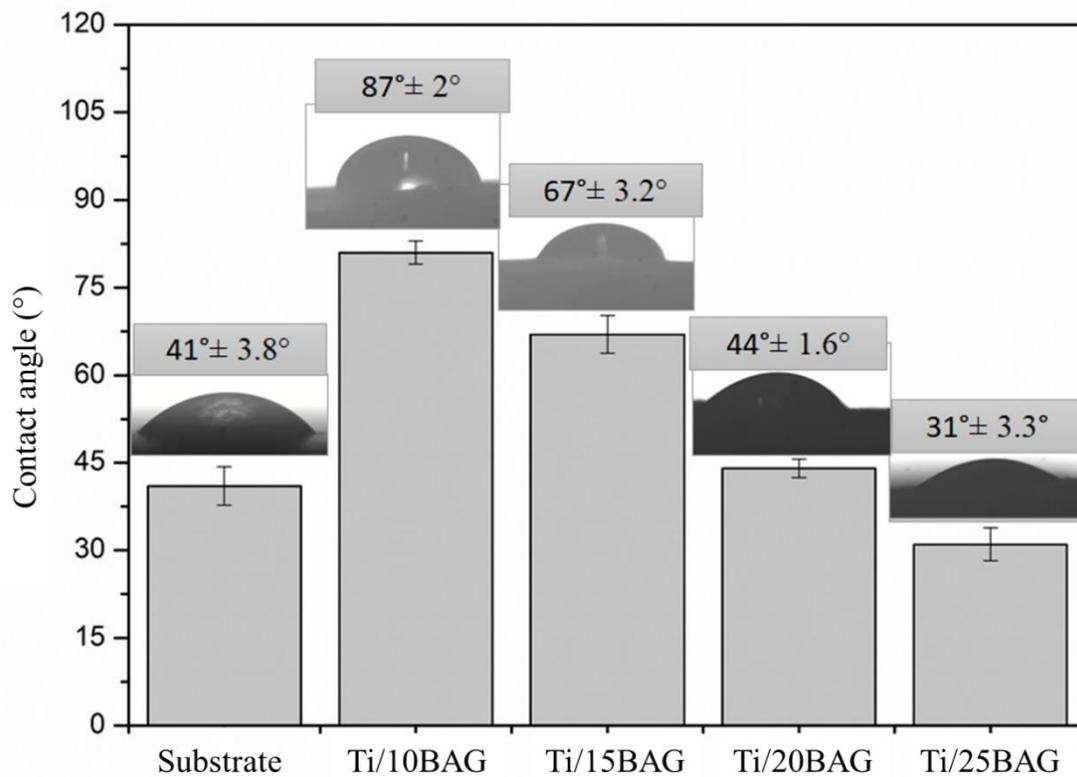
Figure 4.20: Measured contact angle for the substrate and cold-sprayed Ti/BAG composite coatings developed on SS 316L substrate

4.3.3 Biocompatibility Analysis

The percentage of cell viability after 24 hrs of incubation with change in BAG percentage is shown in Fig. 4.21. The percentage of cell viability for all the samples was above the threshold limit, that is, 70%, which indicates that the developed cold-sprayed coatings were biocompatible and had no cytotoxic effects. The percentage of cell viability has increased with the increment in BAG content. It is well established that Ti is biocompatible but not bioactive (Li et al., 2010). However, BAG has been well accepted as a biocompatible, bioactive, and osteoconductive material (Pham et al., 2019; Schumacher et al., 2014). Moreover, the other possible reasons behind the increment in cell viability of Ti/BAG composite coatings can be the increment in surface roughness and hydrophilicity caused by the addition of BAG (Fig. 4.15 & 4.20). In this study, the calculated p-value is found to be 0.01, which is less than the significance level (0.05).

As a result, it is concluded that there is a significant difference in cell viability between the investigated compositions of the coating
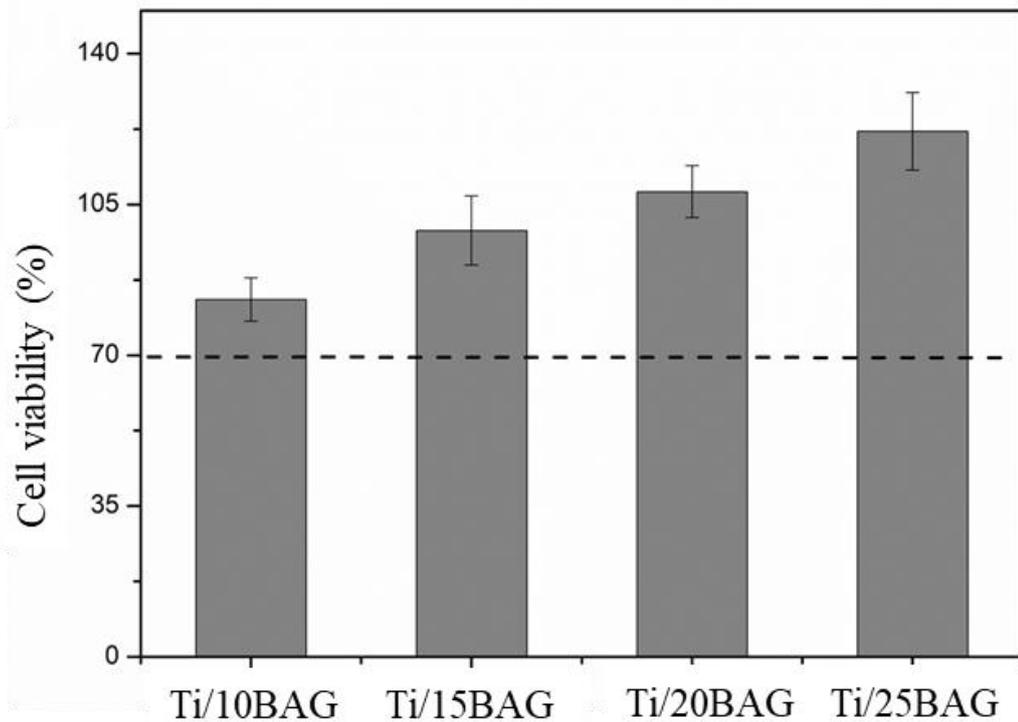
Figure 4.21: Mouse preosteoblast (MC3T3-E1) cell behavior on cold-sprayed Ti/BAG composite coating on SS316L steel

4.4 Laser-Treatment of Titanium/Baghdadite (Ti/BAG) Composite Coatings

The results of experimental trials for Ti/15BAG cold-sprayed composite coating, as shown in Fig. 4.22. The experimental trials of laser processing were done on cold-sprayed Ti/15BAG composite coating because of its better mechanical properties than the other investigated coatings, as discussed above. Marrocco et al. (Marrocco et al., 2011) optimized laser process parameters for the cold-sprayed Ti deposits and reported them in their work. Ti is the major element contributing to the reported composite cold-sprayed coatings development in this work. Hence, the work reported by Marrocco et al. [23] has been considered a reference for the experimental trials. The parameters were chosen in such a way so that the surface temperature of the coating will exceed the recrystallization temperature of Ti and the heat dissipation to the substrate remains minimum.
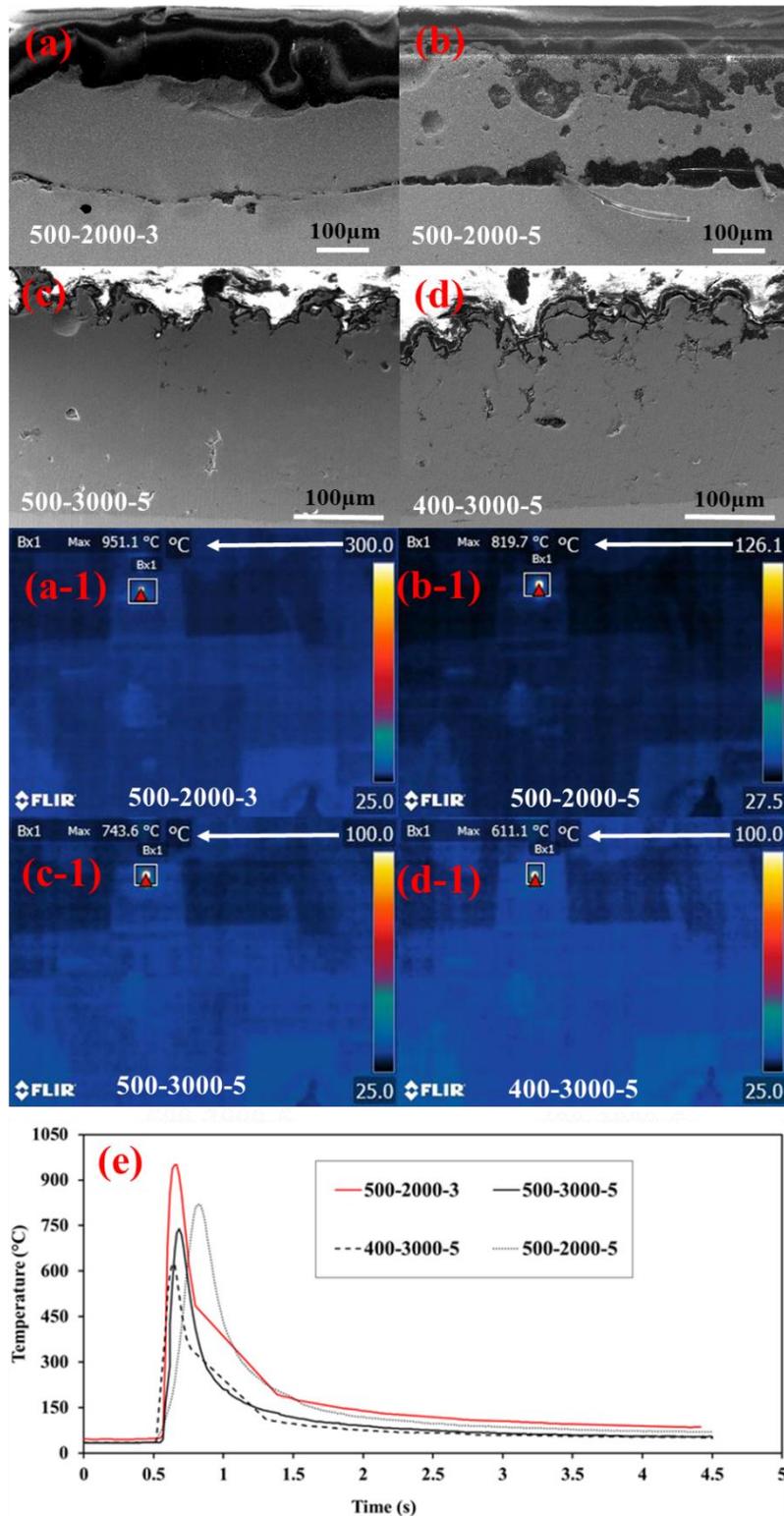
Figure 4.22: Experimentally measured maximum temperature results of laser-treated cold-sprayed Ti/15BAG composite coating along with SEM images at different laser parameters (a, a-1) 500-2000-3 (b, b-1) 500-2000-5 (c, c-1) 500-3000-5 (d, d-1) 400-3000-5 and (e) temperature distribution profile

The process parameters used for experimental trials are reported in Table 4.2. SEM images of the laser-treated coatings are shown in Fig. 4.22. The melting of the coating and substrate was observed at the power-500 W, scanning speed-2000 mm/min, and beam diameter-3 mm. The maximum surface temperature of the coating measured using a thermal imaging camera was observed 951 °C, which caused damage to the surface of the coating and substrate (Fig. 4.22). The change in beam diameter from 3 to 5 mm while keeping the laser power constant, caused the heat distribution in larger area. The measured temperature on the surface of the coating, in this case, was 819 °C, and this led to the removal of the coating from the substrate (Fig. 4.22). It could be because of the thermal expansion mismatch of the coating and substrate. The power of the laser source was reduced from 500 to 400 W, and the scanning speed increased from 2000 to 3000 mm/min by keeping all other parameters the same to reduce the effect of temperature at the interface. The SEM images show that the coating adhered well with the substrate, and inter-particle adhesion/cohesion has also improved. The temperature of the coating surface, in this case, was observed to be 611 °C, which is below the recrystallization temperature of Ti. Therefore, the power of the laser source was changed from 400 to 500 W by keeping all other parameters the same in order to achieve the coating's surface temperature above recrystallization temperature (Fig. 4.22). The obtained surface temperature, in this case, was 743 °C; SEM analysis revealed that there is no adverse effect at the interface because of this localized heating. Hence, all other cold-sprayed composite coatings have been laser-treated using the same laser parameters.

Table 4.2: Details of the laser process parameters used for the laser-treatment of Ti/15BAG coatings

Designation	Power (W)	Scanning speed (mm/min)	Beam diameter (mm)
500-2000-3	500	2000	3
500-2000-5	500	2000	5
500-3000-5	500	3000	5
400-3000-5	400	3000	5

4.4.1 Microstructural Characterization

The surface SEM micrographs of the as-sprayed and laser remelted cold-sprayed coatings, as shown in Fig. 4.23. The surface pores over the surface of the coatings are visible in the as-deposited coatings. Partial remelting of the deformed particles due to laser irradiation is clearly visible from the surface micrographs, which has also helped in reducing the surface pores. Moreover, remelting of the coatings also influenced the surface roughness of the cold-sprayed deposits, as reported in Table 4.3.

Table 4.3: Surface roughness analysis of the cold-sprayed coatings before and after laser-treatment

S. No.	As-sprayed coatings		Laser-treated coatings	
	Ra (µm)	Rz (µm)	Ra (µm)	Rz (µm)
1	12 ± 2.17	54.3 ± 4.67	9 ± 1.08	29.1 ± 5.19
2	13 ± 1.24	72.8 ± 6.15	10 ± 1.24	34.6 ± 4.65
3	17 ± 1.36	86.7 ± 4.23	12 ± 3.28	44.5 ± 3.45
4	21 ± 3.21	103.2 ± 8.11	14 ± 3.96	56.7 ± 5.83
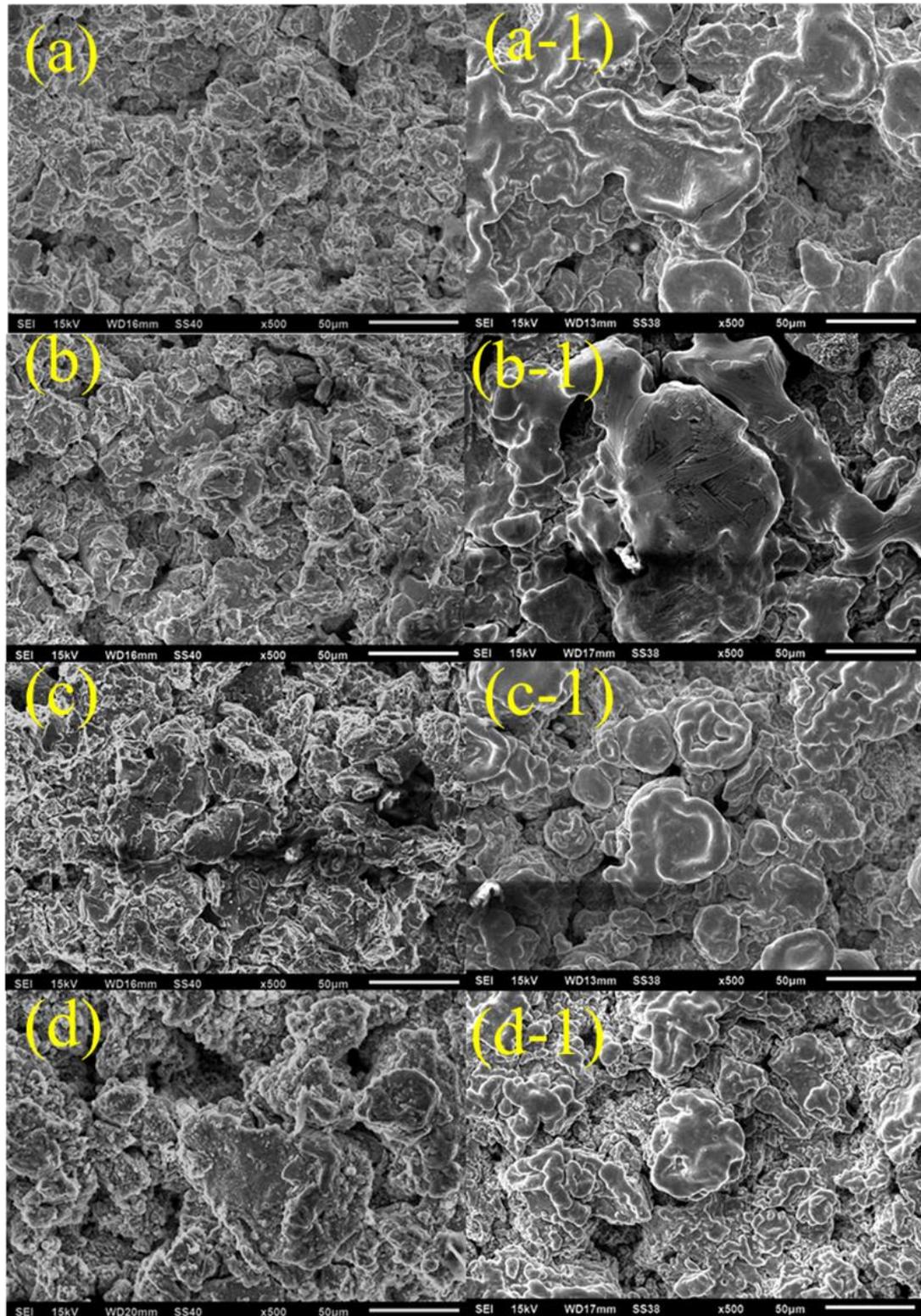
Figure 4.23: Surface SEM/EDS images of the cold spray deposits on biomedical
SS316L steel (a) Ti/10BAG (b) Ti/15BAG (c) Ti/20BAG (d) Ti/25BAG, and laser-
treated coatings (a-1) Ti/10BAG-L (b-1) Ti/15BAG-L (c-1) Ti/20BAG-L (d-1)
Ti/25BAG-L

Cross-sectional high magnification SEM images of Ti/BAG cold-sprayed deposits after laser post-processing are shown in Fig. 4.24. In all the coatings, it can be seen that inter-splat gaps or voids are reduced, and the splats' bonding has also improved. The reason for this is the laser-remelting of Ti particles. The adhesion between the coatings and substrate is also improved except in the case of Ti/25BAG coating, as shown in Fig. 4.24. A thick crack at the interface of Ti/25BAG-L is observed because of the thermal expansion mismatch between the coating and substrate. The reason ascribed to this is the high heat transfer from the coating to the substrate as Ti/25BAG-L coating thickness is relatively smaller.

Furthermore, to understand the effect of laser-remelting, grain analysis of Ti/15BAG-L has been done at three different locations, as shown in Fig. 4.24 (b1, b2, b3). SEM images of etched top layers revealed the formation of equiaxed refined and coarse grains, as shown in Fig. 4.22(b1). As the maximum surface temperature has reached to 743 °C (Fig. 4.22 (c-1)), it leads to the recrystallization of Ti splats. Cold-sprayed coatings are well known for their high dislocation density because of the severe plastic deformation of sprayed particles. The energy stored within cold-sprayed Ti grains or the high-density dislocations within cold-sprayed Ti grains and rapid cooling during laser-remelting is believed as the motivating forces for recrystallization (Li et al., 2021). Ti is well known for its HCP structure (α-Ti) below 882 °C. Therefore, these recrystallized α-Ti grains formed the bimodel structure, having refined as well as coarser grains. Finer grains help to achieve strength but at the expense of ductility. On the other hand, coarser grains help to retain the ductility of the deposited coating (Shen et al., 2017). Fig. 4.24(b2) shows two types of grain, i.e., equiaxed at the top and columnar at the bottom. Higher laser heating caused the formation of equiaxed grains at the top, and insufficient laser heat caused the formation of columnar grains. Columnar grains are relatively weaker and brittle than the equiaxed grains because of the higher dislocation density in that region. Fig. 4.24(b) shows the transition of columnar grains to base metal splats.
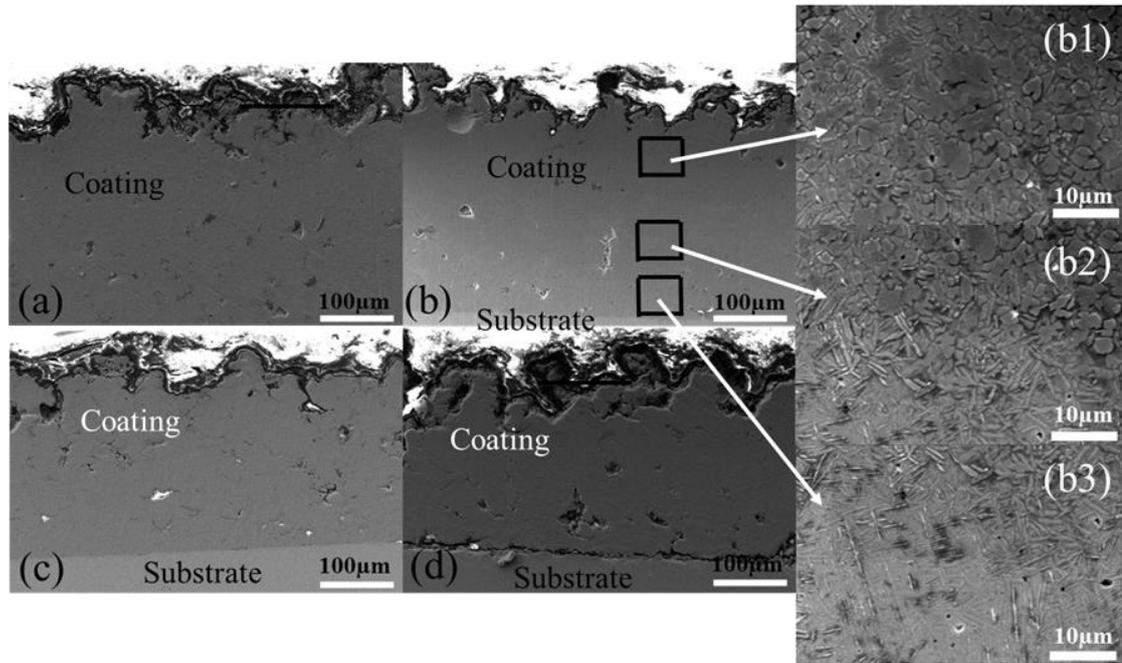
Figure 4.24: High magnification cross-sectional SEM images of laser-remelted cold-sprayed deposits (a) Ti/10BAG-L (b) Ti/15BAG-L (c) Ti/20BAG-L (d) Ti/25BAG-L, and (b1, b2,b3) etched images of Ti/15BAG-L deposit at different locations

4.4.2 Mechanical Characterization

The porosity of the coatings has been calculated by analyzing the high magnification SEM cross-sectional micrographs at different locations using ImageJ software. It is observed from the analysis that the BAG content has influenced the porosity, as reported in Fig. 4.15. The porosity of the coatings has increased with the increment in BAG content. This is attributed to the interaction of the BAG particle with the substrate/and Ti particle. It is well known that ceramic (BAG in this case) particle does not make any bond with the adjacent particle/substrate in cold spraying and leaves voids/gaps at the inter-splat boundaries (Z. Zhang et al., 2019). After laser treatment, the porosity of the coatings has reduced significantly, and for all the cases, it went below 2% except for Ti/25BAG-L, as shown in Table 4.4. The porosity in laser-treated coatings has been reduced due to the improvement in inter-particle adhesion/cohesion, which is attributed to the high temperature remelting of the particles.

The BAG content has significantly influenced the microhardness of as-sprayed coatings as discussed above. The microhardness value has increased up to 15% of BAG content

and then decreased. Up to 15% of BAG content, the interaction of ceramic-ceramic (BAG-BAG) or ceramic-metallic (BAG-Ti) particles might have left a hammering effect on the already deposited Ti splats, leading them to deform more severely (Qiu et al., 2018). This severe deformation causes the formation of high dislocation density in Ti splats, which further may help in improving the microhardness value of the coatings. However, the interaction between ceramic-ceramic particles increases beyond 15% of BAG content, reducing the incoming particles' impact velocity. It leads to a lack of bonding between the deposited particles and reduces the microhardness value (Seo et al., 2012). The maximum value of microhardness is observed in Ti/15BAG (176 ± 4 $HV_{0.5}$) and minimum in Ti/25BAG (120 ± 6), as discussed above. After laser-remelting, the microhardness for all the coatings has been found to increase four times, especially at the top layer, as shown in Fig. 4.25 (a). The maximum microhardness value is 714 ± 21 $HV_{0.5}$ for Ti/15BAG-L observed. The microhardness value decreases with the coatings' depth. The finer equiaxed grains at the top helped in achieving higher hardness, and then columnar grains at the bottom of remelted coatings led to a decrease in the microhardness value. The density of the laser-remelted coatings is higher than the as-sprayed coatings. It is because laser-remelting helped in the reduction of gaps or voids between the splats, as shown in Fig. 24.

Table 4.4: Details of the coating's composition, designation, and porosity before and after laser treatment.

S. No.	Composition (wt %)		As-sprayed coatings		Laser-treated coatings	
	Ti	BAG	Designation	Porosity	Designation	Porosity
1	90	10	Ti/10BAG	3 ± 0.003	Ti/10BAG-L	1.19 ± 0.04
2	85	15	Ti/15BAG	4 ± 0.138	Ti/15BAG-L	1.11 ± 0.68
3	80	20	Ti/20BAG	11 ± 0.095	Ti/20BAG-L	1.26 ± 1.33
4	75	25	Ti/25BAG	14 ± 0.993	Ti/25BAG-L	3 ± 1.920
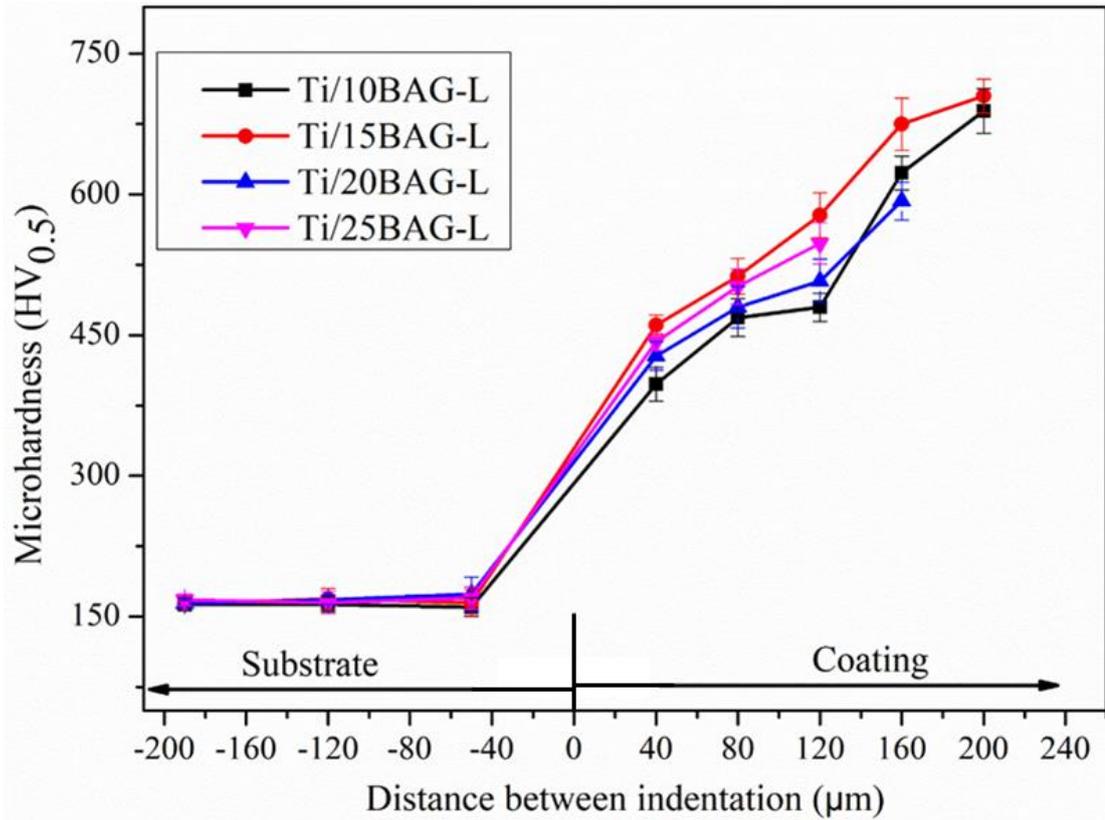
Figure 4.25: Micro-hardness analysis of the laser-remelted cold spray deposits on SS316L substrate

4.5 Summary of the Chapter

Based on the scratch test results and cross-sectional SEM micrographs of single pass cold-sprayed Ti/20TiO2 coatings, it can be concluded that among the as-received, ground-polished, and mirror-polished substrates, mirror-polished SS316L surfaces display the strongest adhesion for cold-sprayed Ti-based coatings. The high-pressure cold spray process was used to deposit three different compositions of Ti/TiO2 (Ti/20TiO2, Ti/40TiO2, and Ti/60TiO2) onto MP SS316L steel. All of the coatings were found well intact with the respective substrates. Cold-sprayed Ti/20TiO2 composite coating exhibited a higher microhardness in comparison with the substrate and cold-sprayed pure titanium coating (Wong et al., 2010).

Furthermore, the deposition of four different compositions of Ti/BAG coatings (Ti/10BAG, Ti/15BAG, Ti/20BAG, and Ti/25BAG) onto MP SS316L steel substrates using cold spray has been demonstrated. The study found that all the Ti/BAG coatings adhered well to their respective substrates. XRD and EDS analysis confirmed the presence of the BAG phase in the coatings, which is considered a desirable characteristic

95

for high-quality coatings. However, as the BAG content in the feedstock increased, the porosity and surface roughness of the coatings also increased. This could be attributed to the lack of metallurgical bond formation due to increased interaction between ceramic-metallic particles. The study observed that the average microhardness of the coatings increased up to 15% BAG content and then decreased. The Ti/15BAG composite coating exhibited the highest average microhardness (176 ± 4 HV0.5) among the investigated coatings. Beyond 15% BAG content, the interaction of BAG particles dominated the process, resulting in decreased bond strength and subsequently, microhardness of the coatings. The study also found that all the Ti/BAG coatings were biocompatible.

The Ti/15BAG coating was chosen for experimental trials of laser treatment because it showed superior microhardness. Several attempts were made to reach the laser process parameters, which elevated the surface temperature of the coating beyond the recrystallization temperature of Ti while ensuring that the substrate experienced no detrimental effects. All the other cold-sprayed Ti/BAG coatings were laser-treated using these parameters. Upon analyzing the microstructure of the coatings, it was observed that laser treatment resulted in equiaxed grains at the top layers and columnar grains in the middle layers. Laser treatment also led to a significant decrease in porosity and surface roughness, which is a desirable attribute for improving bonding and average microhardness of the Ti/BAG composite coatings.

ELECTROCHEMICAL CORROSION STUDIES

The electrochemical corrosion behavior of the investigated cold spray-coated and uncoated SS316L steel in simulated body fluid enviornment has been described in this chapter. Post-laser treatment of cold spray Ti/BAG coatings was also performed to assess its effect on the corrosion behavior of the coatings. The comparison of as-sprayed and laser-treated cold-sprayed Ti/BAG coatings in terms of corrosion has also been discussed. Post-corrosion analysis of cold spray Ti/BAG coatings has been performed to characterize the corrosion scales. The corroded samples were analyzed using scanning electron microscopy/energy dispersive spectroscopy (SEM/EDS) and X-ray diffractometer (XRD).

5.1 Corrosion Behavior of Titanium/Titanium Oxide (Ti/TiO$_2$) Coated and Uncoated SS316L Steel

The open circuit potential (OCP) and potentiodynamic polarization scans are some of the most widely used electrochemical approaches to evaluate the corrosion performance of biomedical coatings (Anawati et al., 2013; Roland et al., 2013; Singh et al., 2012; Zhou and Mohanty, 2012). Therefore, OCP and potentiodynamic tests were performed to study the corrosion behavior of cold spray Ti/TiO$_2$ coated SS 316L steels in Hank's solution.

5.1.1 Open Circuit Potential

The OCP of uncoated and cold spray Ti/TiO$_2$ coated samples was measured in Hank's solution. Fig. 5.1 depicts OCP measurements of the mirror-polished (MP) steel substrate and developed coatings in Hank's solution. It indicates that the OCP of the steel substrate is minimum, and for Ti/20TiO$_2$, it is maximum. Also, the OCP of the composite coatings has shifted away from the noble direction with the increased TiO$_2$ content. The OCP measured for Ti/20TiO$_2$ was -194 mV, and it was observed at -220 mV for Ti/40TiO$_2$ and -265 mV for Ti/60TiO$_2$ against Ag/AgCl. Ti/20TiO$_2$ has shown the best OCP among the investigated cold-sprayed Ti/TiO$_2$ steels. Higher coating

thickness, lower porosity, and maximum retention of TiO_2 are believed the reason for the better OCP of Ti/20TiO_2.
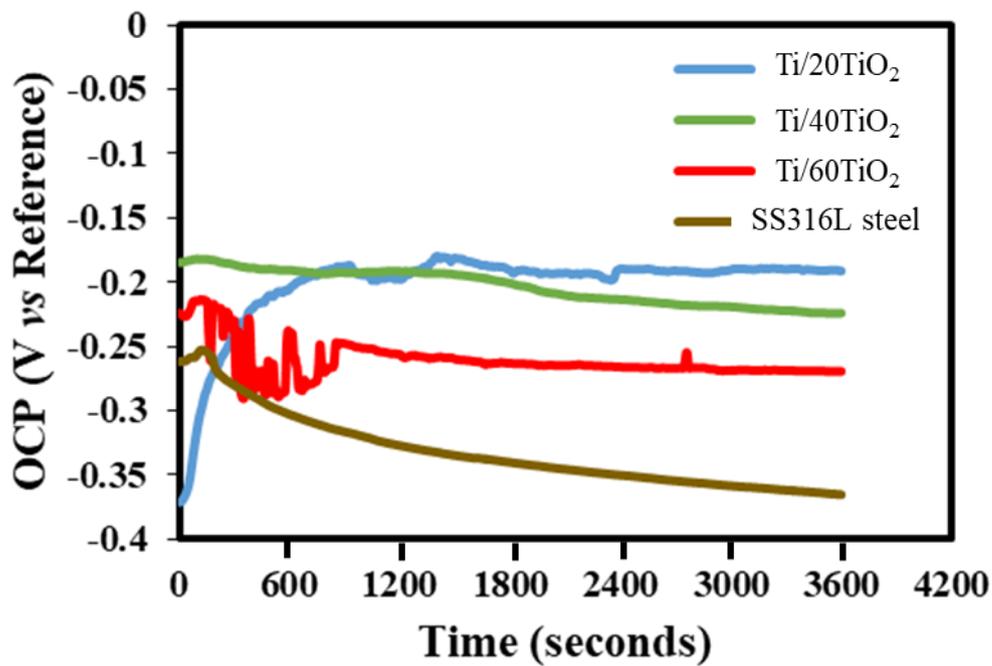
Figure 5.1: Open circuit potential of mirror-polished substrate (SS316L steel) and cold-sprayed Ti/TiO_2 composite coatings in Hank's solution

5.1.2 Potentiodynamic Polarization Scans

The potentiodynamic polarization scans of the cold-sprayed deposits and the mirror-polished (MP) steel substrate are shown in Fig. 5.2(a). The thermodynamic stability (E_{corr} value) of cold-sprayed Ti/20TiO_2 composite coating was found to be the best in Hank's solution among the investigated specimens. The corrosion potential (E_{corr}) and corrosion current density (I_{corr}) (extracted from the Tafel extrapolation using Echem software) for all the investigated coatings and substrates are shown in Fig. 5.2(b). The graph shows that as the TiO_2 content in the coating decreases, the E_{corr} value shifts towards the noble direction and the I_{corr} value decreases, which means that Ti/20TiO_2 composite coating offers the best protection to the substrate against corrosion among all investigated coatings. The E_{corr} and I_{corr} values for the substrate were observed as -370 mV and 37.2 $\mu A/cm^2$, respectively. For cold spray Ti/20TiO_2 coatings, E_{corr} and I_{corr} were -212 mV and 0.138 $\mu A/cm^2$, respectively.
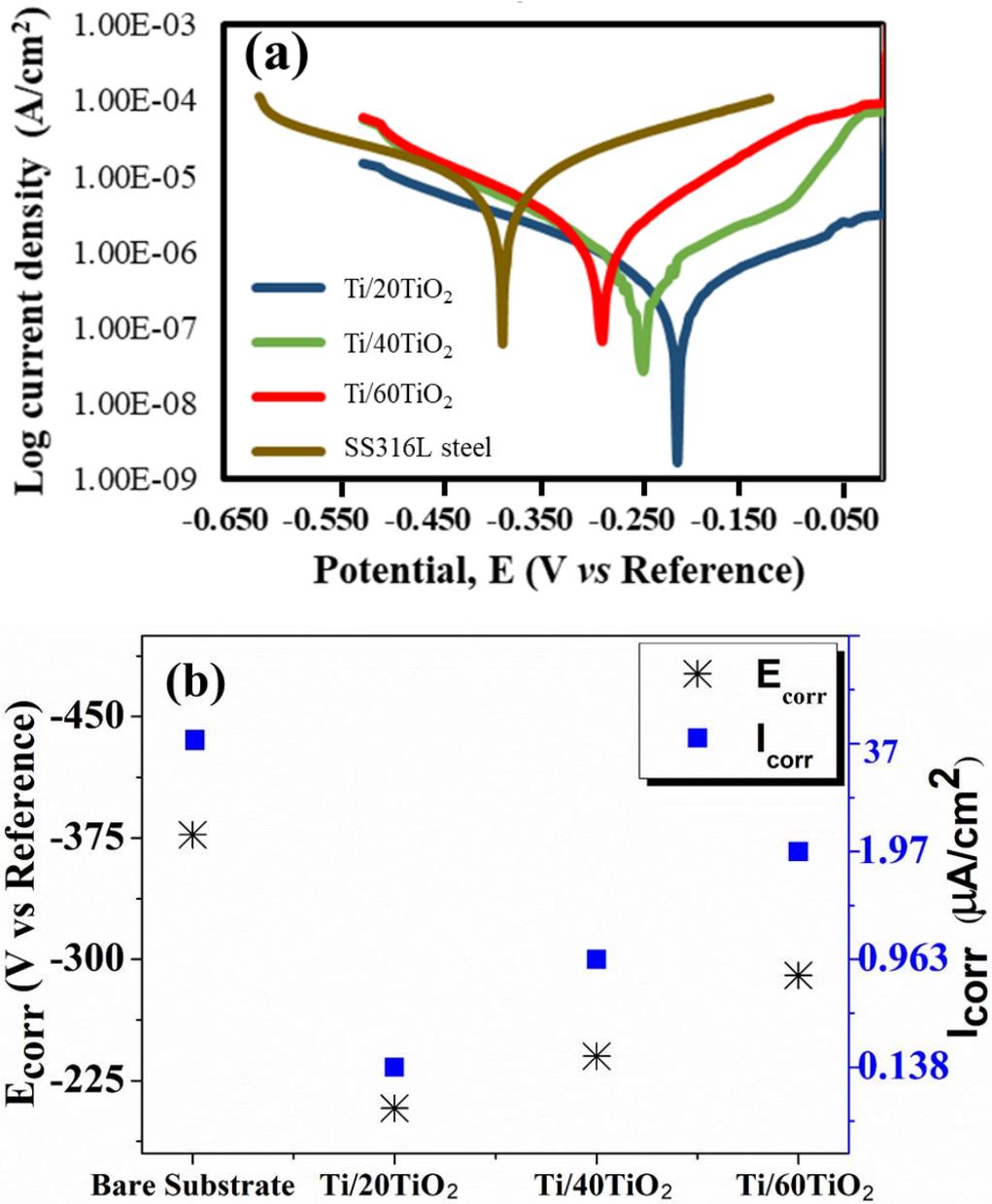
Figure 5.2: Corrosion behavior of mirror-polished substrate (SS316L steel) and cold-sprayed Ti/TiO₂ composite coatings in Hank's solution (a) potentiodynamic scans (b) Tafel extrapolated corrosion current densities and corrosion potentials

In the present research work, cold spray coatings successfully protected the substrate from corrosion in Hank's solution. However, the corrosion performance of the coatings dropped with the rise in ceramic content in feedstock. Also, as Ti is exposed to Hank's solution, it forms a passive layer of TiO_2 and protects the coating from corrosion (Neoh et al., 2012). Zhou and Mohanty (Zhou and Mohanty, 2012) reported the E_{corr} (-445 mV) and I_{corr} (1.37 µA/cm²) values for cold-sprayed pure titanium coatings under Hank's

99

solution in their work. The developed cold-sprayed Ti/20TiO$_2$ composite coatings have outperformed the above mentioned cold-sprayed pure titanium coatings in the same electrolyte. The coating thickness of Ti/20TiO$_2$ cold-sprayed composite coating is significantly higher, and the bonding is also good, as shown in Chapter 4 (Table 4.1 and Fig. 4.6). The higher thickness and lower apparent surface porosity of Ti/20TiO$_2$ coating blocked the penetration of electrolyte into the coating towards the substrate, therefore the corrosion is limited to the coating only. Another reason for this can be the retention of TiO$_2$ particles into the coating. The Ti/20TiO$_2$ cold-sprayed composite coating has retained a relatively higher amount of TiO$_2$ content among all the investigated coatings, as discussed in Chapter 4. TiO$_2$ particles restrict the release of Ti ions from the coating and provide a relatively lesser area (compared to other coatings) to corrode (Padhy et al., 2011).

In the case of Ti/40TiO$_2$ composite coating, as the bonding between the deposited splats is relatively poor, the electrolyte might have penetrated through these pores to cover more area for corrosion. The presence of TiO$_2$ particles retained in the coating may have restricted the release of Ti ions to some extent. Ti/60TiO$_2$ coating has a very small thickness (35 ± 12 µm) and some pores along the splat boundaries. Moreover, the retention of TiO$_2$ is also minimum in this case. Therefore, the Ti surface area exposed to the electrolyte is maximum in this case. Therefore, poor corrosion performance has been observed in this case. This can also be attributed to the fact that as the TiO$_2$ content increases, coating thickness and bonding strength decrease (as discussed in Chapter 4). Therefore, the lack of bonding caused the electrolyte to penetrate in the coating, leading to a relatively more corrosion. The pores in all the deposited coatings were clearly visible, resulting from inter-splat particle interaction (Chapter 4). It might also have contributed to the poor performance of Ti/40TiO$_2$ and Ti/60TiO$_2$ coatings. Moreover, Ti/40TiO$_2$ and Ti/60TiO$_2$ composite coatings have retained low TiO$_2$ content, which is insufficient to restrict the release of Ti ions from the coatings; hence, more corrosion was expected.

5.2 Corrosion Behavior of Titanium/Baghdadite (Ti/BAG) Coated and Uncoated SS316L Steel

5.2.1 Potentiodynamic Polarization Scans

5.2.1.1 As-sprayed Coatings

The electrochemical reactions between the coating and the electrolyte lead to the degradation of the coatings. Potentiodynamic polarization curves of bare SS316L substrate and cold sprayed Ti/BAG composite coatings in Ringer's solution are shown in Fig. 5.3(a, b) and Fig. 5.4. E_{corr} and I_{corr} values of the steel have been found to be the poorest. The results indicate a notable improvement in the thermodynamic stability (in terms of E_{corr}) of the steel after the deposition of the cold spray coatings in Ringer's solution. E_{corr} value of the developed coatings has shown a tendency to shift to the noble direction with increase in BAG content and immersion time. The results (Table 5.1) depict that the corrosion current density has also decreased with the increase in BAG content in the feedstock under Ringer's solution. In other words, the coatings have lowered the release of ions and electrons. The coatings, in general have been successful to develop corrosion resistance in the steel as the corrosion rates of composite coatings has got reduced compared to that of bare SS316L, as shown in Table 5.1.

After 2 hours (hr) of immersion in Ringer's solution, all the deposited coatings successfully protected the substrate from corrosion, as shown in Fig. 5.3(a) and Table 5.1. E_{corr} and I_{corr} values of the substrate were -377 mV and 3.24 $\mu A/cm^2$. Moreover, cold-sprayed Ti/10BAG composite coating has shown an E_{corr} value of -381 mV and an I_{corr} value of 2.29 $\mu A/cm^2$ in Ringer's solution. Furthermore, the corrosion rate of Ti/10BAG coating was 0.806 $\mu m/year$, which is way lesser than the substrate (126.4 $\mu m/year$). However, the corrosion rate was maximum for Ti/10BAG among all investigated coatings. The cold-sprayed Ti/25BAG composite coating performed the

101

best against corrosion attack among all the investigated cases. E_{corr} and I_{corr} values of the Ti/25BAG were -208 mV and 0.62 µA/cm^2 under Ringer's solution.

Moreover, cold-sprayed Ti/25BAG composite coating has retained its best ranking among all the cases even after 16 hr of immersion in Ringer's solution (Fig. 5.3(b)). Once again, all of the coatings performed better than the substrate in terms of corrosion resistance. Ti/25BAG coating showed an E_{corr} value of -157 mV, an I_{corr} value of 0.54 µA/cm^2, and a corrosion rate of 0.19 µm/year after 16 hr of immersion (Table 5.1). Furthermore, E_{corr}, I_{corr}, and corrosion rates have improved with the increase in immersion time, as shown in Fig. 5.5 (a and b).

After the exposure of 40 hr of corrosion, E_{corr}, I_{corr}, and corrosion rate of Ti/25BAG coating were observed to be better than those after 2 hr and 16 hr of immersion in Ringer's solution. Following the same trend, the potentiodynamic scans show that Ti/25BAG cold-sprayed composite coating outperformed all investigated coated and uncoated samples. Additionally, all the coatings were observed to perform better than the substrate against corrosion in Ringer's solution.
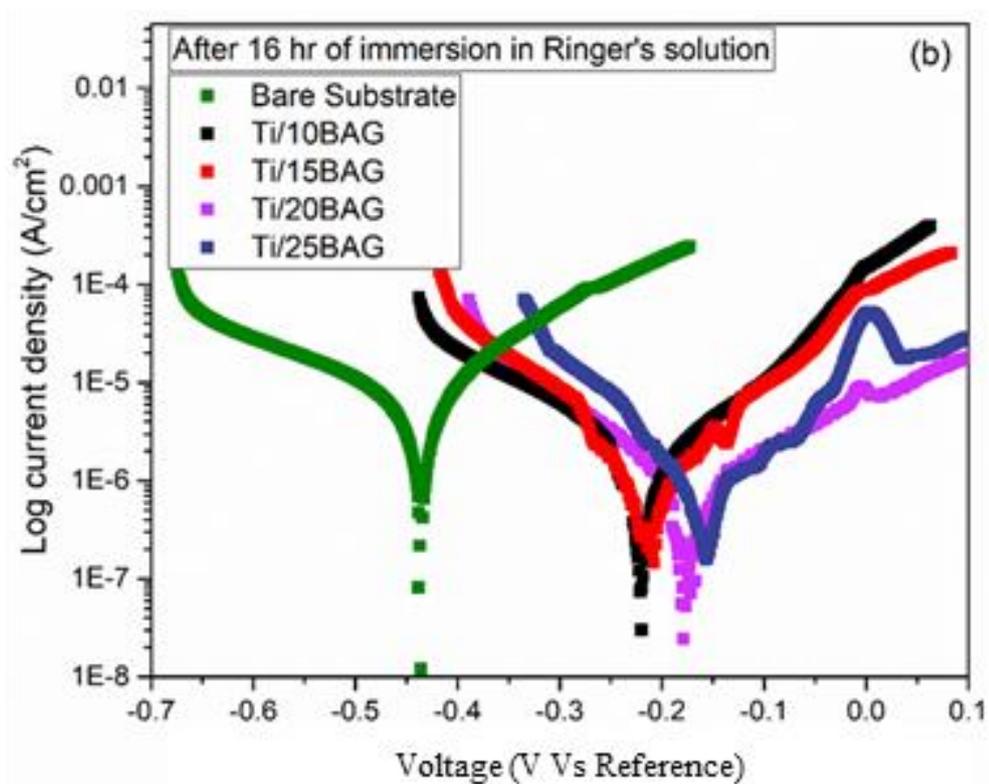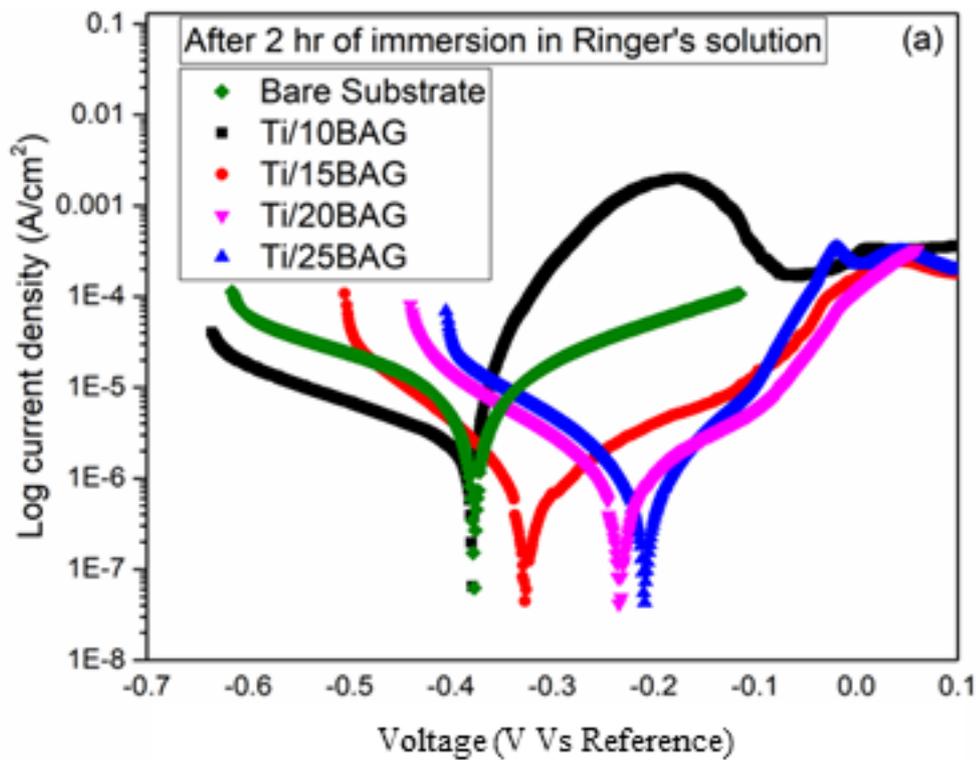
Figure 5.3: Potentiodynamic polarization behavior of bare and cold spray Ti/BAG coated SS316L in Ringer's solution after (a) 2 hr of immersion (b) 16 hr of immersion
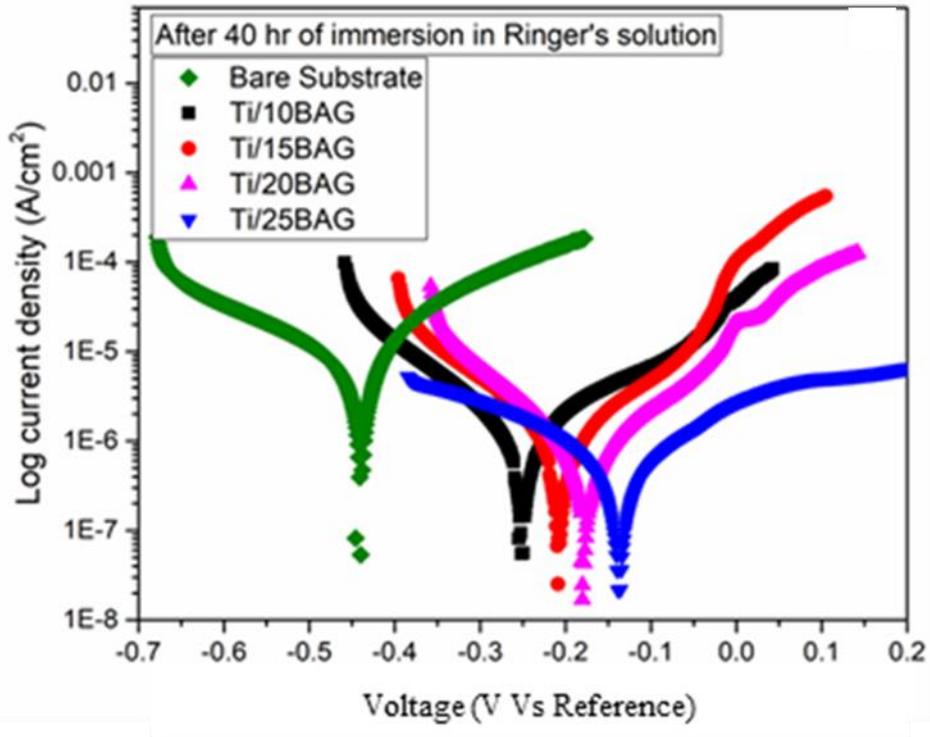
Figure 5.4: Potentiodynamic polarization behavior of bare and cold spray Ti/BAG coated SS316L in Ringer's solution after 40 hr of immersion
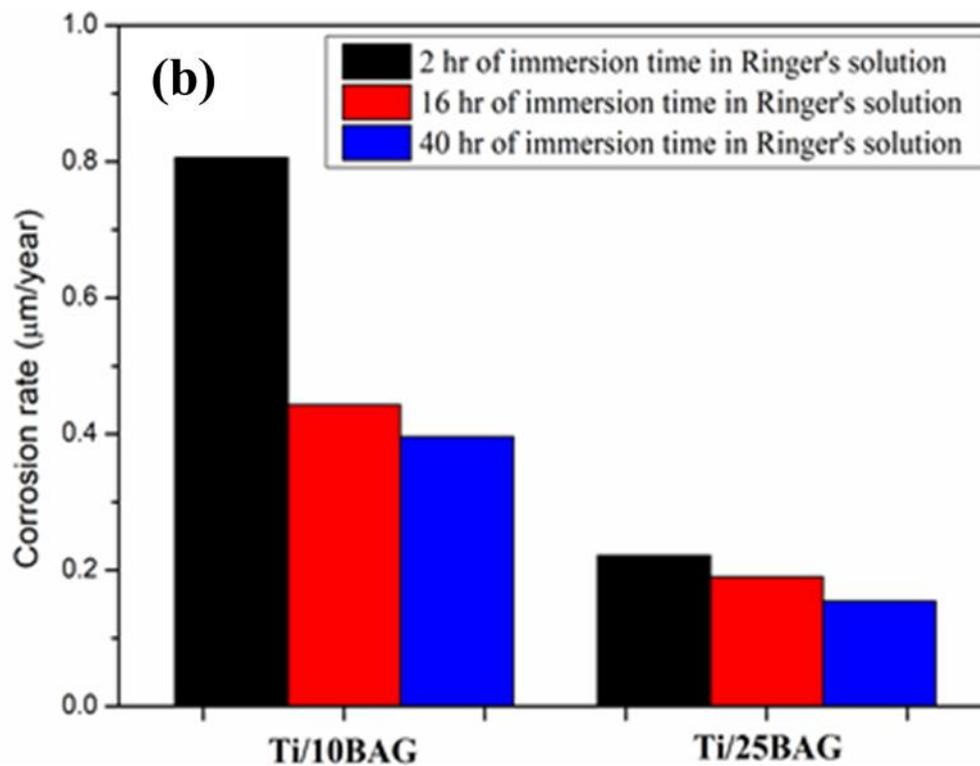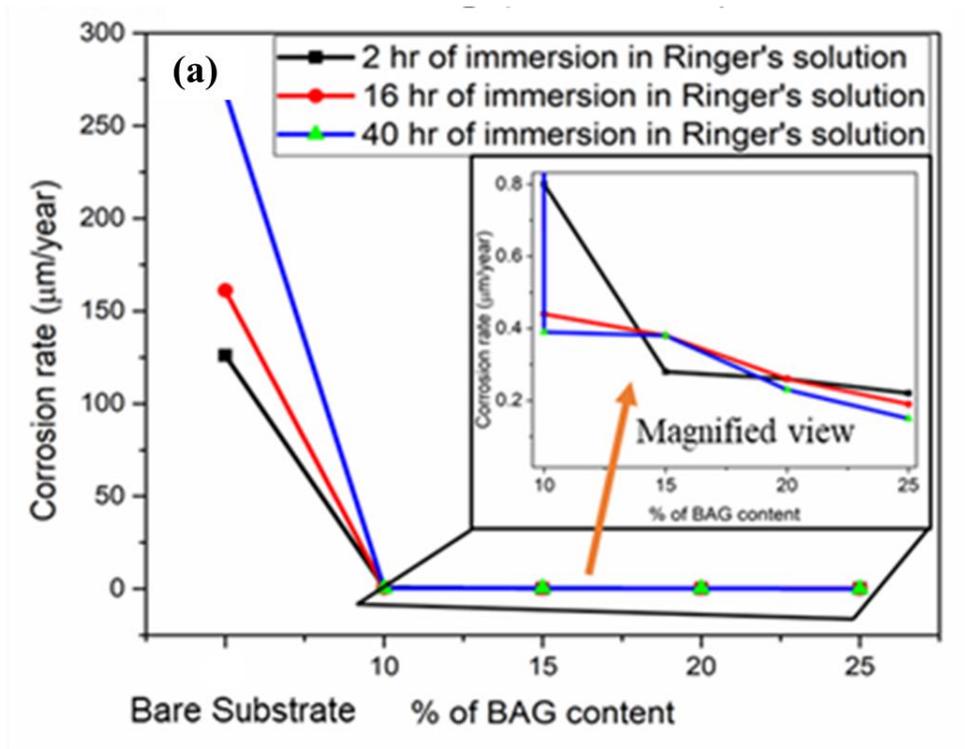
Figure 5.5: Corrosion rate calculated using Tafel extrapolation from potentiodynamic polarization data of bare and cold spray Ti/BAG coated SS316L in Ringer's solution

Table 5.1: Electrochemical corrosion parameters extracted from the Tafel extrapolation using Echem software for coated and uncoated Ti/BAG samples in Ringer's solution

S. No.	Sample ID	E_{corr} (mV)	I_{corr} (μA/cm^2)	β_α(mV)	β_c (mV)	Corrosion rate (μm/year)
(a)	After 2 hr of immersion in Ringer's solution					
1	Substrate	-377.5	3.24	9.02 ± 0.4	-8.03 ± 0.12	126.4
2	Ti/10BAG Coating	-381.38	2.29	36.35 ± 0.88	-4.05 ± 0.02	0.806
3	Ti/15BAG Coating	-326.58	0.80	4.38 ± 0.09	-9.57 ± 0.05	0.284
4	Ti/20BAG Coating	-233.34	0.74	6.80 ± 0.07	-8.89 ± 0.06	0.263
5	Ti/25BAG Coating	-208.52	0.62	9.66 ± 0.15	-10.97 ± 0.11	0.221
(b)	After 16 hr of immersion in Ringer's solution					
1	Substrate	-435.23	3.83	8.31 ± 0.05	-6.04 ± 0.03	161.5
2	Ti/10BAG Coating	-218.13	1.258	8.05 ± 0.06	-9.42 ± 0.16	0.443
3	Ti/15BAG Coating	-209.73	1.099	8.42 ± 0.24	-9.75 ± 0.30	0.387
4	Ti/20BAG Coating	-176.50	0.7634	7.29 ± 0.05	-10.36 ± 0.08	0.269
5	Ti/25BAG Coating	-157.8	0.540	8.62 ± 0.78	-9.69 ± 0.56	0.19
(c)	After 40 hr of immersion in Ringer's solution					
1	Substrate	-441.09	6.39	10.12 ± 0.02	-9.03 ± 45	268.2
2	Ti/10BAG Coating	-248.03	1.12	8.32 ± 0.06	-8.49 ± 0.08	0.396
3	Ti/15BAG Coating	-208.29	1.10	11.23 ± 0.02	-9.11 ± 0.07	0.388
4	Ti/20BAG Coating	-178.30	0.66	9.48 ± 0.03	-9.04 ± 0.03	0.235
5	Ti/25BAG Coating	-136.8	0.43	9.78 ± 0.03	-8.11 ± 0.07	0.154

5.2.1.2 Laser-Treated Coatings

The potentiodynamic scans of laser-treated cold spray Ti/BAG coatings are shown in Fig. 5.6. The potentiodynamic scans of laser-treated coatings reveal that post-laser treatment of cold-sprayed deposits helped significantly in reducing I_{corr} value for each case relative to the as-sprayed coatings, as shown in Fig. 5.7. The comparison of as-sprayed Ti/BAG coatings and laser-treated coatings in Ringer's solution after 2 hr of immersion in terms of E_{corr} and I_{corr} values is shown in Fig. 5.7 (a and b). It was observed that E_{corr} value shifted in the noble direction after laser treatment. I_{corr} value for as-sprayed Ti/10BAG coating was 2.29 µA/cm^2, which changed to 0.11 µA/cm^2 after laser treatment. For Ti/25BAG coating after 2 hr of immersion, I_{corr} value has dropped from 0.62 to 0.081 µA/cm^2 due to laser post-processing. It is observed that laser-treatment reduced I_{corr} value upto 94% and 86% for Ti/10BAG and Ti/25BAG coatings, respectively. Similarly, E_{corr} value for Ti/10BAG composite coating was measured as -381 mV, and after laser treatment, it was measured as -337 mV. E_{corr} value after 2 hr of immersion for Ti/25BAG was -208 mV, and the laser treatment took it to -191 mV.
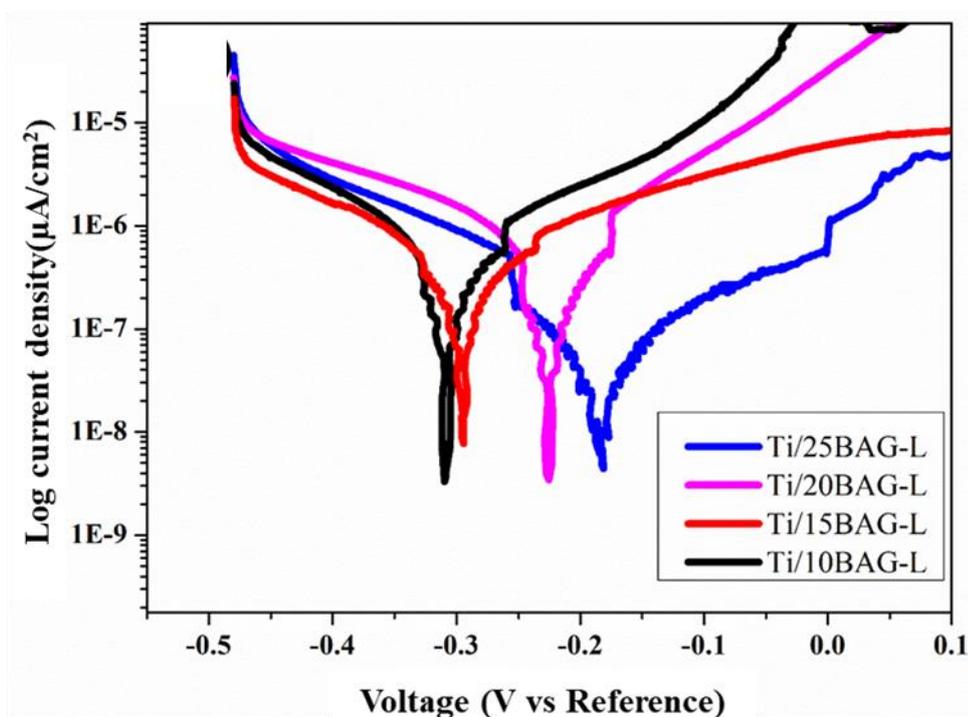
Figure 5.6: Electrochemical corrosion behavior of laser-treated cold spray coatings in Ringer's solution after 2 hr of immersion
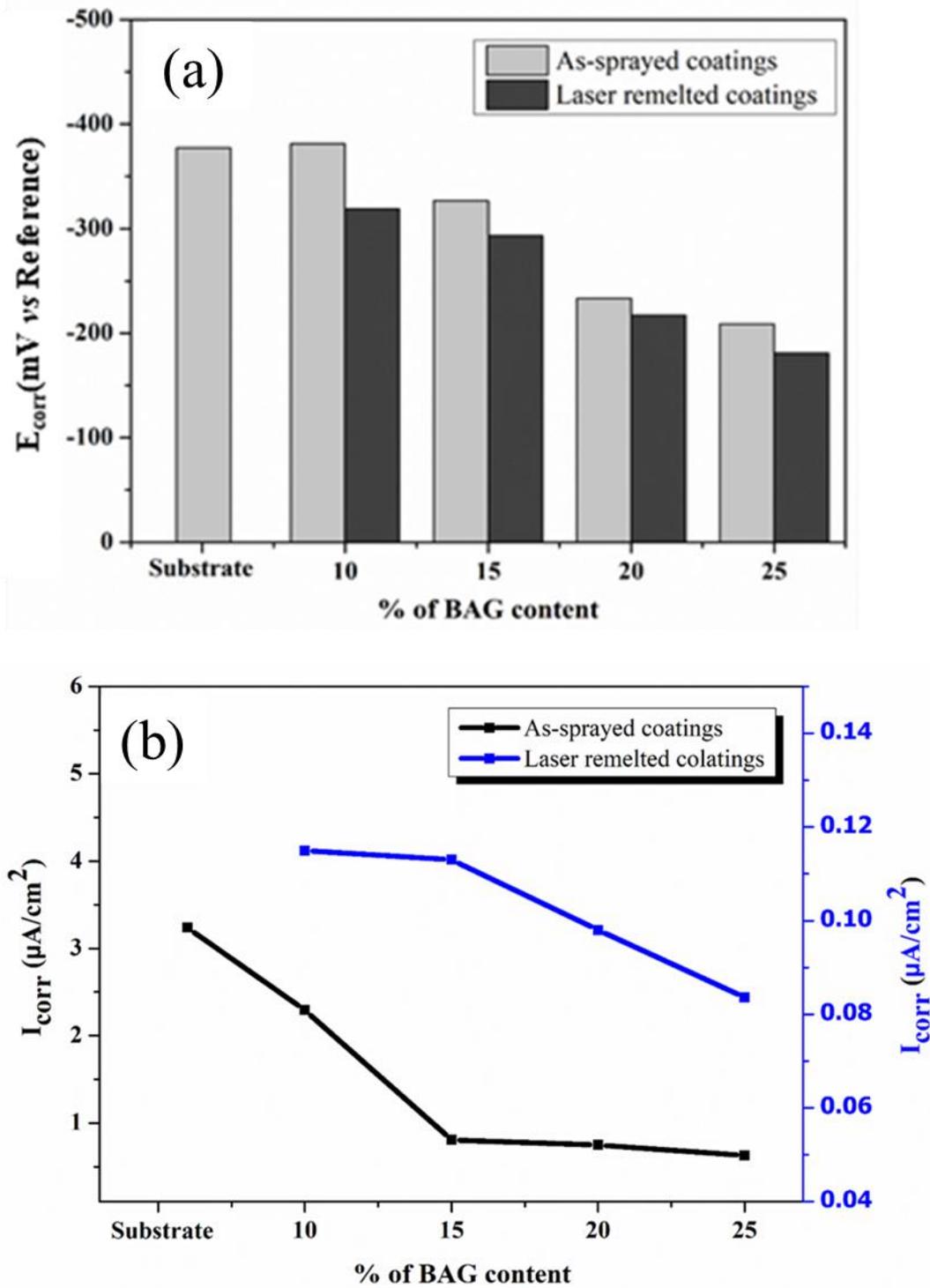
Figure 5.7: Electrochemical corrosion behavior of laser-treated cold spray coatings in Ringer's solution (a) E_{corr} value comparison with as-sprayed coatings (b) I_{corr} value comparison with as-sprayed coatings

5.2.2 Electrochemical Impedance Scans

The electrochemical impedance spectroscopy (EIS) results followed the same trend as the potentiodynamic polarization results for the cold-sprayed coatings in Ringer's solution. An equivalent two-layer model circuit is fitted to calculate the physical parameters of the corrosion behavior, as shown in Fig. 5.8. Rs in the equivalent circuit represents the electrolytic resistance, Rp as the charge transfer resistance of the coating, Cp as the capacitance of developed coatings, Rb as the polarization resistance of substrate, and the double layer capacitance as Cb. Rh and Ch represent the capacitance and resistance of precipitates into the pores.
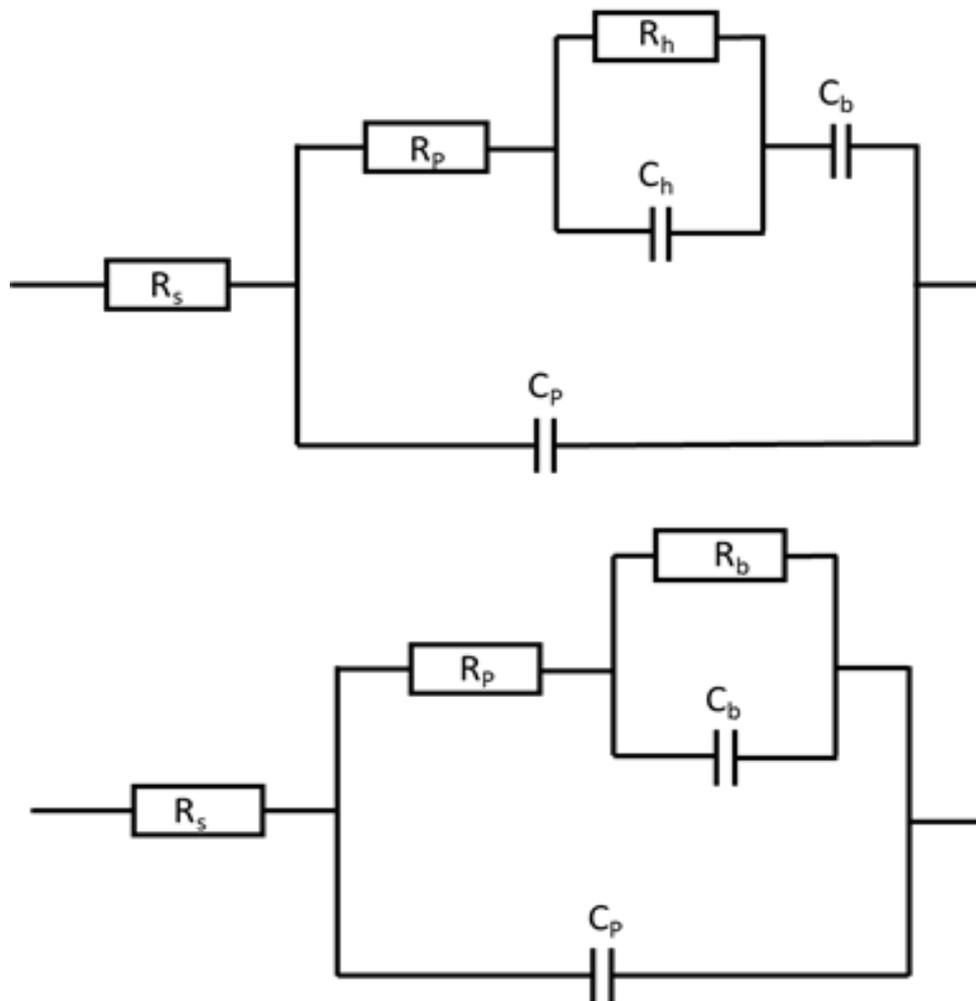
Figure 5.8: Equivalent circuit fitted for electrochemical impedance spectroscopy (EIS) analysis of Ti/BAG composite coatings on SS316L

The Nyquist representation of impedance for Ti/BAG composite coatings is displayed in Fig. 5.9. The data is plotted for the real part of impedance (resistance) versus the imaginary part of impedance (capacitance) in Ringer's solution. The Nyquist plots of Ti/BAG coated steels show two capacitive loops (semicircles) except for 40 hr of immersion time in Ringer's solution. The low frequency loop is associated with second oxide layer, whereas the high frequency loop is related to first oxide layer. The shape of the Nyquist plots for all the coated samples was semicircle (capacitive), but the diameters were different. The semicircle diameter of all the coating samples was observed to increase with the increase in BAG content. The bigger the semicircle diameter, the better the corrosion resistance because it indicates the formation of a thicker protective passive oxide layer. The Ti/25BAG composite coating has shown the biggest semicircle, indicating its superior corrosion performance in Ringer's solution (Fig. 5.9 (a)). The charge transfer resistance (R_p) was also found to be maximum for Ti/25BAG composite coating and minimum for Ti/10BAG composite coating, which was calculated from the fitted data using Echem software. The R_p value for Ti/25BAG was 3.46 kΩ-cm^{2,} and for Ti/10BAG composite coating, it was 0.68 kΩ-cm^2 after 2 hr of immersion in Ringer's solution.

The Nyquist plot shows that the size of the semicircle continued to increase with the increase in BAG content as the immersion time was increased from 2 hr onwards (Fig. 5.9(b) and Fig. 5.10(a)). It can be clearly observed from Fig. 5.10(b) that the size of the semicircle has increased with immersion time. The R_p of Ti/25BAG composite coating after 2 hr of immersion, 16 hr of immersion, and 40 hr of immersion in Ringer's solution was 3.46 kΩ-cm^2, 3.64 kΩ-cm^2, and 4.37 kΩ-cm^2, respectively. Therefore, it can be concluded that with the increase in immersion time, the coatings displayed better corrosion behavior in Ringer's solution.
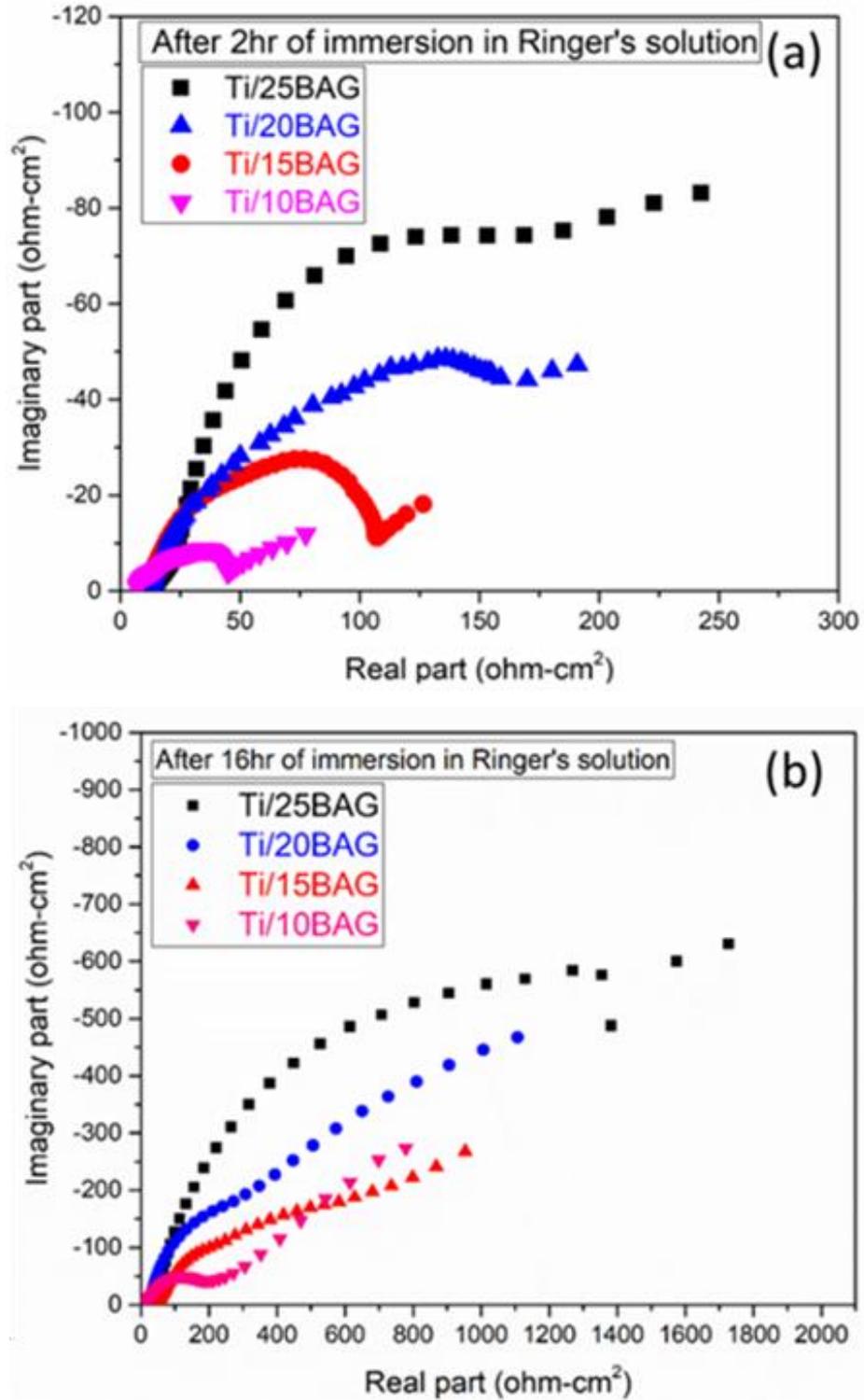
Figure 5.9: Nyquist behavior of cold sprayed Ti/BAG composite coatings on SS316L in Ringer's solution (a) 2 hr of immersion time (b) 16 hr of immersion time
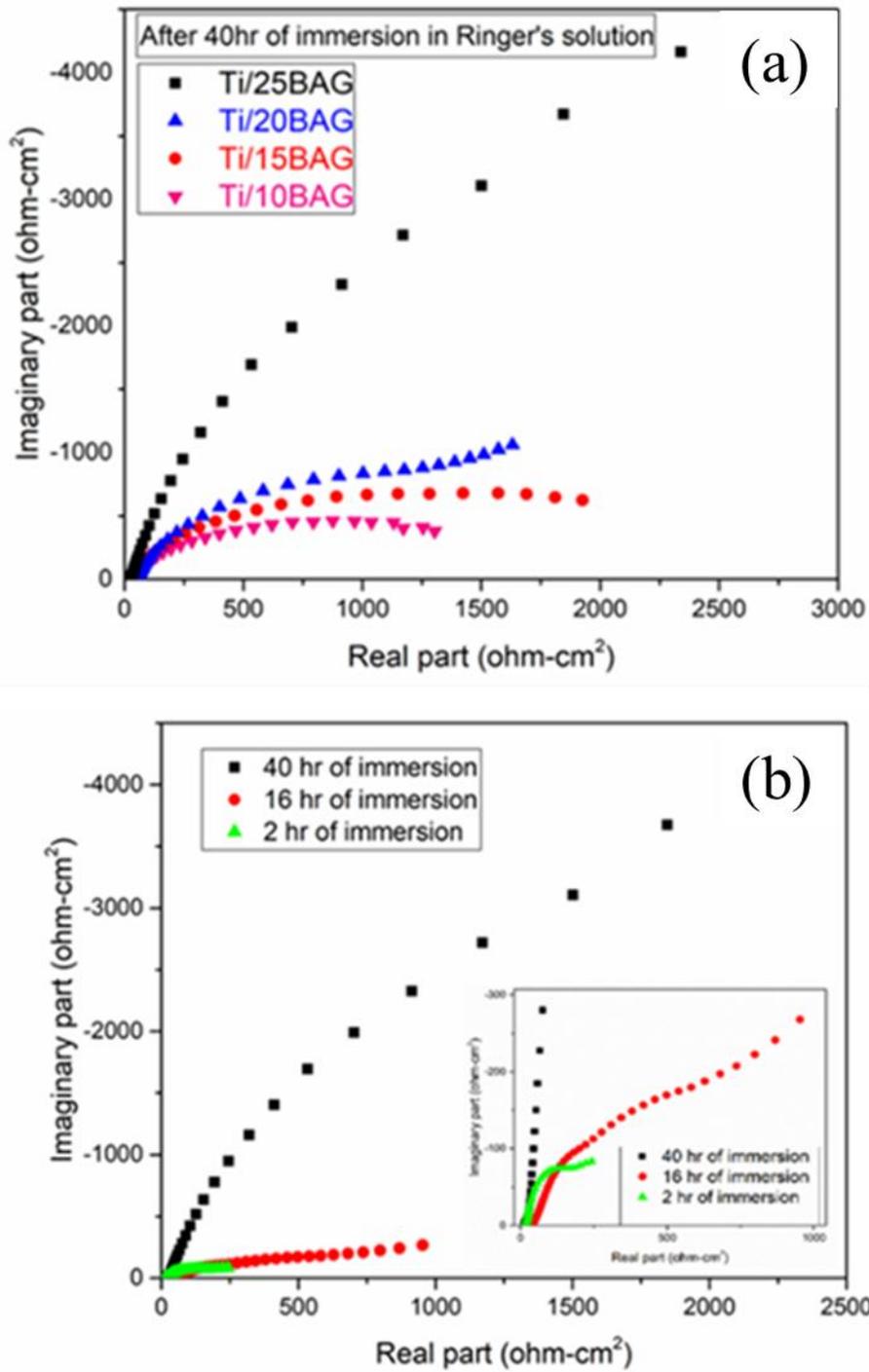
Figure 5.10: Nyquist behavior of cold sprayed Ti/BAG composite coatings on SS316L in Ringer's solution (a) 40 hr of immersion time (b) Ti/25BAG with immersion time

The Bode plots (Fig. 5.11 and Fig 5.12 (a and b)) also depict that all the coatings were capacitive in nature. The effect of BAG and immersion time in Ringer's solution on impedance is shown in Fig. 5.13. In the lower frequency region, the impedance value was consistent with the increase in BAG content and the increment in immersion time, which indicates that the developed Ti/BAG composite coatings exhibit an anti-corrosion behavior. The maximum logarithmic value of impedance at lower frequency region for Ti/10BAG composite coating after 2 hr of immersion in Ringer's solution was 80 kΩ-cm^2, and for Ti/25BAG, it was 502 kΩ-cm^2. After 16 hr and 40 hr of immersion in Ringer's solution, Ti/25BAG composite coating performed even better. The maximum obtained logarithmic impedance value for Ti/25BAG coating in the lower frequency region after 16 hr of immersion and after 40 hr of immersion was measured as 1832 kΩ-cm^2 and 4705 kΩ-cm^2, respectively (Fig. 5.13).
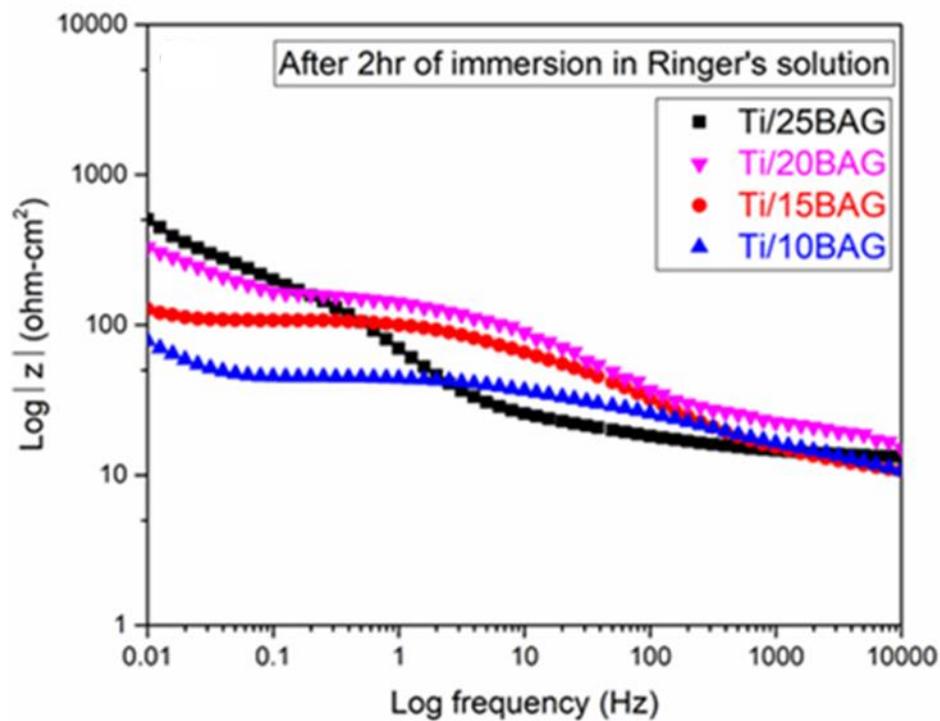
Figure 5.11: Bode plot of the cold sprayed Ti/BAG composite coatings on SS316L after 2 hr of immersion

113
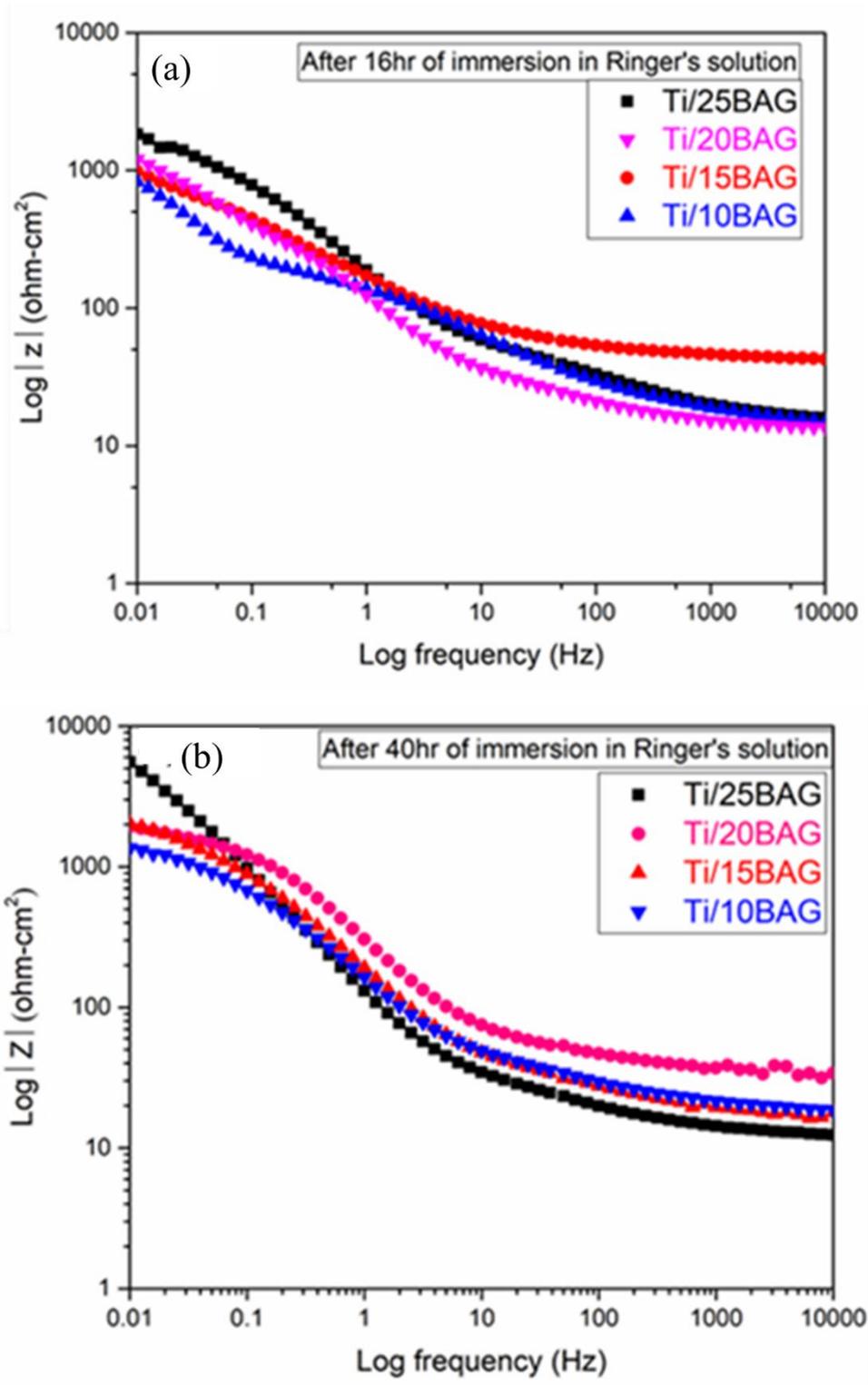
Figure 5.12: Bode plot of the cold sprayed Ti/BAG composite coatings on SS316L

after (a) 16 hr of immersion, (b) 40 hr of immersion
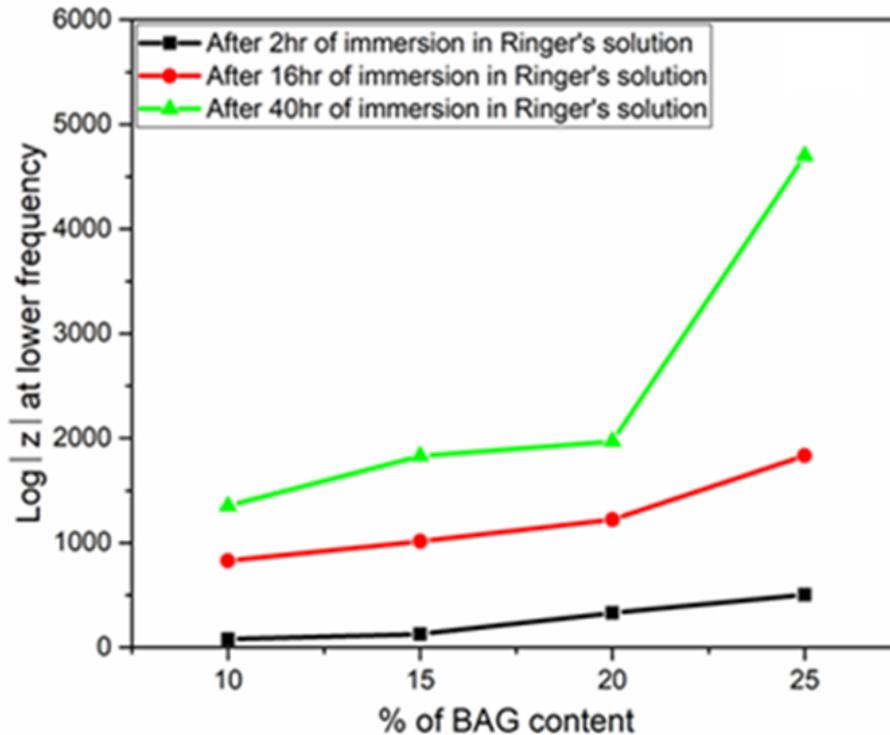
Figure 5.13: Bode plot of the cold sprayed Ti/BAG composite coatings on SS316L impedance at low frequency (Log 0.01, Hz)

5.2.3 Post-Corrosion Analysis

SEM surface micrographs of the mirror-polished SS316L substrate before and after the electrochemical corrosion test in Ringer's solution are shown in Fig. 5.14. A significant corrosion of the substrate is clearly visible. The oxide scale of the substrate has got spalled-off after 40 hr of exposure to Ringer's solution. SEM micrographs of Ti/BAG composite coatings after 2 hr, 16 hr, and 40 hr of immersion time in Ringer's solution are also taken and shown in Fig. 5.15, 5.16, and 5.17. The micrographs show that the coatings suffered comparatively lesser corrosion than the substrate, as no crack-like features are observed over the coating surfaces. EDS elemental compositions of corroded samples are also shown in Fig. 5.15, 5.16, and 5.17. The results reveal that the corroded coatings have more than 65% oxygen in their oxide scale compositions. In contrast, the oxygen content before corrosion was less than 12% for each of the coating surfaces, as shown in Chapter 4. It indicates that the coatings have experienced oxidation reactions to form passive oxides. Furthermore, it was observed that even after 40 hr of exposure in Ringer's solution, all the coatings were well intact with the substrate and no spallation was observed.

Cold-sprayed Ti/25BAG coated steel performed best against corrosion among all the investigated steels. Therefore, elemental mapping of corroded Ti/25BAG composite coating after 2 hr of immersion in Ringer's solution was performed using EDS and is reported in Fig. 5.18. A significant amount of oxygen and titanium content was observed from the EDS maps. Moreover, traces of calcium, silicon, and zirconium were also observed. These observations indicate the formation of a passive oxide layers over the coating surface. The cross-sectional SEM/EDS analysis of Ti/25BAG also supports the formation of oxides over the surface after 2 hr of immersion in Ringer's solution, as shown in Fig. 5.19. Also, it has been observed that the intensity of the formed oxides was significantly higher at the top, and it decreased with the depth into the coating. It indicates that the electrolyte has not penetrated much into the coating, which indicates towards its protective nature. These passivities of corrosion layers were further confirmed by XRD analysis of the exposed coated samples (Fig. 5.20 (a)). The analysis confirms the formation of TiO, TiO_2, CaO, SiO_2, and ZrO_2 passive oxides in the exposed samples. Laser-treated corroded samples were also assessed using XRD, as shown in Fig. 5.20(b). The XRD data of the corroded samples revealed the formation of TiO_2, CaO, SiO_2, and ZrO_2.
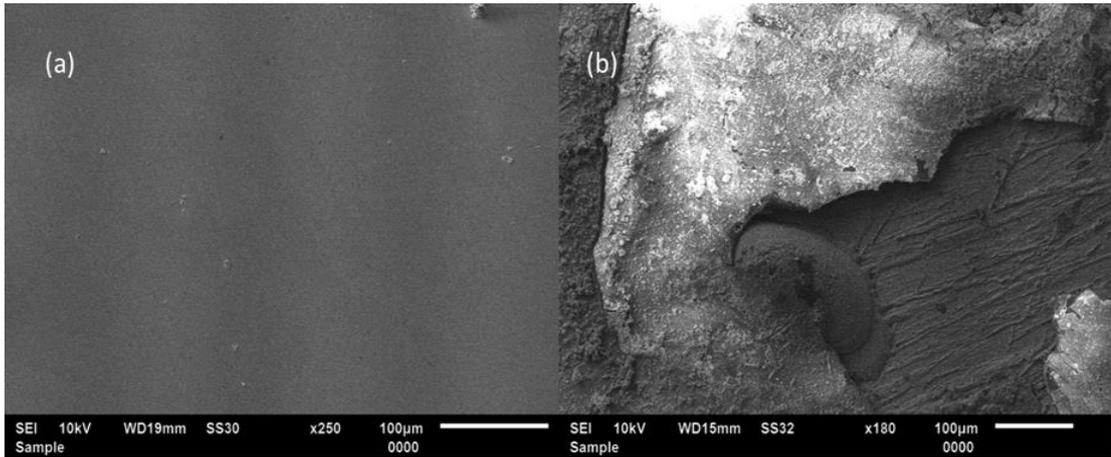
Figure 5.14: Surface SEM micrographs of SS316L (a) before corrosion (b) after corrosion

O: 68%
Ti: 31%
Ca, Si, Na, and Cl in traces

O: 74%
Ti: 25%
Ca, Si, Na, and Cl in traces

O: 70%
Ti: 29%
Ca, Si, Na, and Cl in traces

O: 71 %
Ti: 28%
Ca, Si, Na, and Cl in traces
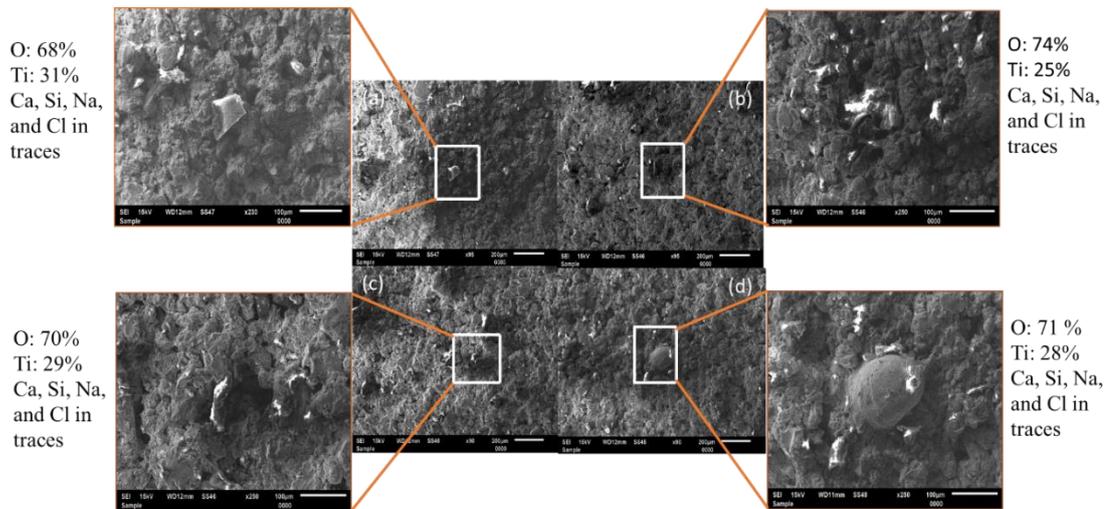
Figure 5.15: Surface SEM micrograph of corroded cold sprayed Ti/BAG composite coatings after immersion in Ringer's solution for 2 hr (a) Ti/10BAG (b) Ti/15BAG (c) Ti/20BAG (d) Ti/25BAG
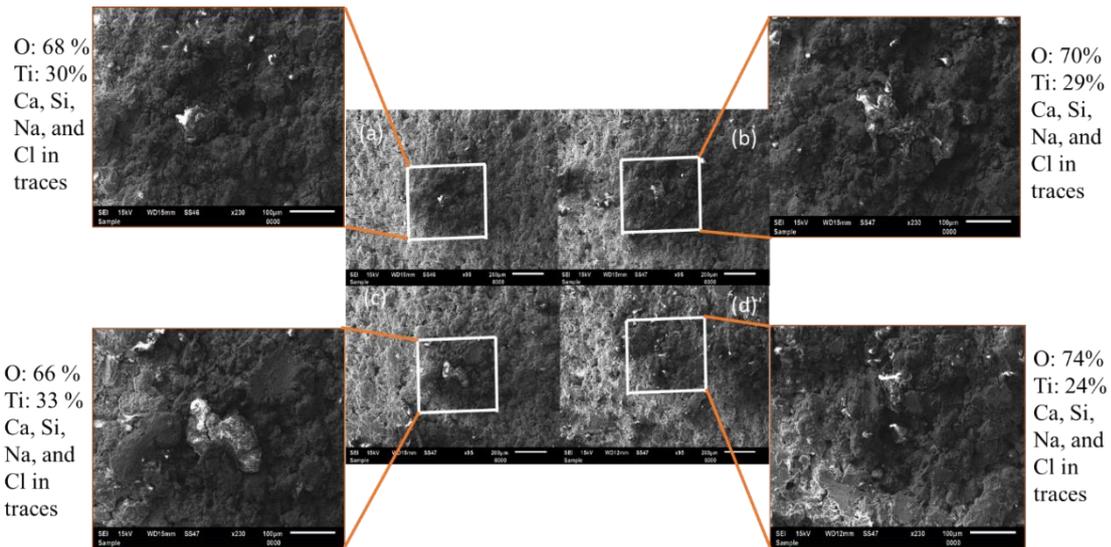
Figure 5.16: Surface SEM micrograph of corroded cold sprayed Ti/BAG composite coatings after immersion in Ringer's solution for 16 hr (a) Ti/10BAG (b) Ti/15BAG (c) Ti/20BAG (d) Ti/25BAG
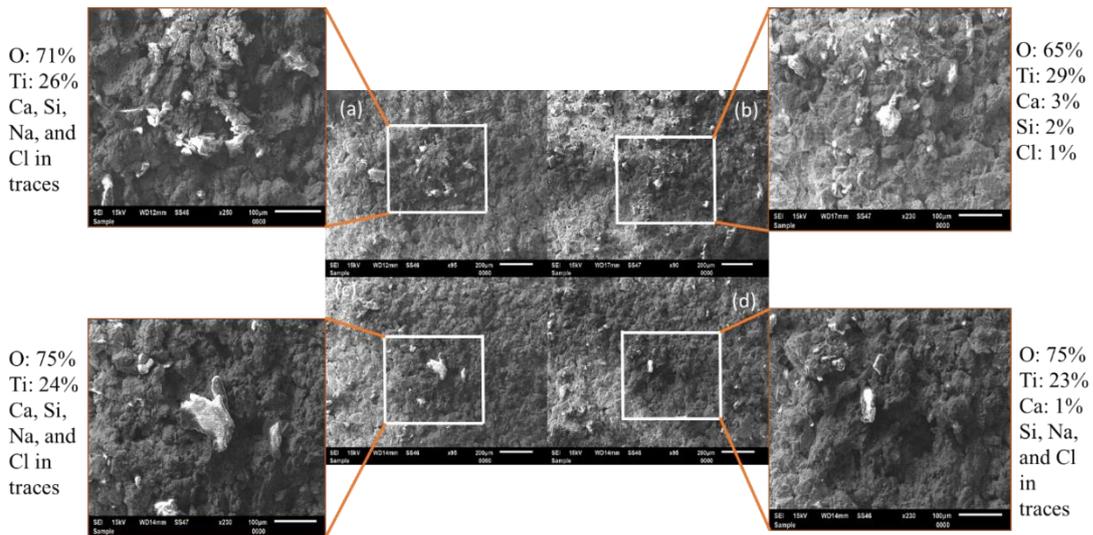
Figure 5.17: Surface SEM micrograph of corroded cold sprayed Ti/BAG composite coatings after immersion in Ringer's solution for 40 hr (a) Ti/10BAG (b) Ti/15BAG (c) Ti/20BAG (d) Ti/25BAG
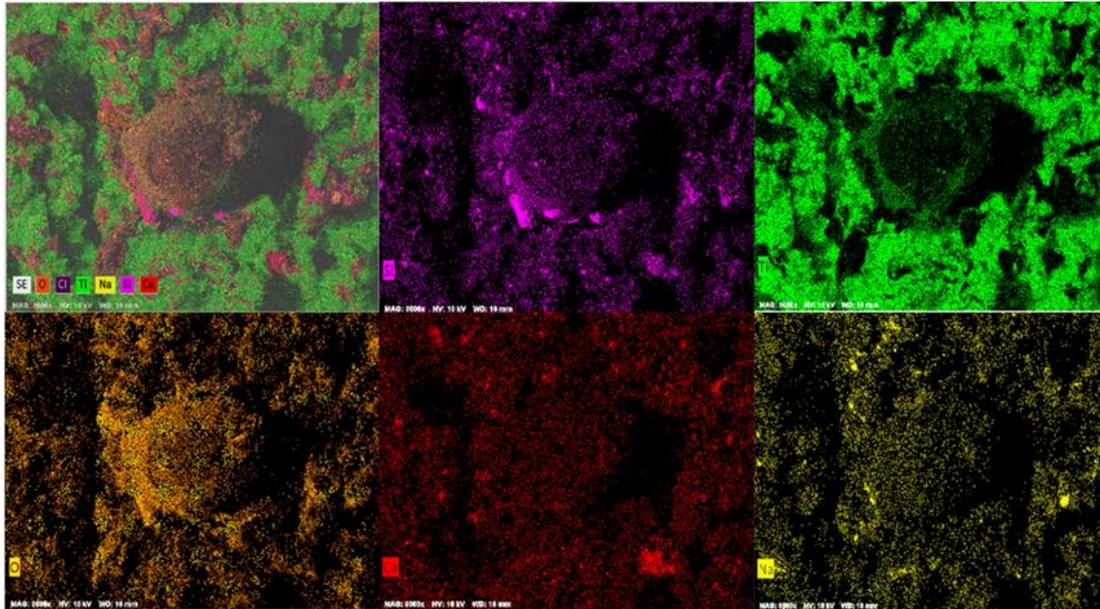
Figure 5.18: Surface EDS mappings of the corroded cold sprayed Ti/25BAG composite coating on SS316L after 2 hr of immersion in Ringer's solution
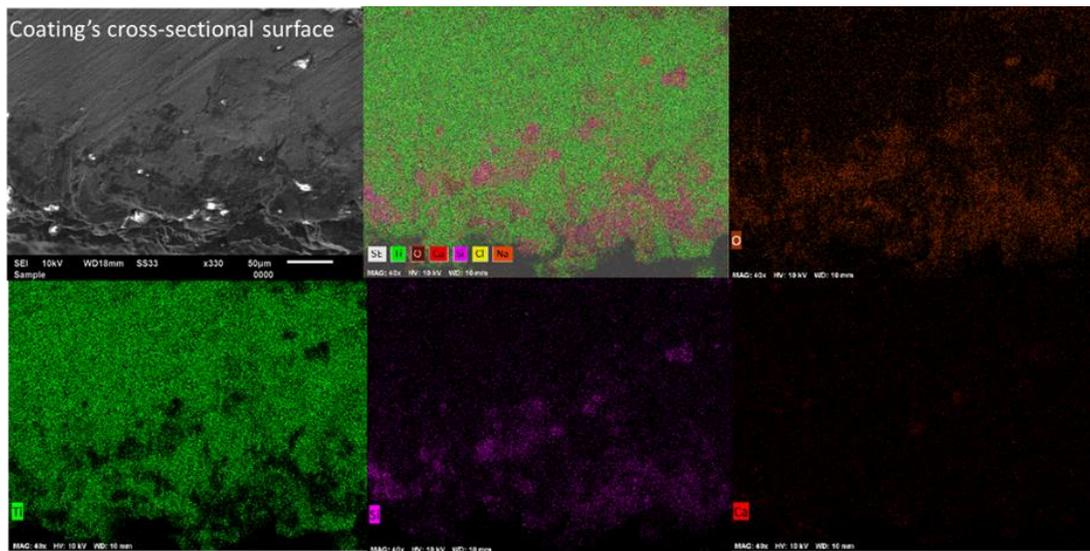
Figure 5.19: Cross-sectional SEM micrograph and EDS mappings of corroded cold sprayed Ti/25BAG composite coating on SS316L after 2 hr of immersion in Ringer's solution
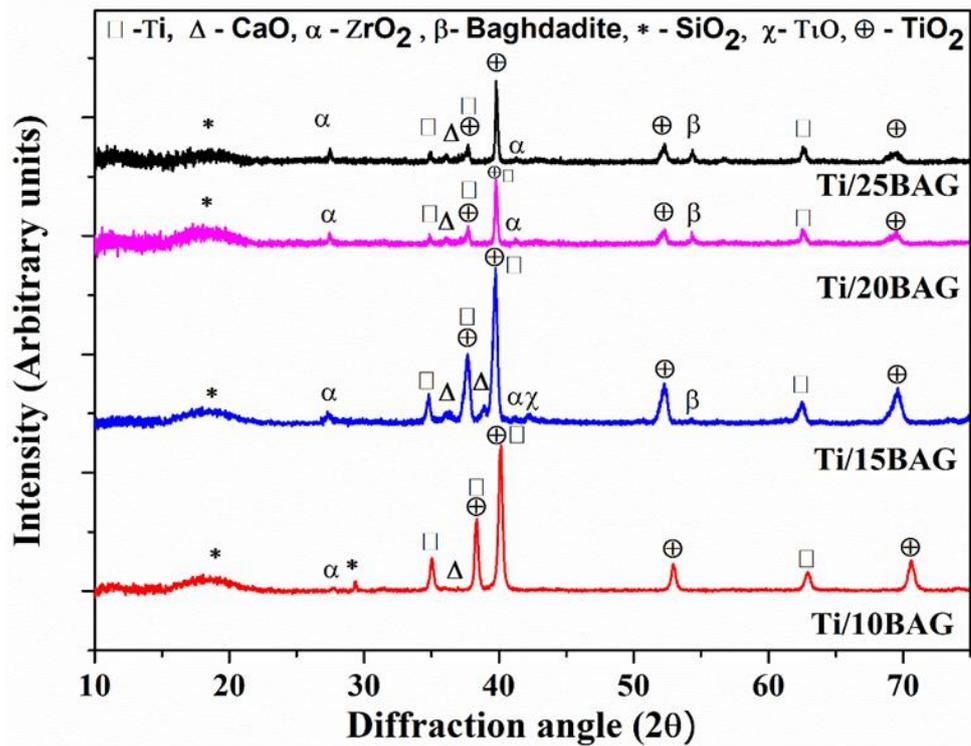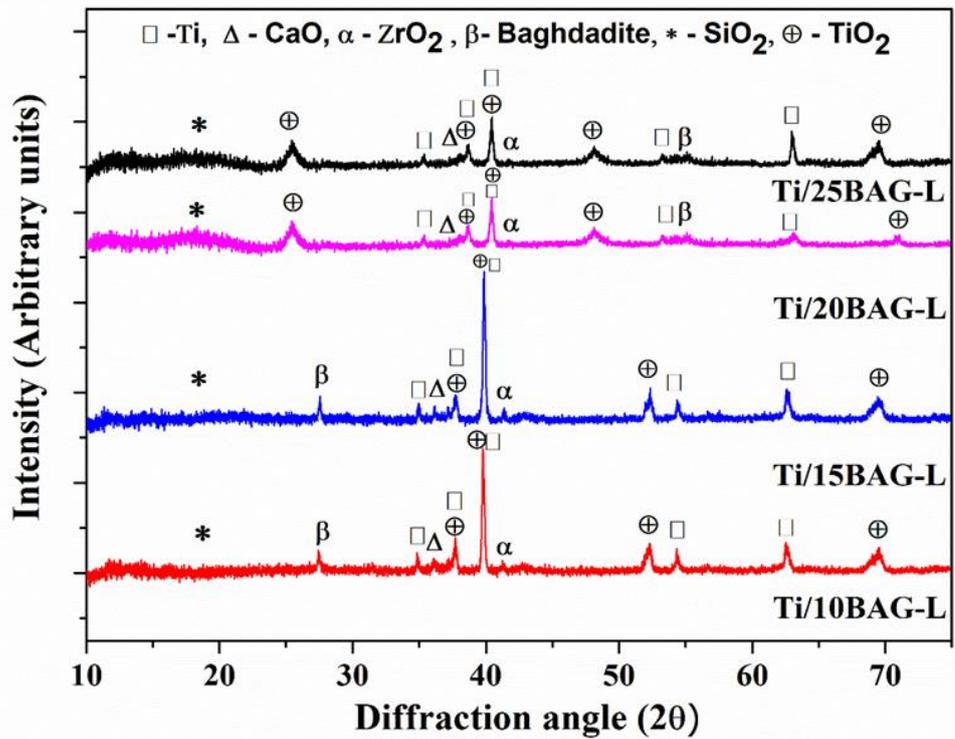
Figure 5.20: XRD analysis of corroded cold sprayed Ti/BAG composite coating on SS316L after 2 hr of immersion time in Ringer's solution (a) as-sprayed (b) laser-treated

5.2.4 Discussion

5.2.4.1 As-sprayed Coatings

In general, the investigated cold-sprayed coatings, that is, Ti/10BAG, Ti/15BAG, Ti/20BAG, and Ti/25BAG, have been successful to protect the steel substrate. Based on the corrosion rate and I_{corr} values, the corrosion performance of the coated and uncoated samples in Ringer's solution for any of investigated immersion times can be arranged in the following order:

$$\text{Substrate} > \text{Ti/10BAG} > \text{Ti/15BAG} > \text{Ti/20BAG} > \text{Ti/25BAG}$$

Moreover, it can be reckoned that the relative corrosion performance of Ti/25BAG is the best among all the investigated coatings in Ringer's solution. From the potentiodynamic scans, it has been observed that all the cold-sprayed coatings performed better than the substrate surface. It is because Ti forms a passive protective layer of titanium oxide when exposed to Ringer's solution.

Surface XRD results indicated the formation of passive oxides such as TiO_2, CaO, SiO_2, and ZrO_2 in the corrosion scale of the coatings. It indicates that the BAG available into the coatings might have dissolved and formed CaO, SiO_2, and ZrO_2 when exposed to Ringer's solution. EDS analysis further supports the formation of these phases. Moreover, the corrosion performance of these coatings has been observed to improve with the immersion time in Ringer's solution. The growth of these passive oxides of Ti, Si, Zr, and Ca to cover the surface of the coatings increases with the increase in immersion time, which produces a barrier to corrosion by separating the coatings from the corroding environment. SiO_2 is well known for its anti-corrosion and biological properties (Qin et al., 2020), (Catauro et al., 2016). Catauro et al. (Catauro et al., 2019) reported the anti-corrosion effect of ZrO_2-SiO_2 composite coatings over titanium substrate in their study for biomedical applications. Krupa et al. (Krupa et al., 2005) reported in their work that the implantation of calcium ions over titanium leads to the formation of CaO when exposed to a body fluid environment and further helps in improving the corrosion resistance of the coating. Thus, the formation of these oxide phases is a boon for protection against corrosion. Additionally, it is reported in Chapter 4 that the retention of BAG was maximum in Ti/25BAG cold-sprayed composite coating, which means the metal (Ti) surface exposure to the Ringer's solution is minimum. Hence, the minimum corrosion rate was observed in this coating.

EIS data also supports the potentiodynamic scan results. The Nyquist plot shows that all of the coatings formed semicircles of different diameters. Ti/25BAG composite coating formed the largest semicircle among all the investigated cases for all the immersion times. It means the Ti/25BAG composite coating forms the most stable thick protective oxide layer over the surface of the coating. Additionally, Nyquist plots showed that for all the coatings two capacitive loops were observed subjected to 2 hr and 16 hr of immersion times, which indicate the pitting or cracking of the first oxide layer and hence the signatures of second oxide layer formation were observed for each type of the coatings. However, in the case of 40 hr of immersion time in Ringer's solution, there was no signature of ions release or second layer formation. It may be because, after 2 hr and 16 hr of immersion in Ringer's solution, the protective oxide layers were not stable, and they might have broken up. Because of this, the ions were released, and second capacitive loops were observed. In the case of 40 hr immersion in Ringer's solution, the protective passive oxide layer was stable and thick enough. Because of this, there was no signature of second-layer development or ions release. The Bode plots also indicated that Ti/25BAG offers the best protection to the substrate as it shows the maximum impedance in lower frequency region, which is in good agreement with the potentiodynamic scans and Nyquist plot results. Moreover, there was no evidence observed from potentiodynamic or EIS results that indicates the removal of coating from the substrate. Therefore, on the basis of above facts, it can be concluded that the composite coatings were more corrosion-resistant than the bare substrate. The corrosion rate for each of the investigated coatings was found to be below 1 micron/year. As per the ISO standard, the surface would be perfectly stable if the corrosion rate is less than 1 micron/year (ISO, n.d.). Zhou and Mohanty (Zhou and Mohanty, 2012) developed cold-sprayed pure Ti and 20 wt.% HA/Ti composite coating and reported Ecorr and Icorr values for Ti as 0.362 $\mu A/cm^2$ and - 241 mV and for 20 wt.% HA/Ti as 0.934 $\mu A/cm^2$ and - 379 mV in Ringer's solution. Compared with them, the Ti/20BAG cold-sprayed composite coating showed better Ecorr and Icorr values (0.668 $\mu A/cm^2$ and - 178 mV). It indicates that the cold-sprayed Ti/20BAG composite coating outperformed the cold-sprayed pure Ti and 20 wt. % HA/Ti composite coating in Ringer's solution. This observation indicates towards the potential of BAG to replace HA in biomedical applications.

As mentioned in Chapter 4, the porosity has been observed to increase with the increase in BAG content. It is well established that porosity is one of the crucial factors in promoting corrosion. Contrary to this, it was observed that the corrosion resistance and porosity increased with the increase in BAG content in this work. This can be explained by the two-layer model discussed above in electrochemical impedance spectroscopy fitted data. The coatings had a porous layer at the top and a dense layer at the bottom. The dissolution of BAG led to the formation of dense passive oxides such as SiO_2, CaO, and ZrO_2 in Ringer's solution. It might have further led to the precipitation of Ringer's salt, which blocks the pores (Pan et al., 1996). Additionally, Ti forms passive TiO_2 when exposed to Ringer's solution and is very well known for its excellent corrosion resistance. Therefore, BAG might have compensated for the effect of porosity by blocking the pores due to the precipitation of Ringer's salt. Souto et al. (Souto et al., 2003) have also reported similar results for hydroxyapatite coating on Ti6Al4V in simulated body fluid environment.

5.2.4.2 Laser-treated Coatings

Laser treatment of as-sprayed coatings reduced apparent surface porosity and surface roughness, as reported in Chapter 4. Marrocco et al. (2011) (Marrocco et al., 2011) reported similar results for laser-treated cold-sprayed Ti coatings. From the microstructural characterization (reported in Chapter 4), it was also observed that the laser treatment led to the formation of equiaxed grains at the top layers of the coating. Garbach et al. (Garbacz et al., 2007) reported that the surface texture may influence the quality and thickness of passive oxides. However, grain sizes do not affect the thickness of the passive oxide layer on the titanium surface. Wei et al.(Wei et al., 2019) reported that laser treatment reduces the residual stresses and dislocation density of the additively manufactured titanium parts. In another work, Kim and Kim (Kim and Kim, 2014) claimed that a reduction in dislocation density and residual stresses enhanced the corrosion performance of titanium. Hence, laser-treatment of investigated coatings might have reduced the dislocation densities and residual stresses of the cold-sprayed coatings and further improved the corrosion resistance in Ringer's solution. Ti/25BAG-L composite coating performed best among all the investigated coatings after 2 hr of immersion in Ringer's solution. The surface area exposed to Ringer's solution was expected to decrease due to the reduction in porosity and surface roughness after the

laser treatment of as-sprayed coatings. Thus, the better corrosion performance of the laser-treated coatings was expected.

After 2 hr of immersion in Ringer's solution, the potentiodynamic scans of laser-treated cold spray coatings show that the E_{corr} value has shifted towards the noble direction, and the I_{corr} value has decreased significantly. Based on E_{corr} and I_{corr} values, the corrosion performance of laser-treated and as-sprayed coatings after 2 hr of immersion in Ringer's solution can be arranged in the following order:

For E_{corr},

Ti/10BAG > Substrate > Ti/10BAG-L > Ti/15BAG > Ti/15BAG-L > Ti/20BAG > Ti/20BAG-L > Ti/25BAG > Ti/25BAG-L

For I_{corr},

Substrate > Ti/10BAG > Ti/15BAG > Ti/20BAG > Ti/25BAG > Ti/10BAG-L > Ti/15BAG-L > Ti/20BAG-L > Ti/25BAG-L

The I_{corr} value reflects the corrosion performance of the composite coatings under Ringer's solution. Surface XRD results revealed that oxides such as TiO_2, CaO, SiO_2, and ZrO_2 have formed after corrosion in Ringer's solution. These oxides of Ca, Si, and Zr are well-known to produce a barrier against corrosion (Catauro et al., 2016), (Catauro et al., 2019).

SLIDING WEAR STUDIES

This chapter deals with the findings of sliding wear testing of the developed cold spray Ti-based coatings on the biomedical steel (SS316L) substrate. Pin-on-disc (PoD) sliding wear configuration was used to assess the tribological behaviour of cold spray-coated and uncoated materials. The results of wear rate and coefficient of friction (CoF) in dry and Hank's solution have been reported and discussed. Post-wear analysis has also been performed to characterize the wear signatures. The worn-out coated samples and counter discs were analyzed using scanning electron microscopy (SEM), electron dispersive spectroscopy (EDS), and X-ray diffraction (XRD).

6.1 Wear Behavior of Titanium/Titanium Oxide (Ti/TiO$_2$) Coated and Uncoated SS316L Steel

6.1.1 Friction

The coefficient of friction (CoF) is plotted versus sliding distance for SS316L substrate, Ti/20TiO$_2$, Ti/40TiO$_2$, and Ti/60TiO$_2$ composite coatings in Fig.6.1. The substrate exhibited an initial friction spike above 0.125 followed by a short run-in period, after which CoF remained regularly between 0.078 and 0.084. The friction plots show that each coating shows different behavior. The cold-sprayed Ti/40TiO$_2$ coating was observed to have the highest average CoF and the largest variation in friction behavior. The CoF fluctuated between 0.190 and 0.136 for cold-sprayed Ti/40TiO$_2$ composite coating. The cold-sprayed Ti/20TiO$_2$ coating displayed the smallest variation in CoF. The CoF was observed to vary between 0.120 and 0.095. The cold-sprayed Ti/60TiO$_2$ coating shows an initial rise in CoF up to 0.161 and then drops consistently up to 0.123, after which it enters in a steady state.

The average CoF of the cold-sprayed Ti/TiO$_2$ composite coatings and the substrate is shown in Fig.6.2. The average CoF was observed to be maximum for cold-sprayed Ti/40TiO$_2$ composite coating. The substrate has been observed to offer minimum CoF among all the investigated Ti/TiO$_2$ coated and uncoated SS316L steel. The average CoF

for the investigated coatings was observed to increase with the increase in ceramic content from 20% to 40% (in the feedstock); after that, the coating failed, and CoF decreased (Fig. 6.1).

The CoF has been observed to be minimum for the substrate and alumina tribopair; it may be because the used substrate is mirror polished, and the asperities responsible for the generation of frictional force have already been removed. Superior microhardness and good bonding between the particles of Ti/20TiO$_2$ coating may be the reason for the asperities to resist the alumina surface (counterface), leading to smaller CoF caused by the minimum real area of contact (Yoon et al., 2005). However, the increase in ceramic content up to 40% in feedstock led to an increase in CoF caused by poor bonding and lower microhardness, leading to a higher contact area. Further increase in ceramic content of feedstock from 40% to 60% led to complete failure of the coating from the substrate caused by the poor bonding, and a decrease in CoF was observed. After the removal of the coating, the contact area increased; however, rubbing the counter alumina surface on an already polished (MP) substrate would have caused a reduction in CoF. These large steps in friction data show the sticking and sliding behavior of welded junctions. Sudden increases in the Coefficient of Friction (CoF) signify the occurrence of sticking, whereas sudden drops indicate sliding behavior.
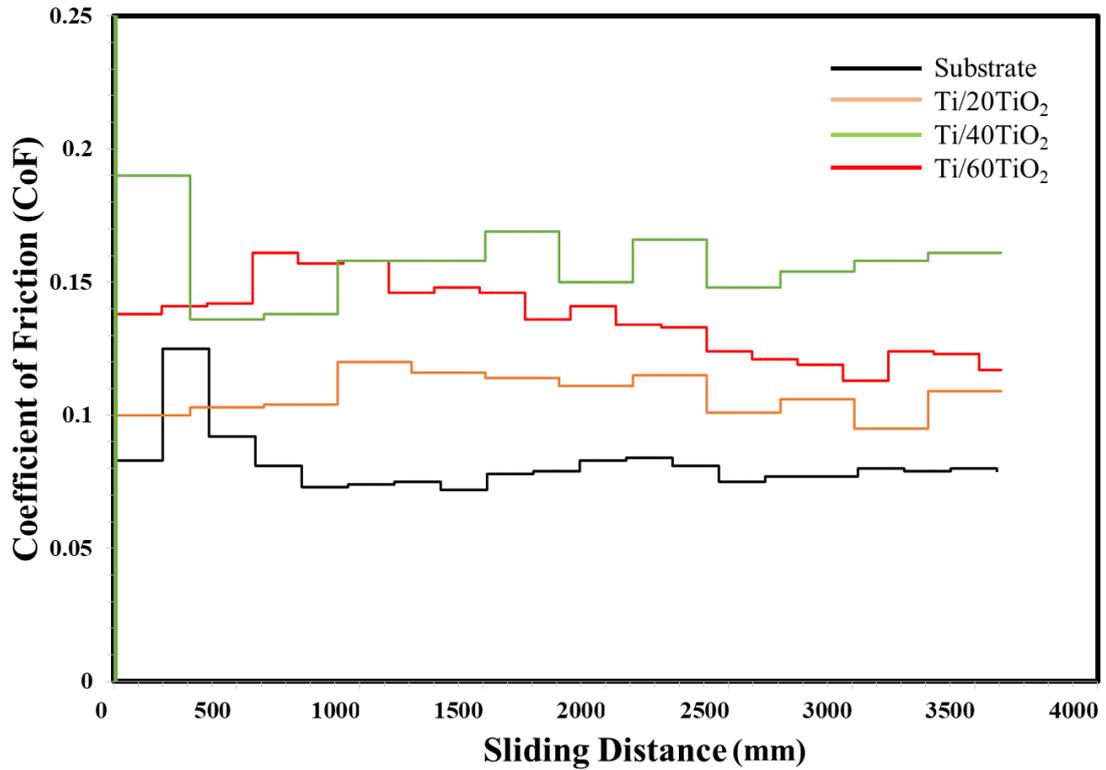
Figure 6.1: Coefficient of friction (CoF) versus sliding distance plots for the in-situ pin-on-disk sliding wear tests on cold sprayed Ti/TiO$_2$ coated and uncoated SS316L steel against alumina disk

6.1.2 Wear

The wear rate calculated from the mass loss and density after PoD tests for the substrate, Ti/20TiO$_2$, Ti/40TiO$_2$ were 23.33×10^{-5} mm^3/N-m, 7.50×10^{-5} mm^3/N-m, and 29.82×10^{-5} mm^3/N-m, respectively. The reported results indicate that the substrate has better wear resistance than the developed coatings except for Ti/20TiO$_2$ composite coating. Moreover, the Ti/60TiO$_2$ coating failed during PoD testing.

Wong et al. (Wong et al., 2010) deposited pure Ti using the cold spray at the same process parameters which have been used in this work and have reported the microhardness value of deposited coating in the range of 177-208 HV. The deposited Ti/20TiO$_2$ composite coating has shown microhardness in the range of 234-256 HV. However, for Ti/40TiO$_2$, it has dropped to 145-171 HV, as reported in Chapter 4. It is noticeable that the addition of TiO$_2$ up to 20% has contributed to achieving higher

hardness. However, beyond 20% content, the retention of TiO_2 has decreased, which influenced the microhardness of the coatings as well.

These wear behavior of investigated composite coatings can be explained by Archard's wear equation (Archard, 1953),

$$W = (K \times F) / (3 \times H) \qquad (6.1)$$

Where W represents the wear volume per sliding length, K is the wear coefficient, F is the applied load, and H is the hardness of the coating material. As per Archard's wear law (Equation 6.1), the wear rate is inversely proportional to the hardness of the softer contacting surface (cold-sprayed coatings in this case) in the tribopair (Archard, 1953). It was observed from the results that the microhardness and wear resistance followed a similar trend. As per the discussion in Chapter 4, the micro-hardness value of the $Ti/20TiO_2$ composite coating was maximum, which could be one of the reasons for its superior wear resistance. Koricherla et al. (Koricherla et al., 2021) reported the microhardness value and wear behavior of cold-sprayed titanium coating in their work. They stated that cold-sprayed Ti had microhardness and wear rates ranging from 189 to 219 HV and 84×10^{-5} mm^3/N-m to 116×10^{-5} mm^3/N-m, respectively. The deposited $Ti/20TiO_2$ composite coating has shown a wear rate in the range of 6.3×10^{-5} mm^3/N-m to 9.2×10^{-5} mm^3/N-m, which is way better than the cold-sprayed Ti coatings. It indicates that the presence of TiO_2 (20%) in the Ti matrix significantly helped in improving the wear resistance of the coatings. However, the wear rate continued to increase beyond 20% of TiO_2 in the Ti matrix, and it could be because of poor cohesion and adhesion of the Ti and TiO_2 splats, as discussed in Chapter 4.
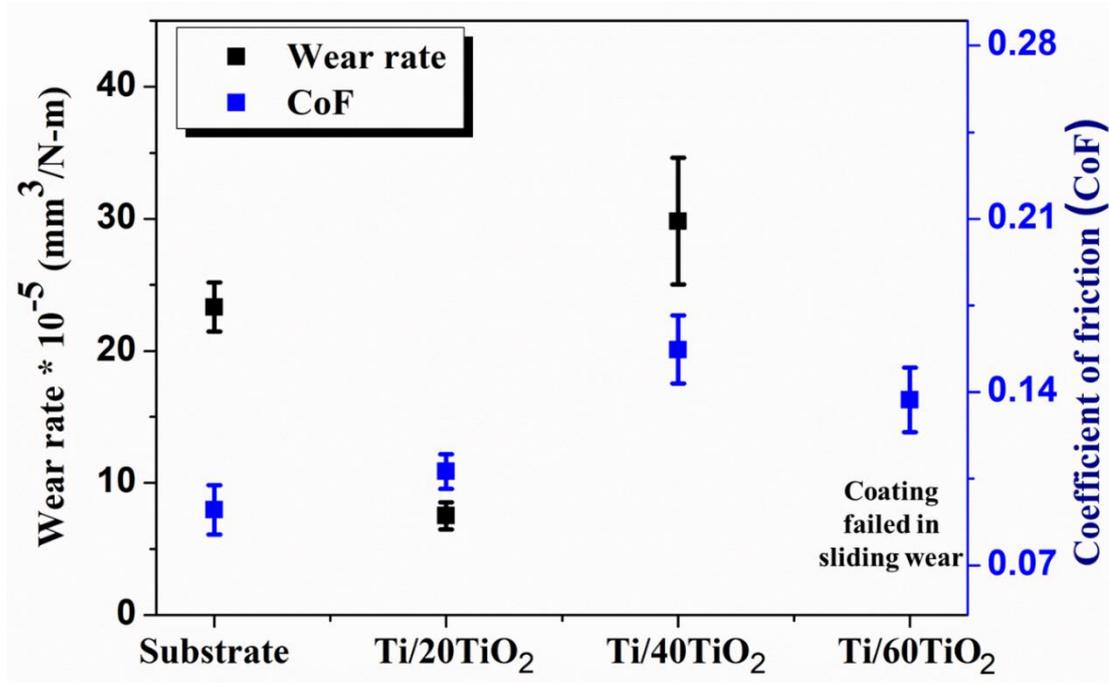
Figure 6.2: Wear rate and the average coefficient of friction (CoF) of the cold sprayed Ti/TiO$_2$ coated and uncoated SS316L steel against alumina disk

6.1.3 Wear Mechanism

The wear mechanism has been explored by analyzing the worn coating surfaces. SEM/EDS micrographs of the coatings after PoD tests are shown in Fig 6.3. SEM micrographs of the worn surfaces, Ti/TiO$_2$ coated, and uncoated steel revealed abrasion along with ploughing action in sliding direction. The abrasive grooves might have formed due to the entrapment of the wear debris between the tribopair. Munagala et al. (Munagala et al., 2020) discussed the sliding wear behavior of cold-sprayed Ti6Al4V coating against alumina disk. They observed similar signatures of sliding wear in their work. The entrapment of wear debris between the coatings and counterface was proved to be the reason for it. The other possible reason for the formation of abrasive grooves could be the micro-cutting action of the counterface. The hard counterpart (alumina) surface peaks penetration into the relatively softer composite coating, causing the micro-cutting action, which further leads to the formation of cracks and pits.

The plastic deformation of the Ti splats caused by the rubbing action between the coatings and the counterpart was believed to be one of the reasons for the development of cracks at the inter-splat boundaries. The formation of these cracks further leads to the

delamination of the splats from the coating and promotes wear rate. The TiO_2 splats in the Ti matrix tend to provide strength to the deformed Ti splats into the composite coating and protect the coating from wear. Tesfay et al. (Tesfay et al., 2009) discussed the effect of TiO_2 on wear behavior of the Al/TiO_2 composite. They reported that the decreased real area of metal contact with the counterface and good mechanical properties of TiO_2 were the reason for the good wear resistance of composites. However, after a threshold value (beyond 20% in this case), these TiO_2 splats adversely affect the bonding between the splats and promote wear rate. Moreover, the TiO_2 splats tend to fracture on sliding against the counterface and contribute to wear debris formation. The formed wear debris works as a third body and promotes wear rate.

Additionally, the signatures of adhesive wear were also observed over the coating surface. It is believed that high temperature during sliding led to the formation of weld junctions. The ploughing action leads to the transfer of material from one place (coatings) to the other (counterface) by breaking the weld junctions (Lisowski and Stolarski, 1981). The micro-cutting, delamination, and micro-cracks signature have been found to be more severe in the cold-sprayed $Ti/40TiO_2$ composite coating than in $Ti/20TiO_2$ composite coating (Fig. 6.3). Hence, it leads to relatively poor wear resistance.
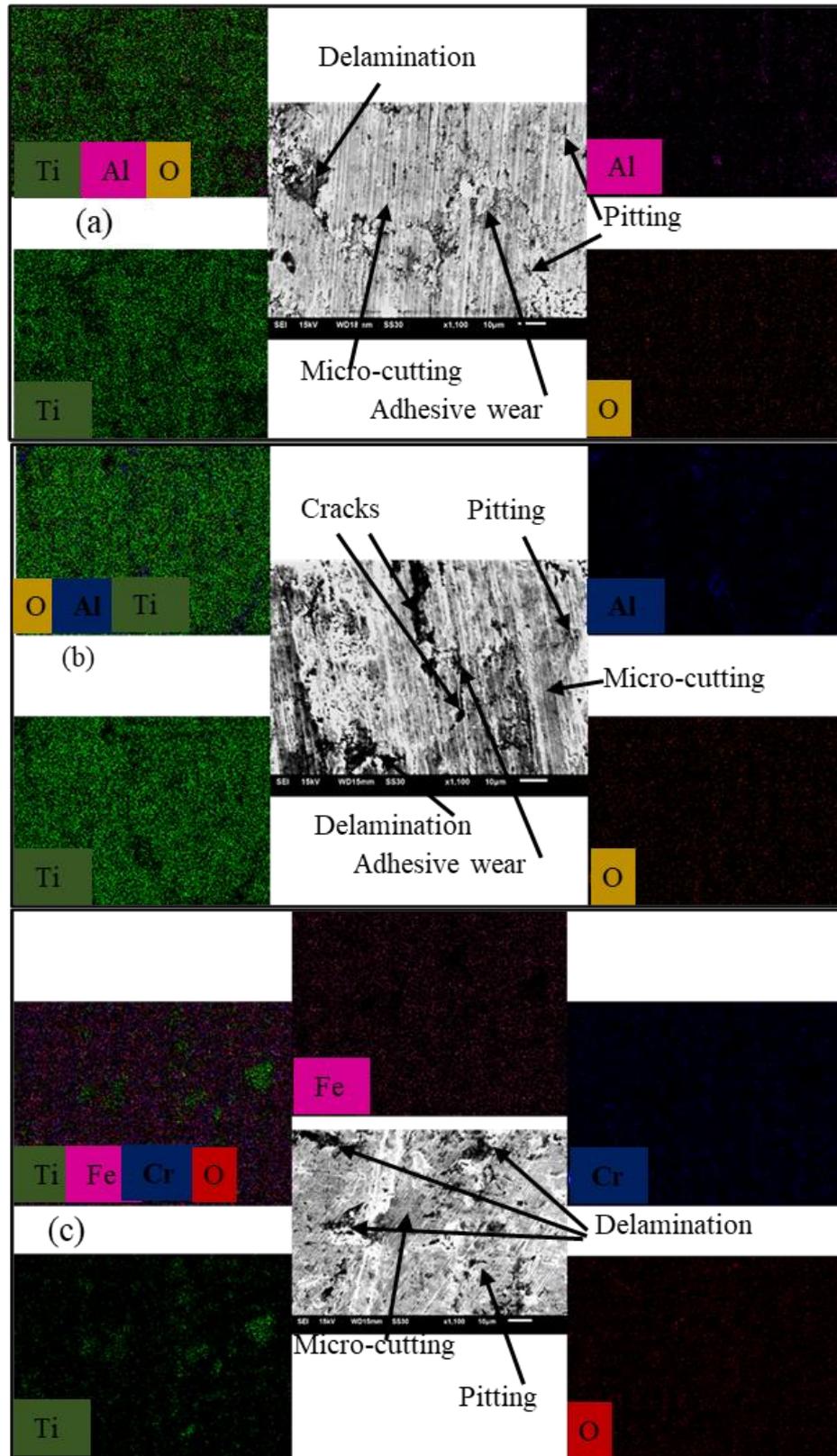
Figure 6.3: SEM micrographs along with EDS mappings of cold-sprayed SS316L
steel surfaces subjected to wear test in a dry environment (i) Ti/20TiO$_2$ coating (ii)
Ti/40TiO$_2$ coating (iii) Ti/60TiO$_2$ coating

6.2 Wear Behavior of Titanium/Baghdadite (Ti/BAG) Coated and Uncoated SS316L Steel

6.2.1 As-Sprayed Coatings

6.2.1.1 Friction

The CoF against sliding distance graphs for the cold-sprayed Ti/BAG coated and uncoated SS316L steels are shown in Fig. 6.4(a and b). Friction plots show that each coating behaved differently. In dry condition, Ti/25BAG coating was observed to have the highest CoF, which fluctuated between 0.146 and 0.235. Ti/20BAG coating exhibited the second-highest CoF, in the range of 0.143 - 0.21. The substrate showed the minimum CoF with minimum fluctuation (0.113 - 0.137). Cold-sprayed Ti/15BAG coating showed the second lowest CoF, The fluctuation in CoF for cold-sprayed Ti/10BAG was found between 0.093 and 0.203. Whereas, in a simulated body fluid environment (Hank's solution), friction plots show significantly low CoF compared to the dry environment (Fig 6.4(b)). Cold-sprayed Ti/15BAG was found to have minimum CoF, and it varied between 0.031 and 0.065. Ti/10BAG coating was observed to have the second lowest CoF after Ti/15BAG. The CoF fluctuated between 0.040 and 0.072. The substrate was shown to have the largest CoF among all the investigated specimens, followed by Ti/25BAG coating. Cold-sprayed Ti/20BAG coating exhibited CoF in the range of 0.049 - 0.087.

The influence of BAG content on average CoF is shown in Fig. 6.5. For dry conditions, the results indicate that the average CoF was minimum for Ti/15BAG coating and maximum for Ti/25BAG coating among all the investigated specimens. It was believed that superior scratch resistance and microhardness of cold-sprayed Ti/15BAG coating could have helped the asperities to withstand the alumina counter surface. It might have led to a smaller real contact area, lesser asperity junctions, and the lowest CoF. Likewise, poor scratch resistance and microhardness of Ti/25BAG coating could have been the reason for the severe plastic deformation of asperities, leading to a higher real area of contact, more asperity junctions, and hence the highest CoF. Yoon et al. (Yoon et al., 2005) discussed the effect of contact area on CoF in their work, which is consistent with the results reported in this study. Moreover, the average CoF values were observed to be relatively smaller in the simulated body fluid environment compared to the dry environment. It is believed that the Hank's solution could act as a lubricant, and also

flush out wear debris from the areas of sliding contact, thereby reducing the real contact area and resulting CoF.
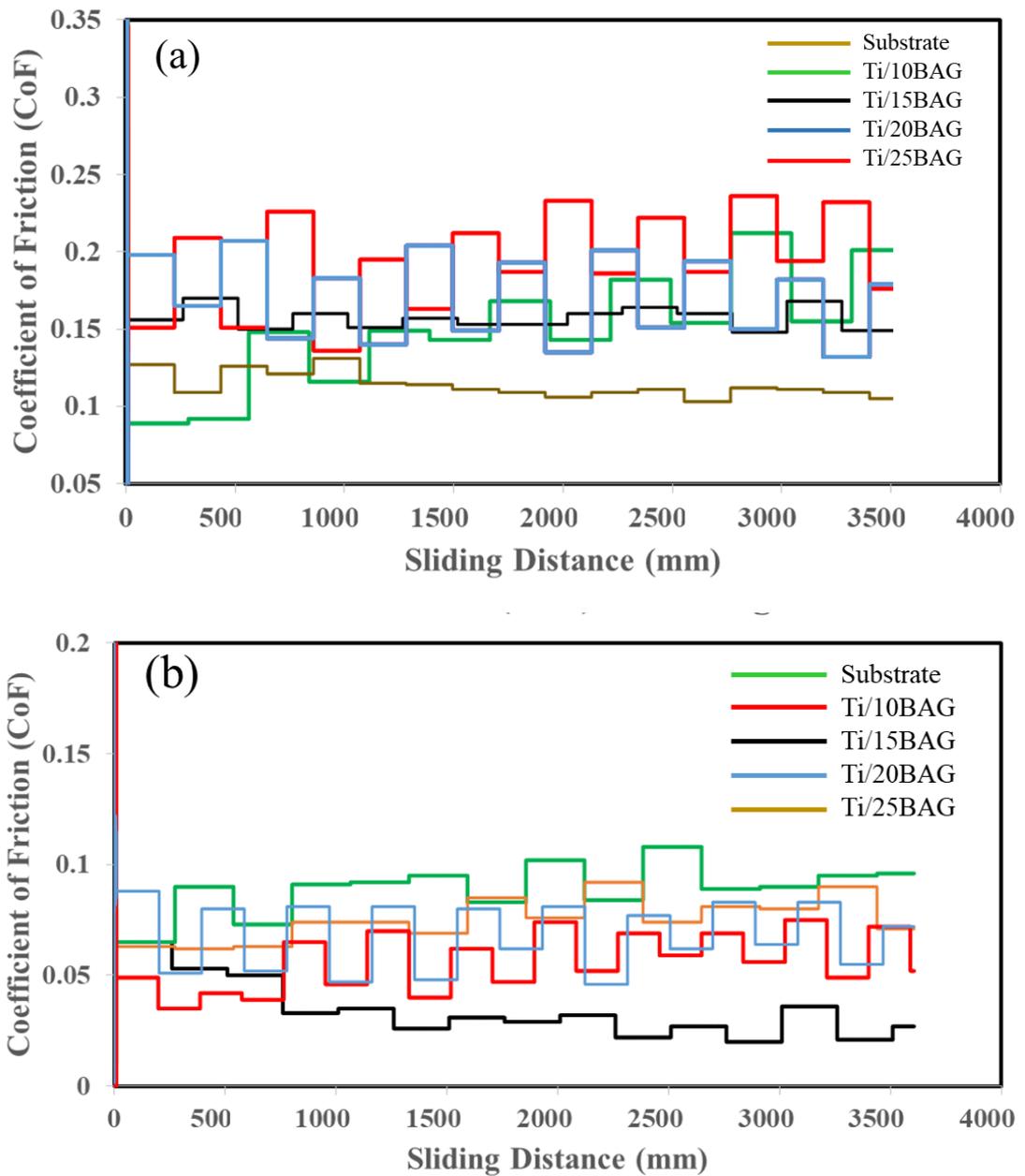
Figure 6.4: Coefficient of friction (CoF) versus sliding distance plots for the pin-on-disk sliding wear tests for cold spray Ti/BAG coated and uncoated SS316L steel against alumina disk under (a) dry condition and (b) Hank's solution
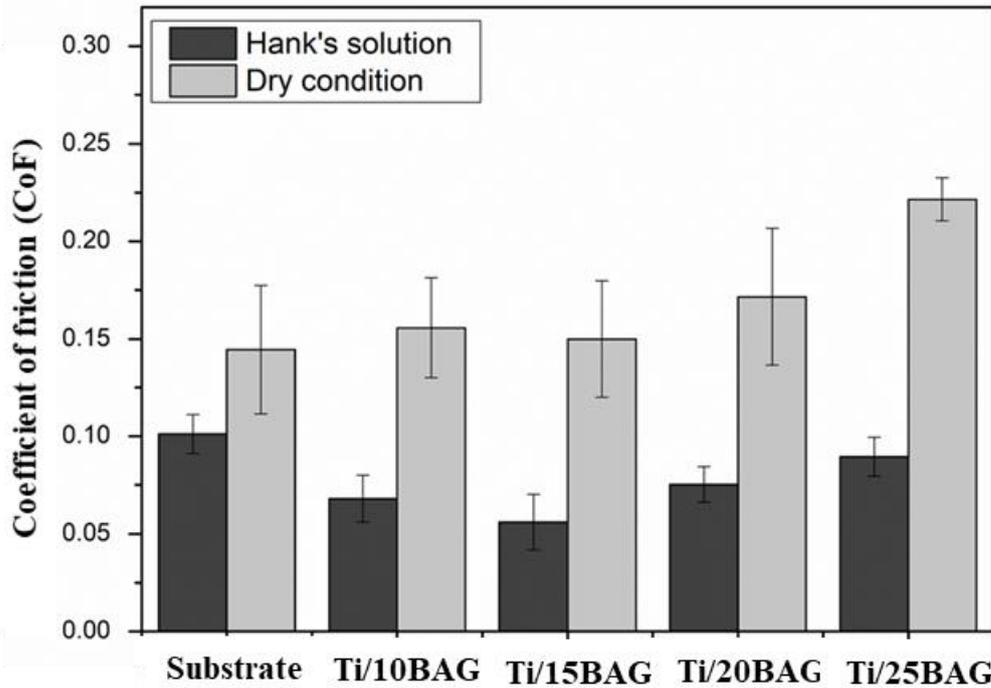
Figure 6.5: CoF of the cold-sprayed Ti/BAG composite coatings on SS316L against alumina disk under dry and Hank's solution conditions

6.2.1.2 Wear

The wear rates calculated at the end of the PoD tests were plotted against the BAG content. Fig. 6.6 depicts the change in wear rate in Hank's solution and dry condition with the BAG content. For the dry environment, the average wear rates for the bare steel, Ti/10BAG, Ti/15BAG, Ti/20BAG, and Ti/25BAG coatings were 20×10^{-5} mm^3/N-m, 29×10^{-5} mm^3/N-m, 7×10^{-5} mm^3/N-m, 98×10^{-5} mm^3/N-m, and 141×10^{-5} mm^3/N-m, respectively. In the simulated body fluid environment, the average wear rate was 15×10^{-5} mm^3/N-m, 13×10^{-5} mm^3/N-m, 8×10^{-5} mm^3/N-m, 33×10^{-5} mm^3/N-m, and 59×10^{-5} mm^3/N-m for the substrate, Ti/10BAG, Ti/15BAG, Ti/20BAG, and Ti/25BAG, respectively. The results signify that the wear resistance of SS316L substrate in the dry condition was better than the developed cold-sprayed coatings, with an exception of Ti/15BAG coating. In other words, Ti/15BAG was successful to reduce the wear loss of SS316L steel. Moreover, it is observed that BAG fraction has a positive effect on wear resistance upto an addition of 15% in Ti-matrix, however beyond 15%, BAG content has a negative effect on wear resistance. Ti/15BAG coating has experienced the

minimum wear rate among all the investigated coatings, whereas Ti/25BAG coating has experienced the maximum wear rate.

The wear behavior of investigated composite coatings can be explained from Archard's wear equation, that is, Equation (6.1), which signifies that on the basis of higher the hardness of the coating lower will be the wear rate. High hardness restricts the plastic deformation of the asperities and limits the number of asperity junctions. The shearing of asperity junctions causes material loss; therefore, the lesser the number of asperity junctions, the wear rate will be lower. Microhardness value is maximum for Ti/15BAG composite coating and minimum for Ti/25BAG composite coating. Hence wear rate trend is consistent with predictions of Archard's equation.

The wear rate in a simulated body fluid environment is relatively less than in the dry environment for all the investigated materials, as shown in Fig. 6.6. Moreover, Ti/10BAG and Ti/15BAG coatings are successful in protecting the substrate from wear in Hank's solution due to their superior microhardness, higher contact angle, and greater scratch resistance. Once again, the wear rate of all the developed coatings depends on the microhardness, in line with Archard's wear equation.

Porosity is also one of the factors that may affect the sliding wear behavior of the developed cold-sprayed coatings in dry and simulated body fluid environments. As the porosity increases, the wear resistance of the coating is expected to decrease as it can contribute to the development of cracks (Sinha et al., 2015). However, in the current study, the wear resistance of the developed coatings has increased with an increase in BAG content up to 15% BAG and 5% porosity. The reason behind this can be the entrapment of wear debris in the pores, which further protects the surface from crack propagation or wear and may have also helped in making the pores relatively stable beneath the worn surface (Simchi and Danninger, 2004). Another possible reason is the retention of BAG particles in well-bonded Ti/10BAG and Ti/15BAG coatings, which may have contributed in protecting the matrix from the destructive action of wear. However, beyond 15% BAG, the higher porosity led to weaker bonding in cold sprayed Ti/20BAG and Ti/25BAG coatings. Therefore, even if the pores are filled with wear debris, the weakly bonded particles will wear out during sliding and lead to higher wear rate. The higher porosity decreases the contact area and produces high strain-induced

stress while sliding, making the pores relatively unstable underneath the worn surface (ZHANG et al., 2008).
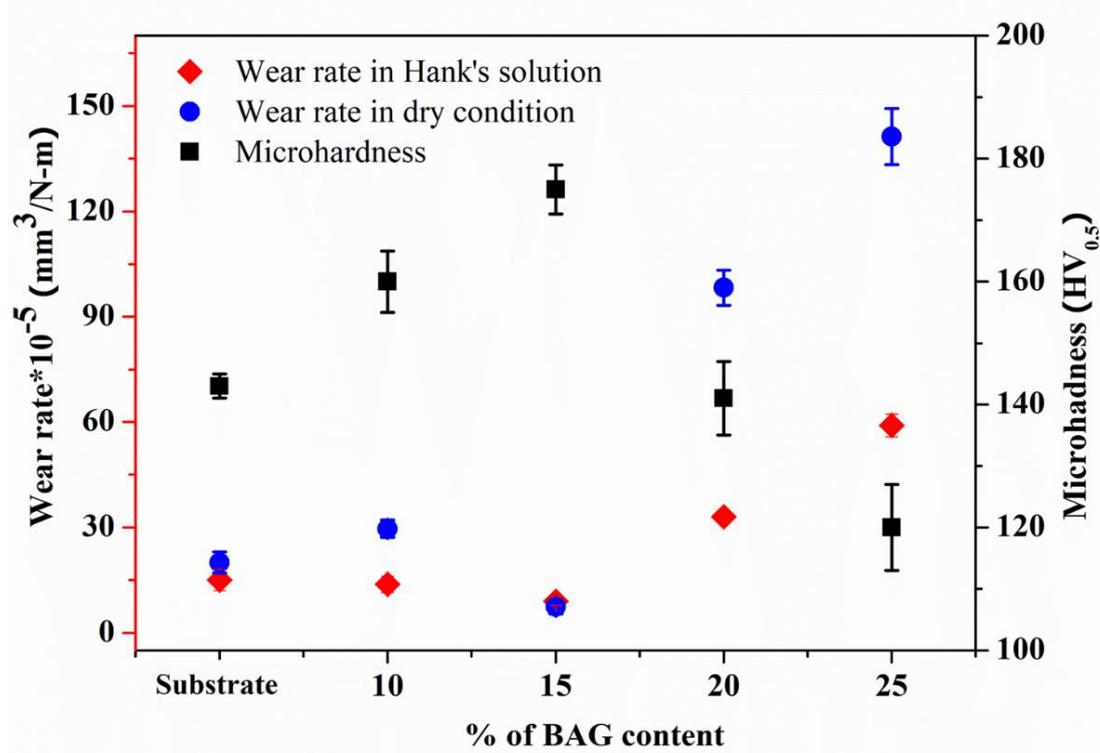
Figure 6.6: Microhardness and wear rate against alumina disk of the cold sprayed
Ti/BAG composite coatings on SS316L

6.2.1.3 Wear Mechanism

Post-wear analysis has been performed on the worn coating surfaces to understand the wear mechanism for the cold-sprayed Ti/BAG composite coatings. SEM/EDS micrographs of the worn Ti/BAG cold sprayed coatings against alumina counterface for dry sliding conditions are shown in Fig. 6.7. In the dry environment, abrasion of the surfaces is observed to be the leading cause of coating's failure. It was observed from the images that three-body abrasion was the dominant wear mechanism in all the investigated coatings. Signatures of micro-cracks, pitting, delamination, and micro-cutting were found over the worn coating surfaces. Micro-cracks present in the coatings may lead to the formation of pits and/or delamination on the coating surfaces. The reason behind the development of these cracks is the plastic deformation caused by the three-body rolling abrasion of the coatings. Micro-cutting features were also observed on the coating surfaces because of the ductility offered by the matrix of the Ti/BAG

coatings. Wear debris present over the surfaces promote wear between the contacting surfaces. Also, it was observed that the size of the wear debris is relatively smaller than that of the powder particle size used for the deposition of the composite coatings. Severe plastic deformation of the coatings against alumina disk leads to large numbers of smaller wear debris, which further affect the wear rate (HONG et al., 2018). In the case of cold-sprayed Ti/15BAG composite coating (Fig. 6.7 (b)), wear debris concentration and plastic deformation were observed relatively less, which can be a reason for the comparatively lower wear rate (Habib et al., 2020).

On the other hand, Ti/25BAG coating (Fig. 6.7 (d)) underwent severe plastic deformation, causing a maximum wear rate among the investigated coatings. Moreover, Ti/10BAG coating has shown relatively more wear than the substrate, even if it has better microhardness. The can be attributed to the fact that this coating higher a roughness in as-sprayed condition. This might result into relatively severe rubbing of rougher peaks over the hard counter surface leading to high-stress concentration, and subsequently severe plastic deformation causing higher wear rates (Shi et al., 2019). On the other hand, the substrate was mirror polished, having relatively lower roughness. Therefore, the reported wear rate, that is, the steady-state wear rate of the substrate, is lesser than that of the Ti/10BAG coating.

The high magnification SEM micrographs of the cold sprayed coating surfaces after the PoD tests in the simulated body fluid environment are shown in Fig. 6.8. The three-body abrasion has been identified the mechanism of failure of the investigated coatings against the hard alumina counter surface. However, the concentration of wear debris responsible for the 3-body abrasion is relatively lesser than that of the dry environment, which in turn helped in reducing the wear rate of the coatings. One of the reasons for the lower wear rate in a simulated body fluid environment could be the formation of a lubricant layer between the contacting surfaces, which may help remove the wear debris from the contact surfaces. The worn-out coating surfaces are relatively smooth, when compared with those of dry worn-out counterparts. This could be attributed to the rapid formation of the oxide layer and its removal in subsequent sliding contact under the simulated fluid environment (Majumdar et al., 2008).
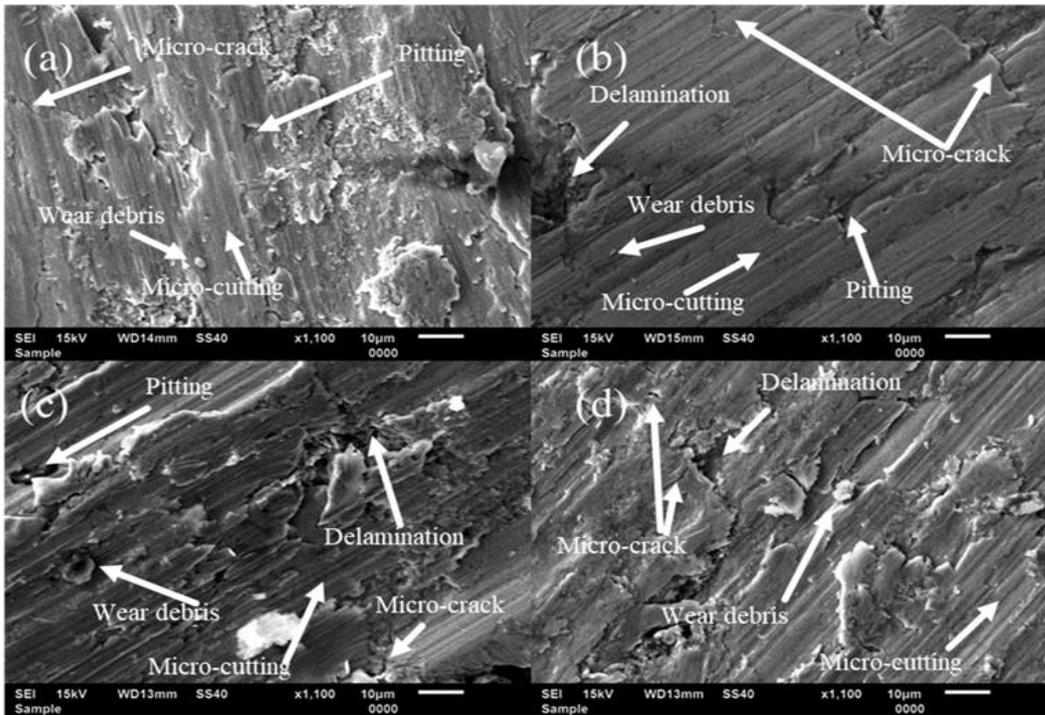
Figure 6.7: Surface SEM micrographs of cold-sprayed SS316L steel surfaces subjected to wear test in a dry environment (a) Ti/10BAG coating (b) Ti/15BAG coating (c) Ti/20BAG coating (d) Ti/25BAG coating
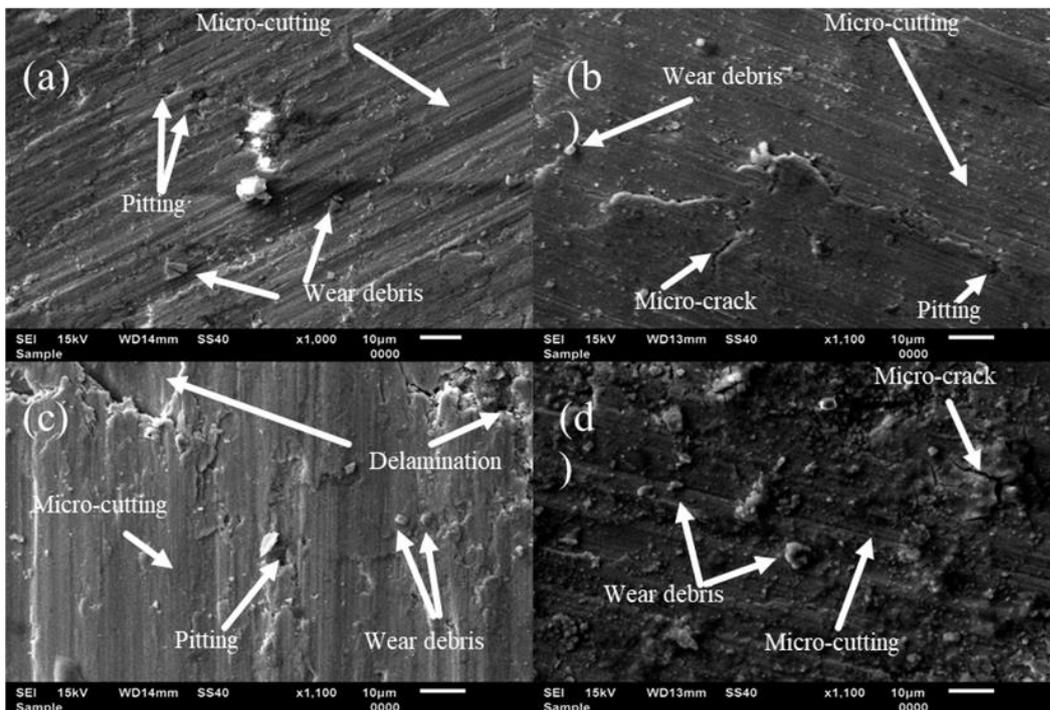
Figure 6.8: Surface SEM micrographs of cold-sprayed SS316L steel surfaces subjected to wear test in Hank's solution (a) Ti/10BAG coating (b) Ti/15BAG coating (c) Ti/20BAG coating (d) Ti/25BAG coating

Furthermore, the alumina counterfaces were analyzed using SEM/EDS to investigate the material transfer during sliding wear testing of the cold-sprayed composite coatings, as reported in Fig. 6.9, 6.10, 6.11, and 6.12. In all the investigated counter surfaces, the coating material was found to have adhered. EDS mapping confirmed the presence of coating material over the counter surface. This may be attributed to the generation of frictional heat and plastic deformation of softer material in the tribosystem caused by the development of welded junctions at the asperities of the sliding surfaces. If the strength of the junction is stronger than the cohesive strength of the coating material, material transfer occurs (Gåård et al., 2010). It has also been observed that the transfer of coating material on alumina disk in Ti/15BAG coating was minimum and maximum for Ti/25BAG composite coating among all the investigated coatings, as shown in Fig. 6.9(b and d). These results are consistent with the wear rate. Traces of calcium, zirconium, and silicon were also observed, indicating the transfer of BAG material over the counter surface.

SEM/EDS analysis of the counterfaces after the PoD tests on the developed coatings in the simulated body fluid environment is also shown in Fig. 6.9. The results suggest that adhesive wear mechanism was dominant in these cases. This can be attributed to the fact that the transfer of coating material observed on the counterface was relatively more than that of the dry environment. Adhesive wear grooves were observed over all the coating surfaces. It was because the shearing of lubricant may have caused the development of high temperature at the contact, which further led to the formation of weld junctions between the asperities of the cold sprayed Ti/BAG composite coating surface and counter alumina surface (Mishina and Hase, 2013; Niinomi et al., 1999). The amount of material transfer was observed to be maximum in Ti/25BAG composite coating and minimum in Ti/15BAG composite coating (Fig. 6.9 (d and b)), which is in good agreement with the obtained wear rates.
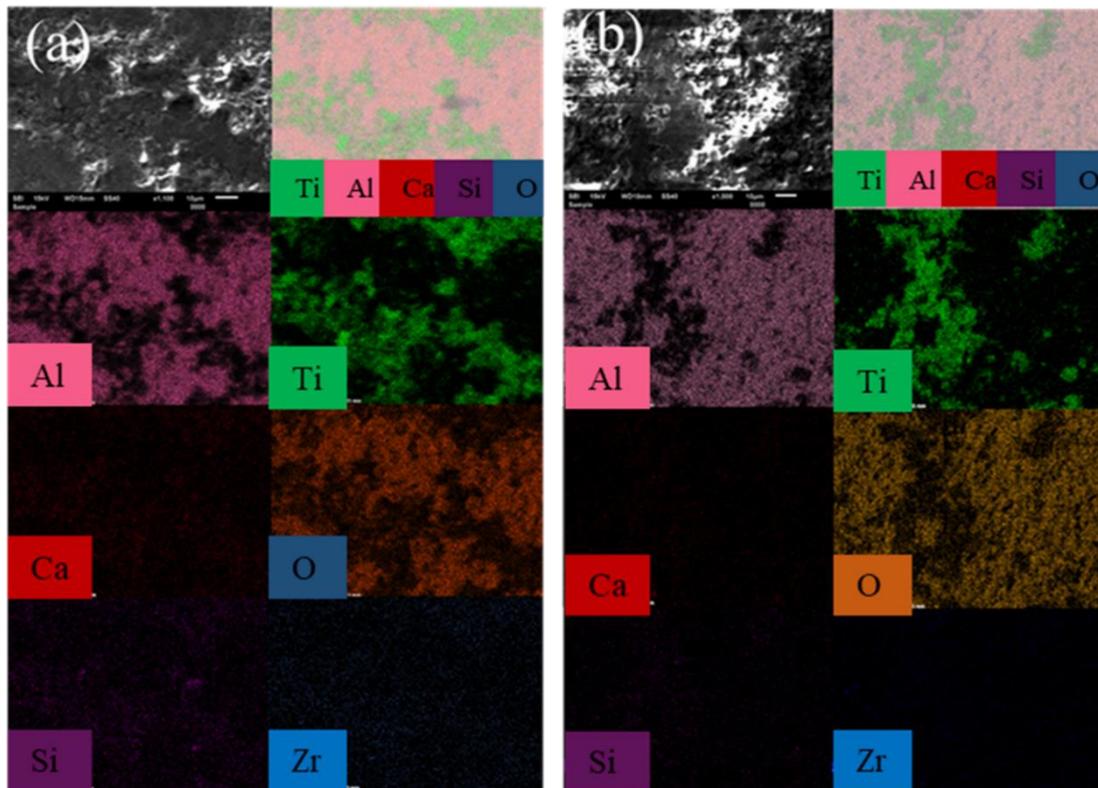
Figure 6.9. Surface SEM micrographs along with elemental mappings of counter alumina surface after pin-on-disk test in dry condition against cold spray SS316L steel (a) Ti/10BAG coating (b) Ti/15BAG coating
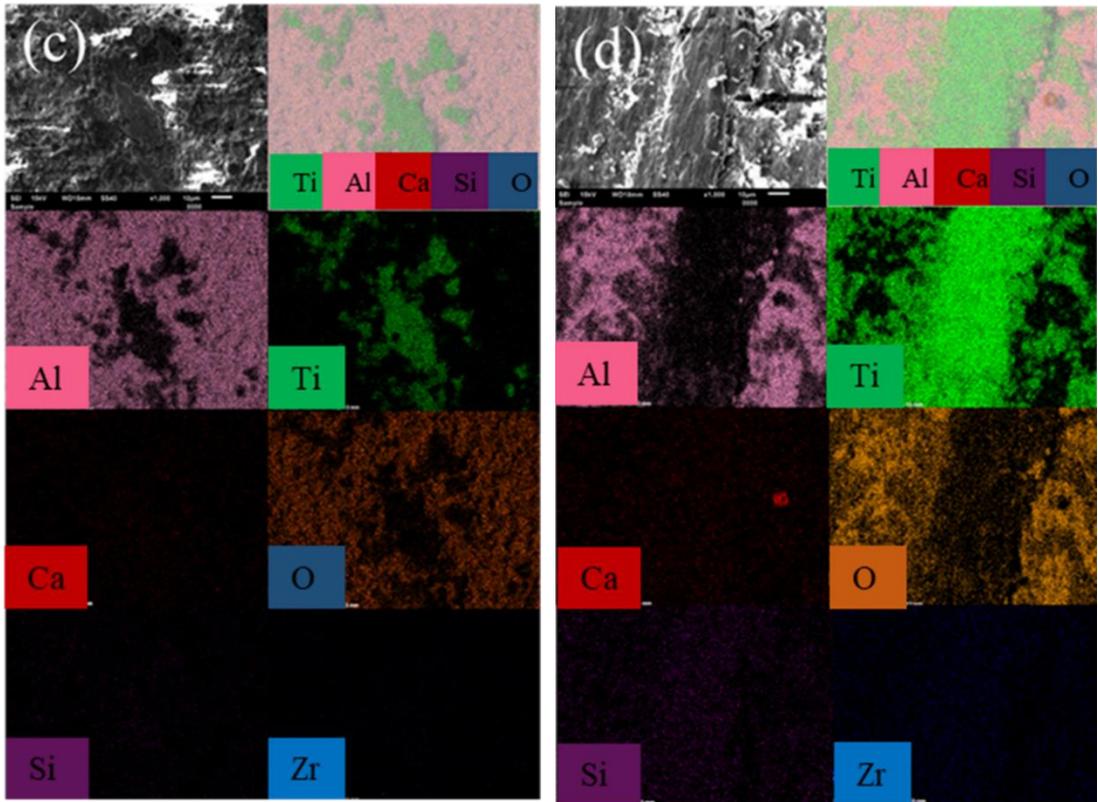
Figure 6.10. Surface SEM micrographs along with elemental mappings of counter alumina surface after pin-on-disk test in dry condition against cold spray SS316L steel (c) Ti/20BAG (d) Ti/25BAG
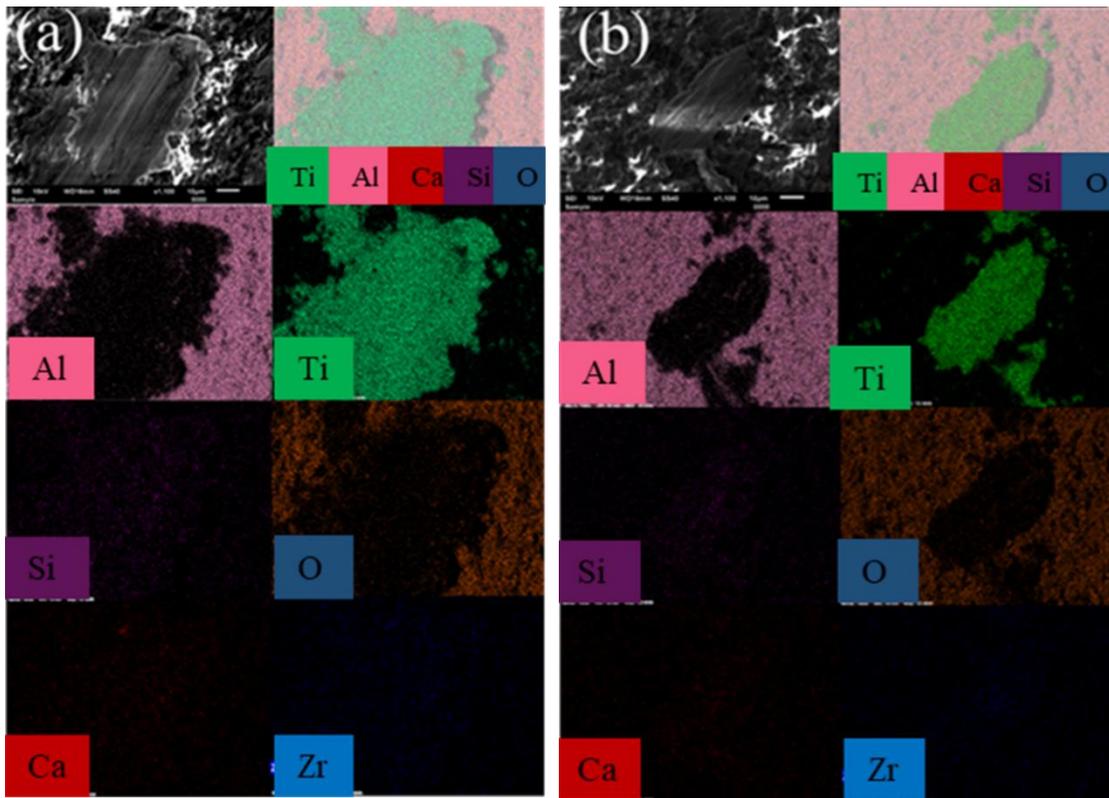
Figure 6.11. Surface SEM micrographs along with elemental mappings of counter alumina surface after pin-on-disk test in Hank's solution against cold spray SS316L steel (a) Ti/10BAG coating (b) Ti/15BAG coating
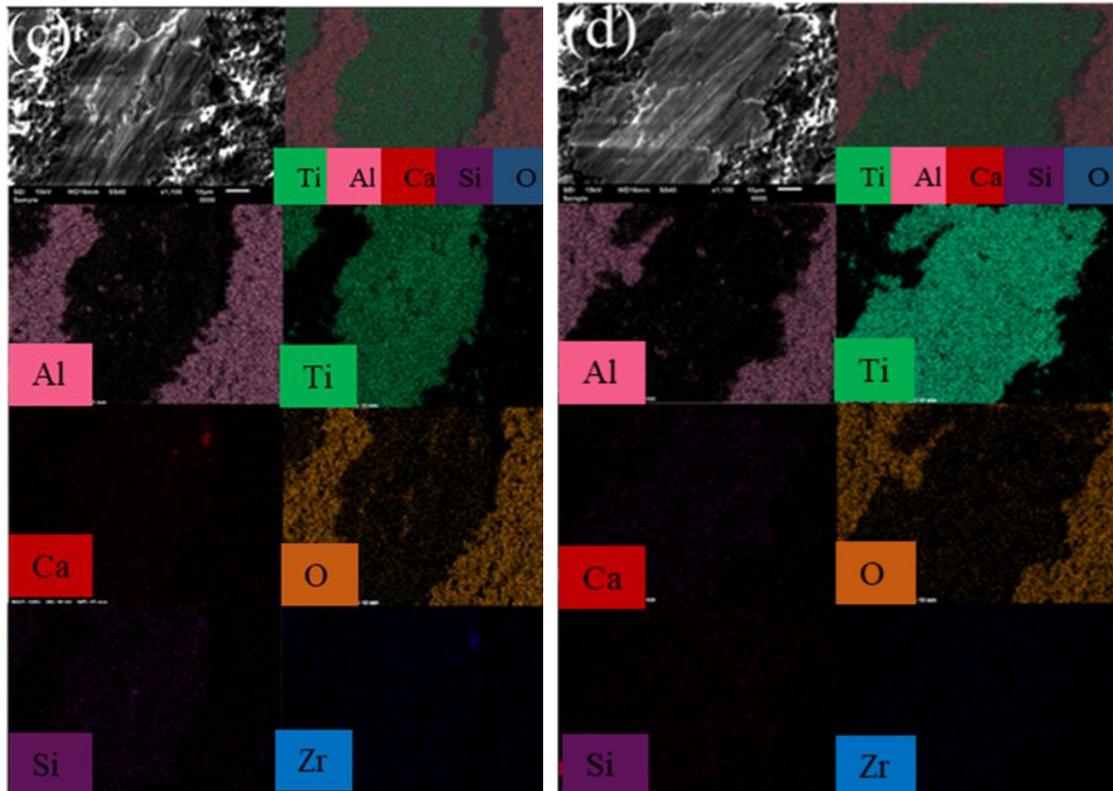
Figure 6.12. Surface SEM micrographs along with elemental mappings of counter alumina surface after pin-on-disk test in Hank's solution against cold spray SS316L steel (c) Ti/20BAG coating (d) Ti/25BAG coating

6.2.2 Laser-Treated Coatings

6.2.2.1 Friction

The average values of CoF before and after laser treatment for the cold-sprayed Ti/BAG composite coatings under a simulated body fluid environment (Hank's solution) are displayed in Fig. 6.13. It can be observed that the laser treatment of cold-sprayed Ti/BAG composite coatings led to a substantial reduction in average CoF. The average CoF dropped approximately 50%, 27%, 62%, and 55% for Ti/10BAG, Ti/15BAG, Ti/20BAG, and Ti/25BAG coatings, respectively. This drop in average CoF can be explained by the improvement in the microhardness of the Ti/BAG coatings due to laser treatment. The microhardness of the cold-sprayed Ti/BAG coatings in the top layers improved several times after laser treatment, as discussed in Chapter 4. The harder asperities are believed to show lesser plastic deformation, which leads to a smaller real area of contact, lesser asperity junctions, and easy relative motion. Hence, low CoF was

observed in all the cases. Mokhtar (Mokhtar, 1982) discussed the effect of hardness on the frictional behavior of materials. He experimentally proved that hard surfaces (after heat treatment) usually show more resistance to adhesion (lesser weld junctions or asperity junctions) and provide low friction. It was because of their high surface energy and lesser internal residual stresses.
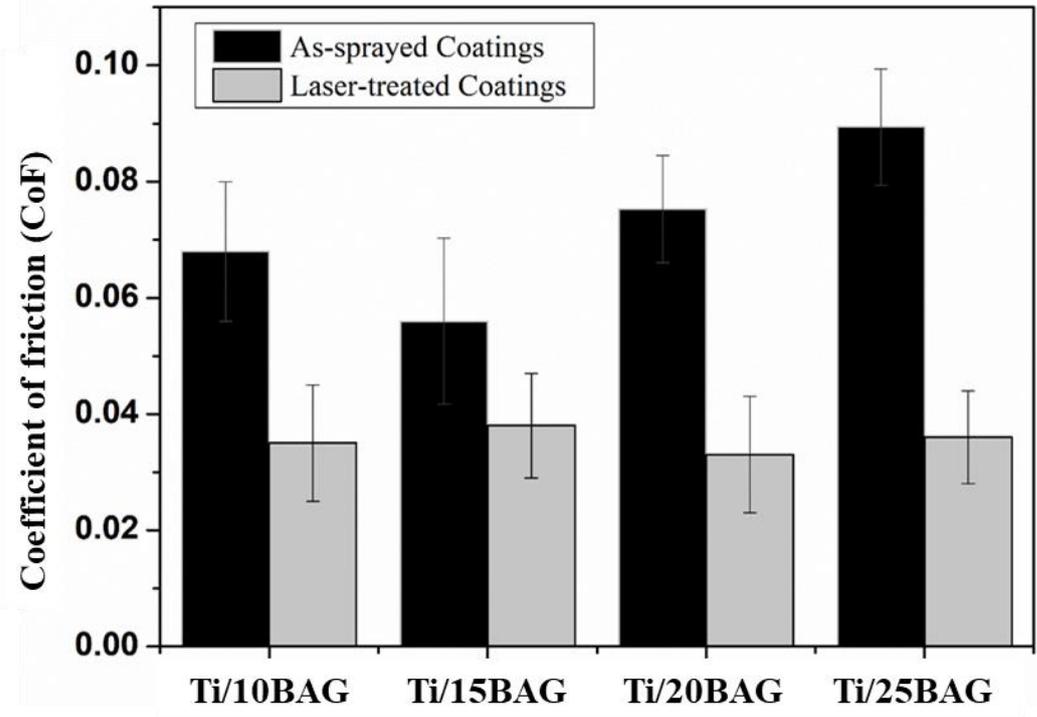
Figure 6.13: Comparative coefficient of friction results of as-sprayed and laser-treated cold spray Ti/BAG coated SS316L steel against alumina disk

6.2.2.2 Wear

The average values of wear rate before and after laser treatment for the cold-sprayed Ti/BAG coatings under the simulated body fluid environment are shown in Fig. 6.14. The calculated values of average wear rate for Ti/10BAG-L, Ti/15BAG-L, Ti/20BAG-L, and Ti/25BAG-L coatings were 24×10^{-5} mm^3/N-m, 14×10^{-6} mm^3/N-m, 66×10^{-6} mm^3/N-m, and 161×10^{-6} mm^3/N-m, respectively. Ti/15BAG-L was found to the best to offer wear resistance to the substrate steel among all the investigated coatings under the simulated body fluid environment in terms of wear. On the other hand, the maximum wear rate was observed for Ti/25BAG-L composite coating among laser-treated coatings.

144

The wear rate trend of the laser-treated coatings under the simulated body fluid environment was observed to follow the microhardness trend. Moreover, the laser laser-treatment reduced the wear rate of the as-sprayed coatings by 83%, 84%, 80%, and 73% for Ti/10BAG, Ti/15BAG, Ti/20BAG, and Ti/25BAG compositions, respectively. This could be attributed to the relatively denser and uniform microstructure of the laser-processed coatings in comparison with that of the as-sprayed coatings (Chapter 4). It has already been reported that the porosity of the coatings was reduced significantly after laser-treatment. Moreover, the microhardness was also improved significantly after laser treatment, which according to Archard's wear equation (Equation 6.1) makes the surfaces more wear resistance. It is well known that the harder surfaces show relatively lesser plastic deformation and a smaller real contact area. Thus, the tribosystem will have lesser asperity weld junctions and subsequently low wear rate (Archard, 1953; Mokhtar, 1982).
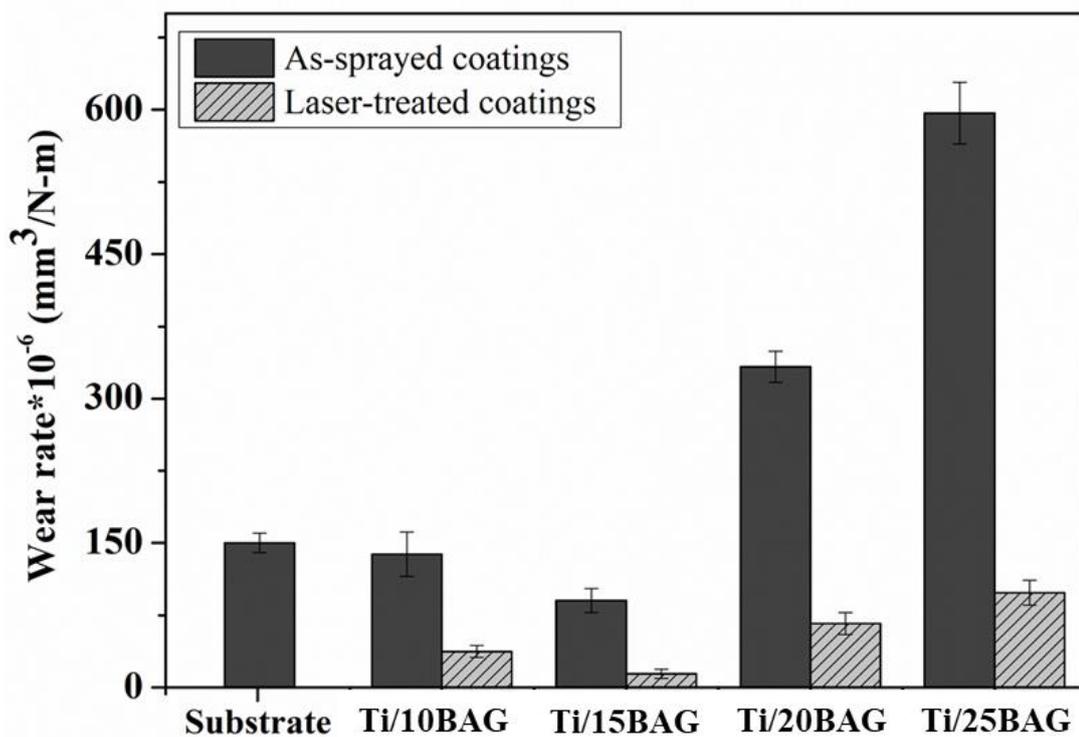
Figure 6.14: Comparative wear rate results of as-sprayed and laser-treated cold spray Ti/BAG coated SS316L steel against alumina disk

6.2.2.3 Wear Mechanism

The post-wear analysis was performed to understand the wear mechanism for as-sprayed and laser-treated coatings against alumina after PoD tests under the simulated body fluid

environment. SEM/EDS micrographs of the worn as-sprayed and laser-treated coating are shown in Fig. 6.15. It is visible from SEM micrographs that as-sprayed coatings underwent severe micro-cutting action relative to laser-treated coatings. Worn-out particles (wear debris) were observed in both the cases on the surfaces of the coating, however, the quantity of wear debris in laser-treated coatings was lesser compared to that in the as-sprayed coatings. Fragmentation and size reduction of the coating materials (in terms of wear debris) were evident from Fig. 6.15. The formed wear debris might have promoted the micro-cutting action between the coating and counterface during PoD tests. Also, the delamination of splats from the coating surfaces has been witnessed in both the cases, refer to Fig. 6.15. In laser-treated coatings, delamination of the ceramic (unmelted BAG) particles was spotted, which could be because of the fracture of BAG during sliding, whereas the Ti particles bonded well to each other and underwent micro-cutting/ploughing action. However, the delamination of matrix and ceramic splats has been found in the as-sprayed coatings. Poor bonding between the splats could be the reason for this behavior. Micro-cracks were detected on the worn as-sprayed coatings surface, which were missing in the laser-treated coatings. Severe plastic deformation of splats in as-sprayed coatings might have led to the micro-cracks formation. However, the equiaxed grains formed due to laser treatment limit the plastic deformation of the splats, and subsequently, no micro-cracks were seen. The above-discussed features are the typical signatures of three-body abrasive wear. It is worth noting that all the mentioned abrasive features are relatively more dominant in as-sprayed coatings.

High magnification SEM/EDS micrographs of alumina disc (counterface) after PoD tests against laser-treated coatings in simulated body fluid are shown in Fig. 6.16. The coating material was detected over the counterface for the as-sprayed as well as laser-treated coatings. The shearing of lubricant due to sliding action leads to the rise of temperature between the contacting surfaces, which are prone to the development of weld junctions (Lisowski and Stolarski, 1981). The bond strength of these formed junctions might have exceeded the shear strength of the coating material and led to material transfer from the coatings to the counterface. The other possible reason can be the accumulation and deformation of wear debris onto the counter-surface. The above observations indicate that adhesive wear also contributed to the wear of laser-treated coatings. However, as-sprayed coatings underwent relatively severe adhesive wear, as

shown in Fig. 6.9 and 6.10. Hence, relatively higher wear rate was observed in as-sprayed coatings.
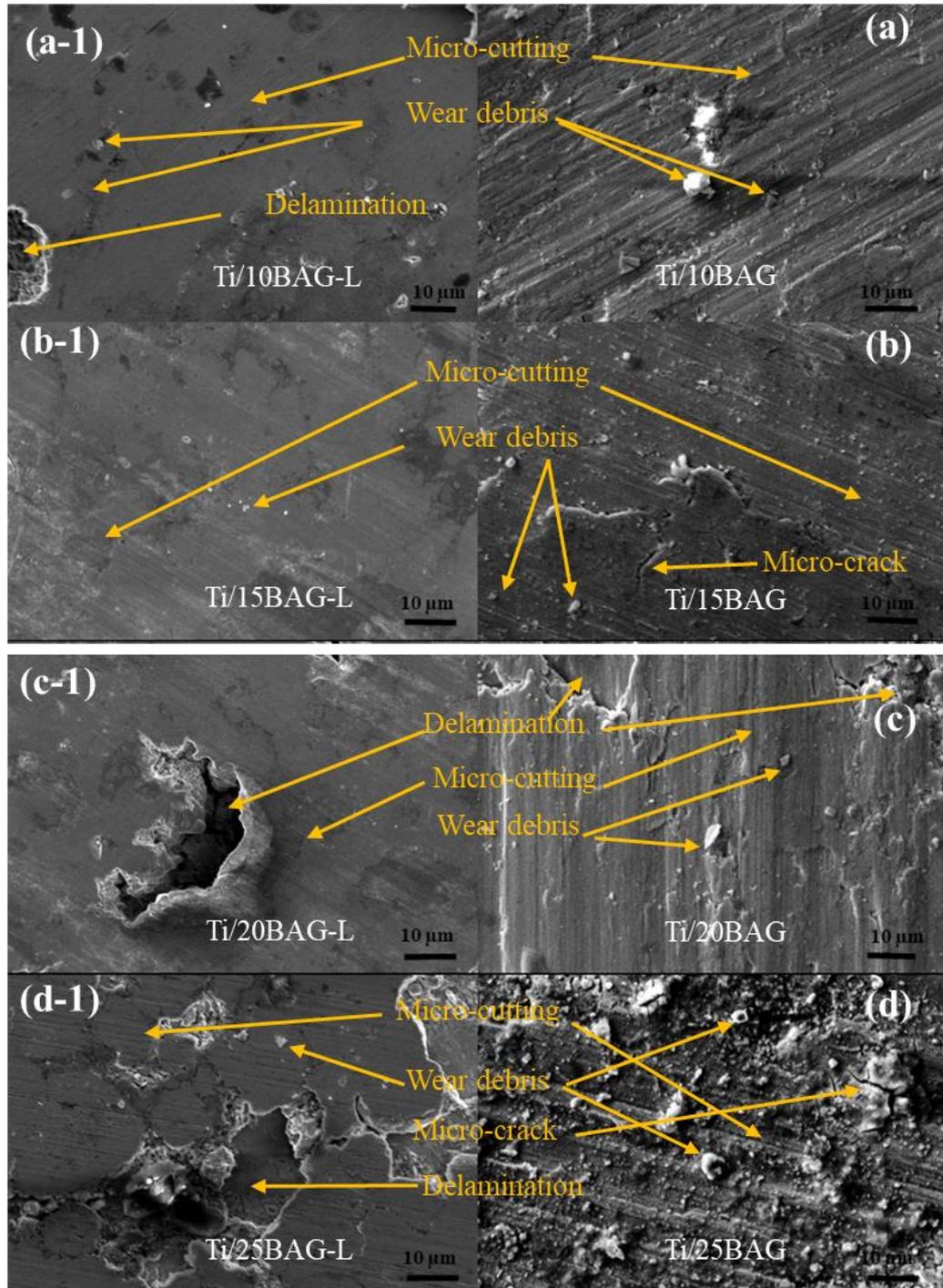
Figure 6.15: Surface SEM micrographs of coated SS316L steel surfaces subjected to wear test in Hank's solution (a) Ti/10BAG coating, (b) Ti/15BAG coating, (c) Ti/20BAG coating, (d) Ti/25BAG coating, and laser-treated (a-1) Ti/10BAG-L coating, (b-1) Ti/15BAG-L coating, (c-1) Ti/20BAG-L coating, and (d-1) Ti/25BAG-L coating
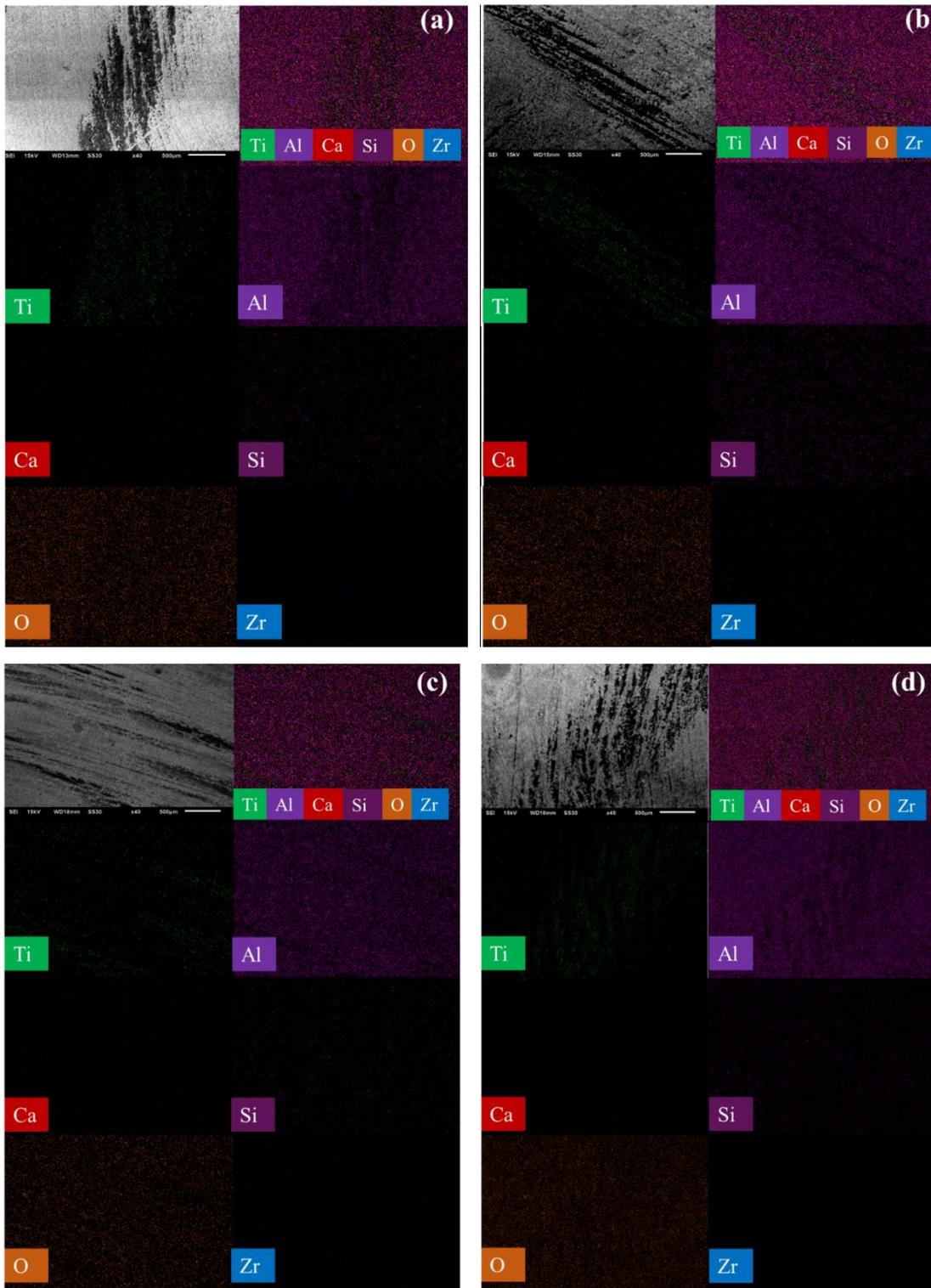
Figure 6.16: Surface SEM micrographs along with elemental mappings of counter alumina surface after pin-on-disk test in Hank's solution against cold spray laser-treated SS316L steel (a) Ti/10BAG-L coating, (b) Ti/15BAG-L coating, (c) Ti/20BAG-L coating, and (d) Ti/25BAG-L coating.

6.3 Comparative Discussion

A comparison of the wear data for the investigated materials indicates that the Ti/20TiO$_2$ coatings successfully reduced the wear of SS316L steel among all the investigated Ti/TiO$_2$ coatings. The average wear rate value calculated for the substrate and Ti/20TiO$_2$ coatings were 23.5×10^{-5} mm^3/N-m and 7.5×10^{-5} mm^3/N-m, respectively. The superior microhardness of Ti/20TiO$_2$ has been ascribed as the reason for its better wear resistance. The results obtained for Ti/BAG coatings suggest that Ti/15BAG composite coating performed best among all the investigated Ti/BAG coatings in terms of wear resistance. As-sprayed Ti/15BAG composite coating and substrate were shown an average value of wear rate 7×10^{-5} mm^3/N-m and 23×10^{-5} mm^3/N-m, respectively. The best wear resistance of Ti/15BAG coating is attributed to its best microhardness among the investigated Ti/BAG coatings. The above-mentioned results indicate that both (Ti/20TiO$_2$ and Ti/15BAG) coatings successfully reduced the wear of SS316L steel. Cold-sprayed Ti/15BAG coated steel has shown relatively better wear resistance than cold-sprayed Ti/TiO$_2$ steel. Moreover, it was observed that BAG showed more influence on wear behavior than TiO$_2$.

CONCLUSIONS

In the current work, some Titanium-based coatings have been developed on SS316L biomedical steel by cold spray. Subsequently, potential of the coatings has been investigated to improve the electrochemical corrosion and wear resistance of the steel for bio-implant applications. Microstructural, mechanical, electrochemical, and tribological analysis were characterized for both the substrate, as well as, the coatings. The coated and bare SS316L steel were also analyzed for corrosion and wear under the simulated body fluid environment. Salient conclusions from this work are enumerated in the following sections.

7.1 Development and Characterization of Coatings

- Mirror-polished SS316L surfaces were found to be most favorable to achieve the best adhesion of the cold-sprayed Ti-based coatings.

- Three different compositions of Ti/TiO$_2$ (Ti/20TiO$_2$, Ti/40TiO$_2$, and Ti/60TiO$_2$) were successfully deposited on SS316L steel using high pressure cold spray process. All of the coatings were well intact with the respective substrates.

- Retention of the TiO$_2$ phase was confirmed from the XRD and EDS analysis. Cold-sprayed Ti/20TiO$_2$ composite coating exhibited a higher microhardness in comparison with the substrate and cold-sprayed pure titanium coating.

- Likewise, four distinct compositions of Ti/BAG (Ti/10BAG, Ti/15BAG, Ti/20BAG, and Ti/25BAG) were prepared and successfully deposited on MP SS316L steel substrate using high-pressure cold spray facility. All Ti/BAG coatings adhered well with their respective substrates. A maximum thickness of 247 µm was achieved for Ti/10BAG coating, whereas, a minimum of 153 µm for Ti/25BAG composite coating. This could be due to the increase in BAG-BAG particle interaction. It is well known that the ceramic particles do not bond to one another and influence the deposition of metallic particles as well during cold spraying (Wang et al., 2010). Hence, a drop in coating thickness was expected for the same number of passes with the increase in BAG content.

- The retention of the BAG phase was confirmed in the coating by XRD and EDS analysis, which is a desirable characteristic for high quality coatings.

- Porosity and surface roughness continued to increase with the BAG content in feedstock. The lack of metallurgical bond formation due to the increase in the interaction of ceramic-metallic particles was ascribed as the reason for this observation.

- The average microhardness was observed to increase up to 15% of BAG content and followed a declining trend. Cold-sprayed Ti/15BAG composite coating showed the best average microhardness (176 ± 4 HV$_{0.5}$) among the investigated samples. It can be attributed to the fact that beyond 15% BAG the process is dominated by the interaction of BAG particles, which do not bond with one another and leads to decrease in bond strength and subsequently microhardness of the coatings.

- All the cold-sprayed Ti/BAG coatings was biocompatible and exhibited excellent cell viability. The cell viability of the developed coatings was observed to increase with BAG content.

- Laser treatment of the cold-sprayed Ti/BAG coatings led to the formation of equiaxed grains at the top layers and columnar grains in the middle layers of the coatings without leaving any adverse heating effect on to the substrate.

- Laser heating led to a minor phase change in the matrix (titanium), however, BAG phase remained unaffected.

- Porosity and surface roughness dropped significantly after laser treatment, which is desirable attribute to improve the bonding and subsequently average microhardness of the Ti/BAG composite coatings.

- The average microhardness of the coatings in the top layers increased several times after the laser treatment of Ti/BAG composite coatings. Recrystallization led to the formation of equiaxed grains at the top, which is believed to be the reason for the high hardness. Ti/15BAG coating exhibited the best microhardness after laser treatment among the investigated coatings.

7.2 Electrochemical Corrosion Behavior of Coated and Uncoated SS316L Steel

- All of the cold-sprayed Ti/TiO$_2$ coatings were found to be successful in reducing the electrochemical corrosion of SS316L steel, with Ti/20TiO$_2$ coating as the best composition.

- The corrosion resistance was found to drop with an increase in TiO$_2$ into the feedstock. Higher coating thickness, lower porosity, and maximum retention of TiO$_2$ into the coatings were ascribed to the reason for the excellent corrosion resistance of Ti/20TiO$_2$ coatings in simulated body fluid environment.

- The cold-sprayed Ti/BAG coatings was found to be successful in reducing the corrosion losses of SS316L steel in the simulated body fluid environment. The corrosion resistance was observed to improve with the increase in BAG content. Ti/25BAG coating was shown to have the best corrosion resistance among all the investigated cases under the simulated body fluid environment.

- A better retention of BAG and the simultaneous formation of passive oxides such as TiO$_2$, CaO, SiO$_2$, and ZrO$_2$ have been recognized as the reason for the superior performance.

- The developed cold-sprayed Ti/BAG coatings outperformed the cold-sprayed Ti/HA coatings in terms of corrosion performance under the simulated body fluid environment (Zhou and Mohanty, 2012). This indicates the potential of BAG to replace HA for bio-implant applications.

- Laser treatment of cold-sprayed coatings was found to be useful to enhance the corrosion resistance in the simulated body fluid environment, which could be attributed to reduction in their porosity and surface roughness.

7.3 Sliding Wear Behavior of Coated and Uncoated SS316L Steel

- Cold-sprayed Ti/20TiO$_2$ coating was successful to protect SS316L steel against sliding wear, whereas Ti/40TiO$_2$ and Ti/60TiO$_2$ coatings failed to protect the substrate, superior microhardness and better retention of TiO$_2$ are believed to be the reasons for the better wear resistance of Ti/20TiO$_2$ coatings.

- Three-body abrasion and adhesion wear were recognized as the main wear mechanisms for the coatings. Signatures of micro-cutting, pitting, delamination, and material transfer were also observed over the worn-out coating surfaces.

- All of the cold-sprayed Ti/BAG coatings were successful to enhance the wear resistance of SS316L steel in dry and simulated body fluid environments.

- Among these compositions, Ti/15BAG coating was witnessed as the best performing candidate, which may be due to its best microhardness and scratch resistance.

- In general, the coatings have been observed to undergo higher wear rates in the dry environment than in the simulated body fluid environment against sliding. The lubrication film into the sliding contact was believed to flush out the wear debris from the contact and further reduced the wear.

- Adhesive wear and three-body abrasive wear were recognized as the wear mechanisms under both dry and simulated body fluid environments for the Ti/BAG coatings. Adhesive wear was dominant in the simulated body fluid environment, and abrasion was severe in the dry environment due to sliding action.

- Signatures of material transfer, micro-cracks, micro-cutting, delamination, and wear debris were also observed over the worn-out coating surfaces.

- Cold-sprayed Ti/BAG coatings performed better than the as-sprayed Ti and Ti/HA (Buciumeanu et al., 2017; Kumar et al., 2013) coatings under the simulated body fluid environment, it could be attributed to the superior microhardness of the cold-sprayed Ti/BAG coatings.

- Laser-treatment was also successful to enhance the wear resistance of the coatings, with a maximum effectiveness for the Ti/15BAG compositions.

- In general, higher hardness and better bonding between the splats of laser-treated coatings resulted in their better wear performance than the as-sprayed coatings. The best performance of Ti/15BAG coating could be attributed to its best microhardness among the investigated coatings.

- For the laser-treated coatings, wear signatures such as micro-cutting, delamination, and wear debris were observed. The material transfer was also observed onto the counterfaces. However, these signatures were less severe in their comparison with that of the as-sprayed counterparts.

7.4 Recommendations

Based upon the overall results and discussion in the light of reported literature, cold-sprayed Ti/BAG coating can be recommended to induce desirable corrosion and wear resistance in the given bio-implant SS316L steel. This coating is found to have a suitable combination of microstructural and mechanical characteristics. Moreover, for the tribological joints of the bio-implant, laser-treated cold-sprayed Ti/15BAG coating can be recommended as a better choice since porosity is not a major concern at these joints.

7.5 Contribution to Knowledge

This thesis will help researchers to address the following issues:

The available literature does not provide clear guidelines on how to prepare the substrate surface for cold spraying of composite powders on hard surfaces. The present study identify the substrate preparation approach for cold spraying of Ti-based composite powders on SS316L substrates. The study concludes that a mirror-polished surface provides the best adhesion compared to as-received and ground-polished substrates.

The available literature on thermal-sprayed BAG coatings is limited, which is mainly focused on using plasma spray process. However, there is a significant decrease in crystallinity during the plasma spraying process. The drop in crystallinity negatively affects the bioactivity of the coating. To address this issue, this study proposes a new method of deposition to protect the crystallinity and bioactivity of BAG, that is, cold spray.

It is common practice to perform post-processing on thermal-sprayed coatings to enhance their performance. For bio-implant applications, plasma-sprayed coatings are treated chemically to restore their bioactivity, however this process does not improve mechanical, electrochemical, or tribological properties. In contrast, this study proposes using laser treatment on cold-sprayed coatings, which significantly enhances their mechanical, electrochemical, and tribological properties.

SUGGESTIONS FOR FUTURE WORK

1. It was concluded from the SEM analysis and scratch test results that the cold-sprayed single-pass cold-sprayed Ti/20TiO$_2$ coating on the mirror-polished substrate provided the best adhesion. It is suggested that adhesion and cohesion strength of thicker (multi-pass) coatings should be analyzed using pull-off adhesion tests following ASTM C-633 standards for further understanding of bonding mechanisms.

2. A comparative study of adhesion in cold spraying of Ti-based powders on grit blasted (with different grit sizes), and polished SS316L substrate surface should be performed.

3. All the investigated coatings have been found to be successful in maintaining continuous surface contact with their respective substrates. The measurement of the adhesion strength of the cold-sprayed coatings should be done, and attempts to improve the same will lead to further enhancing the effectiveness of the given coatings.

4. The composition of Ti/TiO$_2$ coatings should be further optimized to obtain the optimum combined performance against corrosion and wear for bio-implant applications.

5. Investigations to further improve the performance of the Ti/BAG composite coatings should be undertaken by optimizing the cold-spray process parameters. Since, the combinations of the coating materials used in this study were novel without any reported process data, the coatings were deposited after several attempts by varying the cold spraying process parameters, and a systematic parametric optimization study could not be undertaken due to cost and material constraints. It is pertinent to mention that even without optimizing the process parameters, the investigated coatings reduced the corrosion and wear of SS316L steel under a simulated body fluid environment.

6. Although the Ti/BAG coatings were tested for biocompatibility, the bioactivity and antimicrobial testing of the coatings should be evaluated.

7. The coatings should be deposited on the actual bio-implants and tested in a bio-simulator followed by in-vivo studies.

8. Multi-particle simulations can be done in order to optimize the process parameters for cold spraying.

9. A numerical model for depositing the composite powders in cold spraying can be developed to predict the critical velocity of the feedstock.

10. Cost-effectiveness analysis of the developed materials should also be done to explore their commercial use.

ELSEVIER LICENSE
TERMS AND CONDITIONS

Oct 28, 2022

This Agreement between IIT Ropar -- Avneesh Kumar ("You") and Elsevier ("Elsevier") consists of your license details and the terms and conditions provided by Elsevier and Copyright Clearance Center.

License Number	5417480850802
License date	Oct 28, 2022
Licensed Content Publisher	Elsevier
Licensed Content Publication	Progress in Surface Science
Licensed Content Title	Multifunctional cold spray coatings for biological and biomedical applications: A review
Licensed Content Author	Tzu-Ying Liao,Arne Biesiekierski,Christopher C. Berndt,Peter C. King,Elena P. Ivanova,Helmut Thissen,Peter Kingshott
Licensed Content Date	May 1, 2022
Licensed Content Volume	97
Licensed Content Issue	2
Licensed Content Pages	1
Start Page	100654
End Page	0
Type of Use	reuse in a thesis/dissertation

Portion	figures/tables/illustrations
Number of figures/tables/illustrations	1
Format	both print and electronic
Are you the author of this Elsevier article?	No
Will you be translating?	No
Title	Investigation on Ti-based cold-sprayed coatings for bio-implant applications
Institution name	IIT Ropar
Expected presentation date	Oct 2022
Order reference number	1
Portions	Figure 1
Requestor Location	IIT Ropar SW-126 Satluj Hostel, IIT Ropar Near Bir Rupnagar, Punjab 140001 India Attn: IIT Ropar
Publisher Tax ID	GB 494 6272 12
Total	0.00 USD

Terms and Conditions

ELSEVIER LICENSE
TERMS AND CONDITIONS

Feb 27, 2023

This Agreement between IIT Ropar -- Avneesh Kumar ("You") and Elsevier ("Elsevier") consists of your license details and the terms and conditions provided by Elsevier and Copyright Clearance Center.

License Number	5497411065563
License date	Feb 27, 2023
Licensed Content Publisher	Elsevier
Licensed Content Publication	Acta Materialia
Licensed Content Title	Bonding mechanism in cold gas spraying
Licensed Content Author	Hamid Assadi,Frank Gärtner,Thorsten Stoltenhoff,Heinrich Kreye
Licensed Content Date	Sep 3, 2003
Licensed Content Volume	51
Licensed Content Issue	15
Licensed Content Pages	16
Start Page	4379
End Page	4394
Type of Use	reuse in a thesis/dissertation
Portion	figures/tables/illustrations

Number of figures/tables/illustrations	1
Format	both print and electronic
Are you the author of this Elsevier article?	No
Will you be translating?	No
Title	Investigation on Ti-based cold-sprayed coatings for bio-implant applications
Institution name	IIT Ropar
Expected presentation date	Oct 2023
Portions	Fig. 11
Requestor Location	IIT Ropar SW-126 Satluj Hostel, IIT Ropar Near Bir Rupnagar, Punjab 140001 India Attn: IIT Ropar
Publisher Tax ID	GB 494 6272 12
Total	0.00 USD

Terms and Conditions

License Number	5497420446488
License date	Feb 27, 2023
Licensed Content Publisher	Elsevier
Licensed Content Publication	Acta Materialia
Licensed Content Title	Adiabatic shear instability is not necessary for adhesion in cold spray
Licensed Content Author	Mostafa Hassani-Gangaraj,David Veysset,Victor K. Champagne,Keith A. Nelson,Christopher A. Schuh
Licensed Content Date	Oct 1, 2018
Licensed Content Volume	158
Licensed Content Issue	n/a
Licensed Content Pages	10
Start Page	430
End Page	439
Type of Use	reuse in a thesis/dissertation
Portion	figures/tables/illustrations

Number of figures/tables/illustrations	3
Format	both print and electronic
Are you the author of this Elsevier article?	No
Will you be translating?	No
Title	Experimental Investigation on cold-sprayed Ti-based coatings for bio-implant applications
Institution name	IIT Ropar
Expected presentation date	Oct 2023
Portions	Figure 2, 3, and 4
Requestor Location	IIT Ropar SW-126 Satluj Hostel, IIT Ropar Near Bir Rupnagar, Punjab 140001 India Attn: IIT Ropar
Publisher Tax ID	GB 494 6272 12
Total	0.00 USD

Terms and Conditions

PDF Card No and Related Details for All the XRDs

Materials	Peaks position (2θ, degree)	Reference code
As-sprayed coatings		
Ti	35.01, 38.31, 40.08, 52.9, 62.8, 70.54, 76.11, 77.27	00-005-0682
BAG	17.05, 27.65, 29.90, 31.14, 31.45	00-047-1854
Laser-treated coatings		
Ti	35.10, 38.39, 40.19, 52.97, 62.96, 70.66, 76.24	01-089-3073
TiO	42.34	01-073-1581
BAG	19.41, 20.70	01-083-0464
As-sprayed corroded coatings		
Ti	35.15, 38.45, 40.21, 63.00	00-044-1294
TiO_2	39.82, 41.33, 54.41, 69.5	01-089-4920
BAG	54.81	01-083-0365
CaO	37.40, 40.95	00-037-1497
TiO	42.29	01-073-1581
SiO_2	19.01, 29.34	01-075-4410
ZrO_2	29.32	01-081-1315
Laser-treated corroded coatings		
Ti	35.31, 38.63, 40.37, 54.98, 62.90	01-089-5003
TiO_2	25.45, 37.72, 41.32, 48.14, 54.98, 69.57,	01-070-6826
BAG	27.65, 57.97	01-054-0710
CaO	37.32	00-017-0912
SiO_2	21.83	01-085-0460
ZrO_2	41.26	03-065-2328

REFERENCES

Abramoff, B., Caldera, F.E., 2020. Osteoarthritis: Pathology, Diagnosis, and Treatment Options. Medical Clinics of North America 104, 293–311. https://doi.org/10.1016/j.mcna.2019.10.007

Adaan-Nyiak, M.A., Tiamiyu, A.A., 2022. Recent advances on bonding mechanism in cold spray process: A review of single-particle impact methods. Journal of Materials Research. https://doi.org/10.1557/s43578-022-00764-2

Affatato, S., Brando, D., 2013. Introduction to wear phenomena of orthopaedic implants. Wear of Orthopaedic Implants and Artificial Joints 3–26. https://doi.org/10.1533/9780857096128.1.3

Aksakal, B., Yildirim, Ö.S., Gul, H., 2004. Metallurgical failure analysis of various implant materials used in orthopedic applications. Journal of Failure Analysis and Prevention 4, 17–23. https://doi.org/10.1361/15477020419794

Al-Mangour, B., Mongrain, R., Irissou, E., Yue, S., 2013. Improving the strength and corrosion resistance of 316L stainless steel for biomedical applications using cold spray. Surface and Coatings Technology 216, 297–307. https://doi.org/10.1016/j.surfcoat.2012.11.061

Alkhimov, A.P., Kosarev, V.F., Alkhimov, O.A., Lavrushin, V. V, 2000. Device for Gas-Dynamic Spraying of Powder Materials. RU2190695, year of priority (issued).

Alkhimov, A.P., Kosarev, V.F., Papyrin, A.N., 1990. A method of" cold" gas-dynamic deposition. SPhD 35, 1047.

Altman, R.D., 2003. Status of hyaluronan supplementation therapy in osteoarthritis. Current rheumatology reports 5, 7–14. https://doi.org/10.1007/s11926-003-0077-6

Amel-Farzad, H., Peivandi, M.T., Yusof-Sani, S.M.R., 2007. In-body corrosion fatigue failure of a stainless steel orthopaedic implant with a rare collection of different damage mechanisms. Engineering Failure Analysis 14, 1205–1217. https://doi.org/10.1016/j.engfailanal.2006.11.037

Amin, S., Panchal, H., Professor, A., 2016. A Review on Thermal Spray Coating Processes. International Journal of Current Trends in Engineering & Research Scientific Journal Impact Factor 2, 556–563.

An Open-Porous Titanium Coating for Advanced Osseointegration Poster No . 2216 • 55th Annual Meeting of the Orthopaedic Research Society, 2000. 17, 2216.

Anawati, Tanigawa, H., Asoh, H., Ohno, T., Kubota, M., Ono, S., 2013. Electrochemical corrosion and bioactivity of titanium-hydroxyapatite composites prepared by spark plasma sintering. Corrosion Science 70, 212–220. https://doi.org/10.1016/j.corsci.2013.01.032

Archard, J., 1953. Contact and rubbing of flat surfaces. Journal of applied physics 24, 981–988.

Arciola, C.R., Campoccia, D., Speziale, P., Montanaro, L., Costerton, J.W., 2012. Biofilm formation in Staphylococcus implant infections. A review of molecular mechanisms and implications for biofilm-resistant materials. Biomaterials 33, 5967–5982. https://doi.org/10.1016/J.BIOMATERIALS.2012.05.031

Askari, E., Flores, P., Dabirrahmani, D., Appleyard, R., 2015. A review of squeaking in ceramic total hip prostheses. Tribology International 93, 239–256. https://doi.org/10.1016/j.triboint.2015.09.019

Asri, R.I.M., Harun, W.S.W., Samykano, M., Lah, N.A.C., Ghani, S.A.C., Tarlochan, F., Raza, M.R., 2017. Corrosion and surface modification on biocompatible metals: A review. Materials Science and Engineering: C 77, 1261–1274. https://doi.org/https://doi.org/10.1016/j.msec.2017.04.102

Assadi, H., Gärtner, F., Klassen, T., Kreye, H., 2019. Comment on 'Adiabatic shear instability is not necessary for adhesion in cold spray.' Scripta Materialia 162, 512–514. https://doi.org/10.1016/j.scriptamat.2018.10.036

Assadi, H., Gärtner, F., Stoltenhoff, T., Kreye, H., 2003. Bonding mechanism in cold gas spraying. Acta Materialia 51, 4379–4394. https://doi.org/10.1016/S1359-6454(03)00274-X

Assadi, H., Kreye, H., Gärtner, F., Klassen, T., 2016. Cold spraying – A materials perspective. Acta Materialia 116, 382–407.

https://doi.org/10.1016/j.actamat.2016.06.034

Assadi, H., Schmidt, T., Richter, H., Kliemann, J.O., Binder, K., Gärtner, F., Klassen, T., Kreye, H., 2011. On parameter selection in cold spraying. Journal of Thermal Spray Technology 20, 1161–1176. https://doi.org/10.1007/s11666-011-9662-9

Bakhsheshi-Rad, H.R., Hamzah, E., Ismail, A.F., Aziz, M., Hadisi, Z., Kashefian, M., Najafinezhad, A., 2017a. Novel nanostructured baghdadite-vancomycin scaffolds: In-vitro drug release, antibacterial activity and biocompatibility. Materials Letters 209, 369–372. https://doi.org/10.1016/j.matlet.2017.08.027

Bakhsheshi-Rad, H.R., Hamzah, E., Ismail, A.F., Aziz, M., Kasiri-Asgarani, M., Akbari, E., Jabbarzare, S., Najafinezhad, A., Hadisi, Z., 2017b. Synthesis of a novel nanostructured zinc oxide/baghdadite coating on Mg alloy for biomedical application: In-vitro degradation behavior and antibacterial activities. Ceramics International 43, 14842–14850. https://doi.org/10.1016/j.ceramint.2017.07.233

Balani, K., Laha, T., Agarwal, A., Karthikeyan, J., Munroe, N., 2005. Effect of carrier gases on microstructural and electrochemical behavior of cold-sprayed 1100 aluminum coating. Surface and Coatings Technology 195, 272–279. https://doi.org/10.1016/j.surfcoat.2004.06.028

Barros, J., Dias, A., Rodrigues, M.A., Pina-Vaz, C., Lopes, M.A., Pina-Vaz, I., 2015. Antibiofilm and Antimicrobial Activity of Polyethylenimine: An Interesting Compound for Endodontic Treatment. The journal of contemporary dental practice 16, 427–432. https://doi.org/10.5005/jp-journals-10024-1701

Berndt, C.C., Hasan, F., Tietz, U., Schmitz, K.-P., 2014. A Review of Hydroxyapatite Coatings Manufactured by Thermal Spray. https://doi.org/10.1007/978-3-642-53980-0_9

Bezwada, H.P., Cho, R.H., Nazarian, D.G., 2012. Hemiarthroplasty of the hip. Operative Techniques in Adult Reconstruction Surgery 39–54.

Bhattiprolu, V.S., Johnson, K.W., Ozdemir, O.C., Crawford, G.A., 2018. Influence of feedstock powder and cold spray processing parameters on microstructure and mechanical properties of Ti-6Al-4V cold spray depositions. Surface and Coatings Technology 335, 1–12. https://doi.org/10.1016/j.surfcoat.2017.12.014

Bowman, S., Awad, M.E., Hamrick, M.W., Hunter, M., Fulzele, S., 2018. Recent advances in hyaluronic acid based therapy for osteoarthritis. Clinical and Translational Medicine 7. https://doi.org/10.1186/s40169-017-0180-3

Buciumeanu, M., Araujo, A., Carvalho, O., Miranda, G., Souza, J.C.M., Silva, F.S., Henriques, B., 2017. Study of the tribocorrosion behaviour of Ti6Al4V – HA biocomposites. Tribology International 107, 77–84. https://doi.org/10.1016/j.triboint.2016.11.029

Bulina, N. V., Rybin, D.K., Makarova, S. V., Dudina, D. V., Batraev, I.S., Utkin, A. V., Prosanov, I.Y., Khvostov, M. V., Ulianitsky, V.Y., 2021. Detonation spraying of hydroxyapatite on a titanium alloy implant. Materials 14, 1–11. https://doi.org/10.3390/ma14174852

Burris, D.L., Moore, A.C., 2017. Cartilage and Joint Lubrication: New Insights Into the Role of Hydrodynamics. Biotribology 12, 8–14. https://doi.org/10.1016/j.biotri.2017.09.001

Buzdygar, T. V, Kashirin, A.I., Kljuev, O.F., Portnjagin, J.I., 1993. Method for Manufacture of Layer Products of Bulky Discontinuous Configuration. RU2038399, year of priority (issued).

Catauro, M., Barrino, F., Bononi, M., Colombini, E., Giovanardi, R., Veronesi, P., Tranquillo, E., 2019. Coating of titanium substrates with ZrO_2 and ZrO_2-SiO_2 composites by sol-gel synthesis for biomedical applications: Structural characterization, mechanical and corrosive behavior. Coatings 9. https://doi.org/10.3390/coatings9030200

Catauro, M., Dell'Era, A., Ciprioti, S.V., 2016. Synthesis, structural, spectroscopic and thermoanalytical study of sol–gel derived SiO_2–CaO–P_2O_5 gel and ceramic materials. Thermochimica Acta 625, 20–27.

Champagne, V.K., 2007. The cold spray materials deposition process, The cold spray materials deposition process. https://doi.org/10.1533/9781845693787

Chan, C.W., Smith, G.C., Lee, S., 2018. A preliminary study to enhance the tribological performance of CoCrMo alloy by fibre laser remelting for articular joint implant applications. Lubricants 6. https://doi.org/10.3390/lubricants6010024

Chavan, N.M., Vinod Kumar, M., Sudharshan Phani, P., Pant, P., Sundararajan, G., 2019. Influence of Nozzle Throat Cross Section on Microstructure and Properties of Cold Sprayed Coatings. Journal of Thermal Spray Technology 28, 1718–1729. https://doi.org/10.1007/s11666-019-00913-w

Chen, Q., Thouas, G.A., 2015. Metallic implant biomaterials. Materials Science and Engineering R: Reports 87, 1–57. https://doi.org/10.1016/j.mser.2014.10.001

Choy, K.L., 2003. Chemical vapour deposition of coatings. Progress in Materials Science 48, 57–170. https://doi.org/10.1016/S0079-6425(01)00009-3

Chun, D.M., Choi, J.O., Lee, C.S., Ahn, S.H., 2012. Effect of stand-off distance for cold gas spraying of fine ceramic particles (<5μm) under low vacuum and room temperature using nano-particle deposition system (NPDS). Surface and Coatings Technology 206, 2125–2132. https://doi.org/10.1016/j.surfcoat.2011.09.043

Ciulli, E., Di Puccio, F., Mattei, L., Battaglia, S., Affatato, S., 2014. Tribological Behaviour of Ceramic Hip Replacements. 13th International Ceramics Congress - Part C 89, 10–20. https://doi.org/10.4028/www.scientific.net/ast.89.10

Cooper, R.A., McAllister, C.M., Borden, L.S., Bauer, T.W., 1992. Polyethylene debris-induced osteolysis and loosening in uncemented total hip arthroplasty. A cause of late failure. The Journal of Arthroplasty 7, 285–290. https://doi.org/10.1016/0883-5403(92)90050-Z

Corona-Gomez, J., Shiri, S., Mohammadtaheri, M., Yang, Q., 2017. Adhesion enhancement of DLC on CoCrMo alloy by diamond and nitrogen incorporation for wear resistant applications. Surface and Coatings Technology 332, 120–127. https://doi.org/10.1016/j.surfcoat.2017.10.050

Costa, B.C., Tokuhara, C.K., Rocha, L.A., Oliveira, R.C., Lisboa-Filho, P.N., Costa Pessoa, J., 2019. Vanadium ionic species from degradation of Ti-6Al-4V metallic implants: In vitro cytotoxicity and speciation evaluation. Materials Science and Engineering C. https://doi.org/10.1016/j.msec.2018.11.090

Crockett, R., 2009. Boundary lubrication in natural articular joints. Tribology Letters 35, 77–84. https://doi.org/10.1007/s11249-009-9430-x

D'Antonio, J.A., Capello, W.N., Manley, M.T., Geesink, R., 2001. Hydroxyapatite

femoral stems for total hip arthroplasty 10- to 13-year followup. Clinical Orthopaedics and Related Research 101–111. https://doi.org/10.1097/00003086-200112000-00012

Daniel, M., 2012. Role of Surface-Active Lipids in Cartilage Lubrication, 1st ed, Advances in Planar Lipid Bilayers and Liposomes. Elsevier Inc. https://doi.org/10.1016/B978-0-12-396533-2.00007-0

Dargusch, M.S., Balasubramani, N., Yang, N., Johnston, S., Ali, Y., Wang, G., Venezuela, J., Carluccio, J., Lau, C., Allavena, R., Liang, D., Mardon, K., Ye, Q., 2022. In vivo performance of a rare earth free Mg–Zn–Ca alloy manufactured using twin roll casting for potential applications in the cranial and maxillofacial fixation devices. Bioactive Materials. https://doi.org/10.1016/j.bioactmat.2021.10.026

Darr, J.A., Guo, Z.X., Raman, V., Bououdina, M., Rehman, I.U., 2004. Metal organic chemical vapour deposition (MOCVD) of bone mineral like carbonated hydroxyapatite coatings. Chemical Communications 4, 696–697. https://doi.org/10.1039/b312855p

Davis, J.R., 2004. Thermal Spray Technology Edited by, Technology.

Delgado-Noguera, M.F., Forero Delgadillo, J.M., Franco, A.A., Concha, J., Vazquez, J.C., Calvache, J.A., 2016. Corticosteroids for septic arthritis in children. Cochrane Database of Systematic Reviews 2016. https://doi.org/10.1002/14651858.CD012125

Dikici, B., Topuz, M., 2018. Production of Annealed Cold-Sprayed 316L Stainless Steel Coatings for Biomedical Applications and Their in-vitro Corrosion Response. Protection of Metals and Physical Chemistry of Surfaces 54, 333–339. https://doi.org/10.1134/S2070205118020168

Durdu, S., 2019. Characterization, bioactivity and antibacterial properties of copper-based TiO2 bioceramic coatings fabricated on titanium. Coatings 9. https://doi.org/10.3390/coatings9010001

Dykhuizen, R.C., Smith, M.F., Gilmore, D.L., Neiser, R.A., Jiang, X., Sampath, S., 1999. Impact of high velocity cold spray particles. Journal of Thermal Spray Technology 8, 559–564. https://doi.org/10.1361/105996399770350250

Eliaz, N., 2019. Corrosion of metallic biomaterials: A review. Materials 12. https://doi.org/10.3390/ma12030407

Erli HJ, Rüger M, Ragoβ C, Jahnen-Dechent W, Hollander DA, Paar OO, von Walter M. The effect of surface modification of a porous TiO2/perlite composite on the ingrowth of bone tissue in vivo. Biomaterials. 2006;27:1270-1276

Erratum: Global, regional, and national incidence, prevalence, and years lived with disability for 354 diseases and injuries for 195 countries and territories, 1990–2017: a systematic analysis for the Global Burden of Disease Study 2017 (The Lancet (2018), 2019. . The Lancet. https://doi.org/10.1016/S0140-6736(19)31047-5

Feng, S.Q., Ma, B., Wang, X.L., Liu, G., Zheng, Z.Y., Pan, L.P., 2014. Effects of standoff distance and particle size on quality of NiCoCrALY coating by cold spraying. Applied Mechanics and Materials 513–517, 265–268. https://doi.org/10.4028/www.scientific.net/AMM.513-517.265

Fleck, C., 2008. Corrosion, fatigue and corrosion fatigue behaviour of metal implant materials, especially titanium alloys. 17th European Conference on Fracture 2008: Multilevel Approach to Fracture of Materials, Components and Structures.

Gåård, A., Hallbäck, N., Krakhmalev, P., Bergström, J., 2010. Temperature effects on adhesive wear in dry sliding contacts. Wear 268, 968–975. https://doi.org/10.1016/j.wear.2009.12.007

Gao, L., Dowson, D., Hewson, R.W., 2017. Predictive wear modeling of the articulating metal-on-metal hip replacements. Journal of Biomedical Materials Research - Part B Applied Biomaterials 105, 497–506. https://doi.org/10.1002/jbm.b.33568

Gao, P.H., Li, Y.G., Li, C.J., Yang, G.J., Li, C.X., 2008. Influence of powder porous structure on the deposition behavior of cold-sprayed WC-12Co coatings. Journal of Thermal Spray Technology 17, 742–749. https://doi.org/10.1007/s11666-008-9258-1

Garbacz, H., Pisarek, M., Kurzydłowski, K.J., 2007. Corrosion resistance of nanostructured titanium. Biomolecular Engineering 24, 559–563. https://doi.org/10.1016/j.bioeng.2007.08.007

Gardon, M., Concustell, A., Dosta, S., Cinca, N., Cano, I.G., Guilemany, J.M., 2014. Improved bonding strength of bioactive cermet Cold Gas Spray coatings. Materials Science and Engineering C 45, 117–121. https://doi.org/10.1016/j.msec.2014.08.053

Geetha, M., Singh, A.K., Asokamani, R., Gogia, A.K., 2009. Ti based biomaterials, the ultimate choice for orthopaedic implants - A review. Progress in Materials Science 54, 397–425. https://doi.org/10.1016/j.pmatsci.2008.06.004

Ghosh, S., Abanteriba, S., Wong, S., Houshyar, S., 2018. Selective laser melted titanium alloys for hip implant applications: Surface modification with new method of polymer grafting. Journal of the Mechanical Behavior of Biomedical Materials 87, 312–324. https://doi.org/10.1016/j.jmbbm.2018.07.031

Gluck, T., 1890. Die Invaginationsmethode der Osteo- und Arthroplastik. Berliner Klinische Wochenschrift 44, 752–757.

Godwin, G., Jaisingh, S.J., Priyan, M.S., Singh, S.C.E., 2021. Wear and corrosion behaviour of Ti-based coating on biomedical implants. Surface Engineering 37, 32–41. https://doi.org/10.1080/02670844.2020.1730058

Goldbaum, D., Shockley, J.M., Chromik, R.R., Rezaeian, A., Yue, S., Legoux, J.G., Irissou, E., 2012. The effect of deposition conditions on adhesion strength of Ti and Ti6Al4V cold spray splats. Journal of Thermal Spray Technology 21, 288–303. https://doi.org/10.1007/s11666-011-9720-3

Grujicic, M., Saylor, J.R., Beasley, D.E., DeRosset, W.S., Helfritch, D., 2003. Computational analysis of the interfacial bonding between feed-powder particles and the substrate in the cold-gas dynamic-spray process. Applied Surface Science 219, 211–227. https://doi.org/10.1016/S0169-4332(03)00643-3

Grujicic, M., Zhao, C.L., DeRosset, W.S., Helfritch, D., 2004. Adiabatic shear instability based mechanism for particles/substrate bonding in the cold-gas dynamic-spray process. Materials and Design 25, 681–688. https://doi.org/10.1016/j.matdes.2004.03.008

Guetta, S., Berger, M.H., Borit, F., Guipont, V., Jeandin, M., Boustie, M., Ichikawa, Y., Sakaguchi, K., Ogawa, K., 2009. Influence of particle velocity on adhesion of cold-

sprayed splats. Journal of Thermal Spray Technology 18, 331–342. https://doi.org/10.1007/s11666-009-9327-0

Habib, K.A., Cano, D.L., Heredia, J.A., Vicente-Escuder, Á., 2020. Effect of debris size on the tribological performance of thermally sprayed coatings. Tribology International 143, 106025. https://doi.org/10.1016/j.triboint.2019.106025

Hajipour, H., Abdollah-zadeh, A., Assadi, H., Taheri-Nassaj, E., Jahed, H., 2018. Effect of Feedstock Powder Morphology on Cold-Sprayed Titanium Dioxide Coatings. Journal of Thermal Spray Technology 27, 1542–1550. https://doi.org/10.1007/s11666-018-0782-3

Harris, W.H., 2001. Wear and periprosthetic osteolysis the problem. Clinical Orthopaedics and Related Research 393, 66–70. https://doi.org/10.1097/00003086-200112000-00007

Hassani-Gangaraj, M., Veysset, D., Champagne, V.K., Nelson, K.A., Schuh, C.A., 2019. Response to Comment on "Adiabatic shear instability is not necessary for adhesion in cold spray." Scripta Materialia 162, 515–519. https://doi.org/10.1016/j.scriptamat.2018.12.015

Hassani-Gangaraj, M., Veysset, D., Champagne, V.K., Nelson, K.A., Schuh, C.A., 2018. Adiabatic shear instability is not necessary for adhesion in cold spray. Acta Materialia 158, 430–439. https://doi.org/10.1016/j.actamat.2018.07.065

Hembus, J., Lux, L., Jackszis, M., Bader, R., Zietz, C., 2018. Wear analysis of cross-linked polyethylene inserts articulating with alumina and ion-treated cobalt-chromium femoral heads under third-body conditions. Wear 402–403, 216–223. https://doi.org/10.1016/j.wear.2018.02.017

Henao, J., Cruz-bautista, M., Hincapie-Bedoya, J., Ortega-Bautista, B., Corona-Castuera, J., Giraldo-Betancur, A.L., Espinosa-Arbelaez, D.G., Alvarado-Orozco, J.M., Clavijo-Mejía, G.A., Trapaga-Martínez, L.G., Poblano-Salas, C.A., 2018. HVOF Hydroxyapatite/Titania-Graded Coatings: Microstructural, Mechanical, and In Vitro Characterization. Journal of Thermal Spray Technology 27, 1302–1321. https://doi.org/10.1007/s11666-018-0811-2

Hernigou, P., 2014. Smith-Petersen and early development of hip arthroplasty.

International Orthopaedics 38, 193–198. https://doi.org/10.1007/s00264-013-2080-5

Herrera, A., Mateo, J., Gil-Albarova, J., Lobo-Escolar, A., Ibarz, E., Gabarre, S., Más, Y., Gracia, L., 2015. Cementless hydroxyapatite coated hip prostheses. BioMed Research International 2015. https://doi.org/10.1155/2015/386461

HONG, W., CAI, W., WANG, S., TOMOVIC, M.M., 2018. Mechanical wear debris feature, detection, and diagnosis: A review. Chinese Journal of Aeronautics. https://doi.org/10.1016/j.cja.2017.11.016

Huang, J., Ma, W., Xie, Y., Fukanum, H., Zhang, K., Wang, G., Huang, R., 2019. Influence of cold gas spray processing conditions on the properties of 316L stainless steel coatings. Surface Engineering 35, 784–791. https://doi.org/10.1080/02670844.2019.1584967

Hussain, T., Mccartney, D.G., Shipway, P.H., Zhang, D., n.d. Bonding Mechanisms in Cold Spraying: The Contributions of Metallurgical and Mechanical Components. https://doi.org/10.1007/s11666-009-9298-1

Hussain, T., McCartney, D.G., Shipway, P.H., Zhang, D., 2009. Bonding mechanisms in cold spraying: The contributions of metallurgical and mechanical components. Journal of Thermal Spray Technology 18, 364–379. https://doi.org/10.1007/s11666-009-9298-1

Irissou, E., Legoux, J.G., Arsenault, B., Moreau, C., 2007. Investigation of Al-Al 2O 3 cold spray coating formation and properties. Journal of Thermal Spray Technology 16, 661–668. https://doi.org/10.1007/s11666-007-9086-8

ISO, S., n.d. 8044: 2000. Corrosion of metals and alloys-Basic terms and definitions.

Jacobs, J.J., Gilbert, J.L., Urban, R.M., 1998. Corrosion of metal orthopaedic implants. Journal of Bone and Joint Surgery - Series A 80, 268–282. https://doi.org/10.2106/00004623-199802000-00015

Jafari, S., Harandi, S.E., Singh Raman, R.K., 2015. A review of stress-corrosion cracking and corrosion fatigue of magnesium alloys for biodegradable implant applications. Jom 67, 1143–1153. https://doi.org/10.1007/s11837-015-1366-z

Jeremy Gilbert, B.L., Christine Buckley, Phd.A., Joshua Jacobs Kim C Bertin Mdl,

Ms.J., Zernich Mdi Chicago, M.R., 1994. Intergranular Corrosion-Fatigue Failure of Cobalt-Alloy Femoral Stems. The journal of Bone and Joint Surgery 110–115.

Jing, Z., Dejun, K., 2018. Effect of laser remelting on friction-wear behaviors of cold sprayed Al coatings in 3.5% NaCl solution. Materials 11. https://doi.org/10.3390/ma11020283

Jodoin, B., 2002. Cold spray nozzle mach number limitation. Journal of Thermal Spray Technology 11, 496–507. https://doi.org/10.1361/105996302770348628

Jodoin, B., Ajdelsztajn, L., Sansoucy, E., Zúñiga, A., Richer, P., Lavernia, E.J., 2006. Effect of particle size, morphology, and hardness on cold gas dynamic sprayed aluminum alloy coatings. Surface and Coatings Technology 201, 3422–3429. https://doi.org/10.1016/j.surfcoat.2006.07.232

Karthikeyan, J., 2004. Cold spray technology: International status and USA efforts. ASBindustries Inc 1–14.

Kashirin, A.I., Kljuev, O.F., Shkodkin, A. V, 2003. Method and Apparatus for Gas-Dynamic Deposition of Coating. RU2237746, year of priority (issued).

Khanna, R., Matsushita, T., Kokubo, T., Takadama, H., 2014. Formation of alumina layer on Ti alloy for artificial hip joint. Key Engineering Materials 614, 200–205. https://doi.org/10.4028/www.scientific.net/KEM.614.200

Kheder, W., Al Kawas, S., Khalaf, K., Samsudin, A.R., 2021. Impact of tribocorrosion and titanium particles release on dental implant complications — A narrative review. Japanese Dental Science Review. https://doi.org/10.1016/j.jdsr.2021.09.001

Khun, N.W., Tan, A.W.Y., Bi, K.J.W., Liu, E., 2016. Effects of working gas on wear and corrosion resistances of cold sprayed Ti-6Al-4V coatings. Surface and Coatings Technology 302, 1–12. https://doi.org/10.1016/j.surfcoat.2016.05.052

Kim, H.S., Kim, W.J., 2014. Annealing effects on the corrosion resistance of ultrafine-grained pure titanium. Corrosion Science 89, 331–337. https://doi.org/10.1016/j.corsci.2014.08.017

Kim, H.W., Koh, Y.H., Li, L.H., Lee, S., Kim, H.E., 2004. Hydroxyapatite coating on titanium substrate with titania buffer layer processed by sol-gel method.

Biomaterials 25, 2533–2538. https://doi.org/10.1016/j.biomaterials.2003.09.041

Klinkov, S. V., Kosarev, V.F., Zaikovskii, V.N., 2011. Influence of flow swirling and exit shape of barrel nozzle on cold spraying. Journal of Thermal Spray Technology 20, 837–844. https://doi.org/10.1007/s11666-011-9621-5

Ko, K.H., Choi, J.O., Lee, H., 2016. The interfacial restructuring to amorphous: A new adhesion mechanism of cold-sprayed coatings. Materials Letters 175, 13–15. https://doi.org/10.1016/j.matlet.2016.03.132

Koivuluoto, H., Näkki, J., Vuoristo, P., 2009. Corrosion properties of cold-sprayed tantalum coatings. Journal of thermal spray technology 18, 75–82.

Kokubo, T., Takadama, H., 2006. How useful is SBF in predicting in vivo bone bioactivity? Biomaterials 27, 2907–2915. https://doi.org/10.1016/j.biomaterials.2006.01.017

Koricherla, M. V., Torgerson, T.B., Alidokht, S.A., Munagala, V.N.V., Chromik, R.R., Scharf, T.W., 2021. High temperature sliding wear behavior and mechanisms of cold-sprayed Ti and Ti–TiC composite coatings. Wear. https://doi.org/10.1016/j.wear.2021.203746

Krishna, N.G., George, R.P., Philip, J., 2020. Anomalous enhancement of corrosion resistance and antibacterial property of commercially pure Titanium (CP-Ti) with nanoscale rutile titania film. Corrosion Science 172, 108678. https://doi.org/10.1016/j.corsci.2020.108678

Krupa, D., Baszkiewicz, J., Rajchel, B., Barcz, A., Sobczak, J.W., Biliński, A., 2005. Effect of sodium-ion implantation on the corrosion resistance and bioactivity of titanium. Vacuum 78, 161–166. https://doi.org/10.1016/j.vacuum.2005.01.020

Kubiak, K.J., Wilson, M.C.T., Mathia, T.G., Carval, P., 2011. Wettability versus roughness of engineering surfaces. Wear 271, 523–528. https://doi.org/10.1016/j.wear.2010.03.029

Kumar, A., Biswas, K., Basu, B., 2013. Fretting wear behaviour of hydroxyapatite-titanium composites in simulated body fluid, supplemented with 5 g l-1 bovine serum albumin. Journal of Physics D: Applied Physics 46. https://doi.org/10.1088/0022-3727/46/40/404004

Kumar, M., Singh, H., Singh, N., Joshi, R.S., 2015. Erosion-corrosion behavior of cold-spray nanostructured Ni-20Cr coatings in actual boiler environment. Wear 332–333, 1035–1043. https://doi.org/10.1016/j.wear.2015.01.043

Kumar, S., Bae, G., Lee, C., 2016. Influence of substrate roughness on bonding mechanism in cold spray. Surface and Coatings Technology 304, 592–605. https://doi.org/10.1016/j.surfcoat.2016.07.082

Kumar, S., Bae, G., Lee, C., 2009. Deposition characteristics of copper particles on roughened substrates through kinetic spraying. Applied Surface Science 255, 3472–3479. https://doi.org/10.1016/j.apsusc.2008.10.060

Kurtz, S.M., Lau, E., Ong, K., Zhao, K., Kelly, M., Bozic, K.J., 2009. Future young patient demand for primary and revision joint replacement: National projections from 2010 to 2030. Clinical Orthopaedics and Related Research 467, 2606–2612. https://doi.org/10.1007/s11999-009-0834-6

Le Guehennec, L., Lopez-Heredia, M.-A., Enkel, B., Weiss, P., Amouriq, Y., Layrolle, P., 2008. Osteoblastic cell behaviour on different titanium implant surfaces. Acta biomaterialia 4, 535–543.

Lee, H., Shin, H., Lee, S., Ko, K., 2008. Effect of gas pressure on Al coatings by cold gas dynamic spray. Materials Letters 62, 1579–1581. https://doi.org/10.1016/j.matlet.2007.09.026

Lee, J., Shin, S., Kim, H.J., Lee, C., 2007. Effect of gas temperature on critical velocity and deposition characteristics in kinetic spraying. Applied Surface Science. https://doi.org/10.1016/j.apsusc.2006.07.061

Levine, D.L., Staehle, R.W., 1977. Crevice corrosion in orthopedic implant metals. Journal of Biomedical Materials Research 11, 553–561. https://doi.org/10.1002/jbm.820110410

Li, C.J., Li, W.Y., 2003. Deposition characteristics of titanium coating in cold spraying. Surface and Coatings Technology 167, 278–283. https://doi.org/10.1016/S0257-8972(02)00919-2

Li, C.L., Wang, C.S., Narayana, P.L., Hong, J.K., Choi, S.W., Kim, J.H., Lee, S.W., Park, C.H., Yeom, J.T., Mei, Q., 2021. Formation of equiaxed grains in selective

laser melted pure titanium during annealing. Journal of Materials Research and Technology. https://doi.org/10.1016/j.jmrt.2021.01.008

Li, D., Chen, X., Gong, Y., Zhang, B., Liu, Y., Jin, P., Li, H., 2017a. Synthesis and Vacuum Cold Spray Deposition of Biofunctionalized Nanodiamond/Hydroxyapatite Nanocomposite for Biomedical Applications. Advanced Engineering Materials 19, 1–6. https://doi.org/10.1002/adem.201700363

Li, D., Gong, Y., Chen, X., Zhang, B., Zhang, H., Jin, P., Li, H., 2017b. Room-temperature deposition of hydroxyapatite/antibiotic composite coatings by vacuum cold spraying for antibacterial applications. Surface and Coatings Technology 330, 87–91. https://doi.org/10.1016/j.surfcoat.2017.09.085

Li, W., Cao, C., Yin, S., 2020. Solid-state cold spraying of Ti and its alloys: A literature review. Progress in Materials Science 110, 100633. https://doi.org/10.1016/j.pmatsci.2019.100633

Li, W.Y., Liao, H., Wang, H.T., Li, C.J., Zhang, G., Coddet, C., 2006. Optimal design of a convergent-barrel cold spray nozzle by numerical method. Applied Surface Science 253, 708–713. https://doi.org/10.1016/j.apsusc.2005.12.157

Li, Wen Ya, Zhang, C., Guo, X., Xu, J., Li, C.J., Liao, H., Coddet, C., Khor, K.A., 2007. Ti and Ti-6Al-4V coatings by cold spraying and microstructure modification by heat treatment. Advanced Engineering Materials 9, 418–423. https://doi.org/10.1002/adem.200700022

Li, W. Y., Zhang, C., Guo, X.P., Zhang, G., Liao, H.L., Coddet, C., 2007. Deposition characteristics of Al-12Si alloy coating fabricated by cold spraying with relatively large powder particles. Applied Surface Science 253, 7124–7130. https://doi.org/10.1016/j.apsusc.2007.02.142

Li, W.Y., Zhang, C., Guo, X.P., Zhang, G., Liao, H.L., Li, C.J., Coddet, C., 2008. Effect of standoff distance on coating deposition characteristics in cold spraying. Materials and Design 29, 297–304. https://doi.org/10.1016/j.matdes.2007.02.005

Li, Y., Zou, S., Wang, D., Feng, G., Bao, C., Hu, J., 2010. The effect of hydrofluoric acid treatment on titanium implant osseointegration in ovariectomized rats.

Biomaterials 31, 3266–3273. https://doi.org/10.1016/j.biomaterials.2010.01.028

Liao, T.Y., Biesiekierski, A., Berndt, C.C., King, P.C., Ivanova, E.P., Thissen, H., Kingshott, P., 2022. Multifunctional cold spray coatings for biological and biomedical applications: A review. Progress in Surface Science 97, 100654. https://doi.org/10.1016/j.progsurf.2022.100654

Lindberg F, Heinrichs J, Ericson F, Thomsen P, Engqvist H. Hydroxylapatite growth on single-crystal rutile substrates. Biomaterials. 2008;29:3317-3323

Lisowski, Z., Stolarski, T.A., 1981. A modified theory of adhesive wear in lubricated contacts. Wear 68, 333–345. https://doi.org/10.1016/0043-1648(81)90180-0

Liu, Y., Dang, Z., Wang, Y., Huang, J., Li, H., 2014. Hydroxyapatite/graphene-nanosheet composite coatings deposited by vacuum cold spraying for biomedical applications: Inherited nanostructures and enhanced properties. Carbon 67, 250–259. https://doi.org/10.1016/j.carbon.2013.09.088

Liu, Y., Zhu, D., Pierre, D., Gilbert, J.L., 2019. Fretting initiated crevice corrosion of 316LVM stainless steel in physiological phosphate buffered saline: Potential and cycles to initiation. Acta Biomaterialia 97, 565–577. https://doi.org/10.1016/j.actbio.2019.07.051

Lorig, K., Konkol, L., Gonzalez, V., 1987. Arthritis patient education: A review of the literature. Patient Education and Counseling 10, 207–252. https://doi.org/10.1016/0738-3991(87)90126-1

Luo, Y., Yang, T., Rao, X., Zhu, J., Li, M., 2018. Thermal oxidation of Zr-2.5Nb alloy and its biotribological properties. International Journal of Advanced Manufacturing Technology 96, 1539–1543. https://doi.org/10.1007/s00170-017-0607-4

Macconaill, M.A., 1961. Lubrication of Joints. The Lancet 278, 823–824. https://doi.org/10.1016/S0140-6736(61)91112-6

MacDonald, D., Fernández, R., Delloro, F., Jodoin, B., 2017. Cold Spraying of Armstrong Process Titanium Powder for Additive Manufacturing. Journal of Thermal Spray Technology 26, 598–609. https://doi.org/10.1007/s11666-016-0489-2

Majumdar, P., Singh, S.B., Chakraborty, M., 2008. Wear response of heat-treated Ti-13Zr-13Nb alloy in dry condition and simulated body fluid. Wear 264, 1015–1025. https://doi.org/10.1016/j.wear.2007.08.005

Manivasagam, G., Dhinasekaran, D., Rajamanickam, A., 2010. Biomedical Implants: Corrosion and its Prevention - A Review~!2009-12-22~!2010-01-20~!2010-05-25~! Recent Patents on Corrosion Science 2, 40–54. https://doi.org/10.2174/1877610801002010040

Marcucci Ribeiro, M.C., 2004. (12) Patent Application Publication (10) Pub . No .: US 2004 / 0092606A1. United States - Patent Application Publication 1, 2002–2005.

Marrocco, T., Hussain, T., McCartney, D.G., Shipway, P.H., 2011. Corrosion performance of laser posttreated cold sprayed titanium coatings. Journal of Thermal Spray Technology 20, 909–917. https://doi.org/10.1007/s11666-011-9637-x

Mathew, M.T., Srinivasa Pai, P., Pourzal, R., Fischer, A., Wimmer, M.A., 2009. Significance of tribocorrosion in biomedical applications: Overview and current status. Advances in Tribology 2009. https://doi.org/10.1155/2009/250986

Memtsoudis, S.G., Ma, Y., Chiu, Y.L., Walz, J.M., Voswinckel, R., Mazumdar, M., 2010. Perioperative mortality in patients with pulmonary hypertension undergoing major joint replacement. Anesthesia and Analgesia 111, 1110–1116. https://doi.org/10.1213/ANE.0b013e3181f43149

Merritt, K., Brown, S.A., 1995. Release of hexavalent chromium from corrosion of stainless steel and cobalt—chromium alloys. Journal of Biomedical Materials Research 29, 627–633. https://doi.org/10.1002/jbm.820290510

Mishina, H., Hase, A., 2013. Wear equation for adhesive wear established through elementary process of wear. Wear 308, 186–192. https://doi.org/10.1016/j.wear.2013.06.016

Mohammadi, S., Wictorin, L., Ericson, L.E., Thomsen, P., 1995. Cast titanium as implant material. Journal of Materials Science: Materials in Medicine 6, 435–444. https://doi.org/10.1007/BF00123367

Mohan, L., Durgalakshmi, D., Geetha, M., Sankara Narayanan, T.S.N., Asokamani, R., 2012. Electrophoretic deposition of nanocomposite (HAp + TiO 2) on titanium alloy for biomedical applications. Ceramics International. https://doi.org/10.1016/j.ceramint.2011.12.056

Mokhtar, M.O.A., 1982. The effect of hardness on the frictional behaviour of metals. Wear 78, 297–304. https://doi.org/10.1016/0043-1648(82)90240-X

Moridi, A., Hassani-Gangaraj, S.M., Guagliano, M., Dao, M., 2014. Cold spray coating: Review of material systems and future perspectives. Surface Engineering 30, 369–395. https://doi.org/10.1179/1743294414Y.0000000270

Morshed, S., Bozic, K.J., Ries, M.D., Malchau, H., Colford, J.M., 2007. Comparison of cemented and uncemented fixation in total hip replacement: A meta-analysis. Acta Orthopaedica 78, 315–326. https://doi.org/10.1080/17453670710013861

Munagala, V.N.V., Akinyi, V., Vo, P., Chromik, R.R., 2018. Influence of powder morphology and microstructure on the cold spray and mechanical properties of Ti6Al4V coatings. Journal of Thermal Spray Technology 27, 827–842.

Munagala, V.N.V., Bessette, S., Gauvin, R., Chromik, R.R., 2020. Sliding wear of cold sprayed Ti6Al4V coatings: Effect of porosity and normal load. Wear. https://doi.org/10.1016/j.wear.2020.203268

Nadaraia, L., Jalabadze, N., Khundadze, L., Rurua, L., Japaridze, M., Chedia, R., 2021. Effects of graphene on morphology, fracture toughness, and electrical conductivity of titanium dioxide. Diamond and Related Materials. https://doi.org/10.1016/j.diamond.2021.108319

Ndumia, J.N., Kang, M., Gbenontin, B.V., Lin, J., Nyambura, S.M., 2021. A review on the wear, corrosion and high-temperature resistant properties of wire arc-sprayed fe-based coatings. Nanomaterials 11. https://doi.org/10.3390/nano11102527

Neoh, K.G., Hu, X., Zheng, D., Kang, E.T., 2012. Balancing osteoblast functions and bacterial adhesion on functionalized titanium surfaces. Biomaterials 33, 2813–2822.

Niinomi, M., Kuroda, D., Fukunaga, K., Morinaga, M., Kato, Y., Yashiro, T., Suzuki, A., 1999. Corrosion wear fracture of new β type biomedical titanium alloys.

Materials Science and Engineering: A 263, 193–199.

Nikitin, P. V, Smolin, A.G., Melendo, M., 1999. The Device for Deposition of a Powder Coating. RU2222638, year of priority (issued).

Ning, X.J., Jang, J.H., Kim, H.J., 2007. The effects of powder properties on in-flight particle velocity and deposition process during low pressure cold spray process. Applied Surface Science 253, 7449–7455. https://doi.org/10.1016/j.apsusc.2007.03.031

Ogston, A.G., Stanier, J.E., 1953. The physiological function of hyaluronic acid in synovial fluid; viscous, elastic and lubricant properties. The Journal of Physiology 119, 244–252. https://doi.org/10.1113/jphysiol.1953.sp004842

Olakanmi, E.O., 2016. Optimization of the Quality Characteristics of Laser-Assisted Cold-Sprayed (LACS) Aluminum Coatings with Taguchi Design of Experiments (DOE). Materials and Manufacturing Processes 31, 1490–1499. https://doi.org/10.1080/10426914.2014.984306

Olmedo, D.G., Duffó, G., Cabrini, R.L., Guglielmotti, M.B., 2008. Local effect of titanium implant corrosion: an experimental study in rats. International Journal of Oral and Maxillofacial Surgery 37, 1032–1038. https://doi.org/10.1016/j.ijom.2008.05.013

Oren-Ziv, A., Hoppenstein, D., Shles, A., Uziel, Y., 2015. Sedation methods for intra-articular corticosteroid injections in Juvenile Idiopathic Arthritis: A review. Pediatric Rheumatology 13, 1–5. https://doi.org/10.1186/s12969-015-0021-0

Østergaard, M., Pedersen, S.J., Døhn, U.M., 2008. Imaging in rheumatoid arthritis - status and recent advances for magnetic resonance imaging, ultrasonography, computed tomography and conventional radiography. Best Practice and Research: Clinical Rheumatology 22, 1019–1044. https://doi.org/10.1016/j.berh.2008.09.014

Padhy, N., Mudali, U.K., Chawla, V., Chandra, R., Raj, B., 2011. Corrosion behaviour of single (Ti) and duplex (Ti-TiO2) coating on 304L stainless steel in nitric acid medium. Materials Chemistry and Physics. https://doi.org/10.1016/j.matchemphys.2011.08.016

Palodhi, L., Das, B., Singh, H., 2021. Effect of Particle Size and Morphology on Critical

Velocity and Deformation Behavior in Cold Spraying. Journal of Materials Engineering and Performance 30, 8276–8288. https://doi.org/10.1007/s11665-021-05997-6

Pan, J., Thierry, D., Leygraf, C., 1996. Electrochemical impedance spectroscopy study of the passive oxide film on titanium for implant application. Electrochimica Acta 41, 1143–1153. https://doi.org/10.1016/0013-4686(95)00465-3

Paper, W., 2016. Indian Orthopedic Devices Market A $ 2 . 4 Bn Opportunity Succeeding in the Evolving Landscape. Sathguru Management Consultants Private Limited 1–56.

Papyrin, A., Kosarev, V., Klinkov, S., Alkhimov, A., Fomin, V.M., 2006. Cold spray technology. Elsevier.

Pattison, J., Celotto, S., Khan, A., O'Neill, W., 2008. Standoff distance and bow shock phenomena in the Cold Spray process. Surface and Coatings Technology 202, 1443–1454. https://doi.org/10.1016/j.surfcoat.2007.06.065

Pham, D.Q., Berndt, C.C., Gbureck, U., Zreiqat, H., Truong, V.K., Ang, A.S.M., 2019. Mechanical and chemical properties of Baghdadite coatings manufactured by atmospheric plasma spraying. Surface and Coatings Technology 378, 124945. https://doi.org/10.1016/j.surfcoat.2019.124945

Popov, B.N., 2015. Corrosion Engineering: Principles and Solved Problems, Corrosion Engineering: Principles and Solved Problems. https://doi.org/10.1016/C2012-0-03070-0

Pouilleau, J., Devilliers, D., Garrido, F., Durand-Vidal, S., Mahé, E., 1997. Structure and composition of passive titanium oxide films. Materials Science and Engineering B 47, 235–243. https://doi.org/10.1016/S0921-5107(97)00043-3

Poza, P., Múnez, C.J., Garrido-Maneiro, M.A., Vezzù, S., Rech, S., Trentin, A., 2014. Mechanical properties of Inconel 625 cold-sprayed coatings after laser remelting. Depth sensing indentation analysis. Surface and Coatings Technology 243, 51–57. https://doi.org/10.1016/j.surfcoat.2012.03.018

Qin, F., Jiang, L., Long, P., Xu, S., Ling, Y., Yu, Y., Wei, G., 2020. Effect of deposition potential on preparation and corrosion resistance of SiO2 film on copper.

International Journal of Electrochemical Science 15, 6478–6487. https://doi.org/10.20964/2020.07.49

Qin, J., Huang, Q., Wang, X., Suo, X., Wang, J., Li, H., 2021. Interfacial metal/ceramic bonding mechanism for metallization of ceramics via cold spraying. Journal of Materials Processing Technology 288, 116845. https://doi.org/10.1016/j.jmatprotec.2020.116845

Qiu, X., Tariq, N. ul H., Qi, L., Wang, J.Q., Xiong, T.Y., 2020. A hybrid approach to improve microstructure and mechanical properties of cold spray additively manufactured A380 aluminum composites. Materials Science and Engineering A 772. https://doi.org/10.1016/j.msea.2019.138828

Qiu, X., Tariq, N. ul H., Wang, J. qiang, Tang, J. rong, Gyansah, L., Zhao, Z. po, Xiong, T. ying, 2018. Microstructure, microhardness and tribological behavior of Al2O3 reinforced A380 aluminum alloy composite coatings prepared by cold spray technique. Surface and Coatings Technology 350, 391–400. https://doi.org/10.1016/j.surfcoat.2018.07.039

Qvistgaard, E., Christensen, R., Torp-Pedersen, S., Bliddal, H., 2006. Intra-articular treatment of hip osteoarthritis: A randomized trial of hyaluronic acid, corticosteroid, and isotonic saline. Osteoarthritis and Cartilage 14, 163–170. https://doi.org/10.1016/j.joca.2005.09.007

Ramaswamy, Y., Wu, C., Van Hummel, A., Combes, V., Grau, G., Zreiqat, H., 2008. The responses of osteoblasts, osteoclasts and endothelial cells to zirconium modified calcium-silicate-based ceramic. Biomaterials 29, 4392–4402. https://doi.org/10.1016/j.biomaterials.2008.08.006

Richer, P., Jodoin, B., Ajdelsztajn, L., Lavernia, E.J., 2006. Substrate roughness and thickness effects on cold spray nanocrystalline Al-Mg coatings. Journal of Thermal Spray Technology 15, 246–254. https://doi.org/10.1361/105996306X108174

Rocheville, C.F., 1963. Device for treating the surface of a workpiece. Us3100724 1–6.

Roland, T., Pelletier, H., Krier, J., 2013. Scratch resistance and electrochemical corrosion behavior of hydroxyapatite coatings on Ti6Al4V in simulated physiological media. Journal of Applied Electrochemistry 43, 53–63.

https://doi.org/10.1007/s10800-012-0504-3

Rubino, F., Astarita, A., Carlone, P., Genna, S., Leone, C., Memola Capece Minutolo, F., Squillace, A., 2016. Selective Laser Post-Treatment on Titanium Cold Spray Coatings. Materials and Manufacturing Processes 31, 1500–1506. https://doi.org/10.1080/10426914.2015.1037912

Sabard, A., McNutt, P., Begg, H., Hussain, T., 2020. Cold spray deposition of solution heat treated, artificially aged and naturally aged Al 7075 powder. Surface and Coatings Technology 385, 125367. https://doi.org/10.1016/j.surfcoat.2020.125367

Sadeghi, E., Markocsan, N., Joshi, S., 2019. Advances in Corrosion-Resistant Thermal Spray Coatings for Renewable Energy Power Plants. Part I: Effect of Composition and Microstructure, Journal of Thermal Spray Technology. Springer US. https://doi.org/10.1007/s11666-019-00938-1

Sakaki, K., Shimizu, Y., 2001. Effect of the increase in the entrance convergent section length of the gun nozzle on the high-velocity oxygen fuel and cold spray process. Journal of Thermal Spray Technology 10, 487–496. https://doi.org/10.1361/105996301770349268

Sarao, T.P.S., Sidhu, H.S., Singh, H., 2012. Characterization and in vitro corrosion investigations of thermal sprayed hydroxyapatite and hydroxyapatite-titania coatings on Ti alloy. Metallurgical and Materials Transactions A: Physical Metallurgy and Materials Science 43, 4365–4376. https://doi.org/10.1007/s11661-012-1175-8

Sasikumar, Y., Indira, K., Rajendran, N., 2019. Surface Modification Methods for Titanium and Its Alloys and Their Corrosion Behavior in Biological Environment: A Review. Journal of Bio- and Tribo-Corrosion 5, 0. https://doi.org/10.1007/s40735-019-0229-5

Schaffer, A.W., Pilger, A., Engelhardt, C., Zweymueller, K., Ruediger, H.W., 1999. Increased blood cobalt and chromium after total hip replacement. Journal of Toxicology - Clinical Toxicology 37, 839–844. https://doi.org/10.1081/CLT-100102463

Schmidt, T., Assadi, H., Gärtner, F., Richter, H., Stoltenhoff, T., Kreye, H., Klassen, T.,

2009. From particle acceleration to impact and bonding in cold spraying. Journal of Thermal Spray Technology 18, 794–808. https://doi.org/10.1007/s11666-009-9357-7

Schmidt, T., De, E., 2006. (12) Patent Application Publication (10) Pub . No .: US 2006 / 0027687 A1 1.

Schmidt, T., Gärtner, F., Assadi, H., Kreye, H., 2006. Development of a generalized parameter window for cold spray deposition. Acta Materialia 54, 729–742. https://doi.org/10.1016/j.actamat.2005.10.005

Schumacher, T.C., Volkmann, E., Yilmaz, R., Wolf, A., Treccani, L., Rezwan, K., 2014. Mechanical evaluation of calcium-zirconium-silicate (baghdadite) obtained by a direct solid-state synthesis route. Journal of the Mechanical Behavior of Biomedical Materials 34, 294–301. https://doi.org/10.1016/j.jmbbm.2014.02.021

Sciences, B., 1999. THE PROBLEM OF CORROSION IN ORTHOPAEDIC IMPLANT MATERIALS IndiaOrth - the Indian Orthopedic Website - http://www.indiaorth.org IndiaOrth - the Indian Orthopedic Website - http://www.indiaorth.org. Update 9, 1–5.

Sedrak, P., Hache, P., Horner, N.S., Ayeni, O.R., Adili, A., Khan, M., 2021. Differential characteristics and management of pseudoseptic arthritis following hyaluronic acid injection is a rare complication: A systematic review. Journal of ISAKOS. https://doi.org/10.1136/jisakos-2020-000438

Sekhar, B.C., 2007. Patent Application Publication (10) Pub . No .: US 2007 / 0197807 A1. Us 2007 / 0197807 a1 1, 19–21.

Seo, D., Sayar, M., Ogawa, K., 2012. SiO 2 and MoSi 2 formation on Inconel 625 surface via SiC coating deposited by cold spray. Surface and Coatings Technology 206, 2851–2858. https://doi.org/10.1016/j.surfcoat.2011.12.010

Sharma, M.M., Eden, T.J., Golesich, B.T., 2015. Effect of Surface Preparation on the Microstructure, Adhesion, and Tensile Properties of Cold-Sprayed Aluminum Coatings on AA2024 Substrates. Journal of Thermal Spray Technology 24, 410–422. https://doi.org/10.1007/s11666-014-0175-1

Shen, J., Chen, B., Ye, X., Imai, H., Umeda, J., Kondoh, K., 2017. The formation of

bimodal multilayered grain structure and its effect on the mechanical properties of powder metallurgy pure titanium. Materials and Design. https://doi.org/10.1016/j.matdes.2016.12.004

Shi, R., Wang, B., Yan, Z., Wang, Z., Dong, L., 2019. Effect of surface topography parameters on friction and wear of random rough surface. Materials 12. https://doi.org/10.3390/ma12172762

Shockley, J.M., Descartes, S., Vo, P., Irissou, E., Chromik, R.R., 2015. The influence of Al2O3 particle morphology on the coating formation and dry sliding wear behavior of cold sprayed Al-Al2O3 composites. Surface and Coatings Technology 270, 324–333. https://doi.org/10.1016/j.surfcoat.2015.01.057

Simchi, A., Danninger, H., 2004. Effects of porosity on delamination wear behaviour of sintered plain iron. Powder Metallurgy 47, 73–80.

Singh, D., Singh, R., Boparai, K.S., Farina, I., Feo, L., Verma, A.K., 2018. In-vitro studies of SS 316 L biomedical implants prepared by FDM, vapor smoothing and investment casting. Composites Part B: Engineering 132, 107–114. https://doi.org/10.1016/j.compositesb.2017.08.019

Singh, H., Bala, N., Kaur, N., Sharma, S.K., Kim, D.Y., Prakash, S., 2015. Effect of additions of TiC and Re on high temperature corrosion performance of cold sprayed Ni-20Cr coatings. Surface and Coatings Technology 280, 50–63. https://doi.org/10.1016/j.surfcoat.2015.08.002

Singh, R., Dahotre, N.B., 2007. Corrosion degradation and prevention by surface modification of biometallic materials. Journal of Materials Science: Materials in Medicine 18, 725–751. https://doi.org/10.1007/s10856-006-0016-y

Singh, R., Martin, M., Dahotre, N.B., 2005. Influence of laser surface modification on corrosion behavior of stainless steel 316L and Ti-6Al-4V in simulated biofluid. Surface Engineering 21, 297–306. https://doi.org/10.1179/174329405X55320

Singh, S., Singh, H., Buddu, R.K., 2020a. Microstructural investigations on bonding mechanisms of cold-sprayed copper with SS316L steel. Surface Engineering 36, 1067–1080. https://doi.org/10.1080/02670844.2019.1698163

Singh, S., Singh, H., Chaudhary, S., Buddu, R.K., 2020b. Effect of substrate surface

roughness on properties of cold-sprayed copper coatings on SS316L steel. Surface and Coatings Technology 389, 125619. https://doi.org/10.1016/j.surfcoat.2020.125619

Singh, S., Singh, P., Singh, H., Buddu, R.K., 2019. Characterization and comparison of copper coatings developed by low pressure cold spraying and laser cladding techniques. Materials Today: Proceedings 18, 830–840. https://doi.org/10.1016/j.matpr.2019.06.509

Singh, T.P., Singh, Harpreet, Singh, Hazoor, 2012. Characterization, corrosion resistance, and cell response of high-velocity flame-sprayed HA and HA/TiO 2 coatings on 316L SS. Journal of Thermal Spray Technology 21, 917–927. https://doi.org/10.1007/s11666-012-9782-x

Singleton, M.C., LeVeau, B.F., 1975. The hip joint: structure, stability, and stress. A review. Physical Therapy 55, 957–973. https://doi.org/10.1093/ptj/55.9.957

Sinha, A., Islam, M.A., Farhat, Z., 2015. Reciprocating wear behavior of Al alloys: effect of porosity and normal load. Int J Metall Mater Eng 1, 117.

Skjöldebrand, C., Tipper, J.L., Hatto, P., Bryant, M., Hall, R.M., Persson, C., 2022. Current status and future potential of wear-resistant coatings and articulating surfaces for hip and knee implants. Materials Today Bio 15. https://doi.org/10.1016/j.mtbio.2022.100270

Smolen, J.S., Aletaha, D., 2015. Rheumatoid arthritis therapy reappraisal: Strategies, opportunities and challenges. Nature Reviews Rheumatology 11, 276–289. https://doi.org/10.1038/nrrheum.2015.8

Soares, F.M.S., Elias, C.N., Monteiro, E.S., Coimbra, M.E.R., Santana, A.I.C., 2021. Galvanic Corrosion of Ti Dental Implants Coupled to CoCrMo Prosthetic Component. International Journal of Biomaterials 2021. https://doi.org/10.1155/2021/1313343

Sochart, D.H., 1999. Relationship of acetabular wear to osteolysis and loosening in total hip arthroplasty. Clinical orthopaedics and related research 135—150.

Sophia Fox, A.J., Bedi, A., Rodeo, S.A., 2009. The basic science of articular cartilage: Structure, composition, and function. Sports Health 1, 461–468.

https://doi.org/10.1177/1941738109350438

Soro, N., Attar, H., Brodie, E., Veidt, M., Molotnikov, A., Dargusch, M.S., 2019. Evaluation of the mechanical compatibility of additively manufactured porous Ti–25Ta alloy for load-bearing implant applications. Journal of the Mechanical Behavior of Biomedical Materials 97, 149–158. https://doi.org/10.1016/j.jmbbm.2019.05.019

Sousa, B.C., Gleason, M.A., Haddad, B., Champagne, V.K., Nardi, A.T., Cote, D.L., 2020. Nanomechanical characterization for cold spray: From feedstock to consolidated material properties. Metals 10, 1–71. https://doi.org/10.3390/met10091195

Souto, R.M., Laz, M.M., Reis, R.L., 2003. Degradation characteristics of hydroxyapatite coatings on orthopaedic TiAlV in simulated physiological media investigated by electrochemical impedance spectroscopy. Biomaterials 24, 4213–4221. https://doi.org/10.1016/S0142-9612(03)00362-4

Sova, A., Grigoriev, S., Okunkova, A., Smurov, I., 2013. Cold spray deposition of 316L stainless steel coatings on aluminium surface with following laser post-treatment. Surface and Coatings Technology 235, 283–289. https://doi.org/10.1016/j.surfcoat.2013.07.052

Steenkiste, T.H.V., Smith, J.R., Teets, R.E., 2002. Aluminum coatings via kinetic spray with relatively large powder particles. Surface and Coatings Technology 154, 237–252. https://doi.org/10.1016/S0257-8972(02)00018-X

Steenkiste, V., 2007. (12) United States Patent 2.

Su, Y.L., Yao, S.H., Leu, Z.L., Wei, C.S., Wu, C.T., 1997. Comparison of tribological behavior of three films - TiN, TiCN and CrN - Grown by physical vapor deposition. Wear 213, 165–174. https://doi.org/10.1016/S0043-1648(97)00182-8

Sun, L., 2018. Thermal Spray Coatings on Orthopedic Devices: When and How the FDA Reviews Your Coatings. Journal of Thermal Spray Technology 27, 1280–1290. https://doi.org/10.1007/s11666-018-0759-2

Syggelos, S.A., Aletras, A.J., Smirlaki, I., Skandalis, S.S., 2013. Extracellular matrix degradation and tissue remodeling in periprosthetic loosening and osteolysis:

Focus on matrix metalloproteinases, their endogenous tissue inhibitors, and the proteasome. BioMed Research International 2013. https://doi.org/10.1155/2013/230805

Tabbara, H., Gu, S., McCartney, D.G., Price, T.S., Shipway, P.H., 2011. Study on process optimization of cold gas spraying. Journal of Thermal Spray Technology 20, 608–620. https://doi.org/10.1007/s11666-010-9564-2

Tan, A.W.Y., Sun, W., Bhowmik, A., Lek, J.Y., Song, X., Zhai, W., Zheng, H., Li, F., Marinescu, I., Dong, Z., Liu, E., 2019. Effect of Substrate Surface Roughness on Microstructure and Mechanical Properties of Cold-Sprayed Ti6Al4V Coatings on Ti6Al4V Substrates. Journal of Thermal Spray Technology 28, 1959–1973. https://doi.org/10.1007/s11666-019-00926-5

Tan, A.W.Y., Sun, W., Phang, Y.P., Dai, M., Marinescu, I., Dong, Z., Liu, E., 2017. Effects of Traverse Scanning Speed of Spray Nozzle on the Microstructure and Mechanical Properties of Cold-Sprayed Ti6Al4V Coatings. Journal of Thermal Spray Technology 26, 1484–1497. https://doi.org/10.1007/s11666-017-0619-5

Tang, J., Zhao, Z., Liu, H., Cui, X., Wang, J., Xiong, T., 2019. A novel bioactive Ta/hydroxyapatite composite coating fabricated by cold spraying. Materials Letters 250, 197–201. https://doi.org/10.1016/j.matlet.2019.04.123

Tang, J.R., Zhao, Z.P., Cui, X.Y., Wang, J.Q., Xiong, T.Y., 2020. Microstructure and bioactivity of a cold sprayed rough/porous Ta coating on Ti6Al4V substrate. Science China Technological Sciences 63, 731–739. https://doi.org/10.1007/s11431-019-1446-0

Tejero-Martin, D., Rezvani Rad, M., McDonald, A., Hussain, T., 2019. Beyond Traditional Coatings: A Review on Thermal-Sprayed Functional and Smart Coatings. Journal of Thermal Spray Technology 28, 598–644. https://doi.org/10.1007/s11666-019-00857-1

Tepzz, Z.T., Christopher, W., John, A., Us, C.T., 2016. Designated Extension States : Designated Validation States : 1, 1–11.

Tesfay, A.W., Nath, S.K., Ray, S., 2009. Effect of transfer layer on dry sliding wear behaviour of cast Al-based composites synthesized by addition of TiO2 and MoO3.

Wear. https://doi.org/10.1016/j.wear.2009.01.033

Thurston, S.H., 1900. Method of Impacting One Metal Upon Another. Us706701 1.

Toh, W.Q., Tan, X., Bhowmik, A., Liu, E., Tor, S.B., 2017. Tribochemical characterization and tribocorrosive behavior of CoCrMo alloys: A review. Materials 11. https://doi.org/10.3390/ma11010030

Toibah, A.R., Sato, M., Yamada, M., Fukumoto, M., 2016. Cold-Sprayed TiO2 Coatings from Nanostructured Ceramic Agglomerated Powders. Materials and Manufacturing Processes 31, 1527–1534. https://doi.org/10.1080/10426914.2015.1090587

Tritschler, B., Forest, B., Rieu, J., 1999. Fretting corrosion of materials for orthopaedic implants: A study of a metal/polymer contact in an artificial physiological medium. Tribology International 32, 587–596. https://doi.org/10.1016/S0301-679X(99)00099-7

Unabia, R., Candidato, R., Pawłowski, L., 2018. Current progress in solution precursor plasma spraying of cermets: A review. Metals 8, 1–18. https://doi.org/10.3390/met8060420

Ure, N.A.T., 1955. NATURE March 26, 1955 175, 6–7.

Uwais, Z.A., Hussein, M.A., Samad, M.A., Al-Aqeeli, N., 2017. Surface Modification of Metallic Biomaterials for Better Tribological Properties: A Review. Arabian Journal for Science and Engineering 42, 4493–4512. https://doi.org/10.1007/s13369-017-2624-x

Venkatraman, V., Wong, M.K., Shalita, C., Parente, B., Lad, S.P., 2020. Cobalt-Induced Toxicity and Spasticity Secondary to Hip Arthroplasty: Case Report and Review of the Literature. Cureus 12, 10–13. https://doi.org/10.7759/cureus.12368

Vilardell, A.M., Cinca, N., Garcia-Giralt, N., Dosta, S., Cano, I.G., Nogués, X., Guilemany, J.M., 2020. In-vitro comparison of hydroxyapatite coatings obtained by cold spray and conventional thermal spray technologies. Materials Science and Engineering C 107, 110306. https://doi.org/10.1016/j.msec.2019.110306

Walker, P.R., LeBlanc, J., Sikorska, M., 1989. Effects of aluminum and other cations on the structure of brain and liver chromatin. Biochemistry 28, 3911–3915.

https://doi.org/10.1021/bi00435a043

Wang, F.F., Li, W.Y., Yu, M., Liao, H.L., 2014. Prediction of critical velocity during cold spraying based on a coupled thermomechanical eulerian model. Journal of Thermal Spray Technology 23, 60–67. https://doi.org/10.1007/s11666-013-0009-6

Wang, H, Zhao, Q., Xin, S., Zhao, Y., Zhou, W., Zeng, W., 2021. Microstructural morphology effects on fracture toughness and crack growth behaviors in a high strength titanium alloy. Materials Science and Engineering A. https://doi.org/10.1016/j.msea.2021.141626

Wang, Q., Eltit, F., Feng, R., Garbuz, D., Duncan, C., Masri, B.A., Greidanus, N., Cox, M.E., Wang, R., 2022. Nature of fretting corrosion products in CoCrMo hip implants from in vivo study to in vitro simulation. Materialia. https://doi.org/10.1016/j.mtla.2022.101433

Wang, Q., Spencer, K., Birbilis, N., Zhang, M.X., 2010. The influence of ceramic particles on bond strength of cold spray composite coatings on AZ91 alloy substrate. Surface and Coatings Technology 205, 50–56. https://doi.org/10.1016/j.surfcoat.2010.06.008

Wang, Y., Yan, Y., Su, Y., Qiao, L., 2017. Release of metal ions from nano CoCrMo wear debris generated from tribo-corrosion processes in artificial hip implants. Journal of the Mechanical Behavior of Biomedical Materials 68, 124–133. https://doi.org/10.1016/j.jmbbm.2017.01.041

Webster, T.J., Siegel, R.W., Bizios, R., 1999. Osteoblast adhesion on nanophase ceramics. Biomaterials. https://doi.org/10.1016/S0142-9612(99)00020-4

Wei, K., Lv, M., Zeng, X., Xiao, Z., Huang, G., Liu, M., Deng, J., 2019. Effect of laser remelting on deposition quality, residual stress, microstructure, and mechanical property of selective laser melting processed Ti-5Al-2.5Sn alloy. Materials Characterization 150, 67–77. https://doi.org/10.1016/j.matchar.2019.02.010

Wong, W., Irissou, E., Ryabinin, A.N., Legoux, J.G., Yue, S., 2011. Influence of helium and nitrogen gases on the properties of cold gas dynamic sprayed pure titanium coatings. Journal of Thermal Spray Technology 20, 213–226.

https://doi.org/10.1007/s11666-010-9568-y

Wong, W., Rezaeian, A., Irissou, E., Legoux, J.G., Yue, S., 2010. Cold spray characteristics of commercially pure Ti and Ti-6Al-4V. Advanced Materials Research 89–91, 639–644. https://doi.org/10.4028/www.scientific.net/AMR.89-91.639

Wong, W., Vo, P., Irissou, E., Ryabinin, A.N., Legoux, J.G., Yue, S., 2013. Effect of particle morphology and size distribution on cold-sprayed pure titanium coatings. Journal of Thermal Spray Technology 22, 1140–1153. https://doi.org/10.1007/s11666-013-9951-6

Wu JM, Xiao F, Hayakawa S, Tsuru K, Takemoto S, Osaka A. Journal of Materials Science: Materials in Medicineacidic titanium tetrafluoride solution. Journal of Materials Science: Materials in Medicine. 2003;14:1027-1032

YAMADA, M., KANDORI, Y., SATO, K., FUKUMOTO, M., 2009. Fabrication of Titanium Dioxide Photocatalyst Coatings by Cold Spray. Journal of Solid Mechanics and Materials Engineering 3, 210–216. https://doi.org/10.1299/jmmp.3.210

Yandouzi, M., Richer, P., Jodoin, B., 2009. SiC particulate reinforced Al–12Si alloy composite coatings produced by the pulsed gas dynamic spray process: Microstructure and properties. Surface and Coatings Technology 203, 3260–3270.

Yin, S., Cizek, J., Cupera, J., Hassani, M., Luo, X., Jenkins, R., Xie, Y., Li, W., Lupoi, R., 2021. Formation conditions of vortex-like intermixing interfaces in cold spray. Materials and Design 200, 109444. https://doi.org/10.1016/j.matdes.2020.109444

Yin, S., Suo, X., Liao, H., Guo, Z., Wang, X., 2014. Significant influence of carrier gas temperature during the cold spray process. Surface Engineering 30, 443–450. https://doi.org/10.1179/1743294414Y.0000000276

Yoo, J.J., Kim, Y.-M., Yoon, K.S., Koo, K.-H., Song, W.S., Kim, H.J., 2005. Alumina-on-Alumina Total Hip Arthroplasty. The Journal of Bone & Joint Surgery 87, 530–535. https://doi.org/10.2106/jbjs.d.01753

Yoon, E.S., Singh, R.A., Oh, H.J., Kong, H., 2005. The effect of contact area on nano/micro-scale friction. Wear 259, 1424–1431.

https://doi.org/10.1016/j.wear.2005.01.033

Zahiri, S.H., Fraser, D., Gulizia, S., Jahedi, M., 2006. Effect of processing conditions on porosity formation in cold gas dynamic spraying of copper. Journal of Thermal Spray Technology 15, 422–430. https://doi.org/10.1361/105996306X124437

Zeng, G., Zahiri, S.H., Gulizia, S., Chen, Y., Xu, C., Chen, X.B., Cole, I., 2020. A comparative study of cell growth on a cold sprayed Ti–Ta composite. Journal of Alloys and Compounds 826. https://doi.org/10.1016/j.jallcom.2020.154014

Zhang, J., Kong, D., 2018. Effect of laser remelting on microstructure and immersion corrosion of cold–sprayed aluminum coating on S355 structural steel. Optics and Laser Technology 106, 348–356. https://doi.org/10.1016/j.optlastec.2018.04.026

ZHANG, L., QU, X. hui, DUAN, B. hua, HE, X. bo, QIN, M. li, 2008. Effect of porosity on wear resistance of SiCp/Cu composites prepared by pressureless infiltration. Transactions of Nonferrous Metals Society of China (English Edition) 18, 1076–1082. https://doi.org/10.1016/S1003-6326(08)60184-3

Zhang, X., Shi, G., Sun, X., Zheng, W., Lin, X., Chen, G., 2019. Factors influencing the outcomes of artificial hip replacements. Cells Tissues Organs 206, 254–262. https://doi.org/10.1159/000500518

Zhang, Z., Liu, F., Han, E.H., Xu, L., Uzoma, P.C., 2019. Effects of Al2O3 on the microstructures and corrosion behavior of low-pressure cold gas sprayed Al 2024-Al2O3 composite coatings on AA 2024-T3 substrate. Surface and Coatings Technology 370, 53–68. https://doi.org/10.1016/j.surfcoat.2019.04.082

Zhou, X., Mohanty, P., 2012. Electrochemical behavior of cold sprayed hydroxyapatite/titanium composite in Hanks' solution. Electrochimica Acta 65, 134–140. https://doi.org/10.1016/j.electacta.2012.01.018

Zou, Y., Qin, W., Irissou, E., Legoux, J.G., Yue, S., Szpunar, J.A., 2009. Dynamic recrystallization in the particle/particle interfacial region of cold-sprayed nickel coating: Electron backscatter diffraction characterization. Scripta Materialia 61, 899–902. https://doi.org/10.1016/j.scriptamat.2009.07.020